SAPIENZA
UNIVERSITÀ DI ROMA

Faculty of Civil and Industrial Engineering
Department of Structural and Geotechnical Engineering

PhD Thesis in Structural Engineering

Macromechanical hysteretic models with damage for the analysis of the nonlinear response of historical masonry structures

A thesis submitted in partial fulfillment of the requirements for the
Degree of Doctor of Philosophy by:

PhD Candidate:
Alessandra Paoloni
XXXVI Cycle

Advisor:
Prof. Daniela Addessi

Co-Advisor:
Prof. Domenico Liberatore

Rome, March 2024

Abstract

The study of the behavior of existing masonry structures has certainly been a topic of great interest for long time, especially considering the large number of existing buildings still in use in Italy and in several other Countries, both of historic interest or commonly used, and their high vulnerability particularly when seismic actions are taken into account.

Several modeling approaches have been developed over time, varying the level of detail required in describing the structural response and the amount of input parameters needed. Obviously, the greater the degree of accuracy requested in the behavior description, the more detailed the available information regarding the material and the entire structure shall be. In addition to classical micromechanical, macromechanical, and multi-scale finite element models, however, macro-models are widely adopted approaches, especially between practitioners', and, more specifically, the equivalent frame model. Thanks to the combination of a low computational burden and a reduced number of input parameters, in fact, it is still possible to achieve a good level of accuracy and the possibility to study the response to dynamic actions.

However, the adoption of advanced constitutive laws, appropriate for the material that shall be described, is a crucial prerequisite for the equivalent frame approach to be competitive in masonry modeling with respect to more detailed modeling techniques. Indeed, the description of the characteristic phenomena of the highly nonlinear masonry material, such as the presence of strength and stiffness degradation, as well as plasticity and energy dissipation, cannot be ignored.

At the same time, classical equivalent frame approaches are based on assumptions, at the structural level, that can result overly idealized with respect to the

real conditions observable in existing buildings, such as box-like behavior or good connections between walls or between walls and floors. Out-of-plane flexural mechanisms, which can occur very easily, as observed in real structures' behavior under recent earthquake events, are therefore commonly neglected in favor of studying in-plane mechanisms only.

This work focuses its attention, then, on the development of a macroelement applicable in the framework of the equivalent frame approach. First, an enhancement of the modified Bouc-Wen constitutive law presented in Liberatore et al. (2019) is given, proposing the introduction of an additional flexibility increase term to the damage term, with the aim of better reproducing the degrading behavior of masonry panels from a phenomenological point of view. The flexibility increase term, by acting as an expansion of the elastic displacement, affects the loading and unloading bramches of the cyclic curve, enhancing the stiffness degradation and affecting the dissipated energy. Thermodynamic admissibility conditions in presence of damage and flexibility increase are studied, entailing constraints on system parameters. Additional constraints arise from consistency conditions on the transformation of the pure hysteretic system into the system with damage and flexibility increase. This advanced constitutive law is then implemented in a force-based beam macroelement with lumped nonlinear shear and flexural hinges. A discussion on the degrading behavior in the dynamic field is carried on. The force-based formulation is then extended to the dynamic field, and considerations are made regarding the effects of different mass matrix evaluation strategies. Beside the classical lumped mass approach, a distributed mass approach consistent with the force-based formulation is introduced. Last, the description of the out-of-plane behavior is introduced, focusing on the degradation effects due to one-way and two-way bending mechanisms. The force-based formulation is extended to its three-dimensional components, and the nonlinear cyclic behavior that describes the degrading mechanisms is accounted by introducing two nonlinear flexural hinges in the out-of-plane direction.

Each implementation is validated through comparison with experimental results available in the literature and, in some cases, with the results obtained through different numerical approaches.

In the end, the results of an experimental campaign involving a masonry wall

and an unreinforced masonry prototype building are also reproduced. The capability of the model to describe the characteristics of real existing masonry structures is then tested and confirmed.

Acknowledgements

Vorrei esprimere tutta la mia gratitudine in primo luogo alla Prof.ssa Addessi e al Prof. Liberatore, per essere stati una guida e un supporto fondamentali nel corso del mio percorso sia dal punto di vista scientifico che umano. Il raggiungimento di questo traguardo è stato possibile solo grazie al loro aiuto, attenzione e dedizione, nonchè alle opportunità di crescita che mi hanno costantemente offerto.

Ringrazio inoltre mia madre e mia sorella Elisa, che sono state sempre presenti nei momenti più difficili, credendo in me e supportandomi nelle fasi più stressanti.

Ringrazio naturalmente Andrea, per essermi stato accanto, aiutandomi a superare le più disparate difficoltà che ci sono state con pazienza e incoraggiamento, aiutandomi ad essere più forte ogni volta.

Non posso non ringraziare Simone, per la sincera amicizia e la condivisione di gioie e ansie di questo percorso, e non solo. Ringrazio anche Cristina, che è molto più che solamente la mia "compagna di stanza 317", e Giuseppe, Giacomo, Sawan, Daniela e Livio, per aver reso migliori anche le più noiose giornate. Infine Alessandra e Francesca, persone davvero preziose.

Infine ringrazio mio padre. Sebbene non possa più essere qui per gioire con me di questo traguardo, penso che lo avrebbe reso orgoglioso. Devo a lui la curiosità, la passione e il desiderio di apprendimento che mi animano e che mi hanno spinta anche ad intraprendere questo percorso.

Contents

List of Figures

List of Tables

Chapter 1

Introduction

The use of masonry as a construction technology dates back at the beginning of human civilization and architecture history. At the earliest stages, huge blocks of stone were employed for megalithic constructions, while, about 6000 years ago, the first raw bricks were employed at the beginning of the Mesopotamian civilization. Since then, masonry has been succesfully employed for several centuries, modifying brick and material technologies or even alternating the use of bricks with natural stone elements, where environmental conditions allowed it. The solidity and durability of the obtained structures, together with the low cost of the single material elements, therefore, allowed this construction technology to be used for a long time, until the early years of the XX century, when alternative materials, such as steel or reinforced concrete, almost replaced it. Nevertheless, a huge part of the architectural and hystorical heritage, as well as residential constructions, is still constituted by masonry structures all over Europe.

Masonry is a composite material, resulting from the arrangement of bricks or blocks of different sizes, which can be natural or artificial and disposed in a more or less regular texture, and possibly connected with mortar. For instance, a simple classification can be based on stone disposition in the construction and refinement in the surface finish, as shown in 1.1. Mortar has been used since the beginning of the Roman Age, with the purpose to act as a bond between the elements, allowing to develop different textures and dispositions of the elements, to realize a monolithic system. The need to obtain a system capable of avoiding discontinuities

or fragile sections in vertical and orthogonal directions of the wall, encouraged the realization of more refined textures, such as the *Opus Quadratum*, in which bricks disposition realized a texture with orthostats and transversal elements.

(a) Rubble   (b) Ashlar   (c) Coursed ashlar
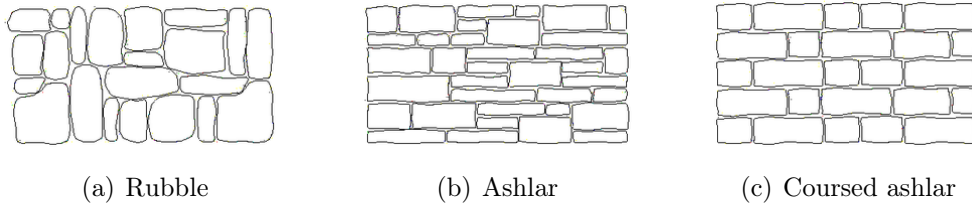
Figure 1.1: Stone masonry textures (from Lourenço (1998))

Due to the strong heterogeneity of the material created by these complex textures, different modelling techniques are available in the literature to reproduce its static and dynamic mechanical behavior. Depending on the scale of the analyzed specimen, as well as on the type of loading conditions and the particular response that should be investigated and reproduced at the structural level, the need is to find adequate computational tools being accurate and efficient. These should be enough refined to reproduce as accurately as possible the mechanical performance of the material, but also easy-to-use and rapid, in terms of computational costs. At the same time, way too complex or refined models risk to remain limited to small portions or simple walls, or to favor theoretical aspects to the detriment of the analysis of a global performance. They may not, in fact, respond to the demands of more articulated projects or the needs of practitioners.

Despite the large variety of arrangements and types of masonry available, the main vulnerabilities of such material can be easily identified. Among these, the main aspect is the low or zero tensile strength, to which a low resistance to horizontal loads is linked, in favor of a high compressive strength and therefore a good response to vertical loads. This makes masonry strongly disadvantaged in case of both monotonic and cyclic loads in the in-plane and out-of-plane cases, and to seismic actions. All these characteristics shoud be properly addressed when a detailed performance assessment is required. Therefore, due to the poor tensile strength of the mortar, fracture phenomena are triggered, which increase as the load is increased. It becomes important, then, to explicitly model the highly

nonlinear behavior of masonry, characterized by the evolution of damage, experienced in terms of loss of strength and stiffness and energy dissipation, as well as the onset of irreversible plastic deformations. The constitutive laws that must therefore be used, should take into account both damage and the phenomenon of strain softening. When a detailed description of the various masonry components, commonly adopted in micromechanical models, is not possible, the adoption of phenomenological constitutive laws allows the description of the main in-plane and out-of-plane mechanisms, both for flexural and shear mechanisms. The adoption of macromechanical models based on the continuum mechanics, and more specifically of macroelement models, allows the above requirements to be satisfied under appropriate hypotheses, permitting a sufficiently realistic reproduction of the structural performance, and compensating for the limited detail of the model.

1.1   Aims and objectives

As mentioned in the previous paraghraph, when choosing between the different modeling strategies avialable to reproduce the behavior of masonry structures, it is necessary to consider the type of analysis that has to be perfomed, being local or global, the kind of structure to be modeled and the level of detail expected when analyzing the structural response. To this end, simple but efficient models are required, especially when complex structures or large scale investigations need to be performed, in order to capture in an accurate but rapid way the structural behavior.

In this framework, aim of this thesis can be summarized with the following points:

- Propose a refined macroelement applicable in the context of the simplified equivalent frame modeling approach. The proposed macroelement bases its formulation of the enforcement of equilibrium in strong form, while lumped hinges are considered to describe the nonlinearity of the masonry material.

- Regarding the consitutive law adopted for these latter, which describes the flexural and the shear behavior, an enhancement of the modified Bouc-Wen

hysteresis already presented in the literature is considered. This enhancement, applicable also to other constitutive laws, consists of the introduction of a flexibility increase term, which helps to reduce the stiffness of the loading and unloading branches of the constitutive curve. Thus, a phenomenological hysteretic law capable of describing the degradation phenomena that occur in masonry due to external actions is introduced in the macroelement.

- The possibility to include the description of the main out-of-plane mechanisms that can occur in masonry structures is also introduced. Out-of-plane mechanisms are often neglected in simplified approaches such as the equivalent frame approach, causing important underestimation of the actual structural behavior and failure modes.

- Finally, the model will be validated considering well-known experimental tests available in the literature in the static field, while parametric analyses will be performed to study the performance of the macroelement and the evolution of damage in the dynamic field. Applications to more complex cases, such as entire structures and experimental tests on small structures, will be presented.

1.2   Structure of the thesis

The present thesis will be divided into 7 Chapters, including the Introduction. A brief description of each of the chapters is given in the following.

- **Chapter 2: Mechanical behavior and modeling techniques for masonry**
  The typical mechanical behavior of masonry is introduced, starting from a brief recall of the single constituents to the description of the composite material, to the main mechanisms involving the structural level. The main modeling procedures and techniques are then revised, focusing in particular on the macroelement and equivalent frame modelling approaches, in both the in-plane and out-of-plane directions.

- **Chapter 3: Nonlinear hinges constitutive model**

  After a brief recall of the main characteristics of the classical Bouc-Wen model, followed by a description of some of the multiple modifications that can be found in the literature regarding the classical formulation, a modified Bouc-Wen model with damage and flexibility increase is proposed and later validated by comparing the numerical outcomes with well-known experimental results available in the literature. Discussions on thermodynamic admissibility and on Drucker's postulate are made, as well as considerations regarding the dissipated energy.

- **Chapter 4: 2D macroelement formulation**

  The proposed macroelement, included in the framework of the equivalent frame approach, and the adopted force-based formulation with lumped hinges in both the static and dynamic cases are described. The performance of the macroelement in the static field is validated. A squat and a slender panel are then studied in the dynamic field, adopting different excitations. A slender wall is then analyzed, considering linear and nonlinear dynamic excitations, and its performance is compared to a 2D finite element model of the same panel.

- **Chapter 5: Three-dimensional macroelement formulation**

  In this chapter, the formulation of the 2D macroelement is extended to the three-dimensional field, giving a detailed formulation for the force-based beam element and the introduction of nonlinear hinges, with the aim of reproducing the main out-of-plane flexural mechanisms typical of masonry walls. The model is then validated through comparison with experimental results available in the literature. A more refined formulation is then proposed, to further enrich the model and capture complex two-way bending mechanisms.

- **Chapter 6: Case studies: experimental tests and numerical simulations**

  Two case studies are analyzed, where the proposed equivalent frame model is adopted to model an unreinforced wall and an unreinforced one-storey pro-

totype, tested under static and dynamic loadings, respectively. The main aspects of the experimental campaign are described, and comparison between the experimental and numerical outcomes are given, exploring the capabilities of the proposed macroelement in reproducing real structural behavior.

- **Chapter 7: Conclusions**
  The final chapter contains the concluding remarks, highlighting the main results obtained in the work and proposing future developments.

Chapter 2

Mechanical behavior and modeling techniques for masonry

The following Chapter intends to give a brief summary of the principal aspects of the mechanical behavior of masonry, as well as the most diffused modeling approaches available in the literature.

In particular, Section 2.1 deals with the main aspects of the mechanical behavior of masonry material, intended as a composite medium, and of masonry structures. In this latter case, the local and global mechanisms developed during the simultaneous application of vertical and horizontal loads are revised, with particular attention to the in-plane and out-of-plane behavior of masonry panels. Examples available in the literature are considered.

Section 2.2 focuses the attention on the Equivalent Frame Model (EFM), starting from the hypoteses according to which the approach can be used, following with the principal macromechanical models developed. A brief revision of the most common modeling approaches, namely Finite Element Models (FEM) and Discrete Element Models (DEM) and limit analysis, is also reported.

2.1 Masonry mechanical behavior

The heterogeneity resulting from the complex interaction between the single constituents of masonry, strongly characterizes its behavior as a structural material,

thus making it an interesting object of study. From a mechanical point of view, three different constituents can be distinguished, namely units, mortar and interface. While the first two affect the global behavior in terms of strength and deformation, the latter is an expression of their mechanical interaction. Mechanical characteristics can thus be evaluated through laboratory tests performed on the single constituents or on small and large assemblages.

2.1.1 Mechanical behavior of the constituents

Compressive tests are widely employed in the literature for the evaluation of the main parameters of masonry constituents.

Units can be investigated through axial tests to determine their compressive strength, and the relationship between compressive and tensile strength can be investigated through bi-axial tests. Instead, prismatic or cylindrical specimens are adopted for the evaluation of mortar compressive response, to determine stiffness characteristics such as Young's modulus E and Poisson ratio ν and the compressive strength. These all depend on the weakness and the type of mortar, and on the applied confinement stress, while the tensile strength can be obtained through indirect tensile or flexural tests. An extensive study on the variation of units and mortar properties depending on different conditions can be found in McNary and Abrams (1985). In general, while units exhibit a more brittle behavior with higher strengths, mortar shows lower values of strength with higher deformations.

Van der Pluijm (1993), van der Pluijm (1997), Van der Pluijm et al. (2000) and Drysdale et al. (1982) contain extensive studies on the behavior of unit-mortar interface, which can be considered as the weakest constituent of masonry. Tensile and shear tests are performed in order to evaluate the behavior of masonry under tension, which appears to be ruled almost completely by the beahvior of the interface. In general, depending on tests set-up and mortar type, low tensile strength and softening behavior can be determined from tensile tests, together with stiffness parameters such as the Young's modulus E of the interface and the corresponding Poisson ratio ν, while from flexural tests the mode I fracture energy G_{fI} can be determined. Moreover, shear tests on small assemblages pointed out the shear behavior: a residual shear stress is reached after a peak phase and a

softening branch; mode II fracture energy G_{fII} can be evaluated, depending on the applied compression load, and dilatancy can be also distingushed (Fig. 2.1).

(a)   (b)
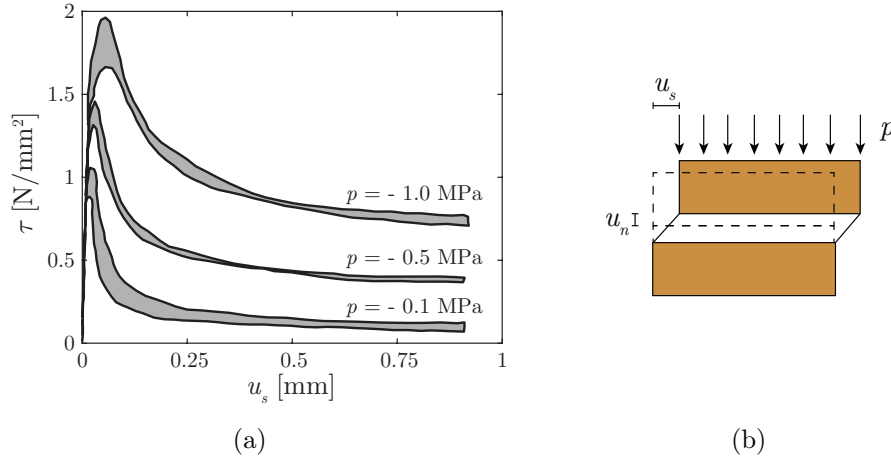
Figure 2.1: Van der Pluijm (1993): (a) shear stress-shear displacement curves for different values of confining stress p; (b) dilatant behavior.

For a more detailed description regarding the consituent behavior, the previously cited literature can be referred.

2.1.2   Mechanical behavior of the composite material

Being a composite material with a nonhomogeneous and anisotropic behavior, the response of masonry has to be investigated beyond the behavior of its single constituents, also giving particular attention to the disposition and the bond between these latter.

Tests on small assemblages can be useful to determine mechanisms that develop in orthogonal, parallel and inclined directions with respect to unit-mortar joints, even if they are not representative of the local or global mechanisms typical of full-scale walls. Planes of weakness depending on mortar joint orientation and applied stresses can be defined, with the respective modes of failure and strengths.

Uni-axial tension and compression and bi-axial tests are useful to identify the main characteristics of the composite material.

2.1.2.1   Uni-axial behavior

In general, masonry can be treated as a quasi-brittle material, showing an evident softening behavior in the post-peak phase, where a gradual decrease of the strength of the system corresponds to increasing deformations. The presence of micro-cracks in mortar or voids and inclusions in units, that progressively grow under increasing stresses or deformations, facilitates the formation of macro-cracks. When displacement or deformation controlled analyses are performed, the growth of these macro-cracks results in a softening branch of the curve after the peak load (Lourenço (1998)).
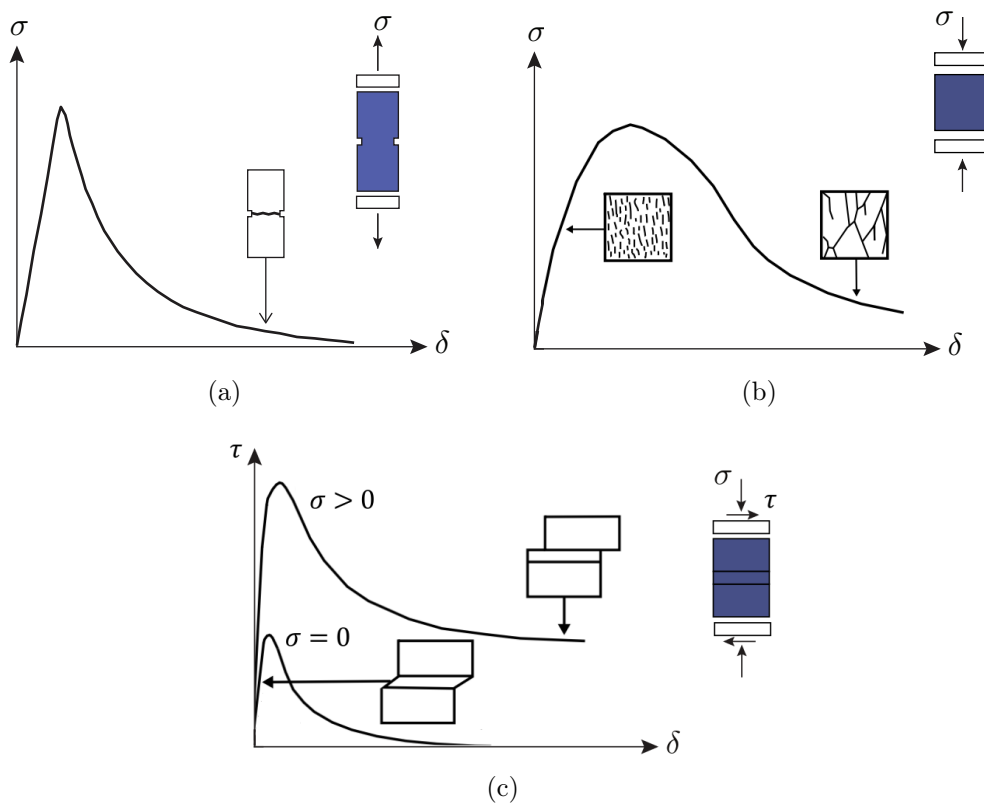
Figure 2.2: Typical response under uni-axial tension (a), compression (b) and shear (c) (modified from Lourenço (1998))

Figs. 2.2 (a), (b) and (c) show typical quasi-brittle stress-strain curves under uni-axial tension and compression and pure shear, respectively. The softening behavior is clearly visible in Figs. 2.2 (a) and (b), where by evaluating the integral

of the stress-strain curves, fracture enery G_{fI} and compressive fracture energy G_{cI} can be obtained for failure mode I. In general, being the compressive strength much higher than the tensile one, compressive fracture energy assumes higher values. Slip of the mortar-unit interface, denoted as failure mode II and giving the response in Fig. 2.2 (c), is described as well by fracture energy mode II G_{fII}. It is noteworthy that for shear cases, softening depends also on a degradation of cohesion, but it is common practice to neglect the effect of shear for continuum models, as it depends on the interface, and to consider it only in micromechanical models.

Compressive and tensile behavior under uni-axial states are now analyzed more in detail, referring to experimental tests available in the literature.

Compressive mechanical properties are considered as more relevant characteristics, since masonry mainly resists in compression while being very weak in tension. This is mainly due to the bond between its constituents, mortar and brick, which exhibits a weak behavior when subjected to tensile stress.

Being so relevant, numerous compressive tests performed on stacks of clay units bonded with mortar under axial force applied in the direction normal to the bed joints can be found in the literature (McNary and Abrams, 1985; Kaushik et al., 2007).

Experimental tests in McNary and Abrams (1985) showed the tendency of mortar to expand laterally more than bricks during compressive tests, due to its lower stiffness compared to that of bricks. However, the bond between mortar and bricks and the friction that originates act as a lateral confinement in the interface, originating shear stresses at the interface that result in an internal stress state composed of a tri-axial compression state in the mortar and a biaxial tension in the brick. Thus, vertical cracks initiate and proceed until failure. Strength and deformation properties that lead to failure are then investigated, also referring to previous theories such as those in Hilsdorf (1969), according to which the difference in the elastic properties of bricks and mortar induces failure, or in Atkinson and Noland (1983), where nonlinear behavior of mortar is also considered. Analytical models are also obtained in following works (Kaushik et al., 2007). The onset and propagation of cracks under compression uni-axial states are then investigated in Page (1981, 1983), being uni-axial state a particular case of bi-axial

tests performed in the study. The variation of failure modes and crack developement is then studied under different orientation of the bed joints with respect to the applied compressive stress (Fig. 2.3).

(a) $\vartheta=0°$ (b) $\vartheta=22.5°$ (c) $\vartheta=45°$ (d) $\vartheta=67.5°$ (e) $\vartheta=90°$
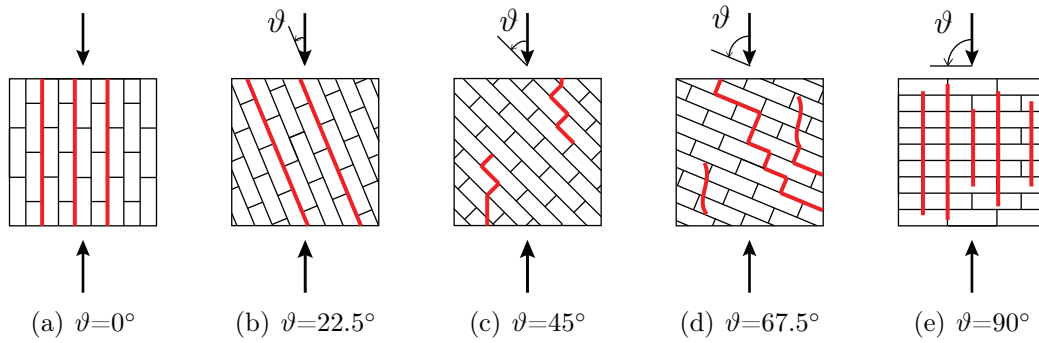
Figure 2.3: Page (1981, 1983): failure modes for uni-axial compressive loads with different orientation ϑ for the bed joint direction

The behavior under uni-axial tension strongly depends on the strength of the bond between mortar and units and on the orientation of tensile stress with respect to the bed joints. For instance, when tensile stress are orthogonal to bed joints, failure is ruled by the weakness of the bond between bed joints and units, and the masonry tensile strenght can be equated to the weaker element between the bond strength or the units strength (Lourenço, 1998). For tensile stresses parallel to bed joints, either a zigzag cracks along bed and head joints or vertical cracks along both bricks and units can occur, depending again on which is the weakest element. The first case depends on the fracture energy of mortar joints, while the second on the fracture energy of both head joints and units (Lourenço, 1998). More detailed experimental tests can be found in Backes (1985).

A complete investigation of the tensile uni-axial behavior under different bed joint orientation is carried out in Page (1981) and Page (1983), and reported in Fig. 2.4.

The nonlinear behavior of mortar joints under combined shear and normal stresses is also investigated in the literature (Van der Pluijm, 1993; Van der Pluijm et al., 2000), being characterized by dilatancy effects, which is influenced by the bond between mortar and units and by the presence of friction, which is increased for higher compression stresses.

(a) ϑ=0° (b) ϑ=22.5° (c) ϑ=45° (d) ϑ=67.5° (e) ϑ=90°
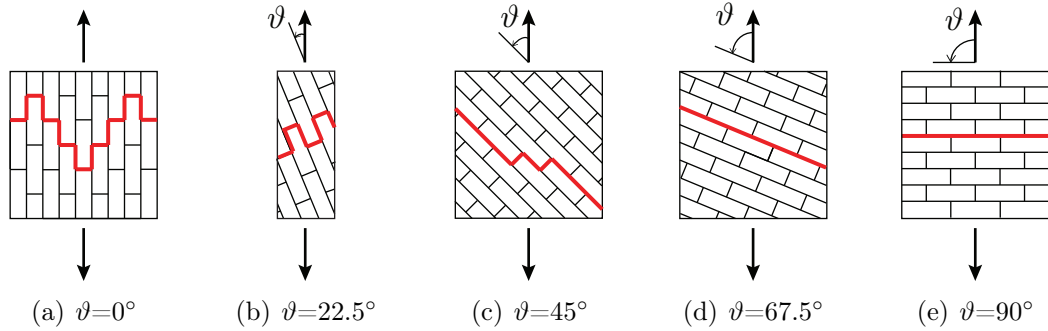
Figure 2.4: Page (1981, 1983): failure modes for uni-axial tensile loads with different orientation ϑ for the bed joint direction

2.1.2.2 Bi-axial behavior

Bi-axial tests, representative of the behavior of in-plane loaded panels, are used to determine failure surfaces in terms of principal stresses, considering also the influence of bed and head joints. By acting as planes of weakness, and depending on their orientation with respect to the principal stresses, these latter influence the response of the specimen giving different properties and enforcing a strong anisotropy in the composite material.

In Page (1983), an extensive study on the influence of the orientation of bed joints with respect to principal stresses on the strength of half-scale square brickwork panels is carried out. Bi-axial tests are performed varying the vertical to horizontal compressive stess ratio. Results allowed to trace a three-dimensional failure surface in terms of applied principal stresses and their orientation with respect to the bed-joints. In general cases, a low influence of the joint orientation on the strength evaluation was showed, and failure occurred by split of the panel in the direction parallel to the free surface of the specimen when bi-axial stress was applied. However, when one principal stress prevails on the other, cracking or sliding failure modes occurred, strongly depending on the orientation of the bed joint, and strength appeared to be heavily reduced (Fig. 2.5). Moreover, for most of the principal stress ratios analyzed, uni-axial strength for loadings parallel to the bed joints underestimated the biaxial compressive strength.

Further tests were performed in the literature for the investigation of bi-axial

(a)

(b)

(c)
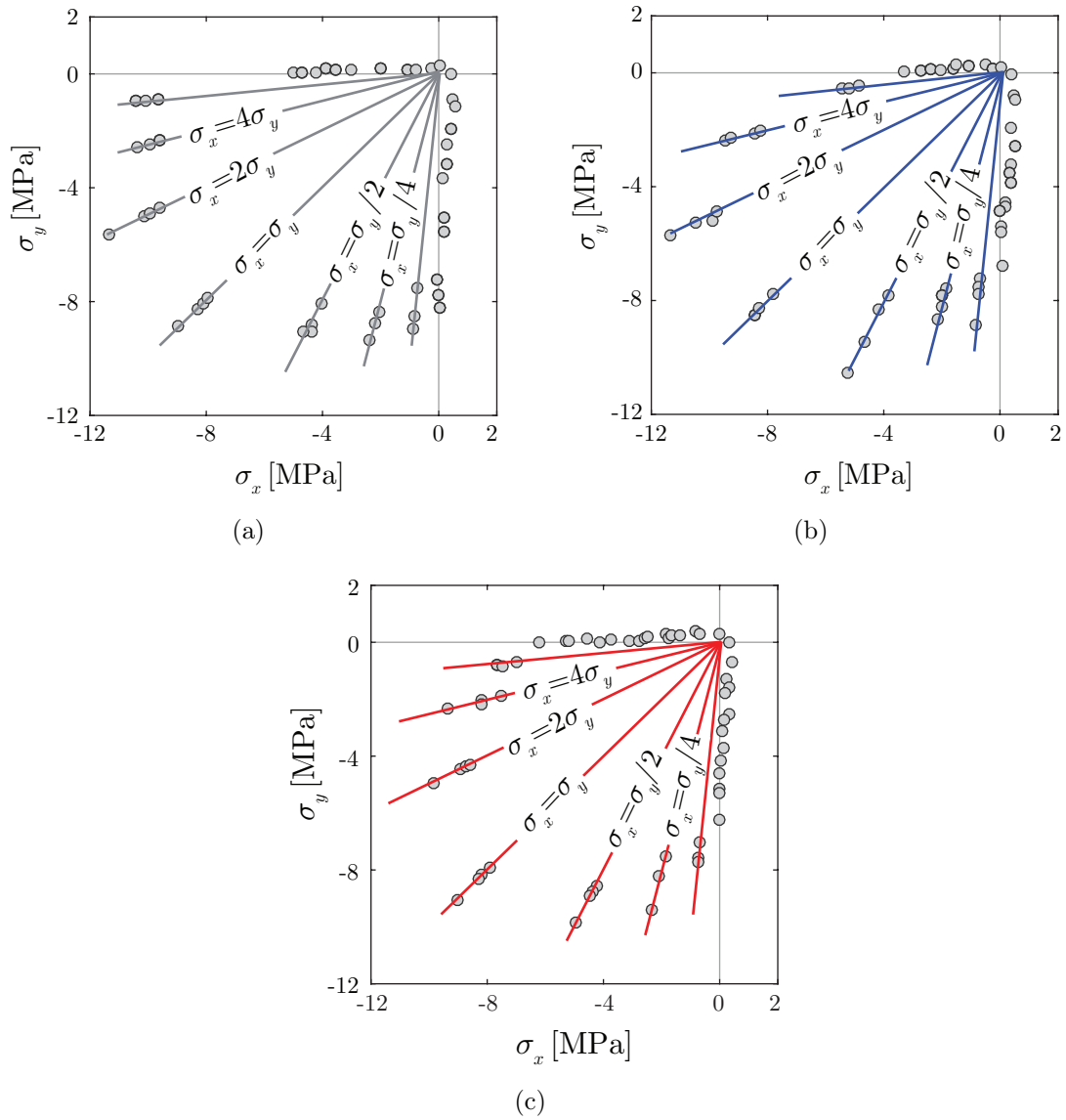
Figure 2.5: Page (1981, 1983): masonry bi-axial strength experimental results for (a) $\vartheta=0°$, (b) $\vartheta=22.5°$, (c) $\vartheta=45°$

behavior of small specimens, allowing to trace nonlinear stress-strain relations for brick panels considering the influence of bed-joints orientation, by both measuring strains during the tests, (Dhanasekar et al., 1985; Naraine and Sinha, 1991), or by adopting empirical relations to evaluate the strains corresponding to the peak stresses (Naraine and Sinha, 1992). Also, different types of masonry have been

investigated under bi-axial test, such as hollow clay brick masonry in Ganz and Thürlimann (1982).

2.1.3 Mechanical behavior of masonry buildings

historical unreinforced masonry constructions are typically composed of load-bearing walls, whose role is to sustain vertical and lateral shear loads, arranged in orthogonal planes and connected with relatively flexible diaphragms. In general, they show a good resistance when subjected to vertical loads, while exhibiting a poor performance under horizontal ones. The low tensile strength proper of the composite material and the high variability of the material texture and mechanical properties emphasize their high vulnerability to these loading conditions. Moreover, critical issues are also represented by inadequate structural details, a scarce quality of connections, such as those wall-to-wall or wall-to-diphragm, or the presence of flexible diaphragms.

(a)   (b)   (c)
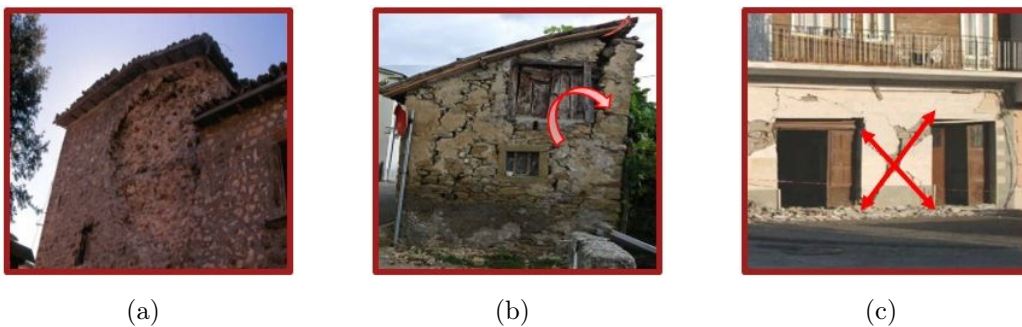
Figure 2.6: Collapse mechanisms of masonry structures: crumbling (a), out-of-plane mechanism (b), in-plane mechanism (c)

Three main collapse mechanisms can then be identified, which are crumbling, out-of-plane and in-plane collapse mechanisms (Fig. 2.6). The adoption of proper textures or material properties can prevent the occurrence of crumbling. Under these conditions, however, the most frequent failure happens because of out-of-plane mechanisms, and when these are prevented, when good connections between orthogonal walls or walls and diqphragms are present and thanks to proper boundary conditions, in-plane mehcanisms can develop.

In the following, in-plane and out-of-plane mechianisms are described, assuming that crumbling is always prevented.

2.1.3.1 In-plane behavior

The observation of experienced damage in experimental tests performed on masonry walls subjected to horizontal in-plane cyclic loading conditions, simulating seismic damage, has shown that two main collapse mechanisms can occur, namely flexural and shear failure, to which different failure modes are associated (Magenes and Calvi, 1997; Calderini et al., 2009). When flexural mechanisms occur, failure mode strongly depends on the relation between the applied vertical load and the compressive strength of the wall. If the vertical load is low with respect to the compressive strength, failure occurs due to *rocking* (Fig. 2.7 (a)): an overturning mechanism starts, with tensile flexural cracking at the corners, and the wall tends to rotate about a toe, where crushing sub-vertical cracks develop, behaving almost like a rigid body. Conversely, for higher vertical loads, failure occurs due to *crushing* of the compressed corner, from which a damage pattern characterized by sub-vertical cracks oriented in the direction of the compressed toe starts to diffuse. Two different failure modes can be distinguished for shear as well. First case is *shear diagonal cracking* (Fig. 2.7 (b)), for which inclined cracks start to develop at the center of the wall and propagate to the corners either following the joint path or passing through the units, depending on the relative strength between units, mortar and interface. Second failure mode is *sliding* (Fig. 2.7 (c)). This is caused by formation of tensile cracks due to the reverse loading under cyclic or seismic actions under low vertical loading or low friction conditions, forming sliding planes along bed-joints usually located at the extremities of the panel.

Experimental tests have been performed to study the influence of geometric parameters, boundary conditions, vertical load and mechanical parameters of the material on the activation of the different failure modes.

For instance, the effect of geometry is investigated in Anthoine et al. (1995), where two specimen with height to width ratio equal to 2 and 1.35 respectively were tested, representing a slender and a squat wall. Loading conditions aimed at reproducing those undergone by piers of common buildings during seismic events,
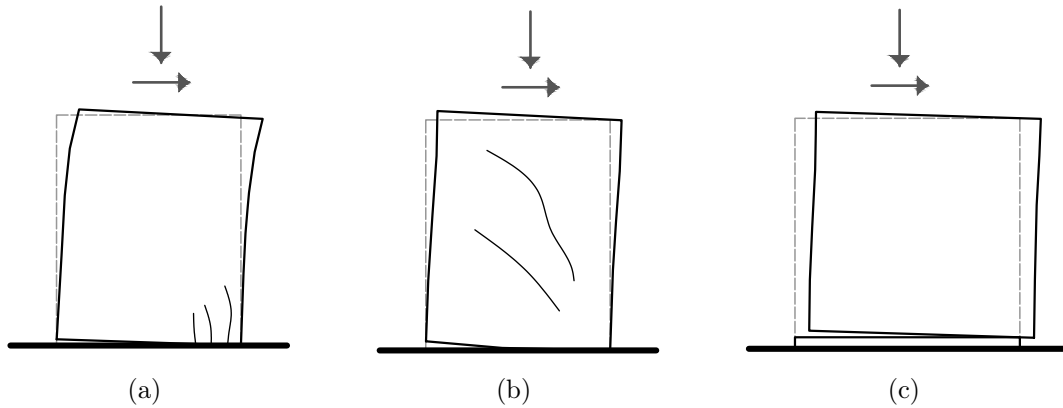
Figure 2.7: In-plane collpase mechanisms of masonry walls: rocking (a), diagonal cracking (b), shear sliding on a horizontal plane (c)

being a constant vertical load and a horizontal quasi-static action. Both ends of the panels were considered fixed, thus enforcing double bending conditions. Results show that the squat wall exhibited a brittle failure with diagonal cracks in the center of the panel, with a dissipating shear behavior, while the slender one showed a rocking mode, with almost no strength degradation, in which damage was located at the top and bottom corners. S-shaped cycles were experienced in this latter case, caused by opening and re-closure of the tensile cracks at the ends. The results, together with a more detailed description of the tests, are reported in Chapter 4.4, where they are adopted for comparisons with numerical results. By performing a second test on the slender wall, increasing the vertical load, it was also seen that a diagonal crack pattern developed.

In general, as pointed out in Calderini et al. (2009), rocking tends to prevail in slender panels, while sliding occurs on in very squat panels. However, when vertical load increases, diagonal cracking tends to prevail over the other modes in moderately slender panels, going from crack propagation along the mortar joints to crack propagation along the units for increasing vertical compression or increasing ratios between mortar and block strength. Increasing interlocking of blocks reduces the possibility to develop diagonal cracking through mortar joints in favour of the other failure modes. Crushing occurs for high levels of vertical compression only.

Experimental tests were made on more complex structures as well, such as the 2-storey masonry building analysed in Magenes et al. (1995), highlighting the variability of failure mechanisms that can occur in unreinforced masonry buildings due to different loading or boundary conditions as well as geometric characteristics.

2.1.3.2 Out-of-plane behavior

Observations made on unreinforced masonry structures after strong earthquakes showed that out-of-plane failure of the structural elements constitutes one of the most serious life-safety hazard for this type of construction (Sorrentino et al., 2017). Considering these observations, according to Lagomarsino et al. (2023), out-of-plane mechanisms can be identified through the geometry of the building, layout of openings, structural details and restraints given by the structure. The two main out-of-plane mechanisms that can occur are one-way and two-way bending modes. The first represents the overturning of the entire wall with the formation of a hinge located at the toe of the wall itself, behaving like a rigid block, and assuming that displacements at the top of the wall are not restrained. The second, instead, is a flexural mechanism that occurs when both the top and base of the panel are restrained, for instance due to a good connection with the upper diaphragm or the presence of a tie-rod. Two hinges are formed in this case at the edges of the panel, and a third hinge forms in the middle, separating two blocks (Fig. 2.8).

Different experimental tests were performed in the literature to investigate the behavior of uncracked masonry walls, such as in Griffith et al. (2004, 2007). The effect of material parameters is investigated, in fact uncracked and pre-cracked conditions are analysed in static tests, showing that the uncracked walls exhibited higher strength values with respect to the pre-crackes walls for the same value of vertical compression. In general, both cases showed an initial linear elastic behavior until the maximum tensile strength, followed by a nonlinear and a decreasing phase when cracks start to evolve, until failure. The curve shows to almost reproduce the behavior of a rocking rigid block.

A comprehensive discussion about the main aspects influencing the out-of-plane mechanisms activation is given in Abrams et al. (2017), where is pointed
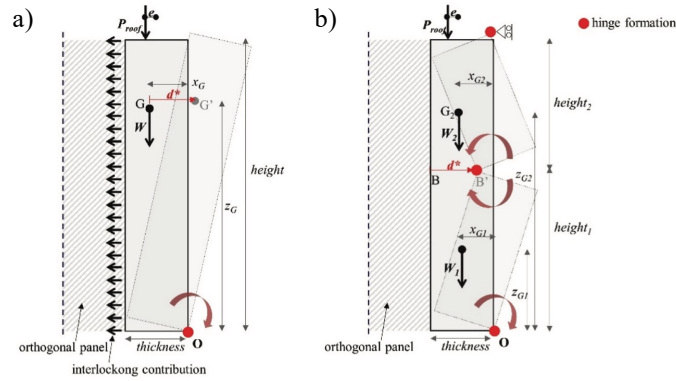
Figure 2.8: Scheme of two possible OOP mechanisms: overturning of the entire wall (a); flexural mechanism of the wall (one-way bending mechanism) (b) (modified from Lagomarsino et al. (2023))

out that beyond boundary conditions, which influence the development of either one-way or two-way bending mechanism, an important role is played by flexural restraints of walls intersections, size and location of openings, the quality of connection between the structural elements and the level of axial force. Moreover, a significant effect is that of the presence of in-plane damage, as the formation of in-plane diagonal cracks due to shear loadings significantly weakens the out-of-plane strength and stiffness, and vice-versa. Accounting for the effect of prior or simoultaneous in-plane actions is then crucial. One last consideration regards the use of dynamic or static analyses. Despite many linear static models are adopted and developed for the estimation of individual walls response, dynamic and non-linear analyses are more accurate and can allow to a better representation and assessment of structural behavior.

2.2 Modeling techniques

Depending on the level of detail needed for the reproduction of masonry response, a different scale of representation of the material can be chosen in the modeling phase. Moreover, the information needed regarding the input parameter and the computational cost of the analyses are important aspects that shall be accounted for in the assessment of the structural response.

Several approaches are available in the literature for modeling masonry constructions. In the following paragraph, the main are recalled.

2.2.1 Macroelement and equivalent frame models

Macroelement models are widespread modeling approaches adopted for the seismic assessment of masonry structures, being the most used even between practitioners and also included in international codes, thanks to the reduced computational cost of the analyses in both 2D and 3D cases and the simple definition of the model and the mechanical parameters. The nonlinear behavior of masonry structures in static and dynamic cases is described in an accurate way, when proper assumptions are satisfied.

The global structural response is usually analyzed when this approach is chosen. The equivalent frame model is, in fact, based on the assumption that crumbling and local out-of-plane mechanisms are prevented, and an almost box-like behavior is assumed Quagliarini et al., 2017; Cattari et al., 2021. Possible local mechanisms, according to classical approaches, should be verified *a priori* through previous local analyses. The behavior is related almost exclusively to the in-plane capacity of the structural elements, even when 3D structures are modeled, and only recently the attention has focused on the description of the out-of-plane mehcanisms (Vanin et al., 2020b; Lagomarsino et al., 2023).

An essential task is a proper identification of the structural elements, namely piers and spandrels. Piers are the vertical elements that can carry both vertical and horizontal loads, while spandrels are the horizontal elements that couple the response of continuous piers horizontally loaded. According to this approach, macroscopic structural elements are defined *a priori* by the modeler through the observation of post-earthquake damage localization and patterns on real buildings. These showed that damage is commonly localized in piers and spandrels, which then can be regarded as deformable elements, while their intersection can be considered as rigid.

The identification of the location and length of piers and spandrels is straightforward when regualr walls are considered, but more complex when the geometry of the structure shows irregular openings distribution. Numerous works can be

found in the literature that discuss this topic (Quagliarini et al., 2017; Berti et al., 2017; Lagomarsino et al., 2013; Parisi and Augenti, 2013; Camilletti et al., 2018; Camata et al., 2022), and some examples are shown in Fig. 2.9.
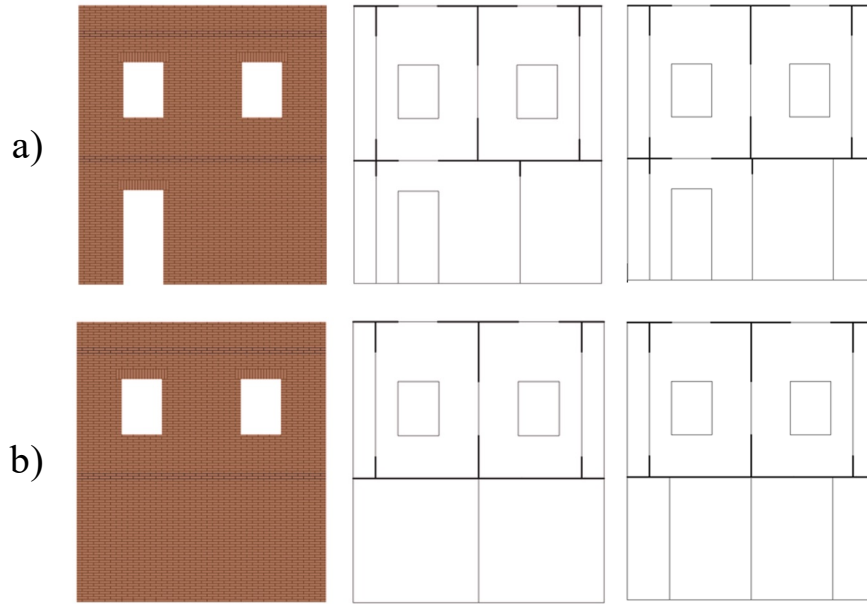
Figure 2.9: Examples of variants of equvalent frame schematization (modified from Camata et al. (2022))

Nevertheless, one of the most adopted is that proposed in Dolce (1991), in which an effective height is defined for piers through a simplified formulation that accounts for the width of the element itself.

In general, being the macroelement modeling technique a simplified approach, it is possible to identify several drawbacks. Even if, as stated before, few recent works can be found in the literature that include the description of the out-of-plane behavior, it is still an ongoing matter of study. In fact, considering that out-of-plane mechanisms are prevented or completely decoupled from the in-plane behavior can lead to underestimation of failure mechanisms or to misleading results, as a simultaneous activation of both in-plane and out-of-plane collapse is possible in real structures. Structural details are also not accurately represented, and connections between orthogonal walls or walls and slabs is not described.

However, the development of computer codes based on macroelement methods,

as that proposed by Lagomarsino et al. (2013), show the competitiveness of the model, being also an efficient tool for practitioners.

According to D'Altri et al. (2019), macroelement models can be divided into two main cathegories, namely equivalent beam or spring-based approaches. Spring-based approaches model structural elements through nonlinear springs in series that model a fictitious frame with an in-plane behavior, such as in Rinaldin et al. (2016).

One of the first works is that of Chen et al. (2008), where two flexural springs, one axial spring and three shear springs are considered in series to model the main in-plane mechanisms of masonry piers, namely the rocking/toe crushing, axial, bed-joint sliding and diagonal tension mechanicsms (Fig. 2.10). The model results from the development of one presented in previous works for the analysis of reiforced concrete walls.
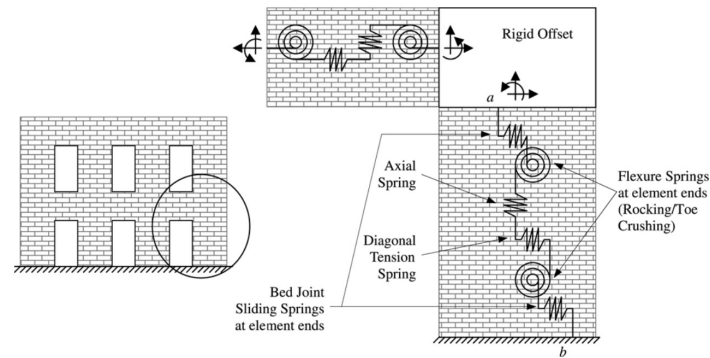
Figure 2.10: Spring-based macroelement, from Chen et al. (2008)

In Penna et al. (2014), an improvement of a previous formulation from Gambarotta and Lagomarsino (1996); Brencich and Lagomarsino (1998) is carried on. A two-node mechanics-based macroelement capable of describing the bending–rocking behavior, the shear behavior and their mutual interaction is proposed (Fig. 2.11). The shear response is decoupled from the axial–flexural response, being concentrated in the central body; the axial-flexural behavior instead is concentrated at the top and bottom interfaces. Further developments are presented in Bracchi et al. (2021) and Bracchi and Penna (2021).

The same model has also been further enriched in Vanin et al. (2020b) with

the introduction of the description of the out-of-plane behavior considering a third node located at midspan (Fig. 2.12). The two blocks are deformable in shear, while the three interfaces enclose the flexural in-plane and out-of-plane behavior, coupled with the axial deformations. The macroelement can also account for second-order geometric effects, and can replicate the rigid block limit analyses of one-way bending out-of-plane mechanisms.
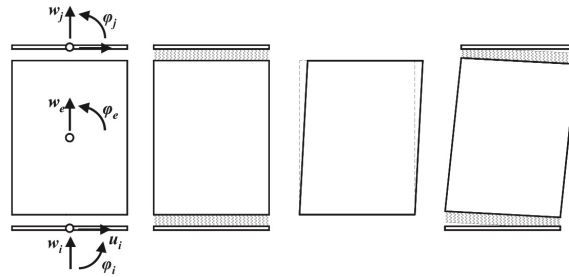
Figure 2.11: Kinematics of the macroelement (from Penna et al. (2014))
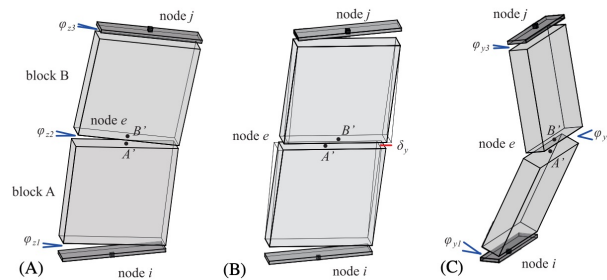
Figure 2.12: Deformation modes of the macroelement: (A) in-plane flexure only, (B) in-plane flexure and shear and (C) out-of-plane response (Vanin et al. (2020b))

A bi-dimensional spring-based element which is worth mentioning in detail, is the one developed by Caliò et al. (2012) and following works. Each macroelement is constituted by a quadrilateral with four rigid edges connected by four hinges and two diagonal nonlinear springs. An interface constituted by a discrete distribution of nonlinear springs orthogonal to the panel side, that govern the flexural behavior, allows the interaction between different panels. An additional longitudinal spring controls the relative motion in the direction of the panel edge. Flexural failure, diagonal shear failure and sliding shear failure are then reproduced under

horizontal and vertical loads. A 3D enrichment of the model has been developed in Pantò et al. (2017) and in Chácara et al. (2018), to evaluate the out-of-plane strength and deformation behavior, in a bi-axial stress regime. In this case, additional degrees of freedom and additional links at the interface are used to simulate torsion effects and out-of-plane mechanisms (Fig. 2.14). For the transversal links, which control both the in-plane and out-of-plane flexural behavior, a modified Takeda hysteresis is adopted in Chácara et al. (2018), as well as for the digonal nonlinear links, while for the shear sliding links an elastic-perfectly plastic behavior is assumed, with the possibility of chosing between a Mohr-Coulomb or a Turnsek-Cacovic yielding criterion.

a)   b)
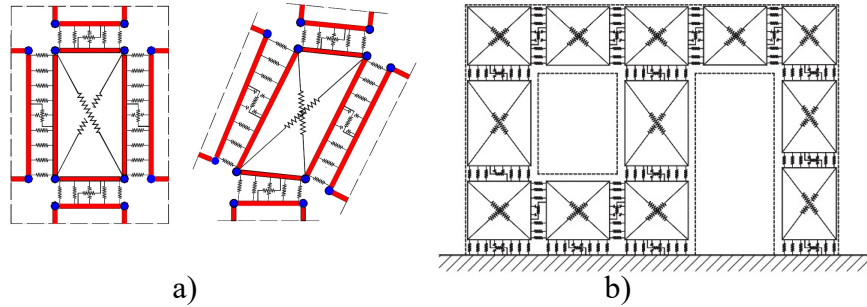
Figure 2.13: Modified from Caliò et al. (2012): basic macro-element in undeformed and deformed configuration (a); macro-element discretization (b)

(A)   (B)   (C)
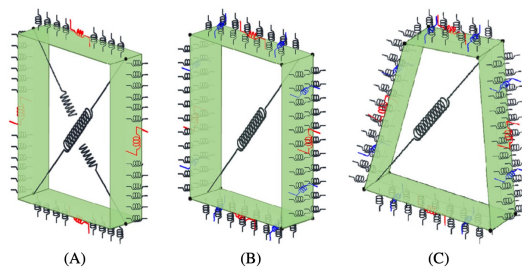
Figure 2.14: Macroelement model: (A) initial plane mechanical scheme, (B) 3-dimensional scheme with regular geometry, and (C) 3- dimensional scheme with irregular geometry (from Chácara et al. (2018))

Other bi-dimensional macroelements, often refferred to in the literature, are those proposed in Braga et al. (1990) and Brencich and Lagomarsino (1998).

A macroelement for the 3D description of in-plane and out-of-plane mechanisms, such as diagonal shear cracking, shear sliding, flexural cracking, toe crushing and diagonal cracking under two-way bending, is proposed in Minga et al. (2020). The macroelement consists in a rectangular block which interacts with adjacent elements through cohesive interfaces along four of its faces, which are used to model the nonlinear mechanisms.

One last type of macroelement models is the one proposed in Malomo and DeJong (2021) and Malomo and DeJong (2022). This particular model, named Macro-Distinct Element Model (M-DEM), is a finite-distinct macroelement model that combines the efficiency of simplified approaches, such as the equivalent frame approach, with interface-based discrete methods. It is capable of reproducing both the in-plane and the out-of-plane mechanisms of a masonry panel, together with their interaction, by means of an assembly of deformable finite element macro-blocks connected by zero-thickness nonlinear interface springs (2.15). The localization of the connection is determined *a priori* by defining an average slope that simulates potential failure planes depending on masonry texture. Out-of-plane behavior is simulated through the introduction of a vertical spring layer which divides the bottom and top macro-blocks, and adequate interface models to reproduce the behavior at the intersection between orthogonal walls is also added. Good results are obtained on C-, U-, and I-shaped components characterized by different masonry types and under quasi-static and dynamic loading conditions.
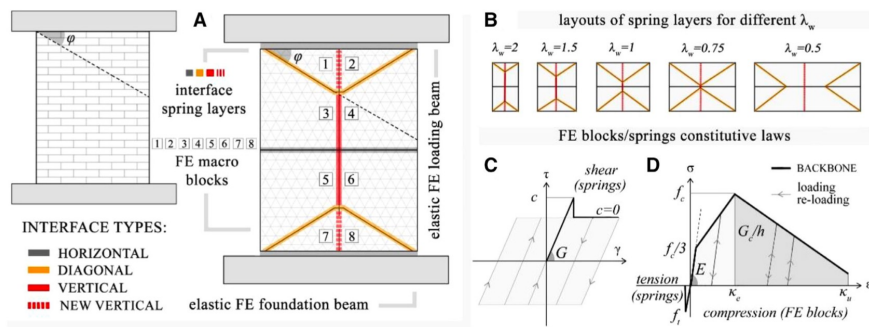
Figure 2.15: (A) Macro-Distinct Element Model (M-DEM) idealization, (B) interface spring layout as a function of the aspect ratio, (C) tension-compression, and (D) shear-compression constitutive laws implemented in the M-DEM model (from Malomo and DeJong (2022))

2.2.1.1   Equivalent Frame Model

In the following, the term "equivalent frame" is used for those macroelements whose behavior can be described through beam elements with a 2D or 3D kinematic behavior, also called "equivalent beam-based approaches" in D'Altri et al. (2019).

One of the first equivalent beam approaches is the one proposed in Tomaževič (1978), where only shear forces in the piers were considered under horizontal loads, while spandrels and nodes were considered a rigid.

Following models, such as Roca et al. (2005) and Belmouden and Lestuzzi (2009), where both spandrels and piers were modeled as deformable elements linked by rigid links, proposed the use of elastic-plasic constitutive laws for the beam elements.

In Addessi et al. (2014), a 2-node beam element with a force-based equilibrated approach for the nonlinear analysis of masonry structures is proposed. A central deformable element with a no-tension constitutive behavior is considered in series with a shear link with an elastic-plastic constitutive law. The model has been later enriched in Liberatore and Addessi (2015) and Addessi et al. (2015) by adding nonlinear lumped plastic hinges with an elastic-plastic behavior, and a predictor-corrector algorithm that allows a proper description of the plasticity in the strength domain. In particular, two flexural hinges and shear link are considered in series with a central elastic Euler-Bernoulli force-based beam element. Activation of the nonlinear hinges is monitored during the different phases of the analysis (Fig. 2.16).

One additional enrichment of the model is proposed in Sangirardi et al. (2019), where the elastic-plastic constitutive behavior is replaced with a Bouc-Wen model modified with the introduction of a damage scalar variable. Additional modifications for the description of pinching are also considered. The model is also described in 4.

The approach described in Lagomarsino et al. (2013) proposes a 2D nonlinear beam with lumped plasticity. A bi-linear constitutive law without hardening and with stiffness degradation is implemented. The model is used in Cattari et al. (2018) for nonlinear dynamic analyses.
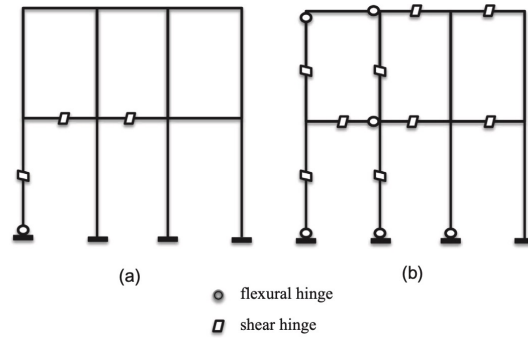
Figure 2.16: Nonlinear hinge activation during two different phases of a pushover analysis (from Liberatore and Addessi (2015))
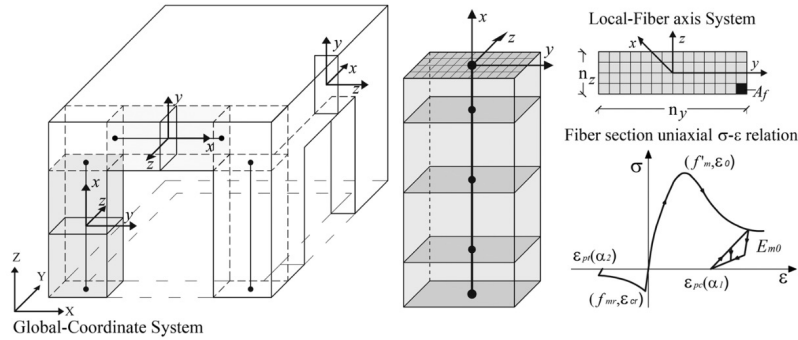
Figure 2.17: Forced-based, fiber-section elements (for masonry piers and spandrels) in the 3D global system; distribution of Gauss–Lobatto points, section subdivision into fibers and fiber nonlinear stress–strain law (from Raka et al. (2015))

One interesting equivalent frame model for unreinforced masonry structures is the one proposed in Raka et al. (2015) and later enriched in Peruch et al. (2019). The element formulation is based on a fiber-section Timoshenko frame element, and the behavior is obtained by numerical integration of the nonlinear response at monitored sections along the element through a Gauss-Lobatto integrations scheme. Cross-sections are discretized, according to the fiber-section approach, and can account for the axial and flexural behaviors and their interaction (Fig. 2.17). A cyclic shear phenomenological constitutive law is also added for the description of shear behavior.

More recent formulations and applications of the equivalent frame approach can be found in Pavanetto et al. (2020) and Cheng and Shing (2022), highlighting

once more the interest shown in the research field for this modeling technique.

2.2.2 Finite Element Models (FEM)

Depending on the scale of representation required for the analysis, Finite Element (FE) formulations constitute a widely adopted modeling procedure, thanks to the possibiltity to choose the most suitable level of detail and to introduce complex nonlinear constitutive laws which can account for advanced mechanisms such as damage, plasticity or friction.

A brief summary of the main FE models available in the literature is presented, divided according to the detail scale.

2.2.2.1 Micromechanical models

A detailed and accurate scale of representation is obtained when micromechanical approaches are used. Local behavior can be described and the actual texture of masonry is reproduced, implicitly taking into account the natural anisotropy of the composite material.

Masonry components are modeled separately, and detailed or simplified modeling strategies can be employed. According to the first case, bricks and mortar can be represented through continuum models, considering their elastic and inelastic properties, while interface is modeled by adopting discontinuous elements with potential crack/slip behavior (Fig. 2.18 (a)). In the second case, mortar joints and interfaces are lumped into discontinuous elements localized at the average plane of the joint thickness, while brick dimensions are expanded and their behavior can be considered as elastic (Fig. 2.18 (b) and (c)) (Lourenço, 1998).

Different constitutive laws are available in the literature for the constituents. For instance, one of the first micromodels presented in the literature is the one proposed by Page (1978), where bricks were modeled as elastic, while mortar joints act as planes of weakness, being nonlinear interface elements with limited shear strength, depending on the bond strength and the level of compression. Material properties and failure criteria, in this case, were derived from experimental bi-axial tests made on half scale brick panels.
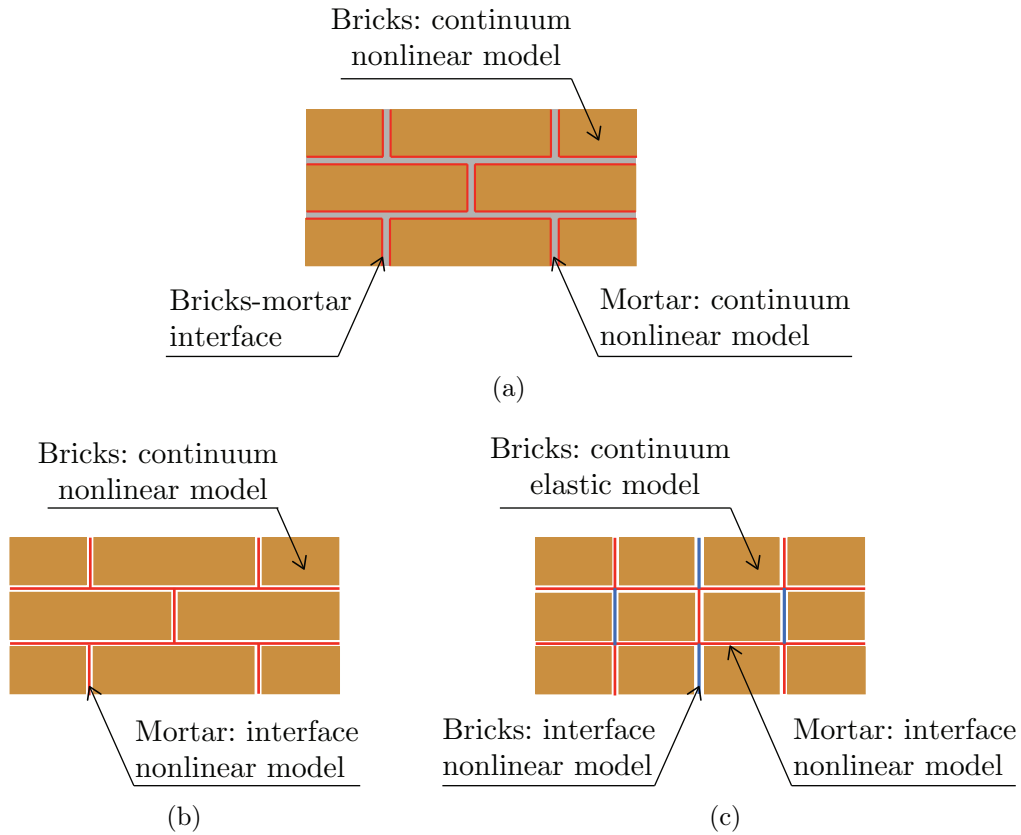
Figure 2.18: Different micromodeling techniques: (a) detailed micromodel, (b) simplified micromodel with crack activation in blocks, (c) simplified micromodel with bricks and interface (Gatta et al. (2019))

A first enhancement of this model, still today diffused for masonry structure analyses, was proposed in Lourenço and Rots (1997), where the entire nonlinear behavior given by shear sliding, compressive crushing and tensile cracking was included in an interface model based on plasticity theories. More enhancements of this latter and other proposed micormechanical models can be found in Gambarotta and Lagomarsino (1997); Oliveira and Lourenço (2004); Sacco and Toti (2010); Addessi and Sacco (2016); Malomo et al. (2018).

The main drawback of micromechanical models is the high computational burden, which often limits the use of these models to small portions or panels, even though few examples of full-scale micromechanical models carried on recently, thanks to advancements in computational tools, can be found in the literature

(D'Altri et al. (2019)).

2.2.2.2 Macromechanical models

Macromechanical approaches model masonry as homogeneized continuum media, not distinguishing between bricks or units, mortar and interface. Phenomenological constitutive laws are considered, derived either from the reproduction of experimental tests performed on large assemblages or panels, or through homogeneization procedures that combine the behavior of the single constituents, in order to obtain constitutive laws that can appropriately approximate the mechanical behavior of the structural element (Fig. 2.19). However, these models are applicable when the dimension of the walls permit to consider that the stresses along the length of the wall are substantially uniform, and the hypothesis of an isotropic material can be adopted. Being an homogeneized medium, mesh discretization is not strictly correlated to the dimension of the constituents. This allows to reduce the computational burden of the analyses and to be capable of modeling both 2D or 3D systems, making it one of the most commonly adopted modeling approaches for real complex structures.
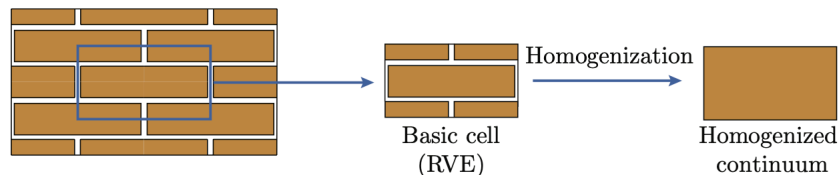
Figure 2.19: Macro-modeling technique: masonry as a homogeneous material (Gatta et al. (2019))

Based on these premises, it is an essential task to chose the most appropriate constitutive law for the equivalent homogeneized material beahvior.

No-tension constitutive laws are one of the first approaches adopted, descending directily from the hypotesis in Heyman (1966). Masonry is idealized as an isotropic material with completely null tensile strength (Maier and Nappi (1990); Angelillo (1994); Alfano et al. (2000); Bruggi and Taliercio (2015); Bruggi et al. (2018)). However, these approaches find limited employement in the study of real cases, also due to their limited application to 3D structures. Moreover, post-peak

behavior cannot be simulated, and even if the no-tensile hypotesis can be considered as conservative, it can lead to different failure mechanisms with respect to those experimentally observed.

A large part of macromechanical models are based on Continuum Damage Mechanics and Plasticity theories. Examples of damage models can be found in Løland (1980); Lubliner et al. (1989); Lee and Fenves (1998); Valente and Milani (2016), used in applications to concrete structures.
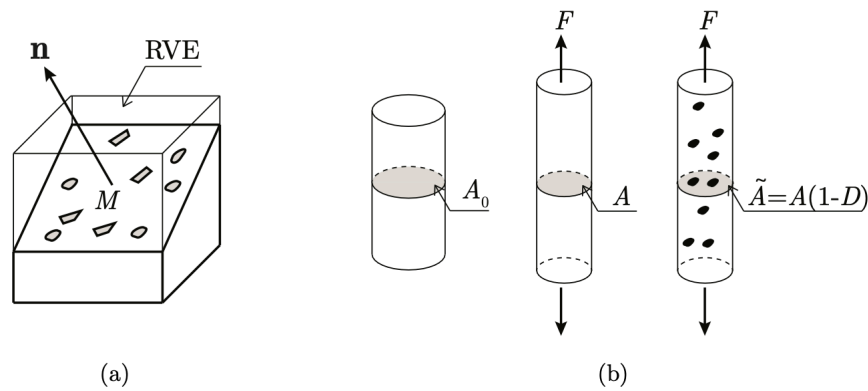
Figure 2.20: Damage Mechanics concepts: (a) RVE, (b) effective area $\tilde{A}$ (Gatta et al. (2019)). A_0 initial transversal area; A reduced cross-sectional area due to transverse strains

Continuum damage models are based on the assumption that the material is treated as a continuum medium, whose strength is deteriorated due to the evolution of cracks under loading conditions. Kachanov (1958) proposed the introduction of an internal scalar variable, whitout a clear phisical meaning, whose role was to measure the internal degradation state of the material. In further developments, the damage variable has been defined as a reduction of the cross-sectional area due to microcracking (Fig. 2.20). Isotropic damage models consider, in the simplest cases, a single scalar variable (Addessi et al., 2002), which multiplies the the initial elastic stiffness tensor, giving a damaged stiffness tensor, while in more refined cases one damage variable in tension and one in compression can be implemented (Gatta et al., 2018). Strain or energy equivalence principles can be considered for the damage formulation (Marfia, 2007).

Despite the assumption of an isotropic behavior results in sufficiently accurate

results, orthotropic nonlinear models have also been developed in the literature (Lourénço et al. (1997); Berto et al. (2002); Pelà et al. (2013); Gatta et al. (2019)). However, an elevated number of mechanical properties, not always available for historical constructions, are required to define material mechanical characteristics, together with a higher computational cost required for the analyses. For these reasons, their application is limited.

One last case are the macromechanical models based on fracture mechanics, i.e. smeared-crack models. These are based on the theory proposed in Rashid (1968) and developed in Rots and De Borst (1987); Jirásek (2011), according to which masonry is treated as a continuum medium, where the total strain is decomposed in an elastic and an inelastic part. This latter, called crack strain, is caused by crack opening, thus being directly related to the traction transmitted across the crack plane.
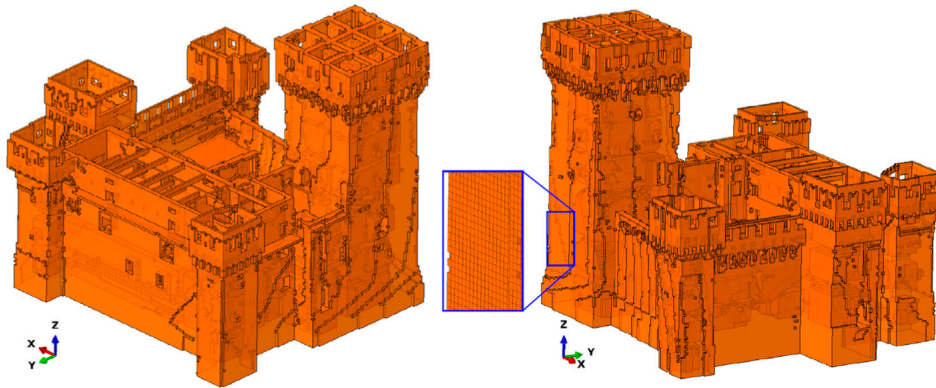
Figure 2.21: 3D finite element model of the fortress. The magnified portion shows the adopted discretization (Degli Abbati et al. (2019))

The capability of this approach to model 2D and 3D complex structures allowed a large variety of applications, not only on masonry historical buildings (Elyamani et al., 2017; Degli Abbati et al., 2019, Fig. 2.21), but also for churches (Milani and Valente, 2015) or bridges (Pelà et al., 2009; Addessi et al., 2021, 2022 Fig. 2.22).

To conclude, macromechanical FE models are one of the most utilized and diffused approaches in commercial codes, thanks to the limited number of param-
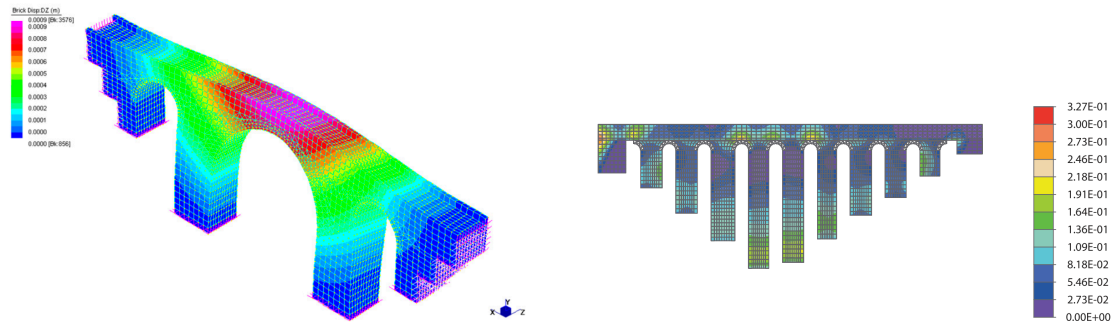
Figure 2.22: Finite element damage models of masonry bridges: a) San Marcello Pistoiese bridge (Pelà et al., 2009); b) Ponte delle Torri in Spoleto (Addessi et al., 2022).

eters that are input in the model and the reduced computational cost, in favour of a good accuracy in the assessment of the response of both simple and more complex structures.

2.2.2.3 Multi-scale models

Multi-scale approaches, which find their location between micro- and macro-mechanical models, have recieved increasing attention in recent periods for the study of heterogeneous microstructured materials. The structural problem is divided in two scales of analysis: a representative volume element (RVE) is selected at the microscale and its stress field is computed and then homogeneized at each material point. This homogeneized constitutive response is then transferred at the macroscale, where the response of an equivalent homogeneized medium is analyzed at the structural level. A *strain-driven* formulation is adopted to evaluate the macroscopic strain vector E at each material point of the macrolevel problem, which is used as input data to solve the Boundary-Value Problem at the RVE level to evaluate its stress-field. According to the Hill-Mandel equivalence principle, the corresponding stress field $\mathbf{\Sigma}$ is evaluated at the macrolevel (Fig. 2.23).

Different proposals are available in the literature for a proper selection of the RVE, considering different geometries, periodicity or non-periodicity (Fig. 2.24), as it should be representative of the material-scale heterogeneity and boundary conditions to obtain a suitable homogeneized behavior.

MACROSCALE   MICROSCALE
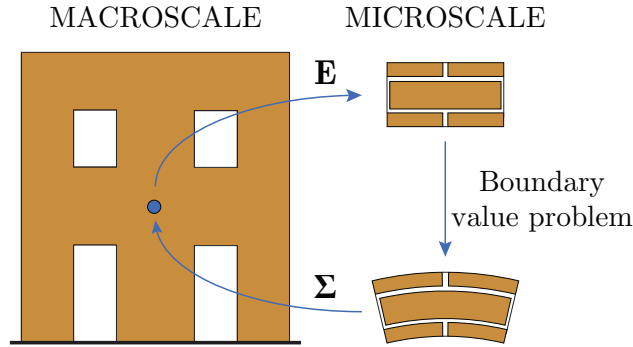
Figure 2.23: Transition from the micro-scale to macro-scale in the multi-scale approach (Gatta et al., 2019)
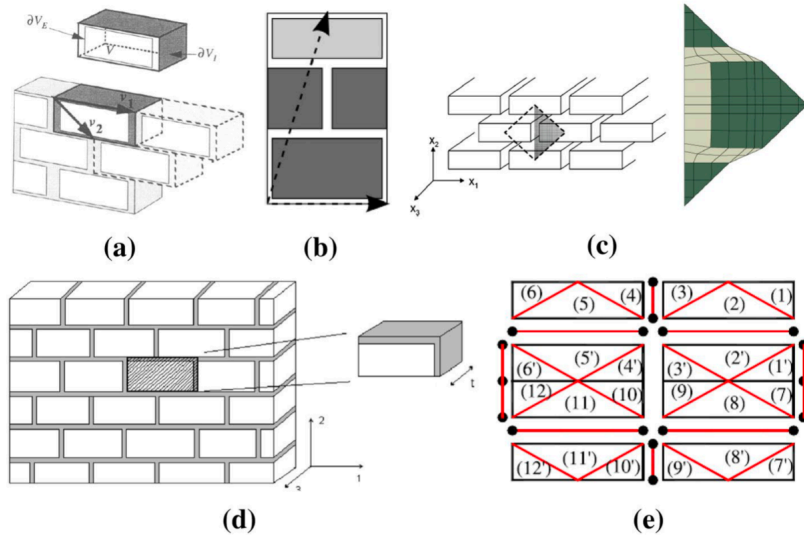
Figure 2.24: Examples of RVEs adopted for the derivation of homogeneized masonry mechanical properties: Anthoine (1995) a); Cavalagli et al. (2011) b); Taliercio (2014) c); Stefanou et al. (2015) d); Milani (2011) e); (D'Altri et al. (2020))

Two main approaches can be adopted, namely a *step-by-step multi-scale approach* or an *adaptive multi-scale approach* (D'Altri et al. (2020)).

Step-by-step approaches can be distinguished according to different formulation strategies. The choice of the most suitable continuum type applied at the macrolevel has been widely debated in the literature, as both classical Cauchy continuum (Luciano and Sacco, 1997; Zucchini and Lourenço, 2009), or Cosserat continuum (Casolo, 2006; Addessi et al., 2010; De Bellis and Addessi, 2011; Ad-

dessi and Sacco, 2012) can be adopted. Localization problems arise when Cauchy continuum is adopted at the macrolevel, being the characteristic lengths of the structural- and material-scales non-intrinsically accounted for in classical Cauchy continuum models, and mesh-sensitivity issues tend to arise when material softening behavior appears (D'Altri et al. (2020)). Cosserat continuum, being a higher-order micro-polar continuum, overcomes localization problems intrinsecally accounting for an internal length of the material. Other approaches can be found that overcome localization issues through different strategies (Massart et al. (2007); Bacigalupo and Gambarotta (2012)). Between the various homogeneization procedures that can be adopted, it is worth mentioning Transformation Field Analysis (TFA) procedure, which is based on the superposition of the effects and requires the computation of localization and transformation tensors (Dvorak, 1992; Sacco, 2009). Step-by-step and point-by-point transitions between the structural- and the material-scale problems are usually considered in these approaches, requiring the adoption of the so-called FE^2 approach, in which Finite Element implementations are made at both the levels of analysis.

Regarding *adaptive multi-scale approaches*, the material-scale model is adaptively inserted and resolved on the structural-scale model thus estabilishing a strong coupling between the two scales. A first-order homogeneized model is used in a first phase to represent the structural response, until a threshold criterion is reached and the interested area is replaced by an heterogeneous behavior. Examples can be found in Leonetti et al. (2018); Lloberas-Valls et al. (2012).

2.2.3   Other modeling approaches

2.2.3.1   Discrete Element Model (DEM)

The Discrete Element (DE) method, proposed originally in Cundall (1971) and extensively revised in Lemos (2007), has the aim of representing masonry as an assembly of distinct component blocks, representative of masonry units, with a mechanical interaction located at their boundaries. As pointed out in Lemos (2007), a classification of this kind of models can be made considering the shape of the elements, dividing *block DE models*, composed of sets of polygonal or polyhedral bodies, which are the most widely used, and *particle DE models*, based on

circular or spherical particles, aimed at a representation of the materials at a finer scale.

Four main assumptions separe DE models from FE models. First, the entire deformability of the system is located at the joints, while only in most recent formulations the blocks are considered as deformable bodies, being originally valid the assuption that blocks were rigid. Second, the interaction between blocks is evaluated in sets of points or edge-to-edge contacts, without a continuous stress distribution throughout the contact surface. Each block can thus be discretized independently from the others (Fig. 2.25). Third, full separation between blocks is allowed, and large displacements are considered. Last, time-stepping algorithms are employed also in the solution of quasi-static problems.

Joint element

Vertex-edge contact

(a)   (b)
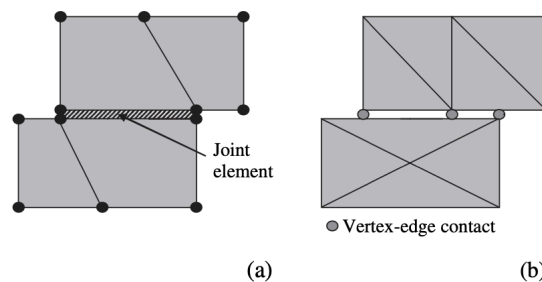
Figure 2.25: Representation of contact between blocks by a) joint elements, and b) point (vertex–edge) contacts. (Lemos (2007))

The mechanical behavior of contact can be represented through a hard (or rigid) or a soft (or deformable) contact. In the first case, no overlap between blocks is enforced; in the second case contact stiffness is defined in normal and shear directions, and contact stresses depend on relative block displacements, resulting in small overlap in compression.

Examples of the application of the DE method can be found in Alexandris et al. (2004); Roca et al. (2010).

2.2.3.2 Limit Analysis

Limit analysis is based on the work of Heyman (1966), where plasticity principles, originally porposed for steel frames, were adopted for the study of masonry structural systems. Three main assumptions are then made, that are that: *i*) masonry

has no tensile strength; *ii*) the general stress levels are so low that the compressive strenght of masonry is infinite; *iii*) sliding of one block upon another cannot occur. Kinematic (upper-bound limit) and static (lower-bound limit) theorems are then formulated to evaluate the collapse mechanisms and collapse multipliers, i.e. the coefficient that multiplied to the external load value gives the collapse condition. If a statically admissible state of equilibrium can be found between the limits given by the two theorems, the structure does not reach the collapse condition.

As pointed out in Heyman (1966), the plastic limit theorems are valid only if the normality condition stands, that is if a simple frictional Coulomb law with associated flow rule is assumed. However, some real cases showed no dilatancy behavior, for which non-associative rules should be assumed.

On the overall, the limit analysis method is a powerful tool to realistically identify the safety level of a structure or to gather information regarding collpase mechanism activation, but no information are given regarding damage evolution during the analysis progression or post-peak response and ultimate displacement. Static theorem can be efficiently employed for the evaluation of equilibrium states, especially for arches and vaulted systems, while kinematic theorem-based approaches are more suitable for the study of masonry structures. According to this latter approach, Giuffrè (1991) proposed the decomposition of the structure in rigid blocks, for which a specific collapse mechanism is identified *a priori*, based on recurrently failure mechanisms actually observed in existing Italian buildings.

Recent advancements in the utilization of limit analysis for the analysis of masonry constructions can be found in Giuffrè (1994); Carocci (2002); Orduña and Lourenço (2005); Baggio et al. (2000), also considering, for instance, the presence of friction at interfaces between rigid blocks in the last reference, or also Betti and Vignoli (2011).

Chapter 3

Nonlinear hinges constitutive model

The use of advanced constitutive models to reproduce the nonlinear response of highly complex materials such as masonry is an important topic, and still presents challenging aspects. A large number of numerical tools use classical hysteretic models, such as elastic or elastic-plastic models, which can lead to oversimplified and less accurate results, not permitting to capture essential aspects of the structural response such as the onset and evoution of damage. However, several advanced hysteretic models can be found in the literature. In particular, the Bouc-Wen model results to be one of the most versatile and accurate when highly nonlinear responses shall be described.

In the following Chapter, a brief review of this model and of one of its modifications is reported, followed by an enrichment of this latter and its validation. In particular, a proposal is made to enrich an existing Bouc-Wen model formulation with damage to describe more accurately stiffness degradation. The description of damage, that reduces the hysteretic force, is then accompanied by the introduction of flexibility increase, which increments the elastic displacement experienced by the system. Both effects influence the energy dissipated by the system.

3.1 Bouc-Wen model

The Bouc-Wen model belongs to the class of endochronic models, initially formulated by Valanis (Valanis, 1976), and is a smooth phenomenological constitutive

law often used to describe a large variety of different behaviors, ranging from structural elements to isolation devices or mechanical systems, and even soil behavior.

The first formulation was made by Bouc (Bouc, 1971), who proposed a model able to describe the hysteresis phenomenon through a rate-independent functional. This latter is defined through a first-order nonlinear differential equation, expressed in terms of internal variables of the system. Subsequently, the model has been extended by Wen (1976), where a modification to the restoring force funcion was implemented. Afterwards, the Bouc-Wen hysteretic model has been extensively applied and modified to reproduce different hysteretic responses in multiple fields of engineering, where both the static and dynamic excitations must be accounted for, arriving to the definition of a proper class of models. A complete review of the literature avialable regarding this model can be found in Ismail et al. (2009), with particular attention dedicated to the consistency of the model, to its main parameters and to the identification techniques adopted in the literature to calibrate them, in order to reproduce the desired hysteretic behavior.

The original Bouc-Wen model, referred to a single degree of freedom system, can be regarded as the arrangement in parallel of two devices, namely a linear elastic spring and a nonlinear hysteretic element, as shown in Fig. 3.1 (a).
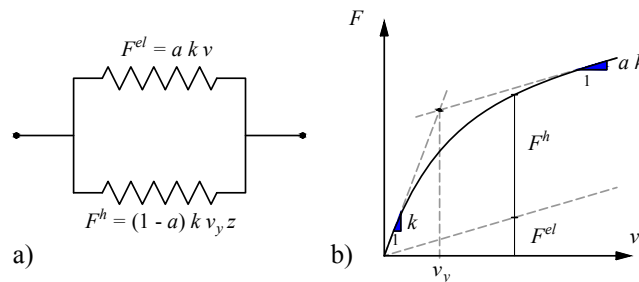
Figure 3.1: Bouc-Wen model: a) rheological element; b) force-displacement law.

Consequently, the total restoring force of the system can be expressed as the superposition of the elastic and the hysteretic forces:

$$F = F^{el} + F^h \tag{3.1}$$

In particular, the elastic force can be expressed as:

$$F^{el} = a\,k\,v \tag{3.2}$$

where a governs the ratio between the initial tangent stiffness k and the asymptotic post-yielding stiffness and can assume values included between 0 and 1, while v is the total input displacement.

The hysteretic force term, instead, is evaluated as:

$$F^h = (1-a)\,k\,v_y z \tag{3.3}$$

where, beside the aforementioned parameters, v_y is the maximum absolute elastic displacement and z is the hysteretic variable, which represents a non-dimensional elastic displacement. The term $v_y\,z$ results in the dimensional elastic displacement. According to this, limit bounds can be set for the hysteretic force F^h:

$$|F^h| \leq (1-a)\,k\,v_y \tag{3.4}$$

The total input displacement v can be written as:

$$v = v_y\,u \tag{3.5}$$

where u is the total non-dimensional displacement, which has the meaning of an equivalent ductility. It can be evaluated as the sum of the plastic (u^p) and the elastic (z) non-dimensional displacements, consistently with the classical plasticity theory:

$$u = z + u^p \tag{3.6}$$

and by substituting Eq. 3.6 in Eq. 3.5, the input displacement becomes:

$$v = v_y(z + u^p) \tag{3.7}$$

In general cases, the relation between u, z and u^p can be expressed through

the derivative of z with respect to u, that depends on z itself and $\text{sign}(\dot{v})$ as:

$$\frac{\mathrm{d}z}{\mathrm{d}u} = f[z, \text{sign}(\dot{v})] \tag{3.8}$$

and depends on the particular hysteresis considered. In particular, in the case of the classic Bouc-Wen model, the differential equation is the following:

$$\frac{\mathrm{d}z}{\mathrm{d}u} = A - [\beta \,\text{sign}(z\dot{v}) + \gamma]|z|^n \tag{3.9}$$

The parameters A, β, γ and n are non-dimensional quantities that govern shape and size of the hysteretic cycles. In particular, n regulates the smoothness of the transition from the initial elastic to the post-yielding branch, being more abrupt when n assumes greater values; β and γ influence the shape of the cycle, which results larger when $\beta > \gamma$ and more S-shaped when $\beta < \gamma$, but have no clear physical meaning; A is the initial stiffness of the $u - z$ curve. By using these parameters, a limit value for z can be set through the expression: $[A/(\beta + \gamma)]^{\frac{1}{n}}$.

However, it was mathematically demonstrated that the Bouc-Wen parameters are formally redundant (Ma et al., 2004; Charalampakis and Koumousis, 2008b). For this reason, the parameter A is usually fixed to a value equal to unity, and the condition $A/(\beta + \gamma) = 1$ holds (Constantinou and Adnane, 1987; Charalampakis and Koumousis, 2008a; Ma et al., 2004).

For the non-dimensional elastic displacement z, the limitation $|z| \leq 1$ holds, being the variable bounded between -1 and 1, which represent the asymptotic values for large negative and positive u-values, respectively. The derivative $\mathrm{d}z/\mathrm{d}u$ is bounded between $(0, 1]$, where 0 is assumed when z reaches its limit values, while 1 holds for the elastic state, for instance the initial state and elastic unloading branches, when present.

3.1.1 Thermodynamic admissibility

The thermodynamic admissibility of the classic Bouc-Wen model has been extensively investigated in the literature, as the original formulation is not based on proper thermodynamic conditions (Erlicher and Bursi, 2008). Typically, to over-

come these issues, intervals regarding the β and γ parameters hold to restore the thermodynamic admissibility condition (Erlicher and Point, 2004).

In general, according to Clausius-Duhem inequality, thermodynamic admissibility requires that dissipated energy shall be non-decreasing, i.e. its time derivative shall be non-negative:

$$\dot{U}^h \geq 0 \tag{3.10}$$

For the pure hysteretic Bouc-Wen system, the condition in Eq. 3.10 can be expressed as:

$$z\dot{u}^p \geq 0 \tag{3.11}$$

and thermodynamic admissibility can be studied according to Eq. 3.11 (Erlicher and Point, 2004; Liberatore et al., 2019). From Eq. 3.6 it follows that:

$$\dot{u}^p = \left(1 - \frac{\mathrm{d}z}{\mathrm{d}u}\right)\dot{u} \tag{3.12}$$

where, according to the previously mentioned conditions on the model parameters, $A = 1$.

Substituting $\mathrm{d}z/\mathrm{d}u$ from Eq. 3.9 provides:

$$\dot{u}^p = [\beta \operatorname{sign}(z\dot{u}) + \gamma]|z|^n \dot{u} \tag{3.13}$$

and combining Eq. 3.11 with Eq. 3.13 leads to:

$$z\,\dot{u}^p = [\beta \operatorname{sign}(z\dot{u}) + \gamma]|z|^n z\dot{u} \geq 0 \tag{3.14}$$

Moreover, by considering that $|z|^n \geq 0$, Eq. 3.14 can be simplified in:

$$[\beta \operatorname{sign}(z\dot{u}) + \gamma]\,z\,\dot{u} \geq 0 \tag{3.15}$$

The behavior of loading and unloading branches following this condition is now analysed. In loading branches, where $z\dot{u} \geq 0$, $z\dot{u} \geq 0$, Eq. 3.15 is satisfied for any choice of the parameters in their admissible ranges, that is $0 \leq \beta \leq 1$, $0 \leq \gamma \leq 1$.

In unloading branches, where $z\dot{v} < 0$, $z\dot{u} < 0$, Eq. 3.15 becomes:

$$\beta \geq \gamma \tag{3.16}$$

meaning that S-shaped cycles are not thermodynamically admissible, and the basic Bouc-Wen model requires the formulation of different enrichments to reproduce them without violating thermodynamic admissibility (Liberatore et al., 2019).

Assuming the condition $\beta + \gamma = A = 1$, it follows:

$$\beta \geq \frac{1}{2} \tag{3.17}$$

For $\beta > 1/2$, this condition results in bulge hysteretic cycles, with positive or negative $\dot{u}^p$, having increasing u^p over unloading branches with positive z and decreasing u^p over unloading branches with negative z. When $\beta = 1/2$, the unloading branches are linear elastic, with $\dot{u}^p = 0$ and $u^p = \text{const}$.

3.1.2 Drucker's postulate

One of the major problems of the Bouc-Wen models, which has been often highlighted in the literature, is the violation of Drucker's postulate (Drucker, 1950), which results in the presence of displacement drifts, force relaxation and non-closure of hysteretic loops for short loading-unloading paths (Charalampakis and Koumousis, 2009; Kottari et al., 2014; Sivaselvan and Reinhorn, 2000). However, when considering work-hardening materials, the postulate needs to be satisfied to have consistent assumptions.

Different solutions to overcome this issue have been proposed in the literature, such as the addition of hysteretic terms with negative energy dissipation (Casciati, 1989) or the addition of a stiffening factor in the hysteretic differential equation (Kottari et al., 2014; Charalampakis and Koumousis, 2009).

In the present thesis, the assumptions made in the work of Liberatore et al. (2019) are considered and here recalled, and conditions on the model parameters hold.

To this end, a hysteretic element on which a force F^h and a displcement v are present, is considered. According to Drucker's postulate (Drucker, 1950; Lubliner,

2008), the element is work-hardening if the product of the time derivative of the hysteretic force $\dot{F}^h$, and the velocity, $\dot{v}$, is positive:

$$\dot{F}^h\,\dot{v} > 0 \tag{3.18}$$

and the product of the time derivative of the hysteretic force and plastic velocity is non-negative:

$$\dot{F}^h\,v_y\,\dot{u}^p \geq 0 \tag{3.19}$$

Being the hysteretic force F^h proportional to z, according to Eq. 3.3, Drucker's postulate can be expressed, after simplifying, by the inequalities:

$$\dot{z}\,\dot{u} > 0 \tag{3.20}$$

$$\dot{z}\,\dot{u}^p \geq 0 \tag{3.21}$$

From Eq. 3.20, it follows that $\mathrm{d}z/\mathrm{d}u > 0$, which is satisfied in loading branches for any choice of the parameters. In unloading branches, it can be shown that Drucker's postulate is satisfied if:

$$\beta \leq \frac{1}{2} \tag{3.22}$$

For $\beta < 1/2$, this latter condition results in S-shaped hysteresis cycles with decreasing u^p when z is positive and increasing u^p when z is negative (Liberatore et al., 2019). Thermodynamic admissibility and Drucker's postulate can be both satisfied over unloading branches assuming:

$$\beta = \frac{1}{2} \tag{3.23}$$

implying that unloading branches are linear elastic and that u^p is constant.

3.2 Bouc-Wen model with damage

The need of reproducing the degrading behavior for nonlinear materials has led to the development of a large number of modifications to the classic Bouc-Wen

model in order to introduce strength degradation, stiffness degradation or both (Baber and Noori, 1985; Sivaselvan and Reinhorn, 2000; Erlicher and Bursi, 2008; Kottari et al., 2014).

The proposal made in Liberatore et al. (2019) is here taken into account to reproduce the effect of degradation. A scalar damage variable D, based on the Continuum Damage Mechanics, is introduced in the constitutive law. This latter affects the hysteretic component of the restoring force through a modification of the secant stiffness. Eq. 3.3 is then modified as:

$$F^h = (1 - D)(1 - a)\, k\, v_y\, z \tag{3.24}$$

According to classical damage mechanics (Lemaitre and Chaboche, 1994), D is bounded in the range $[0, 1)$, where 0 corresponds to the undamaged state and 1 to the fully damaged state. It is worth noting that in the proposed formulation the damage variable affects only the hysteretic force F^h, which vanishes as $D = 1$, whereas the elastic component does not. As a consequence, a residual elastic stiffness persists in the completely damaged condition.

The damage variable D is defined as proportional to the dissipated energy U^h, following the proposal in Baber and Wen (1981) and Baber and Noori (1985):

$$D = \delta_D\, U^h \tag{3.25}$$

where δ_D is the damage parameter ($\delta_D \geq 0$) having the dimension of the inverse of an energy. The dissipated energy U^h can thus be considered as the damage associated variable, ruling its evolution.

By introducing Eq. 3.25 in the expression of the hysteretic restoring force in Eq. 3.24, it results:

$$F^h = (1 - \delta_D\, U^h)(1 - a)\, k\, v_y z \tag{3.26}$$

Damage progression is then ruled by the evolution law defined for the dissipated energy U^h:

$$U^h = \frac{1}{\delta_D}\left\{1 - \exp\left[-2c\,\delta_D \int_0^u \frac{z}{1 - c\delta_D z^2} d(\tilde{u} - z)\right]\right\} \tag{3.27}$$

which allows to have a non-decreasing dissipated energy, from an initial null value to an upper bound equal to $1/\delta_D$. A more detailed description of the model can be read in Liberatore et al. (2019).

3.3 Bouc-Wen model with damage and flexibility increase

Although the model with damage proved to capture the main aspects of the degrading phenomena of masonry elements, especially in terms of strength degradation, some limits emerged in the description of the real reponse of structural elements, and a further enrichment was required. Thus, the model with damage described in Liberatore et al. (2019) is modified in the present thesis to enclose a more refined description of the stiffness degradation. In particular, to overcome these limits, a flexibility increase term is introduced in the definition of the elastic displacement, in terms of a factor equal to $1 + \delta_K U^h$. In the latter expression, δ_K is the flexibility increase parameter, which has the dimension of the inverse of an energy as well as the damage parameter δ_D. Eq. 3.7 becomes, with the introduction of the new term:

$$v = v_y[(1 + \delta_K \, U^h)z + u^p] \tag{3.28}$$

However, the evaluation of the hysteretic restoring force remains unvaried, as in Eq. 3.3 or Eq. 3.24, in case of absence or presence of damage respectively. The inequality $|z| \leq 1$ and Eq. 3.4 are retained in both cases of absence or presence of damage.

It is worth to notice the duality of damage and flexibility increase, given by the different role played in the constitutive law. In fact, damage consists of a *reduction* of the hysteretic force, whereas flexibility increase gives an *expansion* of the elastic displacement.

3.3.1 Dissipated energy

Dissipated energy rules both damage and flexibility increase evolution laws. In the following, the calculation of this latter in presence of damage and flexibility increase is addressed, and its general properties are discussed.

The total energy U of the hysteretic element can be expressed as the composition of the elastic, U^e, and dissipated energy, U^h, as follows:

$$U = U^e + U^h \tag{3.29}$$

or, in terms of their time derivatives:

$$\dot{U} = \dot{U}^e + \dot{U}^h \tag{3.30}$$

This latter can be evaluated as the product of the hysteretic restoring force and the time derivative of the elastic displacement of the system:

$$
\begin{aligned}
\dot{U} = F^h \, \dot{v} &= (1 - \delta_D \, U^h)(1-a)kv_y^2 z \frac{\mathrm{d}}{\mathrm{dt}}\left[(1 + \delta_K \, U^h)z + u^p\right] = \\
&= 2c(1 - \delta_D \, U^h)[\delta_K \, \dot{U}^h z^2 + (1 + \delta_K \, U^h)z\dot{z} + z\dot{u}^p]
\end{aligned}
\tag{3.31}
$$

where:

$$c = \frac{1}{2}(1-a)\, k \, v_y^2 \tag{3.32}$$

The elastic energy term can be expressed as:

$$U^e = \frac{1}{2}F^h(1 + \delta_K U^h)v_y z \tag{3.33}$$

and its maximum initial value, valid when $U^h = 0$ and denoted as $\sup_0 U^e$, is attained for $|F^h| = (1-a)\, k \, v_y^2 = 2\, c$ and $|z| = 1$, so that:

$$\sup_0 U^e = \frac{1}{2}(1-a)\, k \, v_y^2 = c \tag{3.34}$$

In case of absence of flexibility increase, when $\delta_K = 0$, the maximum initial

value of elastic energy coincides with its maximum value:

$$\sup{}_0 U^e = \sup U^e \tag{3.35}$$

The time derivative of the elastic energy results as:

$$
\begin{aligned}
\dot{U}^e &= \frac{\mathrm{d}}{\mathrm{dt}}\left[\frac{1}{2}(1 - \delta_D U^h)(1 - a)\,k\,v_y^2(1 + \delta_K U^h)z^2\right] = \\
&= c[-\delta_D \dot{U}^h(1 + \delta_K U^h)z^2 + (1 - \delta_D U^h)\delta_K \dot{U}^h z^2 + 2(1 - \delta_D U^h)(1 + \delta_K U^h)\,z\,\dot{z}]
\end{aligned}
\tag{3.36}
$$

In general, total and elastic energy are functions of the dissipated energy, being valid Eq. 3.31 and Eq. 3.36 respectively. Thus, an explicit expression for the dissipated energy cannot be written generally. The time derivative of the dissipated energy can, then, be derived on the basis of those evaluated for the total and elastic terms, as:

$$\dot{U}^h = \dot{U} - \dot{U}^e = c\big\{[(1 - \delta_D U^h)\delta_K \dot{U}^h + \delta_D \dot{U}^h(1 + \delta_K U^h)]z^2 + 2(1 - \delta_D U^h)z\,\dot{u}^p\big\} \tag{3.37}$$

Solving with respect to $\dot{U}^h$ gives:

$$\frac{\dot{U}^h}{1 - \delta_D U^h} = \frac{2cz}{1 - c(\delta_D + \delta_K)z^2}\dot{u}^p \tag{3.38}$$

which is a first-order differential equation that governs the evolution of the dissipated energy.

In case of pure flexibility increase ($\delta_D = 0, \delta_K \neq 0$) the differential equation reduces to:

$$\dot{U}^h = \frac{2cz}{1 - c\,\delta_K z^2}\dot{u}^p \tag{3.39}$$

whereas, in case of pure damage ($\delta_D > 0, \delta_K = 0$), it results:

$$\frac{\dot{U}^h}{1 - \delta_D\,U^h} = \frac{2cz}{1 - c\,\delta_D z^2}\dot{u}^p \tag{3.40}$$

The term $-\delta_D U^h$ in Eq. 3.38 represents the effect of strength decay due to

damage, while the term $-c(\delta_D + \delta_K)z^2$ reproduces the effect of stiffness decay due to the combination of damage and flexibility increase.

Strength decay can be considered as a special combination of damage and flexibility increase. Setting $\delta_K = -\delta_D$, Eq. 3.38 becomes:

$$\frac{\dot{U}^h}{1 - \delta_D U^h} = 2\,c\,z\,\dot{u}^p \tag{3.41}$$

which is the differential equation governing the evolution of the dissipated energy of a system with strength decay and no stiffness decay. It is worth to notice that negative values of δ_K represent flexibility decrease. In the following, both positive and negative values of δ_K will be considered for generality.

In case neither damage nor flexibility increase are present ($\delta_D = 0, \delta_K = 0$), Eq. 3.38 reduces to the differential equation of a pure hysteretic system:

$$\dot{U}^h = 2\,c\,z\,\dot{u}^p \tag{3.42}$$

Lastly, integrating Eq. 3.38, the expression of the dissipated energy is obtained as:

$$U^h = \frac{1}{\delta_D}\left\{ 1 - \exp\left[-2c\,\delta_D \int_0^{u^p} \frac{z}{1 - c(\delta_D + \delta_K)z^2} d\tilde{u}^p \right] \right\} \tag{3.43}$$

and the damage evolution law results as:

$$D = 1 - \exp\left[-2c\,\delta_D \int_0^{u^p} \frac{z}{1 - c(\delta_D + \delta_K)z^2} d\tilde{u}^p \right] \tag{3.44}$$

3.3.2 Thermodynamic admissibility

The thermodynamic admissibility condition is now investigated for the hysteretic system with flexibility increase and for the hysteretic system with both damage and flexibility increase.

Starting from the Clausius-Duhem inequality (Eq. 3.10), in the simple case of pure hysteretic system, when neither damage nor flexibility increase are present, it follows from Eq. 3.42 that:

$$z\dot{u}^p \geq 0 \tag{3.45}$$

and by integrating Eq. (3.42), the expression of the dissipated energy is deduced as:

$$U^h = 2c \int_0^{u^p} z \, d\tilde{u}^p \tag{3.46}$$

showing that the dissipated energy U^h has no upper bound.

In case of hysteretic system with flexibility increase only ($\delta_D = 0, \delta_K \neq 0$), in addition to Eq. 3.45, thermodynamic admissibility requires, according to Eq. 3.39 and taking into account that $|z| \leq 1$:

$$\delta_K < \frac{1}{c} = \frac{1}{\sup_0 U^e} \tag{3.47}$$

The expression of the dissipated energy can be obtained by integrating Eq. 3.39:

$$U^h = 2c \int_0^{u^p} \frac{z}{1 - c \, \delta_K z^2} d\tilde{u}^p \tag{3.48}$$

which shows that, as well as in the case of pure hyseretic system, also in the case of flexibility increase the dissipated energy U^h has no upper bound.

When both damage and flexibility increase are present ($\delta_D > 0, \delta_K \neq 0$), Eq. 3.43 can be considered to study thermodynamic admissibility. This latter shows that U^h is bounded in the range $[0, 1/\delta_D)$, where the damage parameter δ_D has the meaning of the maximum dissipable energy:

$$\delta_D = \frac{1}{\sup U^h} \tag{3.49}$$

and damage results as the ratio between dissipated energy and maximum dissipable energy:

$$D = \frac{U^h}{\sup U^h} \tag{3.50}$$

Then, the dissipated energy U^h results to be non-decreasing if

$$\delta_D + \delta_K < \frac{1}{c} = \frac{1}{\sup_0 U^e} \tag{3.51}$$

Moreover, by considering Eq. 3.49, the condition of thermodynamic admissi-

bility can be expressed in the form:

$$\delta_K < \frac{1}{\sup_0 U^e} - \frac{1}{\sup U^h} \tag{3.52}$$

In the case of pure damage, when flexibility increase is null, $(\delta_D > 0, \delta_K = 0)$, Eq. 3.43 provides:

$$U^h = \frac{1}{\delta_D} \left\{ 1 - \exp\left[-2c\,\delta_D \int_0^{u^p} \frac{z}{1 - c\,\delta_D z^2} d\tilde{u}^p \right] \right\} \tag{3.53}$$

showing that U^h is non-decreasing if:

$$\delta_D < \frac{1}{c} \tag{3.54}$$

or, by considering Eqs. 3.34, 3.35 and 3.49:

$$\sup U^e < \sup U^h \tag{3.55}$$

One last special case in studied, which is the case of pure strength decay $(\delta_K = -\delta_D)$. The integration of Eq. 3.41 provides:

$$U^h = \frac{1}{\delta_D} \left\{ 1 - \exp\left[-2c\,\delta_D \int_0^{u^p} z\, d\tilde{u}^p \right] \right\} \tag{3.56}$$

and U^h is non-decreasing for any $\delta_D > 0$.

To summarize, when damage and flexibility increase are present, which is the most general case, thermodynamic admissibility is satisfied according to Eq. 3.51, or equivalently to Eq. 3.52. Additional constrains on the admissible values which can be assumed by the parameters are discussed in the following Section.

3.3.3 Admissible domain of parameters

Additional constraints on the parameters arise from Eq. 3.28, in which the displacement v is expressed as a combination of the non-dimensional elastic (z) and plastic (u^p) displacements. By deriving with respect to time both sides of Eq.

3.28, and substituting Eq. 3.38 in the expression of $\dot{U}^h$, it results:

$$\dot{v} = v_y \left\{ (1 + \delta_K U^h)\dot{z} + \left[1 + \delta_K \frac{2cz^2}{1 - c(\delta_D + \delta_K)z^2}(1 - \delta_D U^h) \right] \dot{u}^p \right\} \qquad (3.57)$$

where the terms which multiply $\dot{z}$ and $\dot{u}^p$ shall be non-negative. Focusing on the first term on right-hand side in Eq. 3.57, $(1 + \delta_K U^h)$, since $0 \leq U^h < 1/\delta_D$, this is non-negative if:

$$\delta_D + \delta_K \geq 0 \qquad (3.58)$$
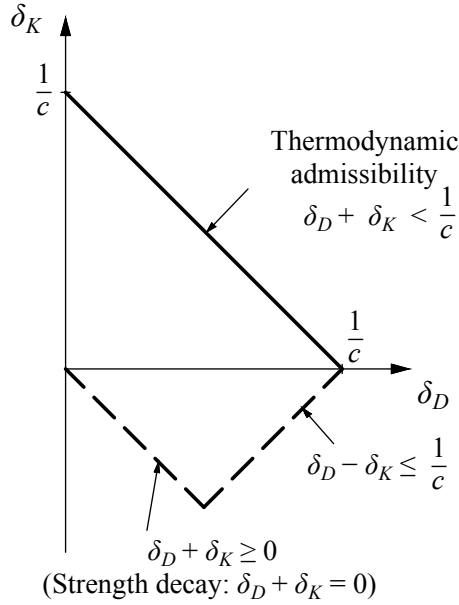
Figure 3.2: Admissible domain of parameters δ_D and δ_K.

It can be noted that $\delta_D + \delta_K = 0$ corresponds to strength decay. When considering the thermodynamic admissibility condition expressed by Eq. 3.51, the term in square brackets which multiplies $\dot{u}^p$ in Eq. 3.57 is positive for any positive value of δ_K. When δ_K is negative, the following inequality holds:

$$1 + \delta_K \frac{2cz^2}{1 - c(\delta_D + \delta_K)z^2}(1 - \delta_D U^h) \geq 1 + \delta_K \frac{2cz^2}{1 - c(\delta_D + \delta_K)z^2} \qquad (3.59)$$

and the right-hand side is non-negative if:

$$\delta_D - \delta_K \leq 1/c \tag{3.60}$$

The admissible domain of the mechanical parameters is reported in Fig. 3.2, where the boundary of thermodynamic admissibility is shown by a continuous line, and the boundaries of Eqs. 3.58, 3.60 by dashed lines. In real situations $\delta_D, |\delta_K| << 1/c$, and thermodynamic admissibility is commonly satisfied, as well as Eq. 3.60, whereas Eq. 3.58 enforces the condition that no overall stiffness increase shall occur.

3.3.4 Drucker's postulate

Drucker's postulate is now analyzed for a hysteretic element with flexibility increase, showing that it is work hardening if the corresponding hysteretic element without flexibility increase is work hardening.

In case of a hysteretic element with flexibility increase and no damage, Eq. 3.58 provides:

$$\delta_K \geq 0 \tag{3.61}$$

Since the case $\delta_K = 0$ refers to a pure hysteretic element, the case $\delta_K > 0$ is analysed in the following. Eqs. 3.19, 3.21 are not affected by flexibility increase. Therefore, if they hold for the hysteretic element without flexibility increase, they also hold when flexibility increase is accounted. Eq. 3.18 can be written, according to Eq. 3.28 and after simplifying, as:

$$\dot{z}[(1 + \delta_K U^h)\dot{z} + \dot{u}^p + \delta_K \dot{U}^h z] > 0 \tag{3.62}$$

Taking into account Eq. 3.39, which provides $\dot{U}^h$ in the case of flexibility increase, the above inequality in Eq. 3.62 can be written as:

$$\dot{z}\dot{u} + \delta_K U^h \dot{z}^2 + \delta_K \frac{2cz^2}{1 - c\delta_K z^2} \dot{z}\dot{u}^p > 0 \tag{3.63}$$

where $\delta_K U^h \dot{z}^2 \geq 0$ and $1 - c\delta_K z^2 > 0$, since $z^2 \leq 1$ and, according to Eq. 3.47,

$\delta_K < 1/c$.

If the following inequalities $\dot{z}\,\dot{u} > 0$ and $\dot{z}\,\dot{u}^p \geq 0$ hold, indicating that the hysteretic element without flexibility increase is work hardening, then Eq. 3.63 holds and the element with flexibility increase is work hardening.

It must be emphasized that, whereas thermodynamic admissibility is mandatory, Drucker's postulate only holds for work hardening models. Softening and snap-back are examples of thermodynamically admissible models which are not work hardening (Liberatore et al., 2019). Eventually, hysteretic models with damage could lead to softening branches. Therefore, in general, they are not work hardening.

To summarize, the Bouc-Wen model with flexibility increase satisfies Drucker's postulate if the basic Bouc-Wen model does, while the Bouc-Wen model with damage in general does not satisfy Drucker's postulate.

3.3.5 Tangent stiffness

When solving the incremental form of the constitutive relationship, the evaluation of the tangent stiffness is required. This is defined as the derivative of total restoring force with respect to total displacement:

$$
\begin{aligned}
k_t = \frac{\mathrm{d}F}{\mathrm{d}v} &= \frac{\mathrm{d}F^{el}}{\mathrm{d}v} + \frac{\mathrm{d}F^h}{\mathrm{d}v} = a\,k + \frac{\mathrm{d}F^h}{\mathrm{d}u}\frac{\mathrm{d}u}{\mathrm{d}v} \\
&= a\,k + (1-a)k\,v_y \left[-\delta_D \frac{\mathrm{d}U^h}{\mathrm{d}u} z + (1 - \delta_D U^h)\frac{\mathrm{d}z}{\mathrm{d}u} \right] \frac{\mathrm{d}u}{\mathrm{d}v} \\
&= k \left\{ a + (1-a)\frac{v_y[-\delta_D \frac{\mathrm{d}U^h}{\mathrm{d}u^p}(1 - \frac{\mathrm{d}z}{\mathrm{d}u})z + (1 - \delta_D U^h)\frac{\mathrm{d}z}{\mathrm{d}u}]}{\frac{\mathrm{d}v}{\mathrm{d}u}} \right\}
\end{aligned}
\tag{3.64}
$$

The derivative $\mathrm{d}v/\mathrm{d}u$ follows from Eq. 3.28:

$$
\begin{aligned}
\frac{\mathrm{d}v}{\mathrm{d}u} &= v_y \left[\delta_K \frac{\mathrm{d}U^h}{\mathrm{d}u} z + (1 + \delta_K U^h)\frac{\mathrm{d}z}{\mathrm{d}u} + 1 - \frac{\mathrm{d}z}{\mathrm{d}u} \right] \\
&= v_y \left[1 + \delta_K \left(\frac{\mathrm{d}U^h}{\mathrm{d}u} z + U^h \frac{\mathrm{d}z}{\mathrm{d}u} \right) \right]
\end{aligned}
\tag{3.65}
$$

and the derivative $\mathrm{d}U^h/\mathrm{d}u$ is:

$$\frac{\mathrm{d}U^h}{\mathrm{d}u} = \frac{\mathrm{d}U^h}{\mathrm{d}u^p}\frac{\mathrm{d}u^p}{\mathrm{d}u} = \frac{\mathrm{d}U^h}{\mathrm{d}u^p}\left(1 - \frac{\mathrm{d}z}{\mathrm{d}u}\right) \tag{3.66}$$

By substituting Eqs. 3.65, 3.66 into Eq. 3.64, the expression of the tangent stiffness is obtained as:

$$k_t = k\left\{a + (1-a)\frac{\left[-\delta_D\frac{\mathrm{d}U^h}{\mathrm{d}u^p}\left(1 - \frac{\mathrm{d}z}{\mathrm{d}u}\right)z + (1 - \delta_D U^h)\frac{\mathrm{d}z}{\mathrm{d}u}\right]}{1 + \delta_K\left[\frac{\mathrm{d}U^h}{\mathrm{d}u^p}\left(1 - \frac{\mathrm{d}z}{\mathrm{d}u}\right)z + U^h\frac{\mathrm{d}z}{\mathrm{d}u}\right]}\right\} \tag{3.67}$$

where the derivative $\frac{\mathrm{d}U^h}{\mathrm{d}u^p}$ follows from Eq. 3.38:

$$\frac{\mathrm{d}U^h}{\mathrm{d}u^p} = \frac{2cz(1 - \delta_D U^h)}{1 - c(\delta_D + \delta_K)z^2} \tag{3.68}$$

3.4 Parametric analysis and validation

A parametric analysis is performed to study more in depth the performance of the model with damage and flexibility increase. In particular, in the analyses performed, one of the two scalar parameters δ_D and δ_K is kept constant while the other one assumes increasing values. A quasi-static cyclic forcing action is applied to each case, made of three cycles of increasing amplitude, with the purpose to highlight the effect of the parameters on the response in terms of progression of the strength and stiffness degradation. The mechanical parameters adopted for each case are listed in Tab 3.1.

Table 3.1: Bouc-Wen models: mechanical parameters

a	A	n	β	γ	k	v_y
$-$	$-$	$-$	$-$	$-$	kN/m	m
0.1	1	1	0.5	0.5	20000	0.01

The cyclic response in terms of experienced displacement and total restoring force is reported in Fig. 3.3 for the four cases. When flexibility increase only is
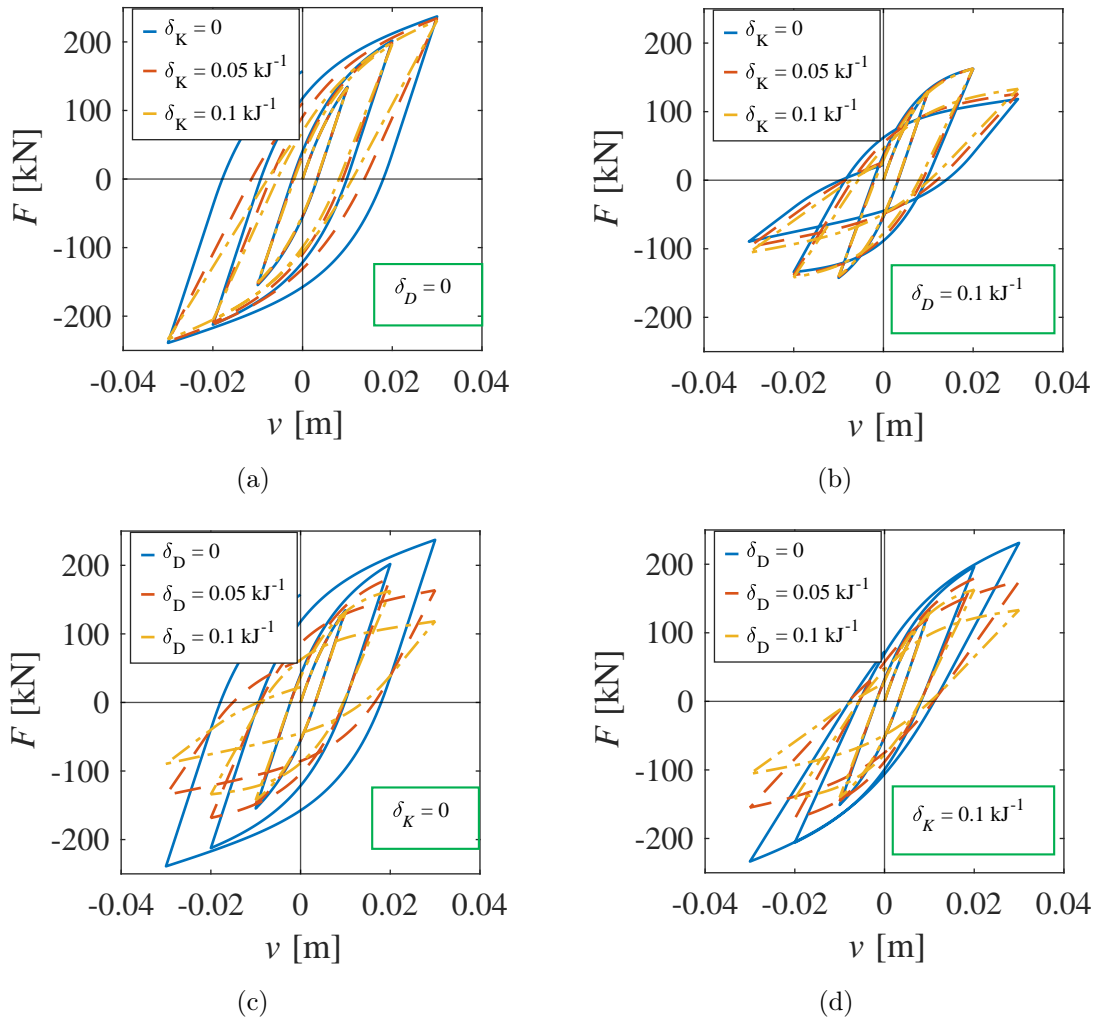
Figure 3.3: Parametric analysis varying δ_D and δ_K

present, and the parameter δ_D is kept constant and equal to 0, the restoring force peaks in the assigned displacement are constant and a shrinkage of the cycles can be detected as the parameter δ_K gets higher. The area of the force-displacements cycles gets lower, and consequently also the dissipeted energy, when the number of cycles increases. When δ_D is equal to $0.1\,\mathrm{kJ}^{-1}$, the combined effect of damage and flexibility increase is observable (Fig. 3.3 (b)), influencing both strength and stiffness degradation. In addition, a small recovery of strength can be detected when δ_K assumes higher values. Moreover, the effect of damage is concentrated

during the third cycle, which is the first cycle experienced after the exceedance of the apparent yielding displacement v_y. In Fig. 3.3 (c), the flexibility increase parameter is kept constant and set equal to 0, and the effect of pure damage is analyzed. A strong influence on the post-yielding branch can be detected, in fact the slope tends to diminish. Finally, when δ_K is equal to $0.1\,\mathrm{kJ}^{-1}$, and different levels of damage occur (Fig. 3.3 (d)), thinner cycles can be seen compared to case (c), as well as strength degradation.

3.4.1   Numerical validation

A first application is presented, in order to validate the hysteretic model through the reproduction of experimental results available in the literature. A comparison between the numerical model and the previous model proposed in Liberatore et al. (2019) is also presented.

One of the two unreinforced masonry specimens tested in 1995 at the Joint Center of Ispra (Anthoine et al., 1995), in particular the squat wall, is considered. The panel is made of brick units and hydraulic mortar, and has a height of $1.35\,\mathrm{m}$ high, a width of $1\,\mathrm{m}$ and a thickness of $0.25\,\mathrm{m}$. The restraints and loading conditions applied to the specimens try to reproduce the real conditions which a pier of a common structure undergoes during seismic events. A vertical load equal to $150\,\mathrm{kN}$, applied during the experimental tests, reproduces the weigth of the surrounding structure, while a quasi-static cyclic displacement-controlled loading hystory is applied horizontally at the top of the panel.

In the numerical model, the panel is schematized as a single degree of freedom (SDOF) structure, and the response to the horizontal loading history is described through the modified Bouc-Wen model, highlighting the damage and shear mechanisms experienced. The vertical load is neglected.

The parameters adopted to describe the nonlinear hysteretic model are reported in Tab. 3.2. The parameters a, δ_D and δ_K are calibrated by imposing the equality between the dissipated energy of the experimental and the numerical curves.

Fig. 3.4 (a) shows a good correspondence between the numerical and the experimental results. The energy dissipation mechanisms, together with the degra-

Table 3.2: Parameters adopted for the Bouc-Wen model

a	A	n	β	γ	k	v_y	δ_D	δ_K
$-$	$-$	$-$	$-$	$-$	kN/m	m	kJ^{-1}	kJ^{-1}
0	1	1	0.5	0.5	80000	0.001	0.15	2.4
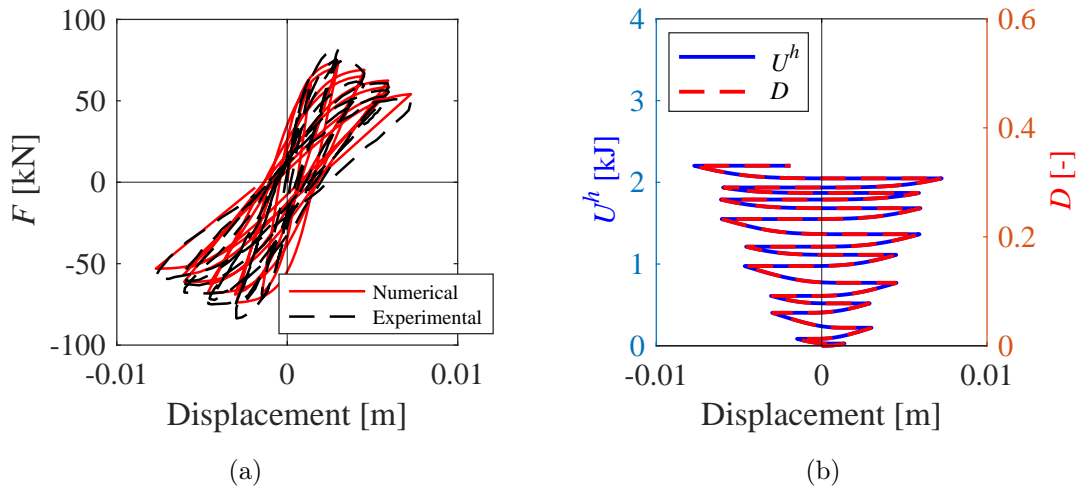
Figure 3.4: Comparison between experimental and numerical results for the Ispra squat wall (a); dissipated energy and damage trends of the shear hinge (b)

dation of both strength and stiffness are accurately reproduced, with the flexibility increase allowing to match the loading and unloading branches of the experimental curves. The trend of the dissipated energy and the evolution of the damage variable D versus the global displcement are also displayed in Fig. 3.4 (b). As expected, the two curves, each plotted with reference to its proper y-axis, are overlapped when proper axis limits are set, being the damage proportional to the dissipated energy. At the end of the analysis the dissipated energy of the system is equal approximately to 2.204 kJ, while the final value of the damage variable $D = \delta_D U^h$ is equal to 0.33; regarding the flexibility increase of the system, the term $\delta_K U^h$ at the end of the analysis reaches the value of 5.29. Consistently with the behavior highlighted in Liberatore et al. (2019), the dissipated energy exhibits an increasing trend in the loading and reloading branches of the curve and remains
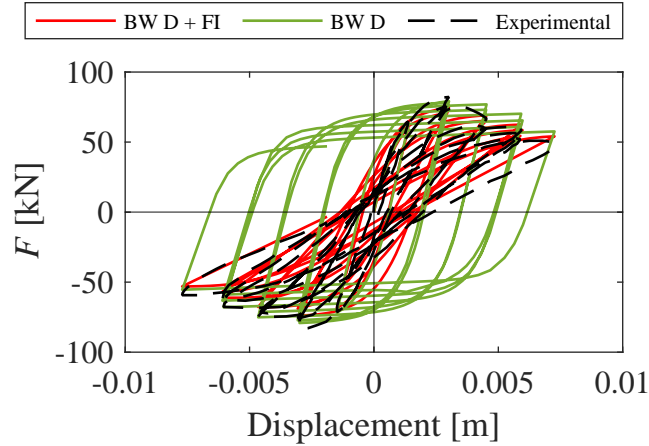
Figure 3.5: Comparison between Bouc-Wen model with damage and flexibility increase, Bouc-Wen model with damage (Liberatore et al., 2019) and experimental results

constant in the unloading branches. Moreover, the growth rate is higher in the first cycles, while gradually decreasing after.

A comparison with the formulation with damage and no flexibility increase (in green or blue) is presented in Figs. 3.5 and 3.6. In this latter case, the mechanical parameters adopted for the system are the same of the case with damage and flexibility increase, with the exception of the damage parameter. A value of δ_D equal to $0.05\,\mathrm{kJ}^{-1}$ is in fact adopted, calibrated with the purpose of reproducing the strength degradation experienced during the test.

Although the strength degradation is well captured, with similar values with respect to the case with damage and flexibility increase, it is evident that the area of the cycles of the Bouc-Wen model with damage is excessively wide, and the dissipated energy is higher with respect to the energy actually dissipated during the experimental test. Moreover, the stiffness degradation due to the damage term does not allow to match the unloading and loading branches and consequently neither the actual stiffness decay experienced during the progression of the shear mechanisms.

Fig. 3.6 (a) shows the response to the first cycle of analysis, showing a similar behavior between the case with damage only and the case with damage and flexibility increase. The two curves are almost overlapped, being the dissipated energy
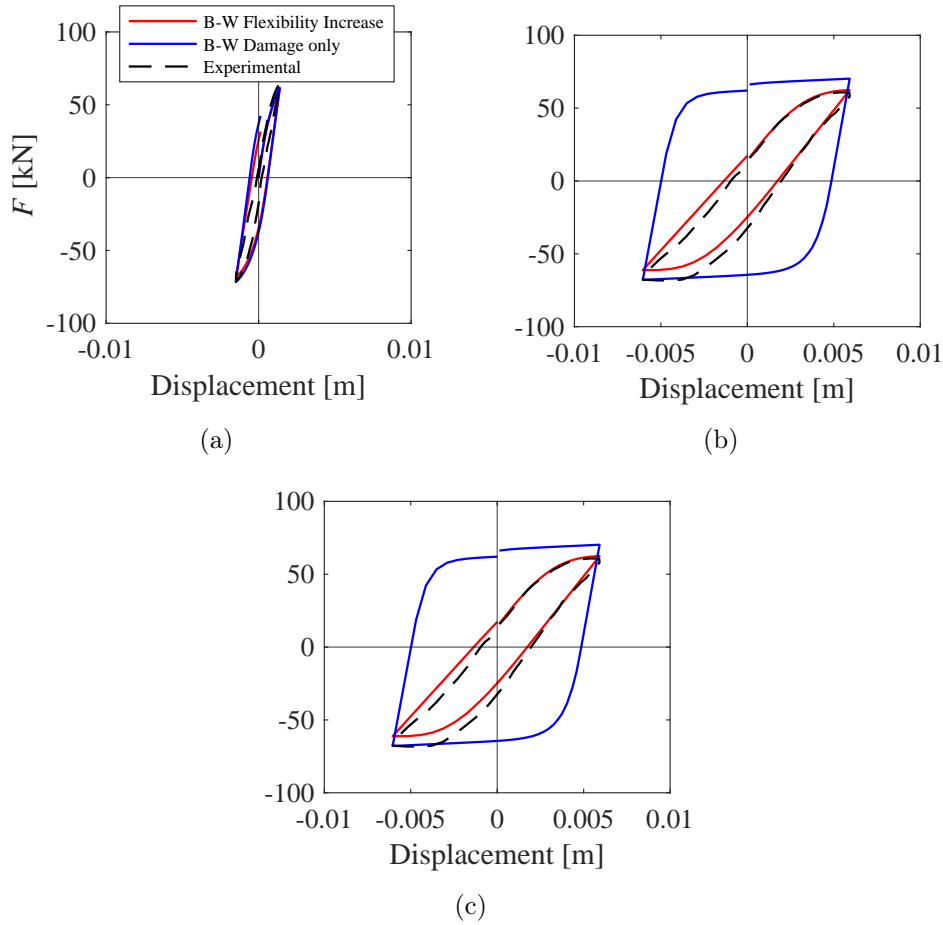
Figure 3.6: Comparison between experimental, Bouc-Wen with damage and flexibility increase and Bouc-Wen with damage only: first cycle (a), sixth cycle (b), last cycle (c)

almost the same. In Fig. 3.6 (b) and (c) the sixth and the last cycles of the analysis are represented, respectively. From both of them, it is clear that flexibility increase profoundly affects the evolution of the response. It is noteworthy that the flexibility increase parameter δ_K is one order of magnitude larger than the damage parameter δ_D. The cycles are visibly thinner compared to the case with damage only; the loading, unloading and reloading branches have a lower slope, reducing the area of the cycle and better representing not only the strength reduction, but also the effective shape of the cycle and, above all, the energy dissipated by the system.

Chapter 4

2D macroelement formulation

Equivalent frame models are a particular subset of macromechanical models, in which the behavior of each structural element is reproduced through a single macroelement with an homogeneized constitutive law. This means that in the case of masonry, no distinction between units and mortar is considered, and proper hysteresis accounting for degradation and nonlinearity must be implemented. Moreover, this latter requires to describe piers and spandrels alike, and to account for rigid zones to model the panel zones.

To this end, a macroelement is proposed, which is described through a 2-node Finite Element (FE) with a force-based formulation, which has proved to be highly efficient for the description of frame structures, and lumped nonlinear hinges, in which the hysteretic behavior is concentrated and reproduced through the modified Bouc-Wen model described in Chapter 3.

Additional nonlinear devices are also considered, following the proposal in Sangirardi et al. (2019). These latter allow a more detailed and accurate description of flexural mechanisms typical of masonry panels, such as pinching, which cannot be neglected as it reproduces the effect of cracks reclosure in loading and unloading branches, visibly affecting the structural response.

The possibility to describe the structural response in the dynamic field is also considered. In particular, the effect of flexibility increase and onset and propagation of damage on the dynamic performance is studied. The limits of the classical dynamic formulation for frame elements are highlighted, and their

influence on the response is analyzed.

Computational aspects are also discussed, considering that both the static and dynamic behaviors of the proposed model are implemented in a Finite Element code. An iterative procedure to allow numerical convergence over the element is also provided, together with information regarding the algorithm adopted for the solution of the nonlinear problem.

Numerical applications are provided for both the static and dynamic formulations. A validation through well-known experimental results available in the literature is proposed for the static macroelement, while the dynamic behavior is explored under different geometric and loading conditions. Finally, the macroelement capability to reproduce numerical outcomes, obtained through different macromechanical approaches, is studied.

4.1   2D in-plane static formulation

The work of Sangirardi et al. (2019) is taken as a basis for the proposal of the 2D macroelement. In particular, a central Euler-Bernoulli linear elastic element with a force-based formulation is assembled in series with two nonlinear lumped flexural hinges located at the end nodes of the element. Consistently with the Euler-Bernoulli beam formulation, plane sections are assumed to remain plane and normal to the axis of the element. Moreover, the whole shear effects and mechanisms are described through the introduction of a nonlinear shear hinge.

An overview of the force-based formulation adopted for the frame element is reported in the following, and basic assumptions and issues are also recalled.

4.1.1   Force-based classic formulation

The force-based formulation relies on the definition of interpolation functions of the stress field, which strictly satisfy exact equilibrium condition along the element. The element state determination requires more complex iterations, but results in a more efficient procedure, especally when lumped nonlinerity is introduced (Addessi and Ciampi, 2006; Spacone et al., 1996). Small displacements and strains are assumed.

The 2-node elastic element is defined in a global reference system $(0, X, Y)$ (Fig. 4.1), in which each node has three degrees of freedom (DOFs), resulting in total in six DOFs for the whole element. These correspond to the six global displacement components, four translational $\mathbf{u}_i$, $\mathbf{u}_j$ and two rotational θ_i and θ_j, which are collected in the vector $\mathbf{u}$:

$$\mathbf{u} = \{u_i \ v_i \ \theta_i \ u_j \ v_j \ \theta_j\}^T \tag{4.1}$$
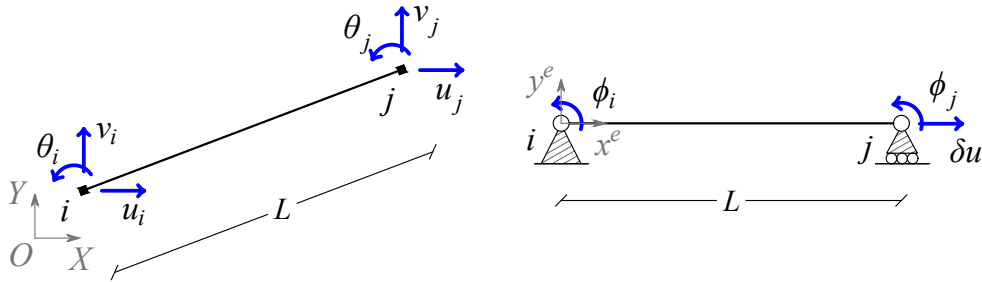
Figure 4.1: Beam finite element in the global reference system and in the basic local reference system

Six force components correspond to the displacement components, which are four nodal forces and two moments, collected in the global vector $\mathbf{p}$:

$$\mathbf{p} = \{p_{x_i} \ p_{y_i} \ m_i \ p_{x_j} \ p_{y_j} \ m_j\}^T \tag{4.2}$$

To enforce equilibrium in a strong form along the axis of the element, as required in the force-based approach, rigid body motions are eliminated, and a simply supported beam configuration is considered. A local basic reference system (i, x^e, y^e) is defined, whose origin is located in node i, axis x^e is parallel to the beam axis and axis y^e is orthogonal to it.

At each section of the Euler-Bernoulli beam element, the generalized section displacement vector $\mathbf{u}_s(x)$ and the section deformation vector $\boldsymbol{\varepsilon}_s(x)$ can be defined:

$$\mathbf{u}_s(x) = \{u(x) \ v(x)\}^T; \quad \boldsymbol{\varepsilon}_s(x) = \{\epsilon_G(x) \ \chi(x)\}^T \tag{4.3}$$

The section stress vector, as well as the section deformation vector, has two components in the Euler-Bernoulli formulation, namely a normal stress $N(x)$ and

a bending moment $M(x)$, considering that the shear component can be derived from the latter:

$$\boldsymbol{\sigma}_s(x) = \{N(x) \ M(x)\}^T \tag{4.4}$$

and the section constitutive equation relates it to the section deformation vector:

$$\boldsymbol{\sigma}_s(x) = \boldsymbol{K}_s(x) \, \boldsymbol{\varepsilon}_s(x) \tag{4.5}$$

in which $\boldsymbol{K}_s(x)$ is the standard section stiffness matrix. In the present case, the section properties do not vary, being both material and section properties constant along the beam axis. Otherwise, an integration over the area of the section should be required for each component of the matrix. Thus, in the following, the section stiffness matrix is reduced to a diagonal matrix, whose two components are the axial stiffness (EA) and the in-plane flexural stiffness (EI):

$$\boldsymbol{K}_s(x) = \begin{bmatrix} EA & 0 \\ 0 & EI \end{bmatrix} \tag{4.6}$$

E is the Young's modulus, A is the area and I is the flexural inertia of the section.

Discrete quantities are required to write the algebraic element equations needed in the displacement-based approach for the solution of the structural problem. To this end, the variation of the section stresses is expressed through the basic element nodal stresses by means of the equilibrium matrix $\boldsymbol{b}_s(x)$:

$$\boldsymbol{\sigma}_s(x) = \boldsymbol{b}_s(x) \, \boldsymbol{\sigma}^e + \boldsymbol{\sigma}_{sq}(x) \tag{4.7}$$

In the in-plane 2D case, the equilibrium matrix is equal to:

$$\boldsymbol{b}_s(x) = \begin{bmatrix} 1 & 0 & 0 \\ 0 & x/L - 1 & x/L \end{bmatrix} \tag{4.8}$$

and $\boldsymbol{\sigma}_{sq}(x)$ is the generalized stress vector due to distributed loads in the normal and transversal direction in the local reference system. However, in the following in-plane formulation, the influence of distributed loads along the beam axis is neglected, and they are always reduced to concentrated forces applied at the end

nodes evaluated through influence areas. According to this assumption, the stress field of the axial and the shear forces are constant along the element, while the bending moment has a linear equation.

The enforcement of the virtual work equivalence, considering the external work done by the basic virtual stresses in the basic displacement and the internal work done by the section stresses in the deformations, is expressed as:

$$\delta \boldsymbol{\sigma}^{e^T} \boldsymbol{\varepsilon}^e \; = \; \int_0^L \delta \boldsymbol{\sigma}_s^T(x) \, \boldsymbol{\varepsilon}_s(x) \, dx \tag{4.9}$$

and gives a relation between the basic displacements and the generalized section deformations:

$$\boldsymbol{\varepsilon}^e \; = \; \int_0^L \boldsymbol{b}_s^T(x) \, \boldsymbol{\varepsilon}_s(x) \, dx \tag{4.10}$$

This also leads to the expression of the flexibility matrix of the beam element, where $\boldsymbol{f}_s(x) = \boldsymbol{K}_s^{-1}(x)$ is the section flexibility matrix, and, in general cases, to the evaluation of the initial basic displacements caused by distributed loads:

$$\mathbf{F}^e \; = \; \int_0^L \boldsymbol{b}_s^T(x) \, \boldsymbol{f}_s(x) \, \boldsymbol{b}_s(x) \, dx \tag{4.11}$$

$$\boldsymbol{\varepsilon}_{0q} \; = \; \int_0^L \boldsymbol{b}_s^T(x) \, \boldsymbol{f}_s(x) \, \boldsymbol{\sigma}_{sq}(x) \, dx \tag{4.12}$$

Local basic displacements and rotations are defined in the three-components vector $\boldsymbol{\varepsilon}^e$:

$$\boldsymbol{\varepsilon}^e = \{\delta u \; \phi_i \; \phi_j\}^T \tag{4.13}$$

where δu is the elongation of the beam in the direction parallel to axis x^e, while ϕ_i and ϕ_j are the rotations at nodes i and j respectively (Fig. 4.1). The kinematic matrix $\mathbf{D}^e$ and the rotation matrix $\mathbf{T}_u^e$ relate the global nodal displacements and the local basic displacements through the relation:

$$\boldsymbol{\varepsilon}^e = \mathbf{D}^e \, \mathbf{T}_u^e \, \mathbf{u} \tag{4.14}$$

being the nodal displacements in the local reference system evaluated as: $\mathbf{u}^e = \mathbf{T}_u^e \mathbf{u}$. The kinematic matrix is defined as:

$$\mathbf{D}^e = \begin{bmatrix} -1 & 0 & 0 & 1 & 0 & 0 \\ 0 & 1/L & 1 & 0 & -1/L & 0 \\ 0 & 1/L & 0 & 0 & -1/L & 1 \end{bmatrix} \tag{4.15}$$

where L is the length of the undeformed element from node i to node j, and eliminates the rigid modes, while the rotation matrix, which projects the global displacements in the local reference system, is written as:

$$\mathbf{T}_u^e = \begin{bmatrix} \cos\alpha & \sin\alpha & 0 & 0 & 0 & 0 \\ -\sin\alpha & \cos\alpha & 0 & 0 & 0 & 0 \\ 0 & 0 & 1 & 0 & 0 & 0 \\ 0 & 0 & 0 & \cos\alpha & \sin\alpha & 0 \\ 0 & 0 & 0 & -\sin\alpha & \cos\alpha & 0 \\ 0 & 0 & 0 & 0 & 0 & 1 \end{bmatrix} \tag{4.16}$$

The stress vector $\boldsymbol{\sigma}^e$, which contains the axial force and two bending moments, is associated to the local basic displacements vector:

$$\boldsymbol{\sigma}^e = \{N_j \ M_i \ M_j\}^T \tag{4.17}$$

and is related to the global force vector through the expression:

$$\mathbf{p} = \mathbf{T}_u^{eT} \mathbf{D}^{eT} \boldsymbol{\sigma}^e \tag{4.18}$$

The relation between the local basic displacements and forces can be derived, also considering Eqs. 4.9 to 4.12:

$$\varepsilon^e = \mathbf{F}^e \boldsymbol{\sigma}^e + \varepsilon_{0q} \tag{4.19}$$

In the common case of a beam with straight axis and constant properties along the axis, the flexibility matrix can be written as:

$$\mathbf{F}^e = \begin{bmatrix} \frac{L}{EA} & 0 & 0 \\ 0 & \frac{L}{3EI} & -\frac{L}{6EI} \\ 0 & -\frac{L}{6EI} & \frac{L}{3EI} \end{bmatrix} \tag{4.20}$$

Rigid offsets are also introduced, following the method in Addessi et al. (2015).

4.1.2 Nonlinear hinges introduction

Kinematic and equilibrium relations are now recalled for the position of the elastic Euler-Bernoulli beam element in series with the nonlinear flexural hinges and the shear hinge, following the approach in Addessi et al. (2015). In particular, the two flexural hinges are located at the end nodes of the macroelement, while the shear hinge is a distributed hinge. Fig. 4.2 shows the arrangement of the hinges, where the shear hinge is located at the center of the element only for sake of representation.
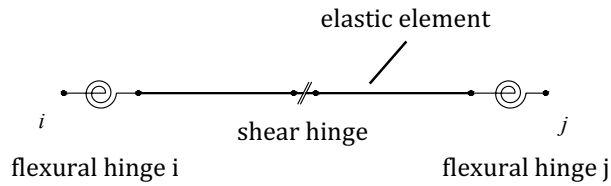
Figure 4.2: Schematization of the macroelement with flexural and shear hinges

The equilibrium condition:

$$M_{i/j} = M_{h_{i/j}} = M_{e_{i/j}} \tag{4.21}$$

on the bending moments of each node holds, where $M_{h_{i/j}}$ is the bending moment of the flexural hinge, while $M_{e_{i/j}}$ is the bending moment evaluated at the ends of the elastic element.

Regarding kinematic conditions, the global rotation at each structural end node is given by the superposition of the rotation of the nonlinear flexural hinge ($\phi_{hb_{i/j}}$), the rotation contribution from the shear hinge (ϕ_{hs}) and the rotation evaluated at the end node of the elastic element ($\phi_{e_{i/j}}$):

$$\phi_{i/j} \; = \; \phi_{h_{i/j}} \; + \; \phi_{hs} \; + \; \phi_{e_{i/j}} \tag{4.22}$$

Differently from Addessi et al. (2015), where the shear hinge was located at the end nodes of the element, in the present work the shear hinge is considered without a defined location, and the shear behavior is distributed along the entire element, thanks to the constant interpolation associated to the shear force. However, the kinematic equation considered remains substantially unchanged, how can be seen in Eq. 4.22.

The constitutive relations of the flexural and the shear hinges written in incremental form are, respectively:

$$\dot{\phi}_{h_{i/j}} \; = \; f_{hb_{i/j}} \, \dot{M}_{i/j} \tag{4.23}$$

$$\dot{\phi}_{hs} \, L \; = \; f_{hs} \, \frac{\dot{M}_i + \dot{M}_j}{L} \tag{4.24}$$

in which $f_{hb_{i/j}}$ and f_{hs} represent the tangent flexibility contributions. In Eq. 4.24, the shear rotation is multiplied by the length of the element, evaluated once rigid offsets are removed, to obtain the shear deformation, consistently with the assumption of a hinge ditributed along the entire element.

By substituting Eqs. 4.23, 4.24 and 4.10 in Eq. 4.22, the flexibility matrix of the complete macroelement can be derived, which in case of a beam with straight axis and constant section is the following:

$$\boldsymbol{F}^e = \begin{bmatrix} \frac{L}{EA} & 0 & 0 \\ 0 & \frac{L}{3EI} + f_{hb_i} + \frac{f_{hs}}{L^2} & -\frac{L}{6EI} + \frac{f_{hs}}{L^2} \\ 0 & -\frac{L}{6EI} + \frac{f_{hs}}{L^2} & \frac{L}{3EI} + f_{hb_j} + \frac{f_{hs}}{L^2} \end{bmatrix} \tag{4.25}$$

By studying the flexibility matrix of the macroelement, it can be highlighted that the axial behavior is completely decoupled from the shear/flexural behavior, and is assigned exclusively to the elastic central element. The axial behavior is then assumed lienar elastic. However, the influence of the external axial force acting on the masonry panel is included in the evaluation of the yielding force, and consequently of that of the yielding displacement, which in turn affects the

activation of the nonlinear behavior of the modified Bouc-Wen model, as will be discussed in Section 4.1.4. The external axial force, then contributes to the evaluation of the yielding thresholds for the modified Bouc-Wen hysteresis in the shear and flexural hinges.

4.1.3 Flexural hinges enhancement

Two enhancements are added to the modified Bouc-Wen model presented in Chapter 3 to constitute the complete flexural hinge. In particular, pinching effect and a modification to the initial elastic stiffness are introduced by means of two additional devices, following the approach introduced in previous works (Baber and Noori, 1985; Liberatore et al., 2019; Sangirardi et al., 2019). The rheological model that results is shown in Fig. 4.3.
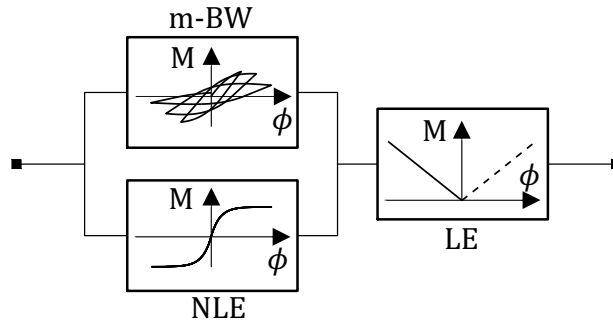
Figure 4.3: Rheological model of the flexural hinges

For the sake of brevity, only the main equations are recalled in the following. Detailed formulation can be found in Liberatore et al. (2019) and Sangirardi et al. (2019).

The nonlinear elastic device introduced in parallel with the modified Bouc-Wen hysteresis to model pinching effect is derived under proper assumptions and values of the parameter β and n from the classic Bouc-Wen model. These assumptions lead to the following expressions for the hysteretic force and the tangent stiffness of the device:

$$F^{NLE} = F_0^{NLE} \, \text{sign}(v) \left[1 - \exp\left(- \frac{k_0^{NLE}}{F_0^{NLE}} |v| \right) \right] \qquad (4.26)$$

$$k^{NLE} = k_0^{NLE} \exp\left(-\frac{k_0^{NLE}}{F_0^{NLE}} |v| \right) \tag{4.27}$$

where F_0^{NLE} is the tangent maximum force reacheable and k_0^{NLE} is evaluated as a portion of the initial tangent elastic stiffness of the hinge:

$$k_0^{NLE} = (1 - a_k)\, k \tag{4.28}$$

where k is the initial tangent stiffness of the hinge, while the portion that contributes to the modified Bouc-Wen device is evaluated as:

$$k^{mBW} = a_k\, k \tag{4.29}$$

The high initial stiffness of slender panels, in which flexural hinges prevail with respect to the shear hinge, is enforced by restoring the initial stiffness of the elastic beam element. A linear elastic device with a negative slope is introduced in series with the other devices, which compensates the contribution of the hinges to the global flexibility of the macroelement by adding a term in the flexural flexibility:

$$f_{hb_{i/j}} = \frac{1}{k^{mBW} + k^{NLE}} + \frac{1}{k^{LE}} \tag{4.30}$$

In Eq. 4.30, the stiffness of the linear elastic device is evaluated, consistently with Liberatore et al. (2019), with the equation:

$$k^{LE} = -\left(1 + \frac{1}{R} \right)\left(k_0^{mBW} + k_0^{NLE} \right) \tag{4.31}$$

with $R > 0$. Eq. 4.30 is obtained from kinematic and equilibrium conditions derived from the position in series and in parallel of the constitutive devices. The series position states that the total basic displacement that belongs to the hinge is given by the superposition of the basic displacement of the parallel of the modified Bouc-Wen and the nonlinear elastic devices and the basic displacement of the linear negative elastic device: $\phi^{tot} = \phi + \phi^{LE}$, while the restoring moment is preserved: $M^{tot} = M = M^{LE}$. This latter is given by the two parallel devices, in which the basic displacement is preserved, while the resporing moment is given by the sum of the restoring moments of the single devices: $M = M^{NLE} + M^{mBW}$.

4.1.4   Initial stiffness and yielding displacement

The initial tangent stiffness of the flexural and the shear hinges is evaluated using the following expressions:

$$k_{hs_0} = \frac{GA}{1.2L}; \quad k_{hb_{i,j}} = \frac{4EI}{L} \tag{4.32}$$

G is the shear modulus, E is the Young's modulus, A is the area of the whole section and I the flexural section inertia.

   The yielding displacement, required in the modified Bouc-Wen constitutive model, is obtained from the yielding moment in case of the flexural hinge and the yielding shear force for the shear hinge, according to the Italian Standard Code (NTC, 2018), which assumes an equivalent stress-block diagram for the compression of masonry piers. For a rectangular section, it holds:

$$M_y = \frac{1}{2}\sigma_0\left(1 - \frac{\sigma_0}{0.85f_c}\right)l^2 t \tag{4.33}$$

where σ_0 is the mean normal stress ($\sigma_0 = N/A$, where N is the axial load and A the section area), f_c is the compressive strength, l and t the section dimensions. In the case of the shear force, for old masonry with diagonal cracking mechanisms, it holds:

$$V_y = \frac{f_t}{b}lt\sqrt{1 + \frac{\sigma_0}{f_t}} \tag{4.34}$$

f_t is the tensile strength for diagonal cracking, $b = L/l$, being $1 \leq b \leq 1.5$.

   For spandel walls, Eqs. 4.33 and 4.34 become:

$$M_y = \frac{H_p l}{2}\left(1 - \frac{H_p}{0.85f_h\,l\,t}\right) \tag{4.35}$$

$$V_y = l\,t\,f_{v0} \tag{4.36}$$

H_p is the minimum value between the tensile strength of the horizontal element in tension and $0.4f_h lt$, f_h is the horizontal compressive strength and f_{v0} is the shear strength in absence of normal stress.

4.2   Dynamic formulation

The description of the static behavior is enhanced with the introduction of the inertia and the damping terms to reproduce also the dynamic behavior.

According to the classical Finite Element solution, the discrete dynamic equilibrium equation of the global structure is written as:

$$\mathbf{M\ddot{u}} + \mathbf{C\dot{u}} + \mathbf{P}^{int}(\mathbf{u}) = \mathbf{P}^{ext} \tag{4.37}$$

where $\mathbf{\ddot{u}}$, $\mathbf{\dot{u}}$ and $\mathbf{u}$ are the global nodal acceleration, velocity and displacement, respectively, where the first two vectors are evaluated as the derivatives of the latter with respect to time. $\mathbf{P}^{ext}$ is the global external force vector, in which each component is a nodal force or moment, while $\mathbf{P}^{int}(\mathbf{u})$ is the internal force vector, in which the nonlinear structural response is considered.

Consistently with the force-based approach, the global mass matrix $\mathbf{M}$ and the global damping matrix $\mathbf{C}$ are evaluated by assembling the element mass matrix $\mathbf{M}^e$ and the element damping matrix $\mathbf{C}^e$ respectively.

The element damping matrix $\mathbf{C}^e$ is obtained through the Rayleigh formulation, being a linear combination of the element mass matrix $\mathbf{M}^e$ and the element stiffness matrix $\mathbf{K}^e$ of the system, updated at each step of the analysis, through the coefficients a_0 and a_1. These latter are evaluated by fixing a damping ratio and considering the elastic angular frequencies ω_i and ω_j of the first two vibration modes. Thus, it holds:

$$\mathbf{C}^e = a_0 \mathbf{M}^e + a_1 \mathbf{K}^e \tag{4.38}$$

Two different approaches are implemented to obtain the element mass matrix, namely a lumped approach and a consistent approach. The lumped approach considers both the translational and the rotational mass, lumped at each node, obtaining a diagonal matrix. This allows to obtain a less accurate structural response when dynamic excitations are considered, but its advantage is a lower computational burden, being the inertia terms uncoupled.

4.2.1 Consistent mass matrix

Although the lumped mass approach is often adopted for the equivalent frame method, it results less accurate when an experimental behavior has to be reproduced or when comparisons with other displacement-based finite element procedures are done. To this end, a consistent mass approach is also considered, where the mass of the macroelement is distributed along the axis, allowing a better precision especially in linear dynamic analyses.

In this approach, both stiffness and mass of the element contribute to the mass matrix calculation, and both shear and rotary inertia effects are taken into account (Di Re et al., 2019; Archer, 1965; Molins et al., 1998; Soydas and Saritas, 2017). The Unit Load Method is adopted to obtain the exact equilibrium-based shape functions (Di Re et al., 2019; de Souza et al., 2003; Shuang et al., 2009; Shen et al., 2014), being a more computationally efficient procedure with respect to the one developed by Molins et al. (1998), based on the Principles of Virtual Work.

It is noteworthy that a Timoshenko formulation is adopted, due to the presence of the shear hinge in the macroelement formulation that allows the representation of the shear behavior. Shear components should then be included in the mass evaluation.

According to the Timoshenko beam formulation, to the generalized section displacements given in Eq. 4.3 the rotation component $\theta(x)$ should be added. The unit work-conjugate virtual forces, applied in line with the Unit Load Method, are then: $\delta\boldsymbol{p}_s = \{p_x\ p_y\ m_z\}^T$, applied at the generic coordinate x of the beam axis. The virtual work equivalence between the external work, given by the generalized displacements and forces, and the internal work, given by the section deformations and stresses, $\delta W^{ext} = \delta W^{int}$ is enforced, and leads to:

$$\delta\boldsymbol{p}_s^T\,\boldsymbol{u}_s(x) = \int_0^L \delta\boldsymbol{\sigma}_s^T(x,\zeta)\,\boldsymbol{\varepsilon}_s(\zeta)\,d\zeta \tag{4.39}$$

where ζ is the generic coordinate to define the integral along the axis. A simply supported beam configuration is considered to solve the virtual static problem for the Unit Load Method, and the virtual nodal reactions are evaluated as:

$$\delta \boldsymbol{p}_r(x) \,=\, \boldsymbol{b}_{rs}(x)\,\delta \boldsymbol{p}_s \tag{4.40}$$

where $\boldsymbol{b}_{rs}(x)$ is the cross-section equilibrium matrix that relates the unit virtual forces to the virtual reactions and is:

$$\boldsymbol{b}_{rs}(x) \,=\, \begin{bmatrix} 1 & 0 & 0 \\ 0 & x/L - 1 & 1/L \\ 0 & x/L & 1/L \end{bmatrix} \tag{4.41}$$

The virtual section stresses are computed from the virtual nodal reactions by means of the matrix $\boldsymbol{b}_r(\zeta)$:

$$\boldsymbol{\sigma}_s(x,\zeta) \,=\, \boldsymbol{b}_r(\zeta)\,\delta \boldsymbol{p}_r(x) \tag{4.42}$$

where:

$$\boldsymbol{b}_r(\zeta) \,=\, \begin{cases} \begin{bmatrix} 1 & 0 & 0 \\ 0 & \zeta & 0 \\ 0 & -1 & 0 \end{bmatrix} & \zeta \le x \\[2em] \begin{bmatrix} 0 & 0 & 0 \\ 0 & 0 & \zeta - L \\ 0 & 0 & -1 \end{bmatrix} & \zeta > x \end{cases} \tag{4.43}$$

The integral is split between the intervals $[0,\,x]$ and $[x,\,L]$ to evaluate the shape functions before and after the generic point of application of the unit forces.

By substituting Eq. 4.40 in Eq. 4.42 and then in the virtual work equivalence (Eq. 4.39), and eliminating the term $\delta \boldsymbol{p}_s^T$ in both sides of the equation, it holds:

$$\boldsymbol{u}_s(x) \,=\, \int_0^L \boldsymbol{b}_{rs}^T(x)\,\boldsymbol{b}_r^T(\zeta)\,\boldsymbol{\varepsilon}_s(\zeta)\,d\zeta \tag{4.44}$$

and substituting $\boldsymbol{\varepsilon}_s(\zeta)$ with its expression in terms of the local basic displacements, considering $\boldsymbol{\sigma}_{sq}(x) = 0$, it holds, with little manipulation of the integral:

$$\boldsymbol{u}_s(x) \;=\; \boldsymbol{b}_{rs}^T(x) \int_0^L \boldsymbol{b}_r^T(\zeta)\, \boldsymbol{f}_s(\zeta)\, \boldsymbol{b}_s(\zeta)\, d\zeta \; \mathbf{E}^e\, \boldsymbol{\varepsilon}^e \tag{4.45}$$

Eq. 4.45 is then related to the local nodal displacements $\mathbf{u}^e$ by means of the matrix $\mathbf{D}^e$ (Eq. 4.15), and rigid modes are also re-introduced. The force-based shape function matrix in the local reference system is then obtained:

$$\mathbf{N}_s(x) \;=\; \boldsymbol{b}_{rs}^T(x) \int_0^L \boldsymbol{b}_r^T(\zeta)\, \boldsymbol{f}_s(\zeta)\, \boldsymbol{b}_s(\zeta)\, d\zeta \; \mathbf{E}^e\, \mathbf{D}^e \;+\; \mathbf{N}_r(x) \tag{4.46}$$

where $\mathbf{N}_r(x)$ is the matrix that eliminates the rigid modes:

$$\mathbf{N}_r(x) \;=\; \begin{bmatrix} 1 & 0 & 0 & 0 & 0 & 0 \\ 0 & 1 - x/L & 0 & 0 & x/L & 0 \\ 0 & -1/L & 0 & 0 & 1/L & 0 \end{bmatrix} \tag{4.47}$$

Finally, the element mass matrix is written in the same form of the displacement based procedure through the shape functions:

$$\mathbf{M}^e \;=\; \int_0^L \mathbf{N}_s(x)^T\, \boldsymbol{m}_s(x)\, \mathbf{N}_s(x)\, dx \tag{4.48}$$

In Eq. 4.48, $\boldsymbol{m}_s(x)$ is the section mass matrix, which depends on the material density ρ and the cross-section area A, which can both vary along the beam axis:

$$\boldsymbol{m}_s(x) \;=\; \int_A \rho(x, y) \begin{bmatrix} 1 & 0 & -y \\ 0 & 1 & 0 \\ -y & 0 & y^2 \end{bmatrix} d\tilde{A} \tag{4.49}$$

The matrix in Eq. 4.49 relates the generalized section accelerations to the generalized section intertia forces.

It is noteworthy that if a constant section and constant properties along the axis are considered, for a rectangular section, the obtained matrix is equal to the one obtained by adopting a displacement-based shape funcions approach.

The correctness of the implementation is validated throug the results obtained in Leissa and Zhang (1983), where the adimensional frequencies of a cubic and a rectangular beam are considered, obtaining a good agreement of the results.

4.3   Computational aspects and solution algorithm

The main computational aspects are briefly discussed. In particular, the iterative procedure and the solution algorithms adopted are described.

The model is implemented in a user frame element in the Finite Element Analysis Program FEAP (Taylor, 2017), and introduced in a displacement-based framework.

The numerical static nonlinear problem is solved through a Newton-Raphson algorithm, which computes the element quantities at each step in the global reference system. The state of each element is then determined, and an iterative procedure is estabilished to enforce the element equilibrium. A second nested iterative procedure is then performed, to enforce equilibrium and compatibility conditions between the two flexural and the shear hinges.

The solution of the finite element dynamic motion equation in the time domain uses an implicit Newmark algorithm, whose coefficients β and γ assume the values of 0.25 and 0.5 respectively, for an unconditionally stable solution procedure. At each time step Δt, the Newton-Raphson algorithm solves the nonlinear problem.

4.3.1   Element state determination

The iterative Newton-Raphson procedure is described in the present paragraph, referred to a single frame element, and labelling with $k+1$ the current iteration and with k the previous one. Incremental equilibrium, compatibility and constitutive equations are considered, in which the quantities are labelled in the following as $\Delta\bullet$.

The global nodal displacements $\mathbf{u}^{k+1}$ and displacement increments $\Delta\mathbf{u}^{k+1}$ are computed at the current iteration $k+1$ of the Newton-Raphson global procedure, and are rotated in the local reference system of the element through the rotation matrix $\mathbf{T}_u^e$:

$$\Delta\mathbf{u}^{e^{k+1}} = \mathbf{T}_u^e\,\Delta\mathbf{u}^{k+1} \tag{4.50}$$

The basic displacement increments are evaluated at the current iteration, on the basis of the displacement increments in the local reference system:

$$\Delta\boldsymbol{\varepsilon}^{e^{k+1}} \;=\; \mathbf{D}^e\,\Delta\mathbf{u}^{e^{k+1}} \tag{4.51}$$

The basic element force increments are computed throught the element flexibility matrix evaluated at the previous iteration, with the hypotesys of a linear relationship between the two quantities:

$$\Delta\boldsymbol{\sigma}^{e^{k+1}} \;=\; (\mathbf{F}^{e^k})^{-1}\,\Delta\boldsymbol{\varepsilon}^{e^{k+1}} \tag{4.52}$$

and are used to evaluate the deformation increments in input in the flexural and shear hinges, by means of the tangent flexibility of each hinge at the previous iteration:

$$\Delta\phi_{h_i}^{k+1} \;=\; f_{hb_i}^k\,\Delta M_i^{k+1} \tag{4.53}$$

$$\Delta\phi_{h_j}^{k+1} \;=\; f_{hb_j}^k\,\Delta M_j^{k+1} \tag{4.54}$$

$$\Delta\gamma^{k+1} \;=\; f_{hs}^k\,\frac{\Delta M_i^{k+1} + \Delta M_j^{k+1}}{L} \tag{4.55}$$

These latter quantities update the deformations evaluated at the previous iteration:

$$\phi_{h_{i/j}}^{k+1} \;=\; \Delta\phi_{h_{i/j}}^{k+1} \;+\; \phi_{h_{i/j}}^k \tag{4.56}$$

$$\gamma^{k+1} \;=\; \Delta\gamma^{k+1} \;+\; \gamma^k \tag{4.57}$$

and enter in the modified Bouc-Wen constitutive law of the hinges.

A second iterative procedure is introduced at this point, described in the following paragraph, to enforce equilibirum and compatibility conditions between the flexural and shear hinges. Tangent flexibility and force terms of each hinge are obtained as output quantities at the current iteration:

$$\phi_{h_{i/j}}^{k+1} \;\rightarrow\; f_{hb_{i/j}}^{k+1};\, M_{h_{i/j}}^{k+1} \tag{4.58}$$

$$\gamma^{k+1} \rightarrow f_{hs}^{k+1}; T_{hs}^{k+1} \tag{4.59}$$

The element flexibility matrix is updated at the current iteration with the new tangent flexibility terms of the hinges ($\mathbf{F}^{e^k} \rightarrow \mathbf{F}^{e^{k+1}}$), while the elastic terms remain unchanged. Deformation residuals, ρ_i and ρ_j, are computed at the current iteration between the equilibrated forces and the hinges output forces, and collected into a deformation residual vector:

$$\mathbf{r}^{e^{k+1}} = \{0, \ \rho_i, \ \rho_j\}^T \tag{4.60}$$

Details on the residuals will be given in the following paragraph.

The local basic forces are then updated:

$$\boldsymbol{\sigma}^{e^{k+1}} = \Delta\boldsymbol{\sigma}^{e^{k+1}} + \boldsymbol{\sigma}^{e^k} - (\mathbf{F}^{e^{k+1}})^{-1} \mathbf{r}^{e^{k+1}} \tag{4.61}$$

Finally, the element stiffness matrix and the element internal force vector are computed at the current iteration as: $\mathbf{K}^{e^{k+1}} = (\mathbf{D}^e)^T(\mathbf{F}^{e^{k+1}})^{-1}\mathbf{D}^e$ and $\mathbf{p}^{e^{k+1}} = \mathbf{D}^{e^T}\boldsymbol{\sigma}^{e^{k+1}}$.

The current element stiffness matrix and force vector are then rotated in the global reference system and are forwarded to the global Newton-Raphson procedure performed by the program FEAP.

4.3.2 Hinges iterative procedure

In Addessi et al. (2015), a consistent procedure to avoid element iterations and to compute local deformation residuals that are used in the global Newton-Raphson algorithm is proposed. However, the high nonlinearity of the modified Bouc-Wen model emplyed as a constitutive model in the flexural and shear hinges, requires an iterative procedure to ensure equilibrium conditions between the output forces from the hinges and the equilibrated local basic forces of the elastic element.

The second iterative procedure begins from Eq. 4.56, where the updated deformations at the current iteration are evaluated for the flexural hinges and are used in input in the subroutine that evaluates the tangent flexibility and the moment in output from the two flexural hinges (Eq. 4.58). The local deformation

residuals are evaluated for each of the two flexural hinges:

$$\rho_i \;=\; f_{hb_i}^{k+1}\left(\Delta M_i^{k+1} \;+\; M_i^k \;-\; M_{h_i}^{k+1}\right) \tag{4.62}$$

$$\rho_j \;=\; f_{hb_j}^{k+1}\left(\Delta M_j^{k+1} \;+\; M_j^k \;-\; M_{h_j}^{k+1}\right) \tag{4.63}$$

If these residual are higher than a tolerance value equal to 10^{-12}, they are used to update the deformation increment of the shear hinge evaluated as in Eq. 4.55 and the respective shear deformation at the current iteration, multiplied by the length of the element to transform residuals in terms of rotation, to residuals in terms of shear deformation:

$$\Delta\gamma^{k+1} \;=\; \Delta\gamma^{k+1} \;+\; \rho_i\,L \;+\; \rho_j\,L \tag{4.64}$$

$$\gamma^{k+1} \;=\; \Delta\gamma^{k+1} \;+\; \gamma^k \tag{4.65}$$

The current value of shear deformation is input in the shear hinge, and the tangent flexibility and shear force are evaluated (Eq. 4.59). The shear deformation residual is obtained by comparing the shear force evaluated through the moments output from the flexural hinges and the output shear force of the hinge as:

$$\rho_{hs} \;=\; \frac{f_{hs}^{k+1}}{L}\left(\frac{M_{h_i}^{k+1} + M_{h_j}^{k+1}}{L} \;-\; T_{hs}^{k+1}\right) \tag{4.66}$$

Equilibrium between the flexural and the shear hinges is enforced in this latter equation. If the residual is greater than a tolerance value equal to 10^{-12}, iterations are enforced and the shear residual updates the shear deformation, until the residual is nullified. By calling $l+1$ and l the current and previous terations respectively, the updated shear deformation increment and shear deformation input in the hinge are:

$$\Delta\gamma^{k+1^{l+1}} \;=\; \rho_{hs^{l+1}} \;+\; \Delta\gamma^{k+1^{l}} \tag{4.67}$$

$$\gamma^{k+1^{l+1}} \;=\; \Delta\gamma^{k+1^{l+1}} \;+\; \gamma^{k+1^{l}} \tag{4.68}$$

Iterations are repeated until the shear residual value is lower than the tolerance value or the maximum numer of iterations imposed is reached.

Iterations over the flexural hinges are now enforced, to lower the rotation residuals under the limit value imposed by the tolerance. Calling $m+1$ and m the current and the previous iterations, respectively, the rotation increments are updated:

$$\Delta\phi_{h_{i/j}}^{k+1^{m+1}} = \rho_{i/j} + \Delta\phi_{h_{i/j}}^{k+1^{m}} \tag{4.69}$$

These are then passed in Eq. 4.56 and iterations are performed. Equilibrium between the equilibrated forces and the moment output values of the flexural hinges is then obtained.

The numerical stability of the macroelement is then improved, at the expense of a low increase of the computational burden.

4.4   Static model validation

A validation of the static behavior of the macroelement is presented. The experimental behavior of the two unreinforced masonry panels tested in 1995 at the Joint Center of Ispra (Anthoine et al., 1995), one of which is already used also in Paragraph 3.4.1, is reproduced through the complete numerical model.

Together with the squat panel, whose heigth is 1.35 m, a slender panel, 2 m high and with the same base and thickness dimensions, is considered. The effective boundary and loading conditions are applied in this case, meaning that in a first phase a vertical load equal to 150 kN for both panels is applied, followed by a quasi-static horizontal displacement history applied on top. The yielding parameters are evaluated according to the perscriptions indicated in Paragraph 4.1.4, adopting the mechanical parameters listed in Tab. 4.1, where f_c is the compressive strength and f_{v0} the shear strength in the absence of normal stress. Tab. 4.2 contains the parameters used for the modified Bouc-Wen hysteretic model of the hinges.

Fig. 4.4 shows that both cases of a slender and a squat panel can be properly reproduced by the model. In particular, the same set of damage parameters is used, as these depend on the degradation of the type of masonry adopted to build

Table 4.1: Masonry mechanical parameters

E	G	f_c	f_{v0}
kN/m^2	kN/m^2	kN/m^2	kN/m^2
$1700 \, 10^3$	$300 \, 10^3$	6200	140

Table 4.2: Nonlinear hinges parameters

Squat wall						Slender wall					
Flexural hinges			Shear hinge			Flexural hinges			Shear hinge		
a	δ_D	δ_K	a	δ_D	δ_K	a	δ_D	δ_K	a	δ_D	δ_K
–	kJ^{-1}	kJ^{-1}	–	kJ^{-1}	kJ^{-1}	–	kJ^{-1}	kJ^{-1}	–	kJ^{-1}	kJ^{-1}
0	0.12	2.0	0	0.12	2.0	0.1	0.12	2.0	0.1	0.12	2.0
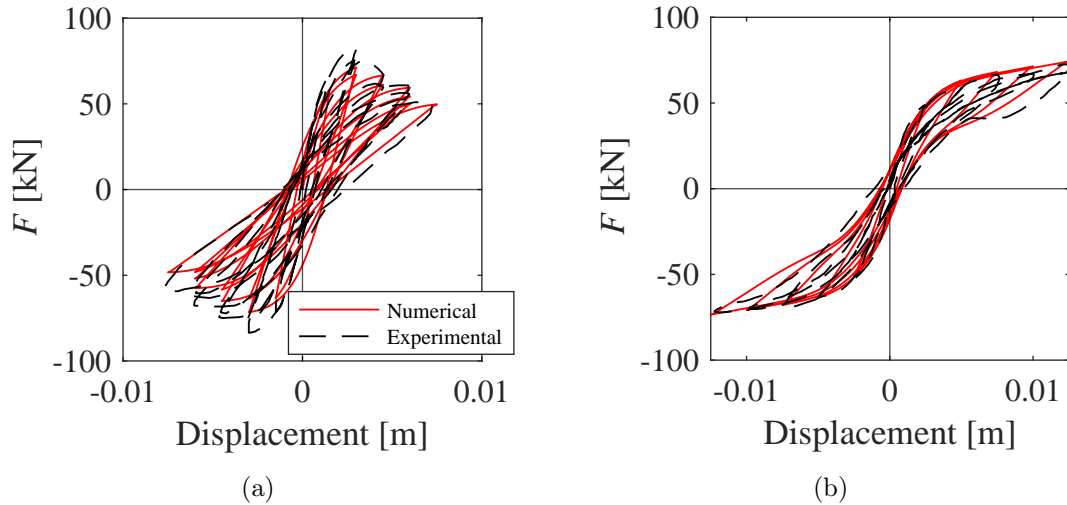
Figure 4.4: Comparison between experimental and numerical results for the Ispra squat wall (a) and Ispra slender wall (b)

the specimens.

The main aspects of the behavior of the squat wall, such as the energy dissipation and the strong strength and stiffness degradation are quite well-captured. In the case of the slender panel, where the two flexural hinges have a strong influence

on the response, the initial stiffness can be quite well reproduced, together with the pronounced pinching and stiffness degradation of the unloading branches. In this latter case, a value of $k_0^{NLE} = 0.25$ and $F_0^{NLE} = 45\,\text{kN}$ are adopted.
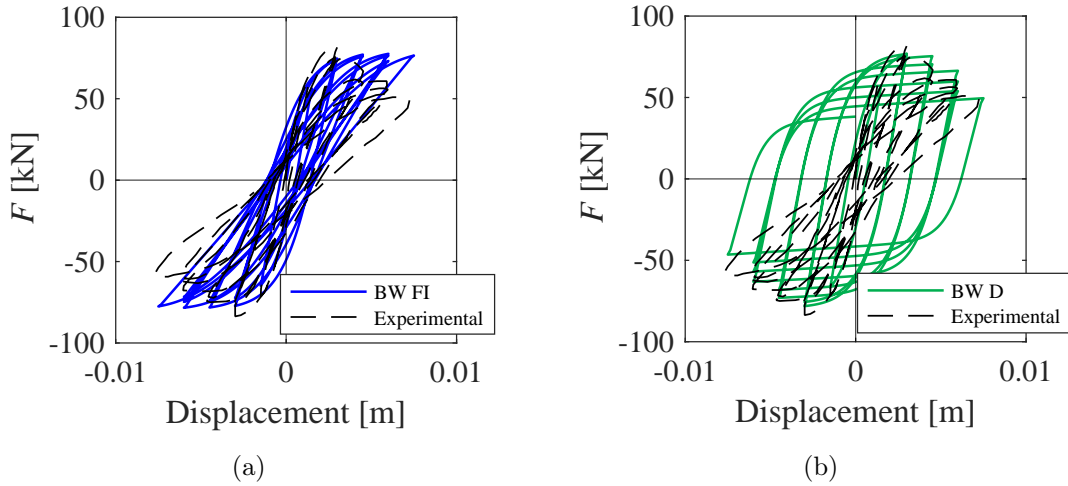
Figure 4.5: Comparison between experimental and numerical results for the Ispra squat wall with a Bouc-Wen model with flexibility increase only (a) and with a Bouc-Wen model with damage only (b)

To better investigate the influence of damage and flexibility increase on the response of the squat panel, two additional cases are presented in Fig. 4.5. Fig. 4.5 (a) shows the presence of flexibility increase only, with a value of δ_K equal to $1.5\,\text{kJ}^{-1}$ and δ_D equal to 0, while in Fig. 4.5 (b) a case with damage only is considered, assuming a value of δ_D equal to $0.04\,\text{kJ}^{-1}$ and δ_K equal to 0. In both cases, the parameters are calibrated with the aim of having a good respondence between the numerical and the experimental results.

The comparison between the experimental results and those obtained with a Bouc-Wen model with flexibility increase only shows a quite good respondence between the two cyclic curves in terms of stiffness degradation (Fig. 4.5 (a)). The area of the cycles is similar to that of the numerical curve, as well as the energy dissiapted at each cycle, thanks to the δ_K parameter which shrinks the cycles. However, no strength degradation is experienced, and the same value of force is reached with the progress of the analysis. Coherently with Fig. 3.5, Fig. 4.5 (b) shows that the model with damage only is able to well capture the strength

degradation, however the area of the force-displacement cycles is considerably wider with respect to that of the experimental curve, and consequently the energy dissipated by the system is excessively higher. Moreover, the effect of the δ_D parameter on the stiffness degradation is too modest to match the actual stiffness degradation experienced.

4.5 Dynamic behavior of masonry panels

The macroelement model is employed for the analysis of two masonry panels, in order to test the performance of the modified Bouc-Wen consitituive law in the dynamic field. In particular, the mechanical parameters described in Tab. 4.1 are adopted fpr both, with the aim of simulating the same unreinforced masonry made of bricks and lime mortar of the Ispra panels, but different geometrical and boundary characteristics are defined. The maximum elastic displacement, which indicates the elastic range threshold, is evaluated according to Par. 4.1.4.

A squat wall and a slender wall are considered, having an aspect ratio equal to 1.35 and 3, respectively, with the aim of highlighting the shear hinge behavior in the first case and the flexural behavior in the second. Three harmonic excitations are applied in each case at the base of the panel, to simulate an acceleration time history, in which the ratio between the angular frequency of the excitation Ω and the one of the panel ω is constant and proximate to resonance, increasing and decreasing. These are derived through acceleration histories whose equation is: $\ddot{u}(t) = U\sin[\Omega(t)\,t]$, where U is the amplitude of the excitation and Ω the angular frequency of the excitation. In addition, for each of the panels, the behavior of the proposed modified Bouc-Wen model is compared to an elastic case, a classic Bouc-Wen hysteresis and a modified Bouc-Wen case with damage only, proposed in Liberatore et al. (2019).

Further modifications to the panels, regarding geometric assumptions and constitutive parameters, are investigated more in detail in the following paragraphs.

4.5.1   Squat panel

The squat panel has a ratio between its height and base equal to 1.35, with a thickness equal to 0.25 m. Regarding the boundary conditions, the rotation is restrained at both the top and base of the panel, allowing the horizontal translation of the top only.

Regarding the dynamic parameters, a 5 % damping factor is assumed, and a density mass equal to $4.8\,\text{t/m}^3$ is set, increased with respect to the literature reference value to get a high natural period for the panel, which permits to attain high displacement amplitudes, to better emphasize the shape of the hysteretic cycles.

The amplitude of the three excitations is set equal to $60\,\text{m/s}^2$, while the ratio between the angular frequency of the excitation and that of the panel (Ω/ω) is taken equal to 0.95 in the constant case, while it ranges between 0.2 and 1.5 in the increasing and decreasing cases.

The values adopted for the flexural and shear hinge parameters of the modified Bouc-Wen case are listed in Tab. 4.3. It is noteworthy that the contribution of the flexural hinges for this panel results as negligible, thus in the following only the shear hinge results are shown.

Table 4.3: Nonlinear hinges parameters for the dynamic analysis of the squat panel

Flexural hinges			Shear hinge		
a	δ_D	δ_K	a	δ_D	δ_K
$-$	kJ^{-1}	kJ^{-1}	$-$	kJ^{-1}	kJ^{-1}
0.1	0.2	0.3	0.1	0.2	0.3

Figs. 4.6, 4.7 and 4.8, show the response of the panel to fixed, increasing and decreasing Ω/ω ratio respectively, presenting in red the proposed modified Bouc-Wen case, in dashed blue the classic Bouc-Wen case and in dashed black the elastic case. Results are shown in terms of global displacement Δ of the top of the panel with respect to its base, shear hinge loops and damage variable D of the shear hinge.
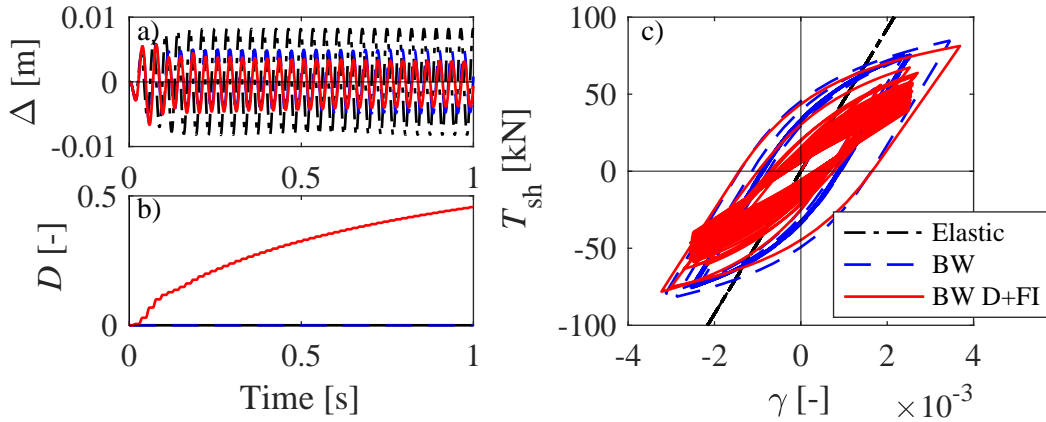
Figure 4.6: Squat panel dynamic response; global horizontal displacement (a), damage trend (b), shear hinge response (c) to the excitation with fixed Ω/ω
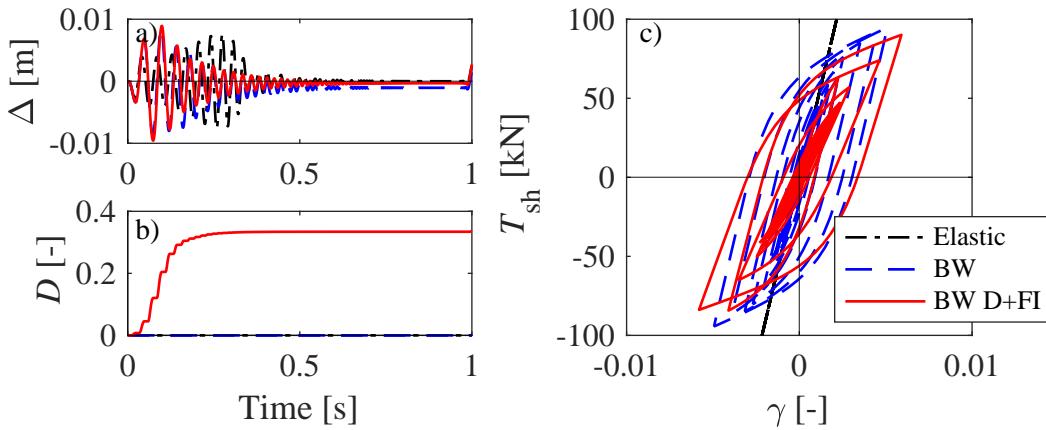
Figure 4.7: Squat panel dynamic response; global horizontal displacement (a), damage trend (b), shear hinge response (c) to the excitation with increasing Ω/ω

Analyzing the case with fixed Ω/ω ratio first, Fig. 4.6 shows that in the first cycle the classic and modified Bouc-Wen models cover a similar path, but depart immediately after, due to the higher displacement, and consequently higher period, reached by the modified case. The damage variable, which assumes values different from zero only in the modified Bouc-Wen case, thanks to its dependency on the dissipated energy and to the thermodynamic assumptions reported in Chapter 3, results to be increasing during the entire analysis, until the vlaue of approximately 0.45. However, its growth shows two different trends, one in
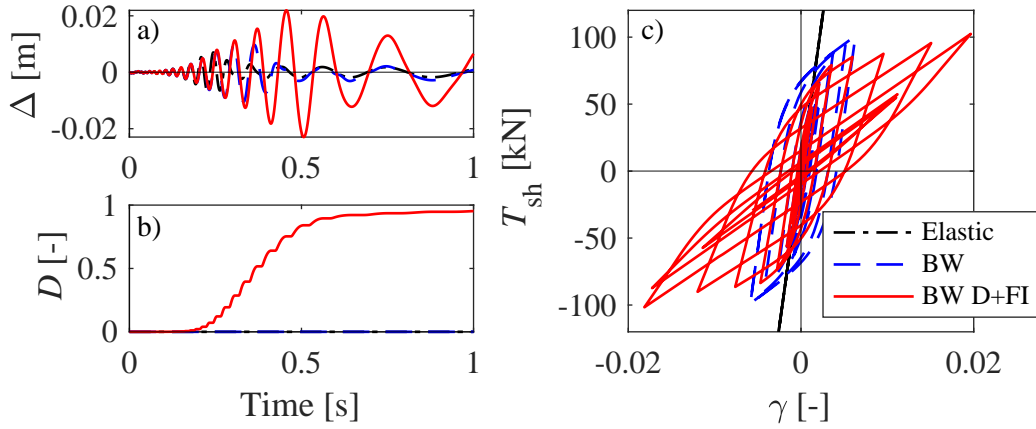
Figure 4.8: Squat panel dynamic response; global horizontal displacement (a), damage trend (b), shear hinge response (c) to the excitation with decreasing Ω/ω

the first $0.1\,\mathrm{s}$, and one in the rest of the analysis. In the first section, a more rapid growth is shown, until the value of 0.1, which is almost a quarter of the maximum value reached. This is strictly connected to the first couple of cycles of the analysis, in which the largest displacements are experienced. After that, the following cycles reach displacement levels that are lower and almost constant. In these latter, the influence of damage on the panel behavior can be detected. The presence of damage and flexibility increase causes strength and stiffness reduction, which is spread during the rest of the analysis and shows a smooth trend. The hysteretic cycles are then narrower, and their equivalent stiffness tends to be reduced at each cycle.

The different frequency content of the excitations with increasing and decreasing Ω/ω ratio, shows significantly different responses of the panel.

The case with increasing Ω/ω ratio is analyzed first. The modified and classic Bouc-Wen models experience similar behavior in terms of global displacement. In fact, they both show a short and rapid raise of the displacement amplitude in the first couple of cycles, followed by an almost continuous decrease for the rest of the duration of the signal, until reaching a stationary response assessed on really low values of residual displacement, with an amplitude of the oscillation that is almost null. Also, the classical Bouc-Wen model shows a residual displacement more pronounced than that of the modified formulation. This discords from the

behavior of the elastic case, which, on the contrary, shows an increasing displacement amplitude until about 0.35 s, followed by a rapid decrease of the response until an almost null oscillation around the zero displacement. The shear hinge of the modified Bouc-Wen hysteresis clearly shows the effects of strength and stiffness degradation with respect to the classic case. This is also highlighted by the shrinkage of the cycles caused by flexibility increase, which enhances their trend to reduce the equivalent stiffness. The maximum value of damage, 0.34, is rapidly reached few steps later than 0.2 s, after which a short and smooth increasing phase can be detected, followed in the rest of the analysis by a constant value. In this latter phase, the decreasing hysteretic cycles tend to have a null area and no further damage is experienced.

In the last case, in which the Ω/ω ratio is decreasing (Fig. 4.8), the rapid increase of the damage variable from 0 to 0.9 is concentrated between 0.2 and 0.6 s, when global displacement with increasing amplitude until the maximum value and fat-shaped and wider shear cycles are experienced. After a first initial short phase in which the classic Bouc-Wen cycles are almost overlapped to those of the modified Bouc-Wen case, damage becomes overriding and strength reduction is experienced. Stiffness is also reduced in the loading and unloading branches due to the presence of flexibility increase, leading to reach higher displacement values whith respect to the classic Bouc-Wen case. The last 0.4 s of the analysis are characterized by a reduction of the displacements amplitude and an increase of the period which results in a low number of cycles experienced. Thin hysteretic cycles can be detected, in which the drastic strength and stiffness degradation leads to an almost null area, to which correspond a loose increase of the damage variable, which goes from the value of 0.9 to 0.95.

It should be emphasized that even if in the increasing sweep case damage increases from the very beginning of the analysis, with respect to Fig. 4.8 where it starts increasing after 0.2 s, its growth is more rapid and is concentrated in a lapse of time that is almost half as much as the case with increasing forcing frequency, while the maximum reached value is a third with respect to the other case.

The hysteretic behavior in presence and absence of flexibility increase is investigated in the following, considering the same three excitations and comparing

the elastic (dashed black line), the proposed modified Bouc-Wen (solid red line) and the case with damage only (dashed blue line). Moreover, to better appreciate the influence of the studied parameter, the flexibility increase parameter δ_K is increased from the value of $0.3\,\text{kJ}^{-1}$ to the value of $5\,\text{kJ}^{-1}$, while the damage parameter δ_D keeps the value assumed in Tab. 4.3. Each case is divided into two figures, with the aim of highlighting different sections of the same curve.
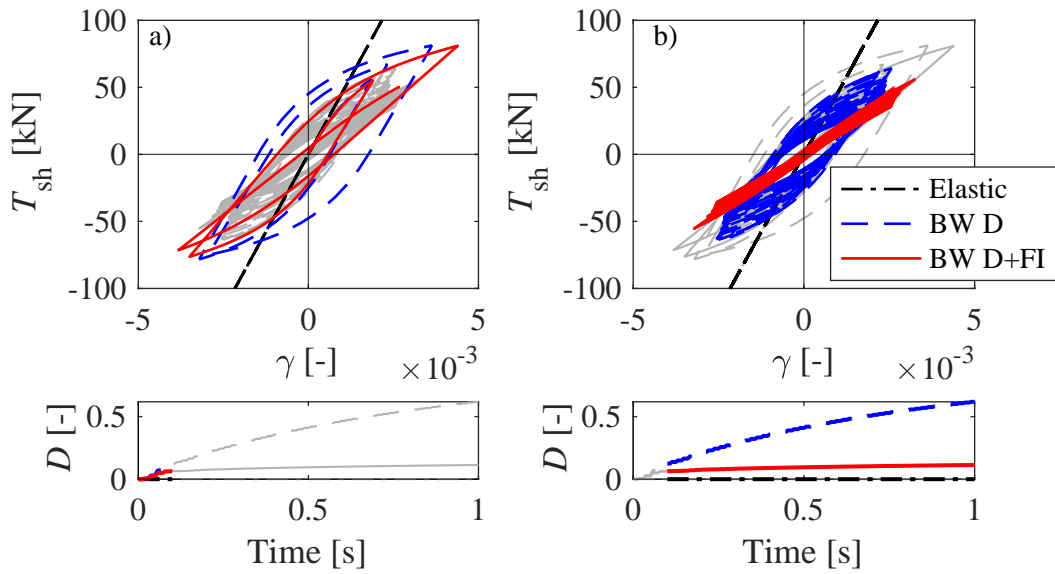
Figure 4.9: Response of the squat panel with $\delta_K = 5\,\text{kJ}^{-1}$: shear hinge response and damage for an excitation with fixed Ω/ω. Zoom on the first cycles (a), zoom on the following cycles (b)

The response to the excitation with fixed Ω/ω ratio is shown in Fig. 4.9, where Fig. 4.9 (a) displays the initial cycles and Fig. 4.9 (b) the second part of the analysis. The flexibility increase effect can clearly be detected in Fig. 4.9 (a) where, despite the same strength degradation level is imposed, a rapid thinning of the cycles, with respect to the case with damage only, can be seen in the modified Bouc-Wen. The evolution of dissipated energy affects and enhances the flexibility contribution with the progression of the analysis, tightening the cycles. This results also in visibly higher shear strain values. In Fig. 4.9 (b), the focus is on the resonant response experienced by the panel. The presence of flexibility increase reduces the cycles almost to lines, lowering also their slope as the analysis

evolves. On the contrary, the cycles with damage only tend to maintain the large shape typical of the Bouc-Wen cycles, showing strength reduction only. Interesting considerations concerning the evolution of damage can be made. The case with damage only, in fact, experiences a higher damage value with respect to the other case during the entire duration of the analysis, with the exception of the first cycle, when the two behaviors are almost coincident. The reduction of the area of the cycles, caused by the increase of the elastic displacement, leads to a lower dissipated energy for each cycle. Consequently, the values of damage reached by the case with flexibility increase are significantly lower, i.e. 0.1 with respect to 0.6 reached by the case with damage only, being the scalar damage variable D directly related to the dissipated energy. The damage graph in Fig. 4.9 (b) clearly shows this trend after 0.1 s, where the level of damage experienced in the case with flexibility increase is almost constant, having the experienced cycles an almost null area, while a significant smooth increase of the variable D until the end of the analysis is observed in the case with pure damage.
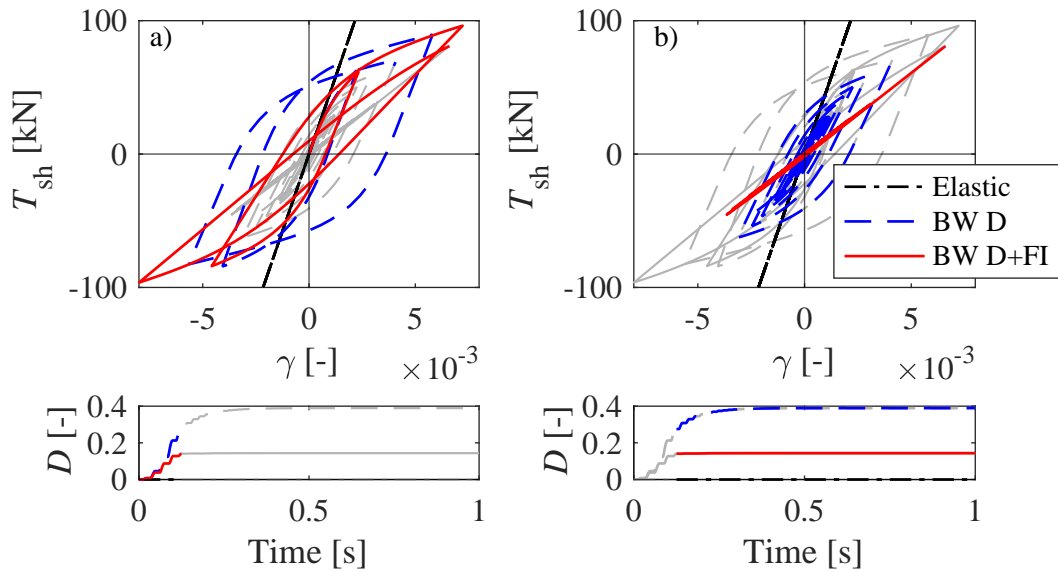
Figure 4.10: Response of the squat panel with $\delta_K = 5\,\text{kJ}^{-1}$: shear hinge response and damage for an excitation with increasing Ω/ω. Zoom on the first cycles (a), zoom on the following cycles (b)

The results shown in Figs. 4.10 (a) and (b) are in agreement with Figs. 4.9
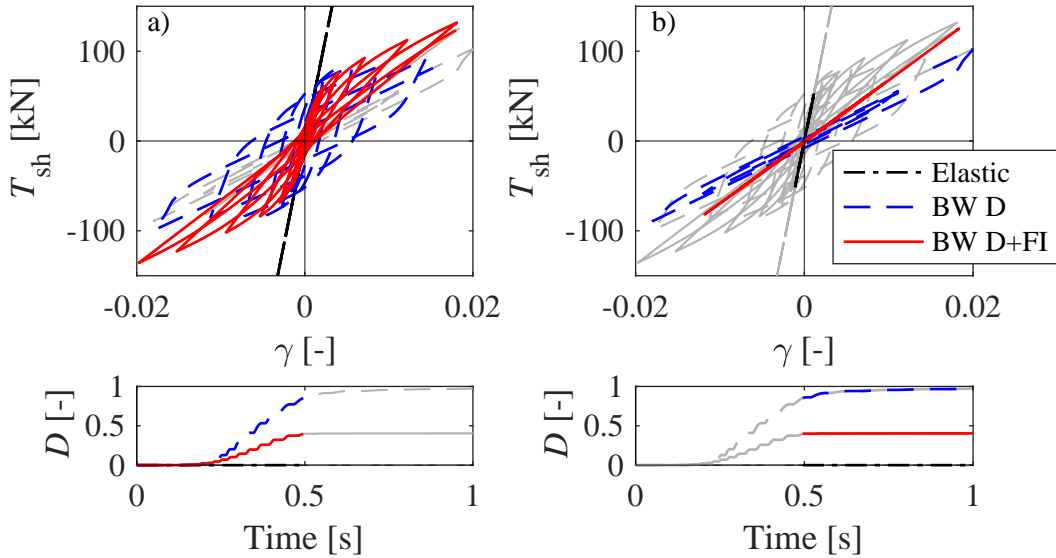
Figure 4.11: Response of the squat panel with $\delta_K = 5\,\text{kJ}^{-1}$: shear hinge response and damage for an excitation with decreasing Ω/ω. Zoom on the first cycles (a), zoom on the following cycles (b)

(a) and (b), confirming that the case with damage only reaches a higher damage variable value. The influence of flexibility increase in shown in both the hysteretic curves from the first cycles of the analysis, in which the panel reaches higher values of shear deformation with considerably lower stiffness in the loading and unloading branches. In both cases, after about $0.12\,\text{s}$, the cycles tend to rapidly collapse around the origin (Fig. 4.10 (b)), as the increasing angular frequency of the excitation makes the panel experience cycles with lower amplitudes with the progression of the analysis. The amplitude of the cycles of the panel with δ_K equal to $5\,\text{kJ}^{-1}$ is rapidly annulled, interrupting the growth of the damage variable. On the contrary, the case with pure damage still shows an increasing variable D, as some of the subsequent cycles still show strength degradation, having a non-null amplitude.

Finally, Fig. 4.11 (a) shows visibly thinner cycles for the modified Bouc-Wen hysteresis, in accordance with the behavior described previously. Damage onsets at about $0.2\,\text{s}$ in both cases, when the panel response exits from the elastic range, and increases until $0.5\,\text{s}$ for the case with flexibility increase and $0.6\,\text{s}$ for the case

with damage only. After that, it continues almost constant until the end of the analysis. This latter section of the curve, shown in Fig. 4.11 (b), corresponds in both cases to thin cycles with low area and consequently with low energy dissipation. In addition, the case with δ_K equal to $5\,\mathrm{kJ}^{-1}$ reaches a maximum value of damage equal to 0.4, even if the experienced cycles are reduced to lines, while the case with null δ_K almost reaches a value equal to 1, being the fully damaged state. The presence of flexibility increase thus reduces the values of the damage variable D reached during the analysis.

Finally, phase space diagrams are also presented for the three excitations, by correlating the displacement to the velocity experienced by the panel, for the initial modified Bouc-Wen case, with $\delta_K = 0.3\,\mathrm{kJ}^{-1}$.
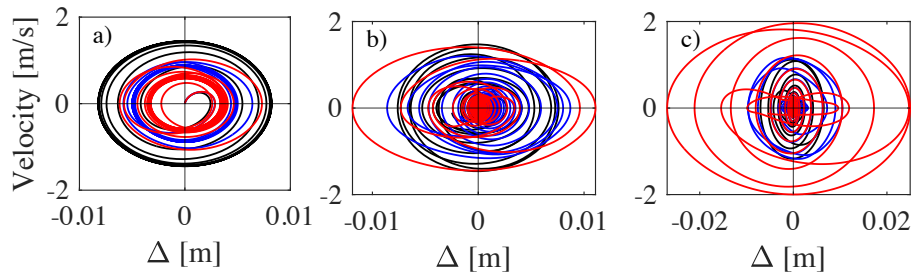
Figure 4.12: Phase space diagrams for the three excitation for the modified Bouc-Wen with damage and flexibility increase (red), the classic Bouc-Wen (blue) and the elastic (black) cases.

The resonant case (Fig. 4.12 (a)) shows how the two Bouc-Wen cases experience always lower cyclies with respect to the elastic case, and are almost overlapped. This is consistent with the results obtained in Fig. 4.6, where the resonant condition of the elastic case experienced the widest displacements with a constant amplitude. In the case of the increasing sweep (Fig. 4.12 (b)), in all three cases the cycles tend to collapse to the origin, consistently with the behavior shown in the previous figures. An oval-shaped trend can be detected for both the Bouc-Wen cases, and the case with flexibility increase experiences wider displacements and velocities. The modified Bouc-Wen case in the decreasing sweep case (Fig. 4.12 (c)) experiences the widest cycles again, on both the displacement and velocity axes, collapsing to the origin in the final instants. The classic Bouc-Wen

and the elastic case both experience really lower amplitude.

4.5.2 Slender panel

The slender panel analyzed is characterized by a height equal to 3 m and base length equal to 1 m, resulting in a geometric ratio equal to 3, while the thickness is equal to 0.25 m. In Tab. 4.4, the parameters adopted for the flexural and shear hinges are listed. Similarly to the squat panel, in the following analyses the major contribution to the response in given by the flexural hinges, and the shear hinge contribution is not relevant.

A damping factor equal to 5 % is assumed, consistently with the squat case, while a density mass equal to $1.8 \, \text{t/m}^3$ is considered.

The three harmonic excitations are obtained by setting the ratio between the frequency of the excitation Ω, and the frequency of the wall ω equal to 0.95, close to the resonance condition, and considering that the period of the excitation varies between 0.2 and 1.5 times the period of the wall for the increasing and decreasing cases. The amplitude of the excitations is equal to 1.2 g, where g is the gravity acceleration, in all cases.

Table 4.4: Nonlinear hinges parameters for the dynamic analysis of the slender panel

Flexural hinges			Shear hinge		
a	δ_D	δ_K	a	δ_D	δ_K
–	kJ^{-1}	kJ^{-1}	–	kJ^{-1}	kJ^{-1}
0.1	10	10	0.1	10	10

In this case as well, the response of the wall clearly highlights how the presence of damage and flexibility increase affects the hysteretic behavior, as can be seen in the following figures. Results are given in terms of global displacement of the top of the panel, variation of the period with respect to the initial elastic period in time and the behavior of the flexural hinge located at the base of the panel in terms of moment and rotation. The proposed modified Bouc-Wen model, represented in solid red line, is compared to the classic Bouc-Wen, in dashed blue line, and

the elastic case, in black. Each case is then divided into two figures, to highlight different sections of the curves.

In all the cases, as expected, the period of the case with degradation results higher than the period of the classic Bouc-Wen hysteresis.
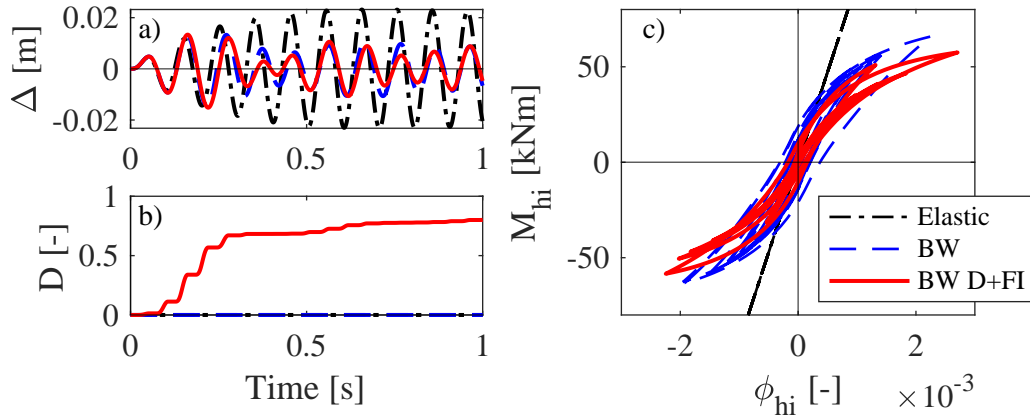
Figure 4.13: Slender panel dynamic response; global horizontal displacement (a), damage trend (b), flexural hinge response (c) to the excitaion with fixed Ω/ω
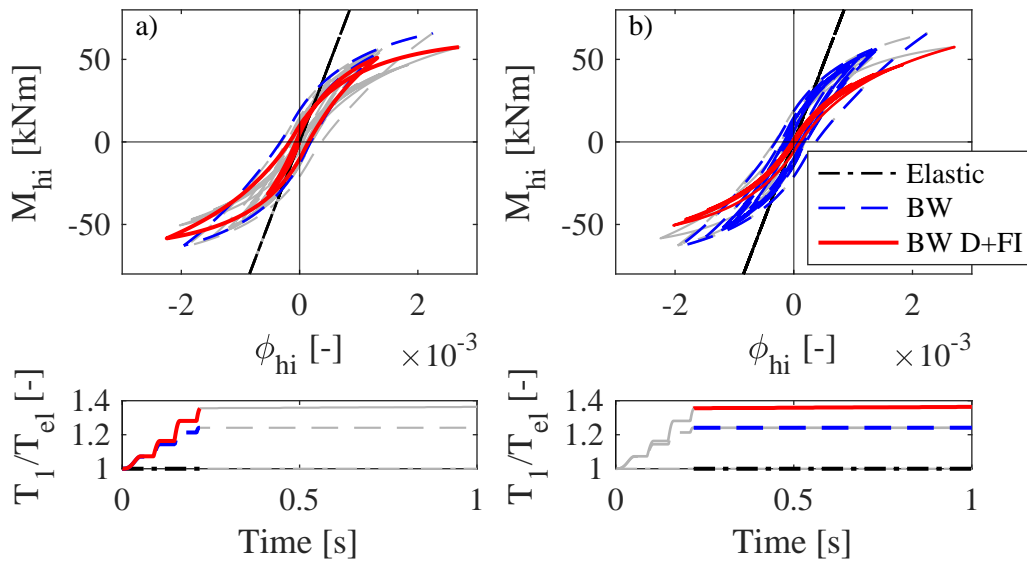
Figure 4.14: Response of the slender panel: flexural hinge response and ratio between the secant and the initial elastic period for an excitation with fixed Ω/ω. Zoom on the first cycles (a), zoom on the following cycles (b)

Fig. 4.13 shows the response to the excitation with fixed Ω/ω ratio. The behavior experienced is close to that seen for the squat panel: after the first couple of cycles, in which the maximum displcement is reached, the case with degradation departs from the elastic displacement and damage increases. This allows the panel with damage and flexibility increase experience lower displcements with respect to the classic Bouc-Wen case (Fig. 4.13 (a)) in some of the following cycles, where the resonance condition is reached for all three cases. The evolution of damage shows a first phase in which a rapid increase is experienced, followed by a second phase with a more gradual growth, due to the reduction of the area of the hysteretic cycles.

Fig. 4.14 (a) clearly shows the effect of degradation in the hinge response of the case with flexibility increase. A modal analysis is performed at each step of the analysis, in order to evaluate the variation of the period in presence of damage and flexibility increase. The secant period is evaluated from the secant stiffness at each time step, thus the maximum value of period is reached in correspondence of the maximum displacement experienced, while in the unloading branches and for lower displacements experienced afterwards, the period remains constant. It is shown that the first cycle of the case with flexibility increase is almost overlapped with the classic Bouc-Wen curve, however from the second cycle on, both the strength and stiffness degradation affect the moment, increasing the rotation experienced at each cycle and consequently the period of the system, which reaches its highest value. The following cycles, in Fig. 4.14 (b), do not contribute to increasing the period, which remains constant, being reached lower displacements. However, the cycles are narrower, due to the presence of the flexibility increase, and the value of the moment is clearly affected by strength degradation.

Figs. 4.15 and 4.16 show the results of the excitations with increasing and decreasing Ω/ω ratio, respectively.

In Fig. 4.15, the widest cycles are experienced in the first $0.3\,\mathrm{s}$ of the analysis, where damage shows a rapid increase in a short lapse of time. On the contrary, the following cycles have a decreasing amplitude, and the period remains constant. Both strength and stiffness degradation can easily be distinguished in the flexural hinge response. Coherently with the case with fixed Ω/ω ratio, the first cycle is almost overlapped to the classic Bouc-Wen model, while the following are visibly
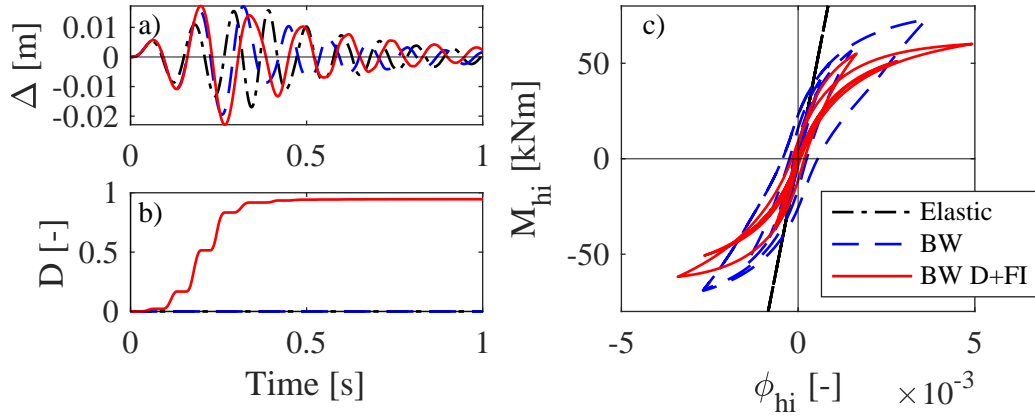
Figure 4.15: Slender panel dynamic response; global horizontal displacement (a), damage trend (b), flexural hinge response (c) to the excitaion with increasing Ω/ω
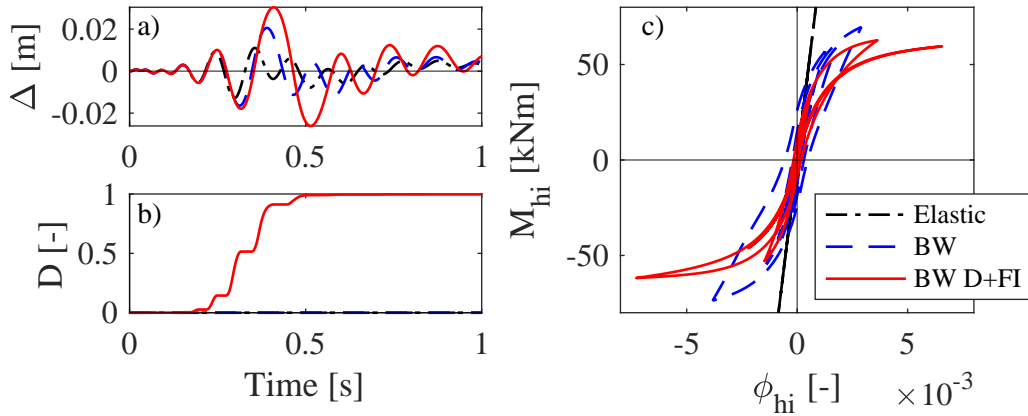
Figure 4.16: Slender panel dynamic response; global horizontal displacement (a), damage trend (b), flexural hinge response (c) to the excitaion with decreasing Ω/ω

thinner, with a strong stiffness degradation in the loading and unloading branches. Moreover, the cycles with decreasing amplitude become almost nonlinear elastic, as the dissipation capacity of the hinge is depleted, the nonlinear elastic device in parallel with the modified Bouc-Wen hysteresis prevails and the damage variable reaches values close to 1.

Regarding the decreasing excitation (Fig. 4.16), the widest cycles are experienced forward in the analysis, approximately between 0.3 and 0.5 s. The shrinkage

of the cycles caused by the flexibility increase can then be recognized, and higher rotation are reached with respect to the classic Bouc-Wen model. It is noteworthy that the value of damage reached in the modified Bouc-Wen is 1, and the panel results fully damaged.
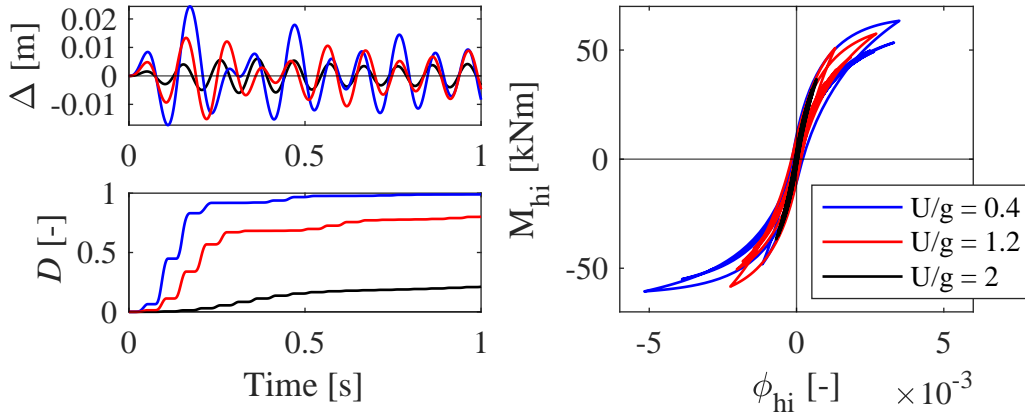
Figure 4.17: Response of the slender panel to the excitation with fixed ratio $\Omega/\omega = 0.95$ and amplitude equal to $0.4\,\mathrm{g}$, $1.2\,\mathrm{g}$, $2\,\mathrm{g}$.

The effect of the amplitude of the excitation on the evolution of damage and flexibility increase is also investigated. Two additional excitations, with amplitude equal to $0.4\,\mathrm{g}$ and $2\,\mathrm{g}$ respectively, are considered for the case with fixed Ω/ω ratio, and compared to the case with $1.2\,\mathrm{g}$ amplitude. The results in Fig. 4.17 show, as expected, that the response to the higher excitation reaches higher displacements. When the amplitude of the excitation is lower, even though the damage variable has smaller values compared to the other cases, its growth is more spread over time. This is due to the circumstance that the maximum displacement experienced is reached by the system later and more gradually, suggesting a more spread distribution of the damage over the wall. On the contrary, the case with higher amplitude shows a more rapid increase of damage in a shorter lapse of time, as the maximum displacement is reached at the second cycle of the analysis.

The resonant case (Fig. 4.18 (a)) shows how the two Bouc-Wen cases experience always lower cyclies with respect to the elastic case, and are almost overlapped. In the case of the increasing sweep (Fig. 4.18 (b)), the largest cycle experienced belongs to the modified Bouc-Wen case, which is also oval-shaped
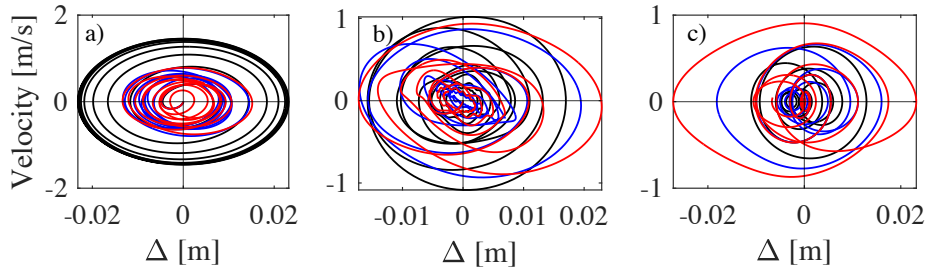
Figure 4.18: Phase space diagrams for the three excitation for the modified Bouc-Wen with damage and flexibility increase (red), the classic Bouc-Wen (blue) and the elastic (black) cases.

with respect to the other cases. The decreasing sweep (Fig. 4.18 (c)) shows the most interestig behavior: the cycles are shifted to the left, due to the residual displacement experienced, and the modified Bouc-Wen case has the widest area. All cases, this latter in particular, have a more squared behavior, due to the presence of the pinching effect.

4.5.3   Masonry slender wall

A second slender wall is analyzed, with the aim of comparing the performance of the macroelement model with a 2D finite element approach in which an advanced consititutive law with damage (Gatta et al., 2018) is implemented. The performance of the macroelement and of the constitutive law with damage and flexibility increase is also tested within nonlinear dynamic analyses.

4.5.3.1   Quasi-static cyclic excitation

The panel wants to reproduce the central portion of a wall in which the length dimension is predominant compared to its height and thickness, loaded in the out-of-plane direction, typical characteristics of historical buildings or churches. A strip is then modeled as it is loaded in the in-plane direction, and the thickness of the wall becomes the base of the numerical model. As an example, the wall of Basilica S. Maria di Collemaggio, in L'Aquila (Italy), is considered for the geometry and mechanical parameters. The numerical model has then a height of 6 m, a base of 1 m and a thickness of 1 m, and the mechanical parameters are

those listed in Tab. 4.5 (Gattulli et al., 2013). Boudary conditions are those of a simple cantilever, with the base fixed.

Table 4.5: Slender wall mechanical parameters

E	G	f_c	f_{v0}
kN/m^2	kN/m^2	kN/m^2	kN/m^2
$4000\,10^3$	$1666.667\,10^3$	4200	290

The shear modulus G is evaluated as $G = E/(2(1 + \nu))$, considering $\nu = 0.2$; the compressive and shear strengths are chosen in accordance with the perscriptions given in NTC (2018). For the modified Bouc-Wen model, which describes the behavior of the flexural hinges, the parameters listed in Tab. 4.6 are adopted. The wall is subjected to its self-weigth first, and then to a quasi-static cyclic displacement history applied at the top. The results (in red), shown in Fig. 4.19, are compared to the results obtained in Gatta et al. (2018) (in black), which adopt a 2D FE macromechanical approach with a constitutive law with damage and plasticity.

Table 4.6: Nonlinear hinges parameters for the dynamic analysis of the 6 m slender wall

Flexural hinges			
a	δ_D	δ_K	n
$-$	kJ^{-1}	kJ^{-1}	$-$
-0.01	0.34	1.25	2

The shear hinge is assumed elastic during the entire analysis, being its contribution negligible due to the high slenderness of the panel. Only the flexural hinge at the basis of the panel is activated, consistently with the damage ivolution experienced in the FE model.

The equivalent frame model is able to capture quite well the main aspects of the response, such as the straight and severe initial elastic branch of the panel and the
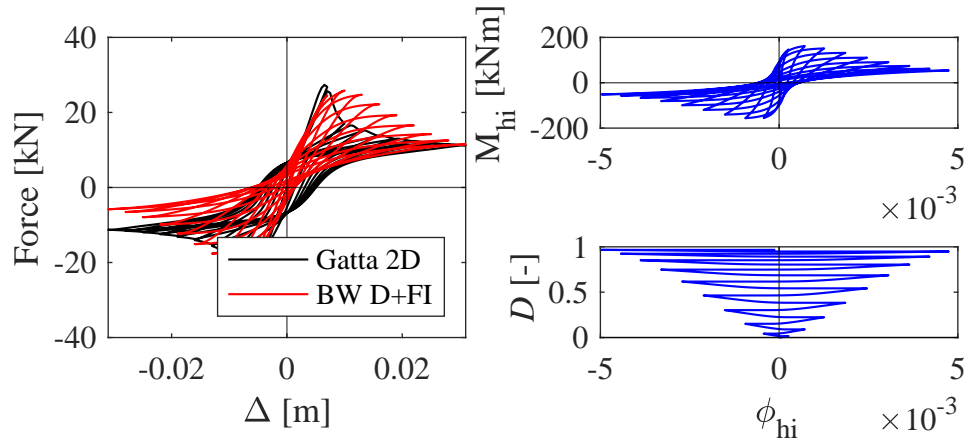
Figure 4.19: Response of the 6 m slender panel to a quasi-static cyclic excitation. Comparison with 2D FE model with plasticity and damage (Gatta et al., 2018) (a), flexural hinge response (b), damage evolution (c).

maximum force reached, or the strong degradation of both strength and stiffness during the evolution of the analysis, confirming its capability to reproduce with sufficient accuracy the response of masonry panels. However, some limits of the macroelement emerge. The pronounced softening behavior of the FE panel, caused by the rocking mechanisms experienced during the analysis, is hardly captured, and a negative hardening parameter a is required. The degrading behavior appears less severe, especially in the second and third cycle, compared to the FE model.
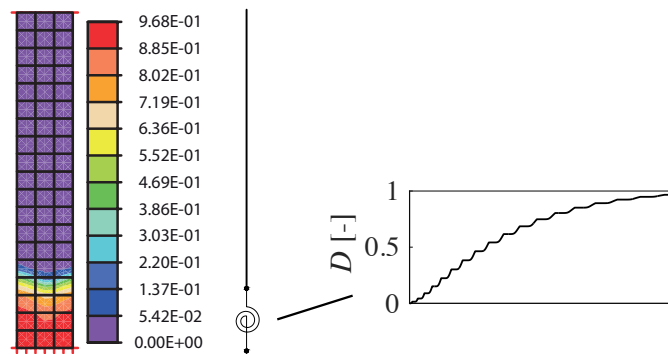
Figure 4.20: Comparison between the damage pattern of the 2D FE Gatta et al. (2018) model and the damage variable D of the equivalent frame model with flexural hinge

Comparable values of the damage parameter are obtained (Fig. 4.20), even if it should be noted that in the 2D FE model damage is spread over the panel and due to tensile states, while in the equivalent frame model it is considered lumped entirely at the base of the panel and related mainly to energy dissipation.

4.5.3.2   Linear dynamic investigation

A linear dynamic analysis in perfomed with the aim of validating the use of a consistent mass matrix instead of a lumped mass matrix when the dynamic behavior is studied.

The results relative to the first three natural vibration frequencies of the F.E. model, of the equivalent frame model with a consistent mass matrix and of the equivalent frame model with a lumped mass matrix are shown in Tab. 4.6, and are evaluated assuming a density mass value ρ equal to $2\,\mathrm{t/m^3}$.

Table 4.7: Comparison of the first three natural vibration frequencies of the Gatta 2D FE model, equivalent frame model with consistent and lumped mass matrix.

	f_1	f_2	f_3
—	Hz	Hz	Hz
Gatta 2D FE	6.23	35.16	86.98
BW D+FI Consistent	6.25	54.57	70.21
BW D+FI Lumped	4.36	53.05	103.31

From the quasi-static cyclic results, the initial stiffness of the panel results to be approximately equal to that of the 2D FE model. All the differences between the vibration frequencies are, thus, exclusively due to the evaluation of the mass matrix.

The lumped mass approach results in really different results, in all three cases, giving a value relative to the first vibration frequency with an error equal approximately to $30\,\%$ with respect to the FE case.

However, as expected, the results of the consistent mass matrix correspond to the 2D finite element model with really good accuracy, with an error equal to $0.3\,\%$. The second vibration frequency results equally inaccurate for both the

lumped and consistent mass approaches, with an error close to 35 %. On the contrary, the third frequency is lower for the consistent case with respect to the finite element model.

4.5.3.3   Nonlinear dynamic excitation

The dynamic response of the panel to a nonlinear dynamic excitation is investigated. The W-E component of the 2009 L'Aquila (Italy) natural record is selected, characterized by a 0.33 g Peak Ground Acceleration (PGA). Three different scale factors, equal to 0.75, 1 and 1.25, are applied to the natural accelerogram, to evaluate the influence of PGA and compare the results and evolution of damage to the 2D finite element case.
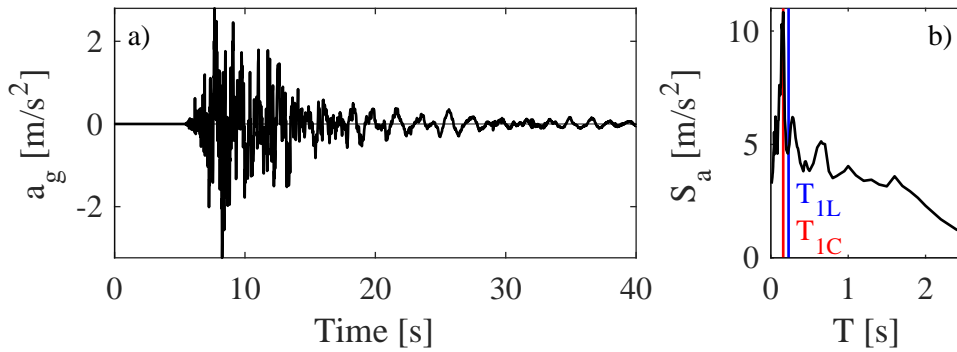
Figure 4.21: Acceleration history of 2009 L'Aquila earthquake (a) and response spectrum (b).

First, an elastic case is performed with the full scale natural accelerogram, to compare the nonlinear response of the consistent and lumped mass approaches. In Fig. 4.22 and following, only the most relevant part of the response is reported, between 6 and 26 s of the natural accelerogram, and is shifted to the origin.

Consistently with the results of the modal analysis, the modified Bouc-Wen case with consistent mass approach results in a closer response to that of the 2D FE model. In the peak phase, between about 2 and 4 s, the consistent mass case experiences displacements that are a little higher, while in the following cycles displacements are a little lower. The lumped mass approach, due to the minor quantity of mass excited at the top node, experiences a different oscillation with

respect to the other cases, and has a lower amplitude until about 6 s, and higher displacements in the rest of the analysis. Fig. 4.21 (b) is useful to explain this phenomenon, as the period of the consistent case is close to the peak of the pseudo-acceleration of the spectrum. The period of the lumped case instead, encounters the spectrum on higher values of the period, where lower pseudo-accelerations are experienced.
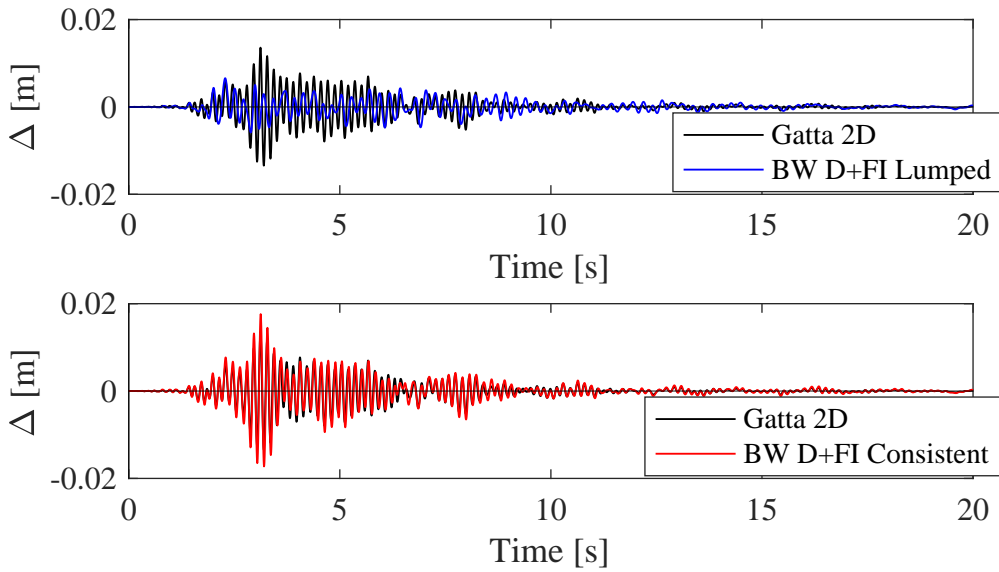
Figure 4.22: Comparison between the elastic response of the Gatta 2D FE model and the modified Bouc-Wen model with a lumped mass matrix, and with that with a consistent mass matrix.

Once the elastic cases are proven to behave similarly, the modified Bouc-Wen model with damage and flexibility increase with consistent mass matrix is compared to the 2D model with damage and plasticity in Gatta et al. (2018), to study how a lumped damage model behaves with respect to a distributed damage model. Damage is localized, in both cases, at the base of the panel only, being the flexural hinge at the base of the panel the only one activated in the macroelement. The responses in terms of displacements and of evolution of damage with respect to time are reported in Figs. 4.23, 4.24 and 4.25, where the two cases are compared.

In general, Fig. 4.23 (a) shows that a higher displacement amplitude is reached during most of the analysis, while the period of the oscillation remains quite similar. The peaks of the response are shifted on higher values of time, and while the

presence of damage in the 2D FE model diminishes the amplitude of the displacement after the first 5 s, in the modified Bouc-Wen model high displacements are still reached later in the analysis. The presence of flexibilty increase reduces the stiffness of the panel, enhancing this behavior. The residual displacement and the last part of the response is comparable between the two cases, being little lower for the macroelement case. The damage variable assumes a completely different behavior. It is noteworthy that while the damage variable of the 2D FE model is a global index of the damage experienced by the panel, in the modified Bouc-Wen case it is relative only to the nonlinear hinge located at the base of the panel, being the contribution of the other hinges neglectible and their damage variable null. This latter is connected to the evolution of dissipated energy, thus when the area of the cycles becomes null, due to the presence of both damage and flexibility increase which shrink the cycles with the analysis progression, it reaches an asimptotic value proximate to 0.18, while the 2D FE case reaches higher values. Moreover, the evolution of damage appears more distributed along the analysis, as each cycle contributes to its growth, while a steeper and abrupt growth is experienced in the other case.
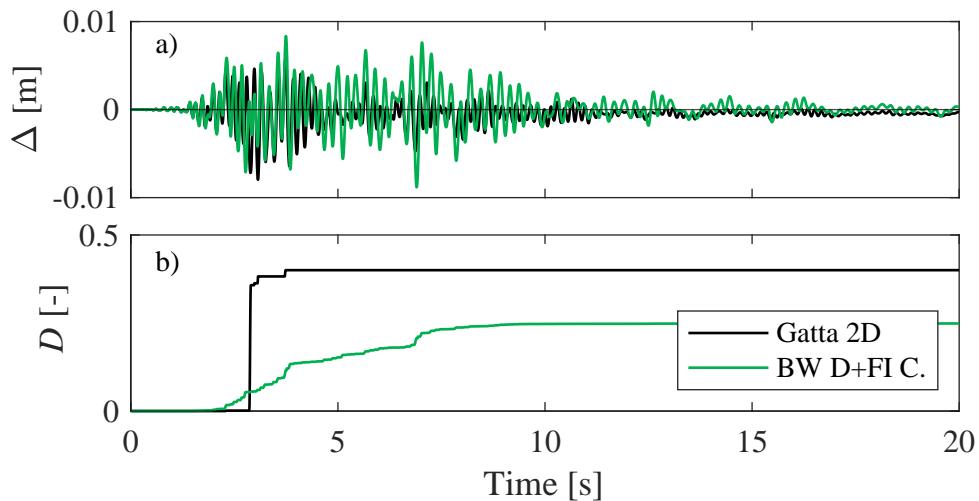
Figure 4.23: Comparison between the Gatta 2D FE model and the modified Bouc-Wen model to the excitiation 75 % L'Aquila.

A similar trend is shown in Fig. 4.24, even if higher residual displacements

are experienced in the macroelement case, together with wider oscillations in the central lapse of the analysis. Damage experiences a similar behavior, reaching its maximum value equal to 0.37. In both Fig. 4.23 and 4.24, however, damage starts to grow few tenths of a second before the 2D FE case, being the flexural hinge activated at the very beginning of the analysis.
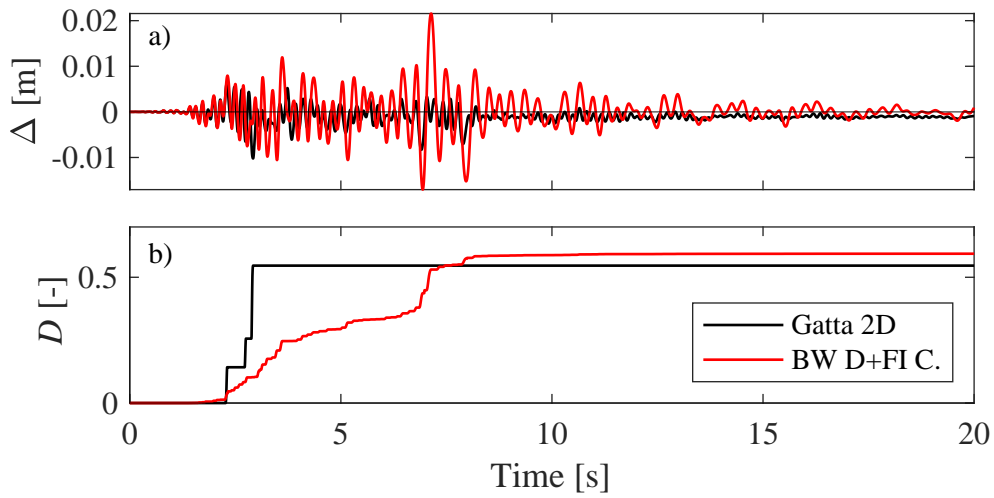
Figure 4.24: Comparison between the Gatta 2D FE model and the modified Bouc-Wen model to the excitiation 100 % L'Aquila.

The last case, in Fig. 4.25, is characterized for the modified Bouc-Wen model by a first phase, until about 7 s that almost follows the 2D F.E. model, with limited amplitude and lower damage experienced. In the second section of the analysis instead, high residual displacements and oscillations are experienced. This is due to the numerical cycles, that have consumed the entire dissipable area, arriving to have a null area and an elastic residual behavior, but continue to lower their slope due to the flexibility increase that still dimishes the stiffness of the system. This causes the increase of the period and also of the amplitude of the oscillation. Damage reaches values that are higher than those of the 2D FE case, with an almost constant value after the second section of the analysis is reached, with a more rapid increase with respect to the rest of the analysis.

One last comparison is carried on, considering the different evolution of damage of the flexural hinge in the three modified Bouc-Wen cases. After the first initial
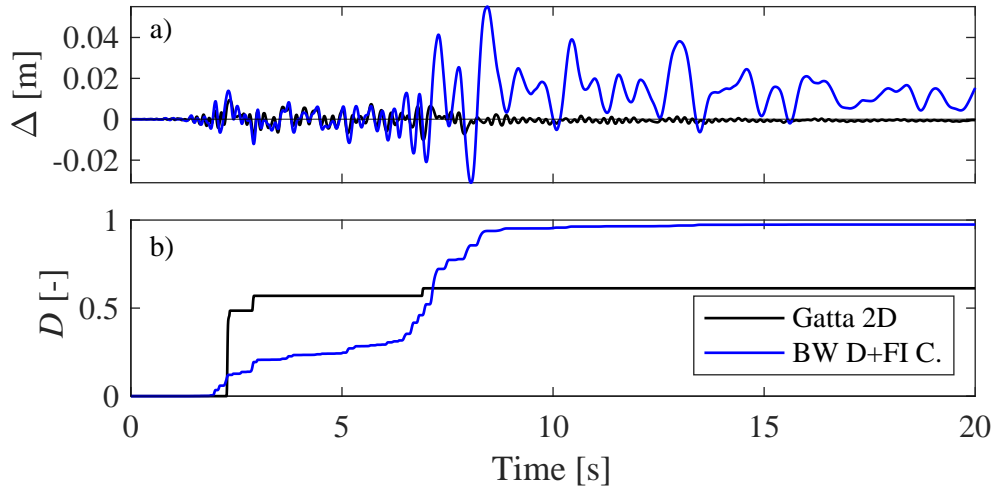
Figure 4.25: Comparison between the Gatta 2D FE model and the modified Bouc-Wen model to the excitiation 125 % L'Aquila.
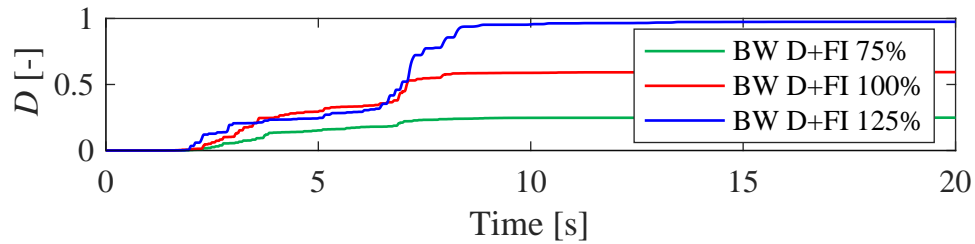
Figure 4.26: Comparison between the damage evolution in 75 %, 100 % and 125 % of L'Aquila excitation.

couple of seconds, where the behavior is still null or elastic, the increase of damage start for the three cases almost at the same time. As expected, the case realtive to the 75 % of the excitation is lower than the other cases during the entire analysis. Between 4 and 6 s, however, the case realtive to the 100 % excitation overcomes the 125 % excitation case, being reached higher displacements. At about 7 s, in correspondance of the second increase of the displacements amplitude, a relevant increase of damage is experienced by all three cases.

In conclusion, the effect of flexibility increase deeply affects the response of the panel. Regarding the evolution of damage, the dependence of damage from the dissipated energy allows a more distributed evolution of the variable, that reaches its maximum value much beyond the 2D FE case.

Chapter 5

Three-dimensional macroelement formulation

Equivalent frame approaches usually focus the attention on in-plane collapse mechanisms, neglecting out-of-plane failure modes in favour of a box-like behavior assumption. In fact, the connections between the walls, as well as the connections between the walls and floor diaphragms, are assumed to be sufficiently resistent to avoid the development of out-of-plane failure mechanisms. However, as highlighted in Chapter 2, disregarding out-of-plane mechanisms can lead to an overestimation of the actual capacity of the structure, avoiding the possibility to describe dangerous and sudden failures and possibly endangering users' safety. In fact, despite being considered as the "first damage mode" mechanisms (Magenes, 2006), out-of-plane mechanisms are usually associated to the local response of the structural element, and thus are analysed separately through rigid-body assumption analyses.

However, in more recent literature works, such as Vanin et al., 2020b,a, the importance of a proper description of out-of-plane mechanisms in equivalent frame approaches has been recognized. Different works, in fact, started to include them even in simplified approaches such as macroelement models, for which a fundamental aspect is to combine an adequate description of the behavior with reduced computational burdens in order to be competetive with more refined Finite Element models. This permits to account for more complex mechanisms, and to be

capable of describing more realistically the structural behavior expected in the cases of existing historical buildings, especially during seismic events, which usually are characterized by timber floor diaphragms and the other poor connections in general.

The main out-of-plane mechanisms are one-way and two-way bending modes, which can evolve depending especially on boundary conditions.

The following Chapter proposes an enhancement of the model described in Chapter 4 to include the out-of-plane components in the force-based formulation, as well as nonlinear hinges for the description of the flexural mechanisms. In particular, two cases are proposed, one with the introduction of two nonlinear hinges, located at the end nodes of the element, and with a third hinge, located at the center of the element.

5.1   3D formulation

This Section describes the 3D formulation of the macroelement. The extension of the force-based formulation adopted for the beam element is given, together with the initial introduction of two flexural hinges for the out-of-plane one-way bending mechanism description. Attention is focused also on the definition of the yielding domain, to evaluate the elastic threshold of the modified Bouc-Wen hysteresis adopted in the nonlinear hinges.

A brief discussion is also made regarding the extension to 3D of the consistent mass formulation in the dynamic field.

5.1.1   3D force-based formulation

A 3D global reference system (O, X, Y, Z) is considered, in which the 2-node beam element is defined. With respect to the procedure expressed in Section 4.1.1, six DOFs at each node are defined, which become twelve DOFs for the entire element. Twelve displacement components are then defined (Fig. 5.1 (a)), six of which are translational while six are rotational, and the global displacement vector becomes:

$$\mathbf{u} = \{u_i \ v_i \ w_i \ \theta_{x_i} \ \theta_{y_i} \ \theta_{z_i} \ u_j \ v_j \ w_j \ \theta_{x_j} \ \theta_{y_j} \ \theta_{z_j}\}^T \qquad (5.1)$$

while the global force vector, containing six forces and six moments, becomes:

$$\mathbf{p} = \{p_{x_i} \ p_{y_i} \ p_{z_i} \ m_{x_i} \ m_{y_i} \ m_{z_i} \ p_{x_j} \ p_{y_j} \ p_{z_j} \ m_{x_j} \ m_{y_j} \ m_{z_j}\}^T \qquad (5.2)$$

(a)

(b)   (c)
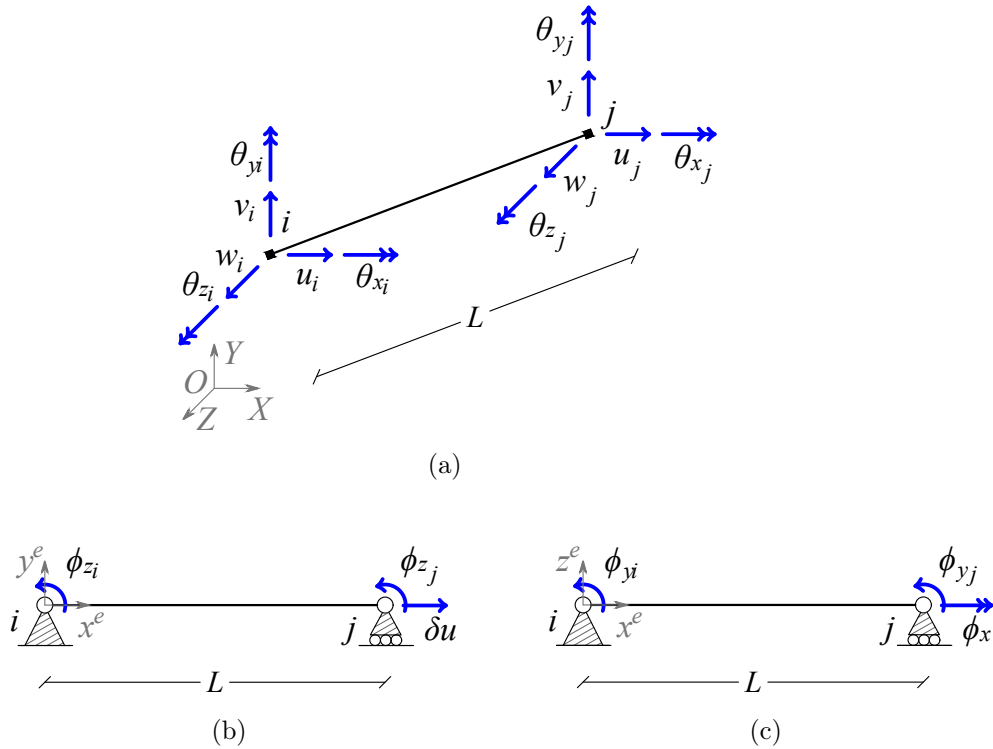
Figure 5.1: Beam finite elemet in the global reference system (a) and in the basic local reference system in the three-dimensional field: in-plane components (b), out-of-plane components (c)

The three-dimensional local reference system, defined by the coordinate system (i, x^e, y^e, z^e), sees the x^e axis parallel to the beam axis, the ye axis orthogonal to it, identifying together with the x^e axis the in-plane displacements direction, and the z^e axis is orthogonal to both, being the x^e-z^e plane the out-of-plane displacements direction (Fig. 5.1 (b) and (c)).

The out-of-plane behavior is described through a Timoshenko formulation,

with the aim of considering the shear behavior within the elastic beam element instead of lumping it in a proper hinge. To this end, in the following, the main Timoshenko three-dimensional vectors and matrices needed for the force-based approach are recalled. It is noteworthy, however, that in the in-plane direction the shear behavior is entirely described through the nonlinear shear hinge, thus the shear components in the in-plane direction are not considered. This is possible being the in-plane and out-of-plane rotational and shear components completely decoupled.

At each section of the Timoshenko three-dimensional beam element, the generalized section displacement $\mathbf{u}_s(x)$ (Fig. 5.2), the section deformation vector $\boldsymbol{\varepsilon}_s(x)$ and the section stress vector $\boldsymbol{\sigma}_s(x)$ are defined as follows:

$$\mathbf{u}_s(x) = \{u(x) \; v(x) \; w(x) \; \theta_x(x) \; \theta_y(x) \; \theta_z(x)\}^T \tag{5.3}$$

$$\boldsymbol{\varepsilon}_s(x) = \{\epsilon_G(x) \; \chi_z(x) \; \gamma_y(x) \; \chi_x(x) \; \chi_y(x) \; \gamma_z(x)\}^T \tag{5.4}$$

$$\boldsymbol{\sigma}_s(x) = \{N(x) \; M_z(x) \; T_y(x) \; M_x(x) \; M_y(x) \; T_z(x)\}^T \tag{5.5}$$

In Eq. 5.4, $\chi_z(x)$ and $\gamma_y(x)$ are the rotational and distorsional components in the in-plane direction, while $\chi_y(x)$ and $\gamma_z(x)$ are the rotational and distorsional components in the out-of-plane direction; $\chi_x(x)$ is the torsional rotation and $\epsilon_G(x)$ is the axial deformation. As well, in Eq. 5.5 the corresponding stresses are written, with $M_z(x)$ and $T_y(x)$ in the in-plane direction and $M_y(x)$ and $T_z(x)$ in the out-of-plane direction.
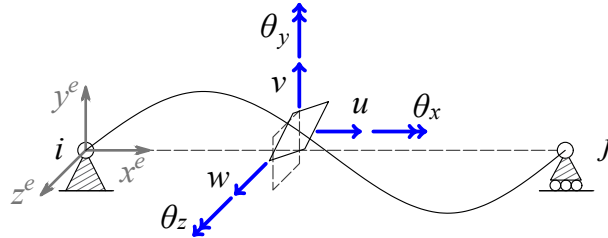
Figure 5.2: Generalized cross-section displacements in the local reference system

Holding Eq. 4.5, the section stiffness matrix accounts now for the additional terms, becoming:

$$\boldsymbol{K}_s(x) = \begin{bmatrix} EA & 0 & 0 & 0 & 0 & 0 \\ 0 & EI_z & 0 & 0 & 0 & 0 \\ 0 & 0 & GA_t & 0 & 0 & 0 \\ 0 & 0 & 0 & GJ & 0 & 0 \\ 0 & 0 & 0 & 0 & EI_y & 0 \\ 0 & 0 & 0 & 0 & 0 & GA_t \end{bmatrix} \tag{5.6}$$

where E is the Young's modulus, A the area of the section, A_t the shear area of the section, I_z the inertia in the in-plane direction, J the torsional inertia and I_y the out-of-plane inertia.

The variation of the section stresses with the basic element nodal forces is still expressed through Eq. 4.7, where in the 3D Timoshenko beam element the equilibrium matrix $\boldsymbol{b}_s(x)$ is a 6x6 matrix expressed as:

$$\boldsymbol{b}_s(x) = \begin{bmatrix} 1 & 0 & 0 & 0 & 0 & 0 \\ 0 & x/L - 1 & x/L & 0 & 0 & 0 \\ 0 & 1/L & 1/L & 0 & 0 & 0 \\ 0 & 0 & 0 & 1 & 0 & 0 \\ 0 & 0 & 0 & 0 & x/L - 1 & x/L \\ 0 & 0 & 0 & 0 & -1/L & -1/L \end{bmatrix} \tag{5.7}$$

The virtual work equivalence holds (Eq. 4.9), together with the relation between the basic local displacements and the section deformations (Eq. 4.10), the evaluation of the flexibility element matrix (Eq. 4.11) and the initial basic displacements due to distributed loads (Eq. 4.12).

The simply supported beam configuration, given by the elimination of rigid motion required to impose the equilibrium in the strong form, allows the definition of six local basic components for the vector $\boldsymbol{\varepsilon}^e$, which are:

$$\boldsymbol{\varepsilon}^e = \{\delta u \ \phi_{z_i} \ \phi_{z_j} \ \phi_x \ \phi_{y_i} \ \phi_{y_j}\}^T \tag{5.8}$$

In Eq. 5.8, δu is the elongation of the beam in the direction parallel to axis

x^e, ϕ_{z_i} and ϕ_{z_j} are the rotations of nodes i and j respectively in the in-plane directions, ϕ_x is the torsion component, while ϕ_{y_i} and ϕ_{y_j} are the rotations of nodes i and j respectively in the out-of-plane directions.

Holding equation 4.14, the kinematic operator becomes a 6x12 matrix, defined as:

$$\mathbf{D}^e = \begin{bmatrix} -1 & 0 & 0 & 0 & 0 & 0 & 1 & 0 & 0 & 0 & 0 & 0 \\ 0 & 1/L & 0 & 0 & 0 & 1 & 0 & -1/L & 0 & 0 & 0 & 0 \\ 0 & 1/L & 0 & 0 & 0 & 0 & 0 & -1/L & 0 & 0 & 0 & 1 \\ 0 & 0 & 0 & -1 & 0 & 0 & 0 & 0 & 0 & 1 & 0 & 0 \\ 0 & 0 & -1/L & 0 & 1 & 0 & 0 & 0 & 1/L & 0 & 0 & 0 \\ 0 & 0 & -1/L & 0 & 0 & 0 & 0 & 0 & 1/L & 0 & 1 & 0 \end{bmatrix} \tag{5.9}$$

where L is again the length of the undeformed element from node i to node j.

The local basic force vector, which is in this case as well correlated to the local basic displacement vector through the stiffness matrix and to the global force vector by means of the equilibrium operator, is the following:

$$\boldsymbol{\sigma}^e = \{N_j \ M_{z_i} \ M_{z_j} \ M_x \ M_{y_i} \ M_{y_j}\}^T \tag{5.10}$$

The relation between nodal basic displacements and forces in Eq. 4.19 holds, and in case of a straight axis and constant properties along the element, the flexibility element matrix is written as follows:

$$\mathbf{F}^e = \begin{bmatrix} \frac{L}{EA} & 0 & 0 & 0 & 0 & 0 \\ 0 & \frac{L}{3EI_z}+\frac{1}{LGA_t} & -\frac{L}{6EI_z}+\frac{1}{LGA_t} & 0 & 0 & 0 \\ 0 & -\frac{L}{6EI_z}+\frac{1}{LGA_t} & \frac{L}{3EI_z}+\frac{1}{LGA_t} & 0 & 0 & 0 \\ 0 & 0 & 0 & \frac{L}{GJ} & 0 & 0 \\ 0 & 0 & 0 & 0 & \frac{L}{3EI_y}+\frac{1}{LGA_t} & -\frac{L}{6EI_y}+\frac{1}{LGA_t} \\ 0 & 0 & 0 & 0 & -\frac{L}{6EI_y}+\frac{1}{LGA_t} & \frac{L}{3EI_y}+\frac{1}{LGA_t} \end{bmatrix} \tag{5.11}$$

To this end, the contributions of the Timoshenko formulation in the flexibility

matrix, being equal to $1/LGA_t$, are eliminated in the matrix components $\mathbf{F}^e(2,2)$, $\mathbf{F}^e(2,3)$, $\mathbf{F}^e(3,2)$ and $\mathbf{F}^e(3,3)$.

Rigid offsets are also included in the 3D formulation, through the kinematic operator, as a 3D extension of the method in Addessi et al. (2015).

5.1.2   OOP flexural hinges introduction

One-way out-of-plane bending failure involves a flexural mechanism that usually occurs in slender panels that are not restrained on top, when loaded with both monotonic or cyclic actions. This mechanism implies a rocking oscillation of the panel about its base, where, before the occurrence of instability and the overturning of the panel, crack propagation evolves at the bottom of the panel causing a rapid degradation of its capacity and stiffness.

To model this degradation phase, in which damage evolves before failure, flexural nonlinear hinges are introduced in correspondence of the end nodes of the elastic beam element in the out-of-plane direction, with the aim of reproducing the flexural mechanism and the corresponding degrading behavior of strength and stiffness. The complete macroelement configuration, in the in-plane and out-of-plane directions, is then provided in Fig. 5.3.
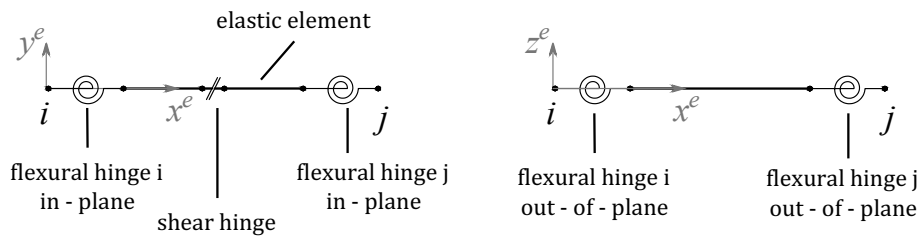
Figure 5.3: Schematization of the 3D macroelement with flexural in-plane and out-of-plane and shear in-plane hinges

The modified Bouc-Wen model with damage and flexibility increase proposed in Chaper 3 is introduced for the nonlinear hinges. The additional devices described in Section 4.1.3, which allow to reproduce the pinching effect by means of a nonlinear elastic constitutive law and to restore the initial elastic stiffness of the elastic element by means of an elastic constitutive law with negative slope,

are also introduced to complete the flexural behavior description.

The procedure described in Section 4.1.2 for the introduction of the flexural hinges is adopted in the out-of-plane direction as well.

The equilibrium condition:

$$M_{y_{i/j}} \;=\; M_{yh_{i/j}} \;=\; M_{ye_{i/j}} \tag{5.12}$$

holds here for the moment in the out-of-plane direction at each node, where $M_{yh_{i/j}}$ is the bending moment of the flexural out-of-plane hinge, while $M_{ye_{i/j}}$ the out-of-plane bending moment at the end of the elastic element.

Kinematic conditions differ from Eq. 4.22, as the shear contribution is included in the Timoshenko formulation adopted for the elastic element and thus shall not be explicitly accounted. The equation becomes then:

$$\phi_{y_{i/j}} \;=\; \phi_{yh_{i/j}} \;+\; \phi_{ye_{i/j}} \tag{5.13}$$

The incremental form of the constitutive equation of each hinge, adopted to obtain the flexibility matrix of the element according to Eq. 4.19, remains unchanged with respect to the in-plane case, giving the equation:

$$\dot{\phi}_{yh_{i/j}} \;=\; f_{yhb_{i/j}} \, \dot{M}_{y_{i/j}} \tag{5.14}$$

Thus, the 6x6 flexibility matrix of the complete macroelement can be derived, obtaining the expression in Eq. 5.15, which considers the contribution of the in-plane and out-of-plane flexural hinges and the in-plane shear hinge.

Flexibility matrix of the complete 3D macroelement:

$$
\mathbf{F}^e =
\begin{bmatrix}
\frac{L}{EA} & 0 & 0 & 0 & 0 & 0 \\
0 & \frac{L}{3EI_z} + f_{hb_i} + \frac{f_{hs}}{L^2} & -\frac{L}{6EI_z} + \frac{f_{hs}}{L^2} & 0 & 0 & 0 \\
0 & -\frac{L}{6EI_z} + \frac{f_{hs}}{L^2} & \frac{L}{3EI_z} + f_{hb_j} + \frac{f_{hs}}{L^2} & 0 & 0 & 0 \\
0 & 0 & 0 & \frac{L}{GJ} & 0 & 0 \\
0 & 0 & 0 & 0 & \frac{L}{3EI_y} + \frac{1}{LGA_t} + f_{yhb_i} & -\frac{L}{6EI_y} + \frac{1}{LGA_t} \\
0 & 0 & 0 & 0 & -\frac{L}{6EI_y} + \frac{1}{LGA_t} & \frac{L}{3EI_y} + f_{yhb_j} + \frac{1}{LGA_t}
\end{bmatrix}
\tag{5.15}
$$

5.1.2.1   Initial stiffness and yielding domain

Consistently with Section 4.1.4, the initial stiffness of the two nonlinear flexural hinges is evaluated as:

$$k_{yhb_{i,j}} = \frac{4EI_y}{L} \tag{5.16}$$

where I_y is the flexural inertia of the section in the out-of-plane direction, E the Young's modulus and L the length of the beam element in the undeformed configuration.

This stiffness is then divided into the three nonlinear devices which compose the flexural hinge, and considering that the $f_{yhb_{i/j}} = 1/k_{yhb_{i/j}}$, the total flexibility contribution of each hinge that is passed to the flexibility element matrix is evaluated as:

$$f_{yhb_{i/j}} = \frac{1}{k^{mBW} + k^{NLE}} + \frac{1}{k^{LE}} \tag{5.17}$$

Each contribution is evaluated as specified in Section 4.1.3, according to Eqs. 4.27, 4.31, for the stiffness of the nonlinear elastic and the elastic negative device, and according to Eq. 3.67 for the modified Bouc-Wen contribution.

A bi-dimensional rectangular yielding domain can be traced by considering the yielding thresholds in the in-plane and out-of-plane directions of the cross-section, in order to evaluate the yielding displacement required for the modified Bouc-Wen constitutive law. It is noteworthy that for both piers and spandrels, the Italian Standard Code does not provide specific formulations for the evaluation of the yielding or ultimate moment in the out-of-plane direction, being the out-of-plane machanisms treated as local mechanisms and thus prescribing different approaches for their verification. To this end, in the following, the formulations prescribed in the in-plane direction are adopted.

In both the in-plane and out-of-plane directions, Eq. 4.33 is adopted for piers to evaluate the yielding moment for a rectangular section, assuming an equivalent stress-block diagram in compression. The section dimensions, l and t, are switched depending on the considered direction. Akin considerations are made regarding spandrels, where Eq. 4.35 is considered instead.

5.1.3 Dynamic formulation

The modification of the dynamic formulation is almost straightforward, as Eq. 4.38 is extended to the three-dimensional field by considering 12x12 mass and damping matrices, including the out-of-plane components, and 12x1 vectors for global nodal accelerations, velocities and displacements.

Both the lumped and consistent mass approaches are extended. In particular, in the lumped mass approach the translational mass on the three directions are considered, as well as the rotational in-plane and out-of-plane masses and the torsional mass for nodes i and j.

5.1.3.1 3D consistent mass matrix

The procedure adopted in Section 4.2.1 should be referred to for an extensive explanation of the procedure. In the following, only the main matrices are recalled and their three-dimensional extension is given.

The virtual work equivalence between generalized displacements and forces and section deformations and stresses in Eq. 4.39 holds, where generalized displacements and section quantities are those in Eq. 5.3, 5.4 and 5.5 respectively, while generalized forces are:

$$\boldsymbol{p}_s = \{f_x \ f_y \ f_z \ \mu_x \ \mu_y \ \mu_z\}^T \tag{5.18}$$

Following the Unit Load Method, virtual nodal reactions are evaluated, and the cross-section equilibrium matrix $\boldsymbol{b}_{rs}(x)$ in Eq. 4.41, relating unit virtual forces and virtual reactions, becomes:

$$\boldsymbol{b}_{rs}(x) = \begin{bmatrix} 1 & 0 & 0 & 0 & 0 & 0 \\ 0 & x/L - 1 & 0 & 0 & 0 & 1/L \\ 0 & 0 & x/L - 1 & 0 & -1/L & 0 \\ 0 & 0 & 0 & 1 & 0 & 0 \\ 0 & -x/L & 0 & 0 & 0 & -1/L \\ 0 & 0 & -x/L & 0 & 1/L & 0 \end{bmatrix} \tag{5.19}$$

Moreover, the matrix $\boldsymbol{b}_r(x)$, for the evaluation of virtual section stresses from

the virtual nodal reactions in Eq. 4.43, becomes:

$$
\boldsymbol{b}_r(\zeta) = \begin{cases}
\begin{bmatrix}
1 & 0 & 0 & 0 & 0 & 0 \\
0 & \zeta & 0 & 0 & 0 & 0 \\
0 & -1 & 0 & 0 & 0 & 0 \\
0 & 0 & 0 & 1 & 0 & 0 \\
0 & 0 & -\zeta & 0 & 0 & 0 \\
0 & 0 & -1 & 0 & 0 & 0
\end{bmatrix} & \zeta \le x \\[4pt]
\begin{bmatrix}
0 & 0 & 0 & 0 & 0 & 0 \\
0 & 0 & 0 & 0 & L-\zeta & 0 \\
0 & 0 & 0 & 0 & 1 & 0 \\
0 & 0 & 0 & 0 & 0 & 0 \\
0 & 0 & 0 & 0 & 0 & \zeta - L \\
0 & 0 & 0 & 0 & 0 & 1
\end{bmatrix} & \zeta > x
\end{cases}
\tag{5.20}
$$

Following the procedure in Eqs. 4.44 to 4.46, the force-based shape function matrix in the local reference system is obtained, where the rigid modes are eliminated through the following matrix:

$$
\mathbf{N}_r(x) = \begin{bmatrix}
1 & 0 & 0 & 0 & 0 & 0 & 0 & 0 & 0 & 0 & 0 & 0 \\
0 & 1-x/L & 0 & 0 & 0 & 0 & 0 & x/L & 0 & 0 & 0 & 0 \\
0 & 0 & 1-x/L & 0 & 0 & 0 & 0 & 0 & x/L & 0 & 0 & 0 \\
0 & 0 & 0 & 1 & 0 & 0 & 0 & 0 & 0 & 0 & 0 & 0 \\
0 & 0 & 1/L & 0 & 0 & 0 & 0 & 0 & -1/L & 0 & 0 & 0 \\
0 & -1/L & 0 & 0 & 0 & 0 & 0 & 1/L & 0 & 0 & 0 & 0
\end{bmatrix}
\tag{5.21}
$$

The element mass matrix is then evaluated through Eq. 4.48, where the section mass matrix $\boldsymbol{m}_s(x)$ is a 6x6 matrix evaluated as:

$$\boldsymbol{m}_s(x) = \int_A \rho(x,y,z) \begin{bmatrix} 1 & 0 & 0 & 0 & z & -y \\ 0 & 1 & 0 & -z & 0 & 0 \\ 0 & 0 & 1 & y & 0 & 0 \\ 0 & -z & y & y^2+z^2 & 0 & 0 \\ z & 0 & 0 & 0 & z^2 & -zy \\ -y & 0 & 0 & 0 & -yz & y^2 \end{bmatrix} d\tilde{A} \qquad (5.22)$$

where ρ is the material mass density.

5.1.4 Numerical procedure

The model with two lumped hinges in the out-of-plane direction located at the end nodes of the element is implemented in the Finite Element Code FEAP (Taylor, 2017), in the framework described in Chapter 4, and in particular in Section 4.3.

The element state determination remains unchanged, with the addition of the evaluation of the deformation increment in correspondence of the newly introduced hinges as:

$$\Delta\phi_{yh_{i/j}}^{k+1} = f_{yhb_{i/j}}^k \Delta M_{y_{i/j}}^{k+1} \qquad (5.23)$$

which allows to evaluate the deformation at the current iteration for each hinge $(\phi_{yh_{i/j}}^{k+1})$. Tangent stiffness and moment terms are then obtained in output at the current iteration, alike in Eq. 4.58. Element flexibility matrix is updated with the new tangent stiffness terms, which are introduced according to Eq. 5.15, and the procedure described in Section 4.3.1 is followed.

The absence of a shear hinge in the out-of-plane direction allows to adopt the consistent procedure described in Addessi et al. (2015) to avoid element iterations and enforce equilibrium conditions between the central elastic element and the quantities in output from the hinges. Local deformation residuals are evaluated as the difference between the equilibrated forces of the element and those obtained from the flexural hinges, multiplied by the tangent flexibility contribution of the hinge, as follows:

$$\rho_{yi} \; = \; f_{yhb_i}^{k+1} \, (\Delta M_{y_i}^{k+1} \; + \; M_{y_i}^{k} \; - \; M_{yh_i}^{k+1}) \tag{5.24}$$

$$\rho_{yj} \; = \; f_{yhb_j}^{k+1} \, (\Delta M_{y_j}^{k+1} \; + \; M_{y_j}^{k} \; - \; M_{yh_j}^{k+1}) \tag{5.25}$$

Local deformation residuals are collected into an element deformation residual vector at the current iteration:

$$\boldsymbol{r}^{e^{k+1}} \; = \; \{0, \; \rho_{zi}, \; \rho_{zj}, \; 0, \; \rho_{yi}, \; \rho_{yj}\}^{T} \tag{5.26}$$

As it can be seen, the first and the fourth positions of the residual vector are empty. This is due to the fact that the first position is related to the axial deformation, which remains elastic and decoupled from the flexural components during the entire analysis, as well as the fourth position which is related to the torsional component. On the contrary, the second and third positions are relative to the flexural in-plane components, whose deformation residuals depend on the performed iterative procedure, described in Section 4.3.2, which enforces the equilibrium between the shear and flexural hinges and the elastic central element. The element deformation residual vector is then pre-multiplyed by the inverse of the element flexibility matrix $(\mathbf{F}^{e^{k+1}})^{-1}$ at the current iteration, obtainig residuals in terms of element forces, and the obtained vector is used to update the local basic force vector:

$$\boldsymbol{\sigma}^{e^{k+1}} = \boldsymbol{\sigma}^{e^{k+1}} \; - \; (\mathbf{F}^{e^{k+1}})^{-1} \, \boldsymbol{r}^{e^{k+1}} \tag{5.27}$$

The procedure continues as described in Section 4.3.1, with the determination of the element stiffness matrix and the element internal force vector at the current iteration as: $\mathbf{K}^{e^{k+1}} \; = \; (\mathbf{D}^{e})^{T}(\mathbf{F}^{e^{k+1}})^{-1}\mathbf{D}^{e}$ and $\mathbf{p}^{e^{k+1}} \; = \; \mathbf{D}^{e^{T}} \boldsymbol{\sigma}^{e^{k+1}}$, which are then rotated in the global reference system and forwarded to the FEAP global Newton-Raphson procedure for the assemble procedure and the determination of the solution. However, in this case, Newton-Raphson global iterations are required to reduce the residual vector $\boldsymbol{r}^{e^{k+1}}$ to a value lower than a specified tolerance value. In particular, the program FEAP performs an energy convergence test, as specified also in Addessi et al. (2015).

5.2 Numerical validation

The model described in the previous Section is adopted to reproduce the out-of-plane nonlinear static behavior of an experimental wall tested at Delft Univesity of Technology (Ravenshorst and Messali, 2016; Messali et al., 2017; Damiola et al., 2018; D'Altri et al., 2019). The experimental campaign originated from the need to study the seismic behavior of masonry structures, largely diffused in the Netherlands, due to the increasing seismic risk caused by induced earthquakes originated from gas extraction in the provence of Groningen. The complete experimental campaign involved testing short walls in the in-plane direction and long walls in the out-of-plane direction by applying uniform horizontal loads through a system of coupled airbags on both sides of the walls. The set-up of each wall was made through a steel-frame system which allowed to restrain all the edges of the walls (Fig. 5.4). More refined details of the experimental set-up can be found in Ravenshorst and Messali (2016); Messali et al. (2017).
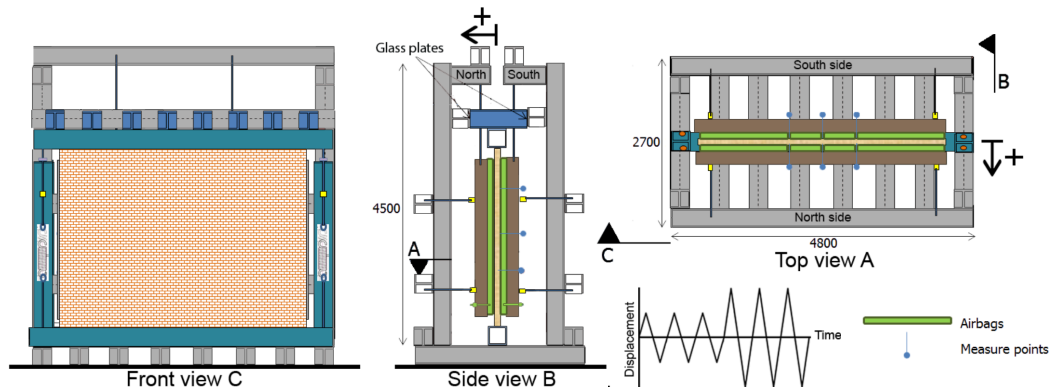
Figure 5.4: Test set-up for COMP-11 specimen subjected to two-way out-of-plane cyclic tests (modified from Damiola et al. (2018)

The steel-framed set-up (Fig. 5.4) was originally built by connecting two beams, positioned at the top and bottom of the wall, to two lateral columns through springs, thus allowing to reproduce a fully fixed restraint condition along all the edges of the wall.

In particular, in the following, one of the long walls tested in the out-of-plane direction for two-way spanning mechanisms is selected, denominated COMP-11.

The related experimental outcomes have been analyzed also in D'Altri et al. (2019), where they were reproduced through a micromechanical damaging block-based numerical model.

The selected specimen has a height equal to 3.874 m, a base long 2.765 m and a thickness equal to 0.102 m, and is built adopting a calcium silicate brick masonry. The mechanical parameters adopted for the numerical model are taken from those adopted in D'Altri et al. (2019), and are listed in Tab. 5.1. In particular, Young's modulus and Poisson ratio are selected from the parameters adopted in the reference for the block behavior, as well as the compressive strength, while shear properties are evaluated from the shear parameters adopted for the contact constitutive law. Tab. 5.2, instead, shows the parameters employed for the out-of-plane flexural nonlinear hinges, calibrated in order to reproduce the experimental curve.

Table 5.1: Mechanical parameters of the wall

E	ν	G	f_c	f_{v0}
kN/m^2	–	kN/m^2	kN/m^2	kN/m^2
$4800\,10^3$	0.17	2051282	6800	84.5

Table 5.2: Nonlinear out-of-plane flexural hinges parameters

Flexural hinges			
a	δ_D	δ_K	n
–	kJ^{-1}	kJ^{-1}	–
0.025	0.28	10.8	1

Two loading phases constituted the test. First, a vertical load equivalent to a pressure of 50 MPa was applied and kept constant during the whole test. After that, a constant lateral load was applied by an airbag on one side of the wall, while a second airbag with a varying pressure loaded the other side of the wall.

The pressure applied was adjusted to achieve the target displacements, realizing an equivalnt displacement controlled test.

The experimental damage pattern was characterized by the formation of horizontal cracks in correspondence of the top, an intermediate height and the base of the wall, as well as diagonal cracks from the wall edges to the center of the wall. Considering that the macroelement model is not capable of describing two-way spanning mechanisms by adopting one single macroelement, a FE model with two macroelements is adopted, as shown in Fig. 5.5. A node located at midheight, in correspondence of the intermediate crack, is then added, where the horizontal displacement equivalent to the pressure of the airbags is given as input.
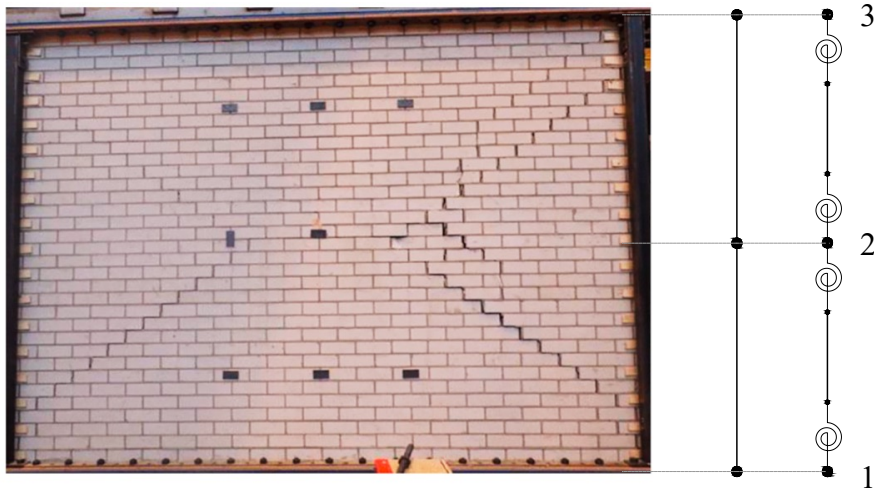
Figure 5.5: Damage patterns of COMP-11 specimen and equivalent frame schematization adopting two macroelements

Fig. 5.6 shows the numerical results (red line) obtained through the equivalent frame model in terms of force - displacement curve compared to the experimental results obtained for specimen COMP-11 in Damiola et al. (2018).

The numerical results show to reproduce with good accuracy the first part of the experimental curve, as can be seen in Fig. 5.7 (a), while the last part shows very different results (Fig 5.6). Accuracy is lost after the displacement peak equal to $0.04\,\mathrm{m}$, where the values of damage and flexibility increase shrink the cycles excessively with respect to the experimental outcomes. In particular, by properly setting the damage and flexibility increase parameters, the dissipated energy and
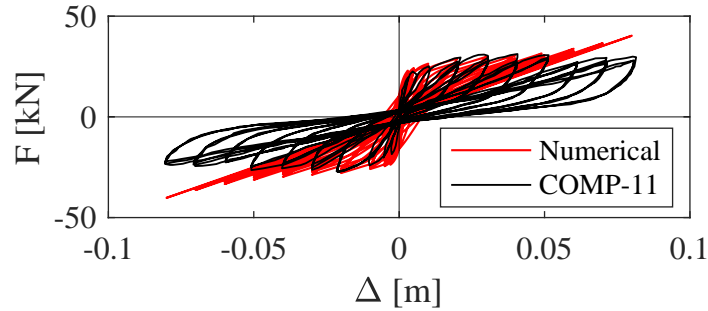
Figure 5.6: Force-displacement curve comparison between numerical and experimental results
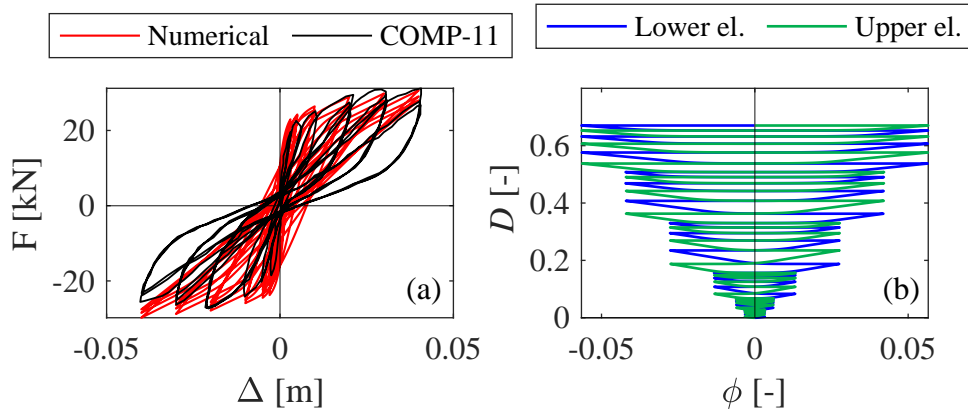
Figure 5.7: Force-displacement curve comparison between numerical and experimental results, zoom on the fisrt cycles (a); damage variable D trend for flexural hinges (b)

the area of the cycles are well-captured, as well as the strong stiffness degradation that cycle after cycle experienced. However, the increase of the damage variable D, when it reaches values proximate to unity, depletes the dissipable energy of the system, and, as showed in Chapter 3, only the elastic terms of the modified Bouc-Wen hysteresis remain. The force experienced thus evidently overestimates the actual force reached in the experimental test. On the contrary, the peak force reached during the first part of the experimental tests is captured quite well, even though a higher strength degradation is experienced in the numerical results. The experimental curve, in fact, shows to experience strength degradation when cycles with same amplitude are covered, but strength is partially recovered when

the increased displacement is reached. The presence of flexibility increase partially allows this strength recover, as also showed in the previous Chapters.

The activation of the hinges at the bottom and top of the panel reproduces the crack pattern experienced by the specimen, even though the diagonal cracks are not captured due to the incapability of the model of reproducing what happens in the length direction. The trend of the damage variable D with the ongoing of the analysis, which is proportional to that of the flexibility increase term $\delta_K U^h$, is given in Fig. 5.7 (b) for the initial part of the analysis, showing an increasing trend, consistent with that of the dissipated energy. The value of the damage variable in correspondence of the cycle with peak equal to $0.04\,\mathrm{m}$ is $D = 0.67$. It is noteworthy that, as pointed out in D'Altri et al. (2019), the presence of the airbags in the two sides of the wall affected the results by increasing the stability of the wall. The high damage variable value D obtained in the present simulation, that reaches a value equal to 0.9 before a peak displacement equal to $0.6\,\mathrm{m}$, thus simulates a condition proximate to the collpase before the maximum dispalcement reached by the wall.

5.3   Third flexural hinge introduction

In the previous Sections, the introduction of flexural hinges to model simple one-way bending mechanisms has been discussed and validated, in order to account for nonlinear damaging phenomena that take place in the out-of-plane direction before collapse occurrence.

However, as shown also in the experimental results considered in Section 5.2, the two-way bending mechanism is a relevant failure mode that shoud be properly accounted. It generally occurs in squat walls supported on the sides (Damiola et al., 2018) or in the case of simply supported walls which span vertically between supports at ceiling and floor levels (Doherty et al. (2002)).

As can be highlighted from the modeling strategy adopted in Section 5.2, a development of the proposed model is needed, in order to mantain the advantage given by adoption of one single macroelement for each structural element even when the description of more complex out-of-plane behaviors is required.

To this end, in the following, the force-based approach is revised with the introduction of an additional rotational degree-of-freedom located in the middle of the elastic element, which allows to model the out-of-plane spanning mode when distributed loads are applied. To this additional degree-of-freedom, a flexural hinge is associated, in which the modified Bouc-Wen model with damage and flexibility increase proposed in Chapter 3 is introduced, to consider the contribution given from the two-way bending mode to the strength and stiffness degradation of the system.

The enhanced force-based formulation relative to the central elastic beam element, as well as the modifications due to the presence of the central flexural hinge, are presented in the following Subsections. The numerical procedure performed at each step of the analysis is then recalled.

5.3.1 Force-based beam formulation

With the aim of reproducing the effect of two-way bending mechanism, which can be seen as a spanning mode of the of the beam element caused by the effect of distributed loads when both the ends of the element are restrained, a rotational degree of freedom, θ_{ym}, is introduced in the central elastic element. The additional degree of freedom, which corresponds to a rotation with the meaning of a deformation, exists only in the out-of-plane direction, in the $x^e - z^e$ plane, without influencing the in-plane components. In-plane and out-of-plane components remain thus decoupled.

In Fig. 5.8 (a) the components of the global dispalcement vector $\mathbf{u}$, which are now 13 instead of 12 and are listed in the following:

$$\mathbf{u} = \{u_i \ v_i \ w_i \ \theta_{x_i} \ \theta_{y_i} \ \theta_{z_i} \ u_j \ v_j \ w_j \ \theta_{x_j} \ \theta_{y_j} \ \theta_{z_j} \ \theta_{ym}\}^T \qquad (5.28)$$

are represented, as well as the local displacement components in the in-plane (Fig. 5.8 (b)) and out-of-plane (5.8 (c)) directions.

Considering Eq. 4.14, the kinematic matrix is modified from Eq. 5.9 to Eq. 5.29:

(a)

(b)   (c)
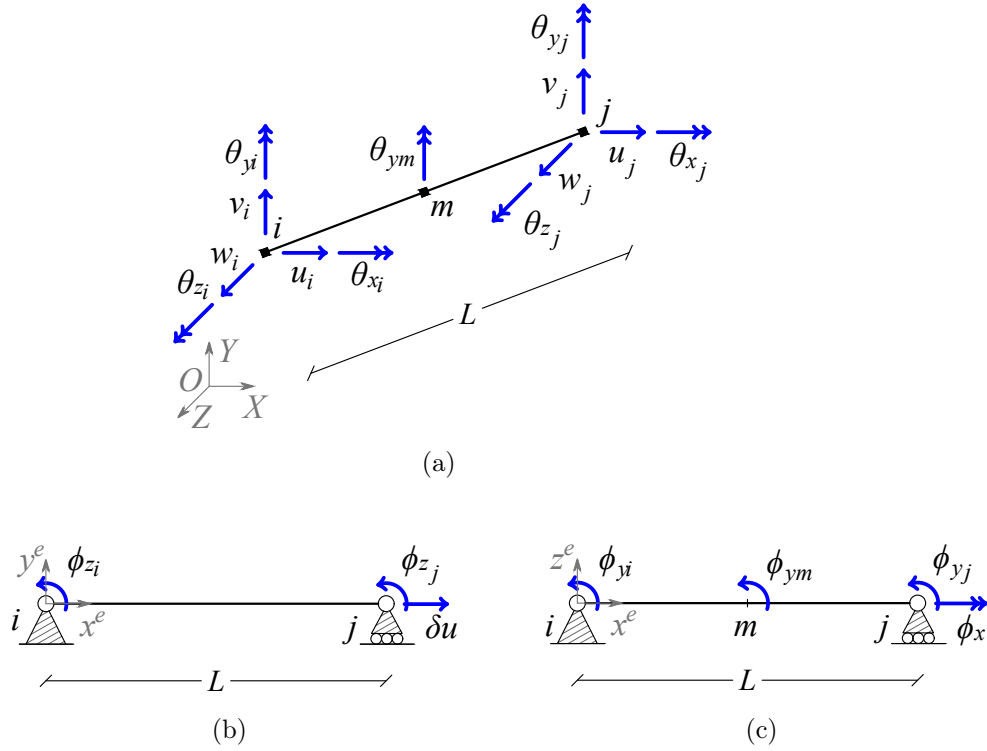
Figure 5.8: Enhanced beam finite elemet in the global reference system (a) and in the basic local reference system in the three-dimensional field: in-plane components (b), enhanced out-of-plane components (c)

$$\mathbf{D}^e = \begin{bmatrix} -1 & 0 & 0 & 0 & 0 & 0 & 1 & 0 & 0 & 0 & 0 & 0 & 0 \\ 0 & 1/L & 0 & 0 & 0 & 1 & 0 & -1/L & 0 & 0 & 0 & 0 & 0 \\ 0 & 1/L & 0 & 0 & 0 & 0 & 0 & -1/L & 0 & 0 & 0 & 1 & 0 \\ 0 & 0 & 0 & -1 & 0 & 0 & 0 & 0 & 0 & 1 & 0 & 0 & 0 \\ 0 & 0 & -1/L & 0 & 1 & 0 & 0 & 0 & 1/L & 0 & 0 & 0 & 0 \\ 0 & 0 & -1/L & 0 & 0 & 0 & 0 & 0 & 1/L & 0 & 1 & 0 & 0 \\ 0 & 0 & 0 & 0 & 0 & 0 & 0 & 0 & 0 & 0 & 0 & 0 & 1 \end{bmatrix} \tag{5.29}$$

One column and one row are added, relating the rotation θ_{y_m} to the local basic rotation ϕ_{y_m} by imposing that $\theta_{y_m} = \phi_{y_m}$. The local basic displacement vector ε^e includes 7 components, which are listed in the following:

$$\boldsymbol{\varepsilon}^e = \{\delta u \ \phi_{z_i} \ \phi_{z_j} \ \phi_x \ \phi_{y_i} \ \phi_{y_j} \ \phi_{y_m}\}^T \tag{5.30}$$

The corresponding local basic forces are collected in vector $\boldsymbol{\sigma}^e$:

$$\boldsymbol{\sigma}^e = \{N_j \ M_{z_i} \ M_{z_j} \ M_x \ M_{y_i} \ M_{y_j} \ M_{y_m}\}^T \tag{5.31}$$

The components of the section stress and deformation vectors in Eq. 5.4 e 5.5 remain unchanged, as the moment equation in the out-of-plane direction is the following:

$$M_y(x) = \left(\frac{x}{L} - 1\right) M_{y_i} + \left(\frac{x}{L}\right) M_{y_j} + M_{y_m} \tag{5.32}$$

where, given the distributed load p_z in the out-of-plane direction, which in case of seismic action can represent inertial distributed forces, M_{y_m} is evaluated as:

$$M_{y_m} = \frac{p_z L}{2}\bar{x} - \frac{p_z \bar{x}^2}{2} \tag{5.33}$$

$\bar{x}$ is the position of the maximum value of the out-of-plane bending moment. The contribution of the distributed loads that are usually collected in the vector $\sigma_{sq}(x)$ is not considered explicitely as in Eq. 4.7, but is included entirely in the evaluation of the moment M_{y_m}. This latter can then be considered equivalent to the bending effect of the distributed load orthogonal to the beam axis in the out-of-plane direction. It is calculated in correspondence of its maximum value and is then included in vector 5.31.

The equilibrium matrix $\boldsymbol{b}_s(x)$ includes then the additional moment, becoming:

$$\boldsymbol{b}_s(x) = \begin{bmatrix} 1 & 0 & 0 & 0 & 0 & 0 & 0 \\ 0 & x/L - 1 & x/L & 0 & 0 & 0 & 0 \\ 0 & 1/L & 1/L & 0 & 0 & 0 & 0 \\ 0 & 0 & 0 & 1 & 0 & 0 & 0 \\ 0 & 0 & 0 & 0 & x/L - 1 & x/L & 1 \\ 0 & 0 & 0 & 0 & 1/L & 1/L & 1/L \end{bmatrix} \tag{5.34}$$

The flexibility matrix of the central elastic beam element $\mathbf{F}^e_{el}$ is calculated by enforcing the virtual work equivalence between the basic virtual stresses and the

basic displacements, and the section stresses and deformations. The matrix listed in Eq. 5.38 is obtained, by considering the additional degree of freedom.

It is worth recalling that the flexibility matrix in Eq. 5.38 is referred to a Timoshenko formulation, but it should be noted that in the in-plane direction the Timoshenko terms are substituted with the shear hinge contributions, while are kept as they are in the out-of-plane components (i.e. from the fourth to the seventh column and row).

Moreover, a simplified assumption is made for the evaluation of the flexibility matrix of the element, that is to localize the third hinge at the center of the elastic element. This is an approximation, as the acutal location of the hinge is not defined, but it moves along the beam axis with the maximum value of the bending moment given by the superposition of the linear equation given by M_{yi} and M_{yj}, and the parabolic equation given by equilibrium of the distributed load.

5.3.2 Nonlinear flexural hinges contributions

Holding the equations reported in Section 5.1.2 that describe kinematic and equilibrium conditions for the in-plane hinges and for the two out-of-plane flexural hinges located at the ends of the elastic element, additional conditions for the introduction of the central hinge are considered.

The configuration of the complete macroelement in the in-plane ($x^e - y^e$ plane) and in the out-of-plane ($x^e - z^e$ plane) is illustrated in Fig. 5.9.

It is noteworthy that the central flexural hinge does not interrupt the continuity of the elastic element, allowing to ensure the following equilibrium condition in correspondence of the central hinge:

$$M_{y_m} = M_{yh_m} = M_{ye_m} \tag{5.35}$$

while the kinematic condition that holds at the generic point m where the hinge is activated is:

$$\phi_{y_m} = \phi_{yh_m} + \phi_{ye_m} \tag{5.36}$$

The incremental form of the constitutive equation relating the moment and
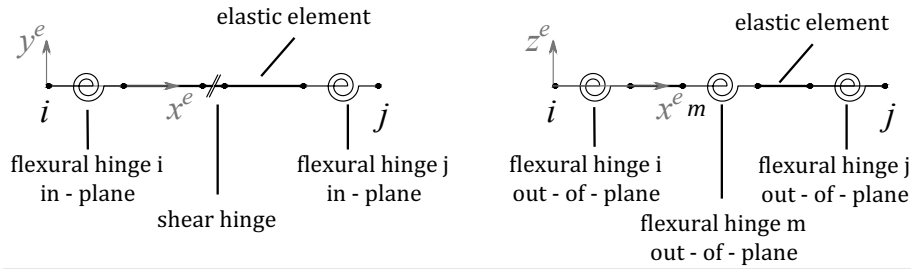
Figure 5.9: Schematization of the 3D macroelement with flexural in-plane and out-of-plane i, j, and m hinges and shear in-plane hinge

the rotation of the flexural hinge is the following:

$$\dot{\phi}_{yh_m} = f_{yhb_m}\, \dot{M}_{y_m} \tag{5.37}$$

Operating substitutions of the constitutive and equilibrium relations into the kinematic equations, following the procedure already decribed in Section 4.1.2, and collecting the terms that multiply the basic local forces into a matrix, the expression of the flexibility matrix given in Eq. 5.39 is obtained.

The initial stiffness adopted for the flexural hinge is that given in Eq. 5.16, and the constitutive relation adopted includes the presence of the modified Bouc-Wen model with damage and flexibility increase arranged in parallel with a non-linear elastic device, which both are in series with an elastic element with negative slope that restores the initial elastic stiffness of the elastic element. Regarding the yielding moment used to evaluate the yielding displacement, required in the modified Bouc-Wen formulation, the same approach adopted for the flexural hinges located at the ends of the element is considered, thus Section 4.1.2 can be referred to.

Flexibility matrix of the elastic force-based beam element:

$$\mathbf{F}^e = \begin{bmatrix}
\frac{L}{EA} & 0 & 0 & 0 & 0 & 0 & 0 \\
0 & \frac{L}{3EI_z}+\frac{1}{LGA_t} & -\frac{L}{6EI_z}+\frac{1}{LGA_t} & 0 & 0 & 0 & 0 \\
0 & -\frac{L}{6EI_z}+\frac{1}{LGA_t} & \frac{L}{3EI_z}+\frac{1}{LGA_t} & 0 & 0 & 0 & 0 \\
0 & 0 & 0 & \frac{L}{GJ} & 0 & 0 & 0 \\
0 & 0 & 0 & 0 & \frac{L}{3EI_y}+\frac{1}{LGA_t} & -\frac{L}{6EI_y}+\frac{1}{LGA_t} & -\frac{L}{24EI_y}+\frac{1}{LGA_t} \\
0 & 0 & 0 & 0 & -\frac{L}{6EI_y}+\frac{1}{LGA_t} & \frac{L}{3EI_y}+\frac{1}{LGA_t} & -\frac{L}{24EI_y}+\frac{1}{LGA_t} \\
0 & 0 & 0 & 0 & -\frac{L}{24EI_y}+\frac{1}{LGA_t} & -\frac{L}{24EI_y}+\frac{1}{LGA_t} & \frac{L}{12EI_y}+\frac{1}{LGA_t}
\end{bmatrix} \tag{5.38}$$

Flexibility matrix of the complete macroelement with two flexural hinges and a shear hinge in the in-plane direction and three flexural hinges in the out-of-plane direction:

$$\mathbf{F}^e = \begin{bmatrix}
\frac{L}{EA} & 0 & 0 & 0 & 0 & 0 & 0 \\
0 & \frac{L}{3EI_z}+f_{zhb_i}+\frac{f_{hs}}{L^2} & -\frac{L}{6EI_z}+\frac{f_{hs}}{L^2} & 0 & 0 & 0 & 0 \\
0 & -\frac{L}{6EI_z}+\frac{f_{hs}}{L^2} & \frac{L}{3EI_z}+f_{zhb_j}+\frac{f_{hs}}{L^2} & 0 & 0 & 0 & 0 \\
0 & 0 & 0 & \frac{L}{GJ} & 0 & 0 & 0 \\
0 & 0 & 0 & 0 & \frac{L}{3EI_y}+\frac{1}{LGA_t}+f_{yhb_i} & -\frac{L}{6EI_y}+\frac{1}{LGA_t} & -\frac{L}{24EI_y}+\frac{1}{LGA_t} \\
0 & 0 & 0 & 0 & -\frac{L}{6EI_y}+\frac{1}{LGA_t} & \frac{L}{3EI_y}+\frac{1}{LGA_t}+f_{yhb_j} & -\frac{L}{24EI_y}+\frac{1}{LGA_t} \\
0 & 0 & 0 & 0 & -\frac{L}{24EI_y}+\frac{1}{LGA_t} & -\frac{L}{24EI_y}+\frac{1}{LGA_t} & \frac{L}{12EI_y}+\frac{1}{LGA_t}+f_{yhb_m}
\end{bmatrix} \tag{5.39}$$

130

5.3.3 Numerical procedure

The detailed steps of the complete element state determination procedure are recalled in Box 5.1, where $k + 1$ represents the current Newton-Raphson algorithm iteration, while k the previous iteration. It is noteworthy that it remains substantially unchanged with respect to that described in Section 4.3.1, with the exception of the dimensions of the considered vectors and matrices, increased with the introduction of the additional degree of freedom, and the evaluation of the local basic forces.

The equilibrated local basic forces shall consider, in the present formulation, the contributions given by the imposition of the concentrated moments applied at the end nodes of the element and that given by the distributed loads. As shown in item 4 in Box 5.1, at the first iteration of each step of the Newton-Raphson procedure, the linear bending moment given by the concentrated moments at the end nodes is evaluated through the basic local dispalcements and the flexibility matrix evaluated at the previous iteration. To update the equilibrated basic forces with the contribution of the distributed loads, the position $\bar{x}$, in correspondence of which the moment is maximum, is evaluated. The value of the moment at the point $\bar{x}$ is obtained, through the moment equation given by the presence of the distributed load, and is then added to the basic force component relative to the additional degree of freedom. This contribution remains unaltered at subsequent iterations, while the moment given by the concentrated moments applied at the nodes is updated at each iteration of the Newton-Raphson procedure.

1. Displacements and displacement increments are given by the Newton-Raphson procedure at the current global iteration:

   $\mathbf{u}^{k+1}$, $\Delta\mathbf{u}^{k+1}$

2. Displacement increments are rotated from the global to the local reference system:

   $\Delta\mathbf{u}^{e^{k+1}} = \mathbf{T}_u^e \Delta\mathbf{u}^{k+1}$

3. Basic local displacement increments are evaluated through the kinematic operator:

   $\Delta\boldsymbol{\varepsilon}^{e^{k+1}} = \mathbf{D}^e \Delta\mathbf{u}^{e^{k+1}}$

4. Basic local forces increments are evaluated through the inverse of the flexibility matrix at ther previous iteration:

   if $k = 1$

   $$\Delta\boldsymbol{\sigma}^{e^{k+1}} = (\mathbf{F}^{e^k})^{-1} \Delta\boldsymbol{\varepsilon}^{e^{k+1}}$$

   $$\Delta\sigma_7^{e^{k+1}} = \Delta\sigma_7^{e^{k+1}} + \Delta M_{z_m}$$

   $$where: \Delta M_{y_m} = \frac{p_z L}{2}\bar{x} - \frac{p_z \bar{x}^2}{2}$$

   $$and\ \bar{x} = \frac{\Delta M_{y_i} + \Delta M_{y_j}}{\Delta p_z L} + \frac{L}{2}$$

   else if $k > 1$

   $$\Delta\boldsymbol{\sigma}^{e^{k+1}} = (\mathbf{F}^{e^k})^{-1} \Delta\boldsymbol{\varepsilon}^{e^{k+1}}$$

   end if

5. Deformation increments for each hinge are evaluated through the hinge flexibility contributions evaluated at the previous iteration:

   i. $\Delta\phi_{zh_i}^{k+1} = f_{zhb_i}^k \, \Delta M_{z_i}^{k+1}$ In-plane flexural hinge i

   ii. $\Delta\phi_{zh_j}^{k+1} = f_{zhb_j}^k \, \Delta M_{z_j}^{k+1}$ In-plane flexural hinge j

   iii. $\Delta\gamma^{k+1} = f_{hs}^k \, \dfrac{\Delta M_{z_i}^{k+1} + \Delta M_{z_j}^{k+1}}{L}$ In-plane shear hinge

   iv. $\Delta\phi_{yh_i}^{k+1} = f_{yhb_i}^k \, \Delta M_{y_i}^{k+1}$ Out-of-plane flexural hinge i

   v. $\Delta\phi_{yh_j}^{k+1} = f_{yhb_j}^k \, \Delta M_{y_j}^{k+1}$ Out-of-plane flexural hinge j

   vi. $\Delta\phi_{yh_m}^{k+1} = f_{yhb_m}^k \, \Delta M_{y_m}^{k+1}$ Out-of-plane flexural hinge m

6. Hinge deformations at the current iteration are updated for each hinge using the hinge deformations at the previous iteration:

$$\phi_\bullet^{k+1} = \Delta\phi_\bullet^{k+1} + \phi_\bullet^k \, ; \qquad \gamma^{k+1} = \Delta\gamma^{k+1} + \gamma^k$$

7. Hinge deformations at the current iteration are used as input quantities in the nonlinear modified Bouc-Wen constitutive law, obtaining the tangent flexibility and the force output quantities at the current iteration for the in-plane and out-of-plane hinges:

$$\phi_{h_\bullet}^{k+1} \to f_{hb_\bullet}^{k+1} \text{ and } M_\bullet^{k+1}; \qquad \gamma^{k+1} \to f_{hs}^{k+1} \text{ and } T_{hs}^{k+1}$$

8. Deformation residuals are evaluated in the in-plane and out-of-plane directions separately:

   i. Nested iterative procedure (described in Section 4.3.2): interations enforce equilibrium between in-plane flexural and shear hinges and local basic forces at the end nodes of the elastic element;

ii. Deformation residuals are evaluated from the residual hinge forces, calculated as the difference between the balanced local basic forces and the constitutive ones:

$$\rho_{yi} = f_{yhb_i}^{k+1}\left(\Delta M_{y_i}^{k+1} + M_{y_i}^{k} - M_{yh_i}^{k+1}\right)$$

$$\rho_{yj} = f_{yhb_j}^{k+1}\left(\Delta M_{y_j}^{k+1} + M_{y_j}^{k} - M_{yhj}^{k+1}\right)$$

$$\rho_{ym} = f_{yhb_m}^{k+1}\left(\Delta M_{y_m}^{k+1} + M_{y_m}^{k} - M_{yhm}^{k+1}\right)$$

and collected in the residual vector:

$$\mathbf{r}^{e^{k+1}} = \{0,\ \rho_{zi},\ \rho_{zj},\ 0,\ \rho_{yi},\ \rho_{yj},\ \rho_{ym}\}^{T}$$

9. Element flexibility matrix $\mathbf{F}^e$ is updated at the current iteration considering the tangent flexibility terms of the nonlinear hinges:

$$\mathbf{F}^{e^k} \rightarrow \mathbf{F}^{e^{k+1}}$$

10. Local basic forces are updated with the out-of-plane residual contributions:

$$\boldsymbol{\sigma}^{e^{k+1}} = \Delta\boldsymbol{\sigma}^{e^{k+1}} + \boldsymbol{\sigma}^{e^k} - (\mathbf{F}^{e^{k+1}})^{-1}\,\mathbf{r}^{e^{k+1}}$$

11. Element stiffness matrix and element internal force vector are computed at the current iteration:

$$\mathbf{K}^{e^{k+1}} = (\mathbf{D}^e)^T (\mathbf{F}^{e^{k+1}})^{-1} \mathbf{D}^e$$

$$\mathbf{p}^{e^{k+1}} = \mathbf{D}^{e^T} \boldsymbol{\sigma}^{e^{k+1}}$$

Box 5.1: Element state determination procedure

Chapter 6

Case studies: experimental tests and numerical simulations

The results of an experimental campaign carried on within the framework of the research project "RIPARA", which involved, among the others, the University of Rome "La Sapienza" and the ENEA Research centre (Agenzia nazionale per le nuove tecnologie, l'energia e lo sviluppo economico sostenibile), are adopted in the following. The aim is to investigate the performance of the proposed macroelement in modeling the static behavior of an unreinforced masonry wall loaded quasi-statically in the in-plane direction and the dynamic behavior of a prototype tested on a shaking table. For this latter, only one of the three natural ground motion records tested is selected. Together with the performance of the model, also its capabilty to capture the main damage mechanisms is tested.

A short description of the experimental tests is given in Sections 6.1.1 and 6.2.1, each followed by the comparison between numerical and experimental results.

6.1   Unreinforced masonry wall

6.1.1   Experimental test

An unreinforced masonry specimen, shown in Fig. 6.1, has been tested in the laboratory of the ENEA Research centre in Casaccia. The specimen is composed

of two unreinforced masonry panels, placed one over the other, whose dimensions are $H = 0.8\,\text{m}$, $B = 0.8\,\text{m}$ and $t = 0.3\,\text{m}$, where H is the height, B the base length and t the thickness of each panel. A concrete curb is located at the base of the lower panel, being $1.2\,\text{m}$ wide, $0.155\,\text{m}$ high and $0.8\,\text{m}$ thick, while a second curb, whose heigth is equal to $h = 0.2\,\text{m}$, separates the two panels. A third concrete curb, having a base $1\,\text{m}$ long, a height equal to $0.3\,\text{m}$ and a thickness equal to $0.5\,\text{m}$, is located on top of the upper panel, restraining the out-of-plane movements and the in-plane rotations. The overall height of the specimen is $2.255\,\text{m}$, as shown in Fig. 6.2.

a)   b)
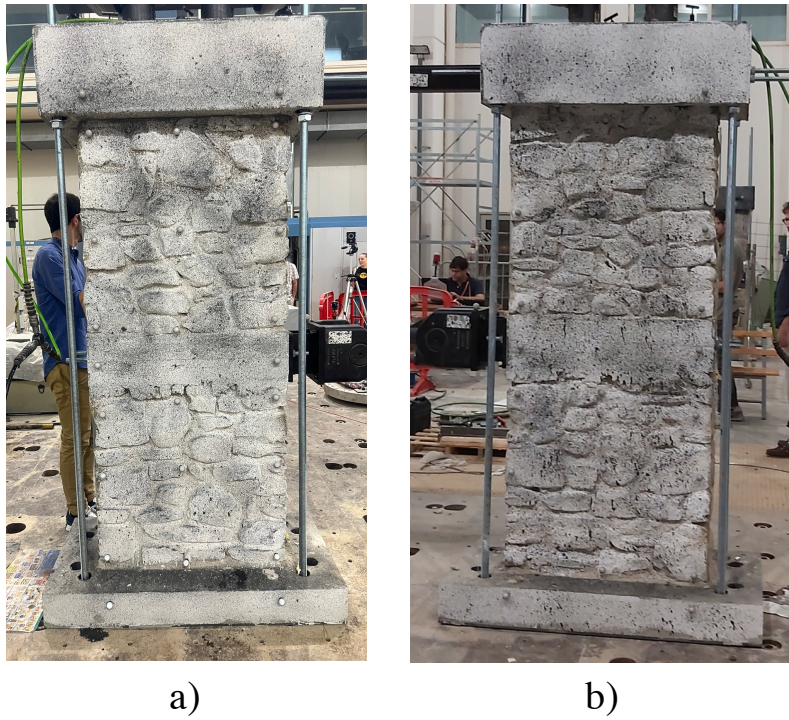
Figure 6.1: Unreinforced masonry wall specimen: first side (a), second side (b)

The panels are made of stone masonry, where the stones were collected from the ruins of the city of Accumoli, taken from some of the buildings that collapsed after the Central Italy seismic sequence in 2016. Consistently, the adopted mortar aims at reproducing the mechanical characteristics of historical masonry typical of residential buildings located in Central Italy. The curbs are made of lightweigth concrete type LEICA 1500.
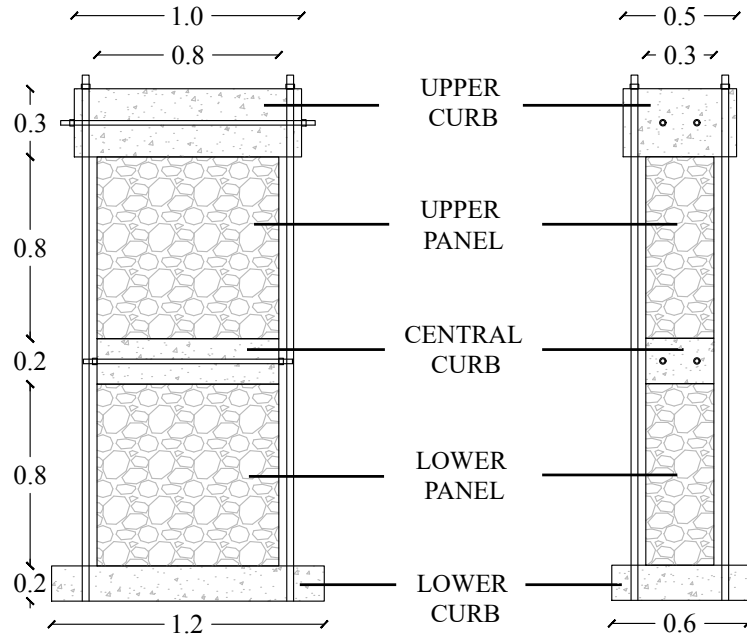
Figure 6.2: Dimensions of the unreinforced masonry wall (dimensions are in meters)

Boundary conditions aim at reproducing a fixed base restraint, while horizontal translations and all the rotations should be restrained on top, while the central curb is restrained only in the out-of-plane displacements.

The specimen has been tested through a Sheppard experimental test (Fig. 6.3), which is usually adopted to study the shear mechanisms that masonry panels undergo when loaded horizontally in the in-plane direction.

After the application of a vertical compressive load equal to $80\,\mathrm{kN}$, applied by means of four pre-loaded steel threaded rods that connect the upper and the lower curbs, a quasi-static cyclic horizontal displacement hystory is applied at the central curb through an hydraulic jack. The amplitude of the displacement assigned to the jack has incremental values until reaching the failure of the wall, with the following theoretical displacement values: $1.0 - 2.0 - 4.0 - 6.0 - 10.0 - 12.0 - 14.0\,\mathrm{mm}$. However, the monitoring system, involving optic-fiber control markers positioned on the panels, on the cubrs and on the jack, showed a difference between the recorded and the applied displacement history. Fig. 6.4 displays the actual recorded displacement, monitored in correspondance of the jack, with respect to

Figure 6.3: Set-up of the Sheppard test

the theoretical displacement input by the computer to the mechanical system. It is possible to notice that non-symmetric displacements are recorded on the jack, where positive values are almost overlapped to the theoretical assigned values, while negative peaks are significantly lower with respect to the theoretical values. Moreover, in contrast with the boundary conditions initially assumed, the wall experienced a rotation of the top face, as recorded by the markers.

The results, obtained in terms of forces recorded in correspondance of the central curb, are related to the displacements monitored by the marker, obtaining the global displacement-force curve shown in Fig. 6.5.

Regarding the experienced damage, Fig. 6.6 shows the crack pattern obtained at the end of the test. In particular, the lower panel experienced higher damage, in contrast with the upper panel which experienced limited damage. In fact, only a diagonal crack in one of the sides of the panel is observed, while on the other side no cracks are visible. A wide diagonal crack is clearly visible in the lower panel,
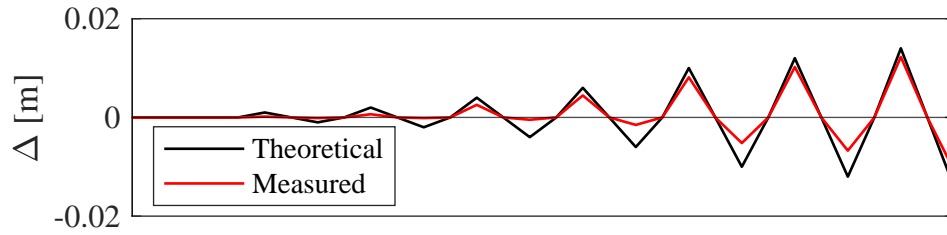
Figure 6.4: Comparison between the theoretical input and the actual experienced displacement measured at the jack
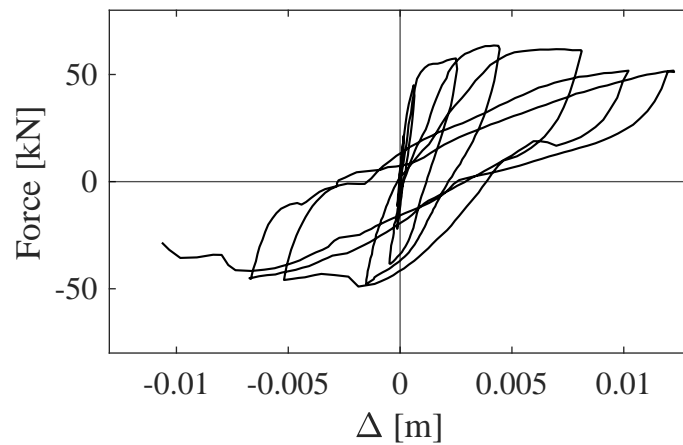
Figure 6.5: Experimental force-displacement results of the wall

together with the expulsion of some of the stones on one of the sides of the panel, showing the realization of a shear mechanism. It is noteworthy that the actual boundary conditions of the upper curb, by allowing the rotation of upper panel, determined a single bending condition for the upper panel and approximately a double bensing condition for the lower. Damage resulted, then, to be higher in the lower panel, as well as the measured shear reaction.

6.1.2 Numerical results

The experimental results shown in Fig. 6.5 are reproduced in the present Section adopting the macroelement described in Chapters 4 and 5.

The mechanical parameters adopted for the numerical model are listed in Tabs. 6.1 and 6.2, where Tab. 6.1 regards the mechanical masonry parameters, while
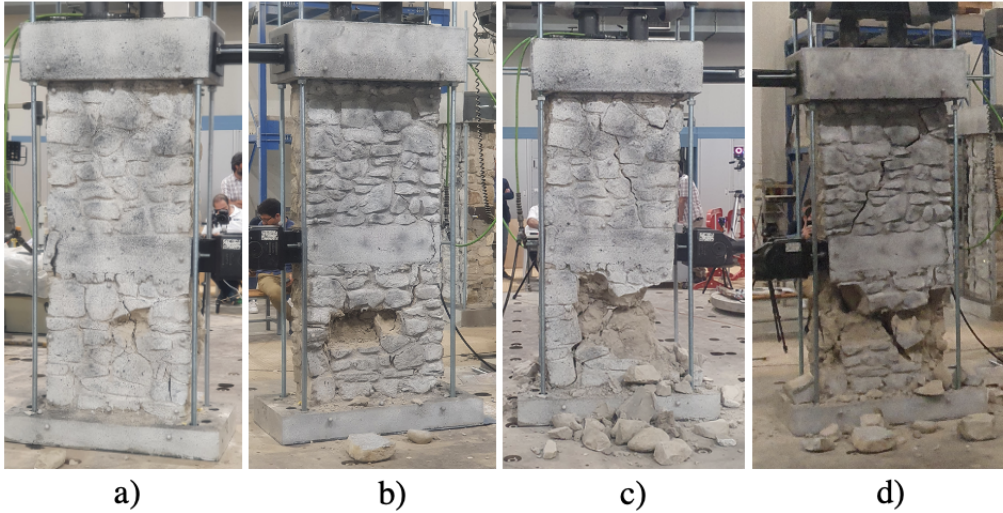
Figure 6.6: Unreinforced masonry wall: damaged before collapse first side (a); damaged before collapse second side (b); collapsed first side (c); collapsed second side (d)

Tab. 6.2 regards those relative to the nonlinear modified Bouc-Wen hysteretic model adopted for the nonlinear flexural and shear hinges. In particular, the Young's modulus E is evaluated from the experimental curve, while the shear modulus G is evaluated from the Young's modulus E considering a Posson ratio equal to 0.2. The compressive strength f_c and the shear strength f_v are assumed from the values available in the Italian Standard Code (NTC, 2018) for a non-periodic stone masonry with irregular stones. The parameters adopted for the nonlinear hinges, instead, are calibrated in order to have a good match between the shape and the dissipated energy of the numerical and the experimental curve, as well as a good accuracy in the reproduction of strength and stiffness degradation.

Table 6.1: Masonry mechanical parameters

E	ν	G	f_c	f_{v0}
kN/m^2	–	kN/m^2	kN/m^2	kN/m^2
$1080\,10^3$	0.2	$450\,10^3$	1000	22

Table 6.2: Modifed Bouc-Wen hysteresis parameters

Flexural hinges			Shear hinges		
a	δ_D	δ_K	a	δ_D	δ_K
$-$	kJ^{-1}	kJ^{-1}	$-$	kJ^{-1}	kJ^{-1}
1	0.8	10.0	0.016	0.8	10.0

Fig. 6.7 shows the schematization to equivalent frame adopted for the wall. Being composed of two distinct panels, with a concrete curb in the middle, two macroelements are used, one for each panel. The lower node is located on top of the lower curb, and a fixed restraint condition simulates the presence of this latter. A second node is located at the middle of the central curb. Being concrete much stiffer with respect to masonry, the presence of the curb is simulated through rigid offsets. The third node is located at the top of the upper panel, thus neglecting the presence of the upper curb. Boundary conditions in general allow vertical translation and in-plane rotations, while the out-of-plane degrees of freedom are restrained, together with the horizontal displacement on top of the panel, consistently with the set-up of the Sheppard test and the observations made after the end of the test.
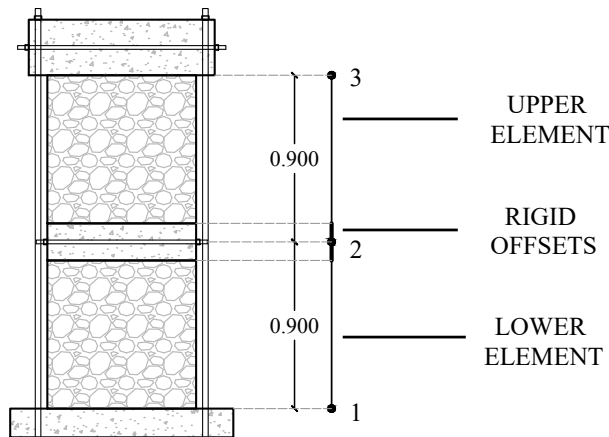
Figure 6.7: Equivalent frame model of the tested wall

Fig 6.8 (a) shows the comparison between the numerical (red line) and the

experimental dashed black line) outcomes in terms of global force-displacement curve. In general, the model is capable of describing with good accuracy the experimental behavior, especially in terms of reached strength in the positive range, while lower accuracy can be seen in the first cycles of the negative side. An evident asymmetrical behavior in terms of strength can be also observed. The initial stiffness of the curve is also well-captured. The hysteretic response of the two panels is shown in Fig. 6.10 (b) in terms of shear hinge response and in Fig. 6.10 (c) in terms of damage evolution with respect to shear deformation experienced. Considering that the two panels have a heigth to base ratio equal to 1, indeed, the flexural hinges are considered as elastic, and only the shear behavior is described by the numerical model. After the initial three cycles, which show opposite trends for the two panels, the hysteretic cycles, and consequently the damage evolution, tend to overlap. The lower panel experiences wider cycles after the first half of the cyclic action, and thus higher damage.

The energy dissipated at each cycle is reproduced through the adoption of an adequate set of parameters (Fig. 6.9), which also allows to describe the strength and stiffness degradation that the wall experienced. The first couple of cycles tends to unterestimate the energy actually dissipated by the wall, however an improvement of the match can be seen in the following cycles. On the overall, however, the total dissipated energy of the numerical model, does not differ substantially from the one resulting from the experimental test.

Interesting considerations can be made regarding damage evolution of the numerical model with respect to the experimental observations. Fig. 6.10 shows the damage patterns of the most damaged side of the wall and the evolution of damage of the numerical model during the ongoing of the test. The numerical outcomes of the lower panel reach a damage variable value $D = 0.85$ for the shear hinge of the lower panel and $D = 0.77$ for the upper panel, proximate to the maximum value of the unity, which represents the fully damaged state. This outcome is able to qualitatively describe quite well the strong damage experienced by the lower panel, which reaches almost the collpase condition. However, different behavior is described for the upper panel, which underwent limited damage in the experimental test. The numerical model in fact shows dissipation and degradation which are almost comparable to that of the upper panel, highlighting the discrepancy

with the experimental outcomes.
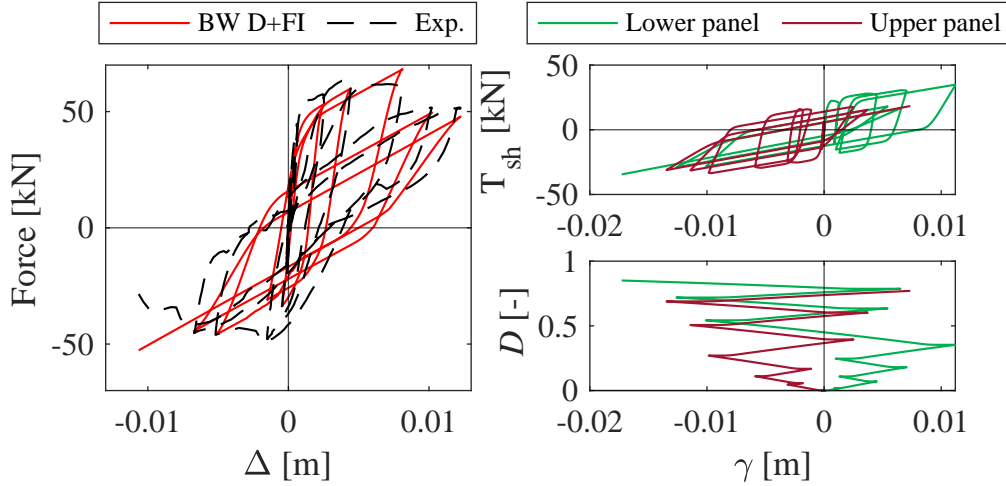
Figure 6.8: Comparison between experimental and numerical outcomes (a); response of the shear hinges of the lower and upper panels (b); damage evolution with respect to the deformation of the lower and upper panels (c)

6.2   Unreinforced building prototype

6.2.1   Experimental test

A prototype building, whose main features are representative of historical masonry buildings typical of Central Italy, has been tested in the laboratory of the ENEA Research centre in Casaccia, in a second phase with respect to the wall previously described.

The prototype is a full-scale one-storey unreinforced masonry structure, with an overall heigth equal to $H = 2.4\,\mathrm{m}$. Four two-leaf shear walls compose the structure, three of which are symmetrical with a door opening located at the center of the wall, while the fourth presents an off-centered window. Each wall is $3.3\,\mathrm{m}$ long, with a thickness equal to $0.3\,\mathrm{m}$. Dimensions and disposition af the walls, together with the layouts of the openings, are shown in Fig. 6.11, while photos of each wall can be seen in Fig. 6.12.
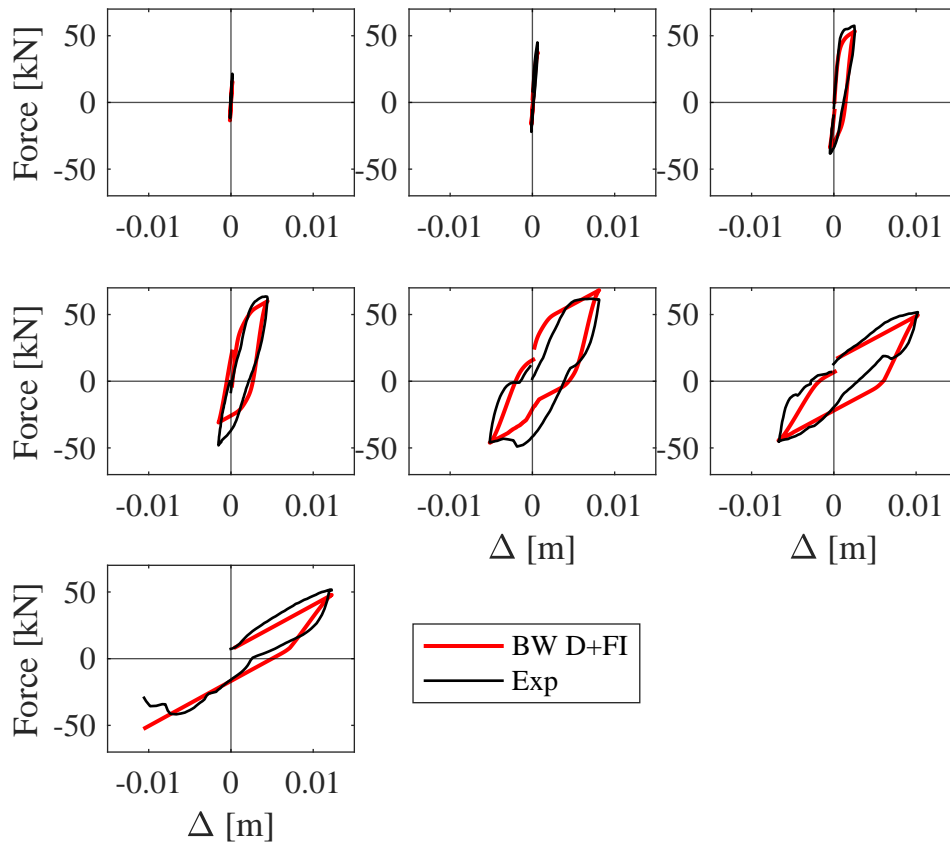
Figure 6.9: Force-displacement response at each cycle of the numerical model with respect to the experimental wall response

Stone masonry is employed for the prototype as well, consistently with the wall described in Section 6.1.1. Mortar and stones from Accumoli are utilized, with the aim of reproducing as closely as possible the actual mechanical characteristics of typical Italian historical masonry.

A wooden architrave is positioned above all the openings, having a heigth equal to 0.08 m, a thickness equal to that of the wall and a length equal to 0.94 m, thus bulging 0.12 m on each side of the opening. Seven wooden beams, supported by the front and the rear walls, reproduce the presence of a flexible slab, not being able neither to couple the walls, nor to give a stiff diaphragm condition. On top of these beams, nine pairs of steel weights are arranged, adding 1.8 t at the total mass of the structure, with the aim of reproducing the effect of the presence of
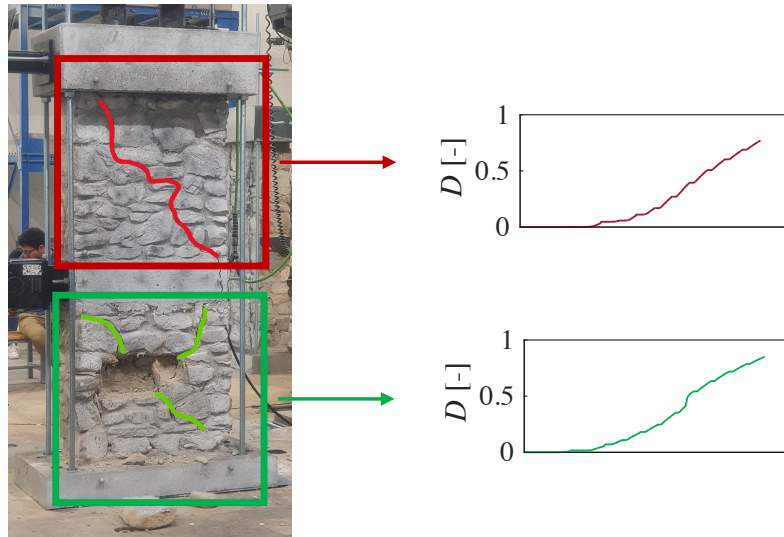
Figure 6.10: Crack patterns compared to the damage evolution
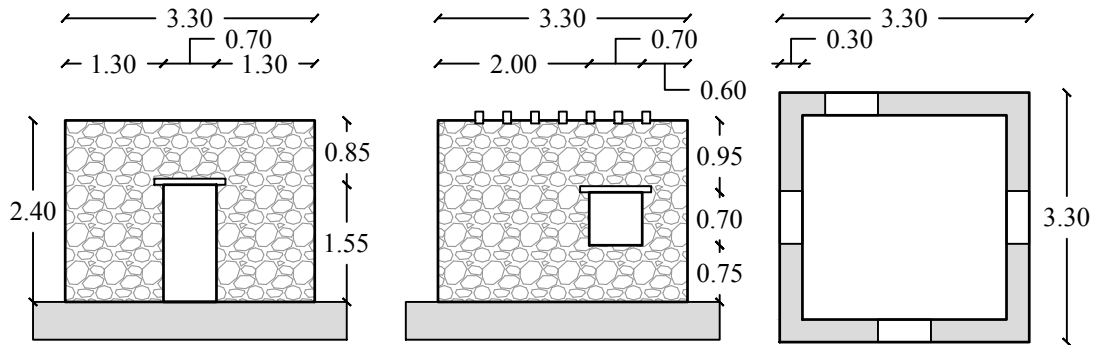
Figure 6.11: Unreinforced masonry prototype: dimensions of front, right and left wall (a); dimensions of rear wall (b); floor plan (c)

additional floors above.

The first two natural frequencies of the prototype were experimentally evaluated through instrumental tests, obtaining the values $f_1 = 9.5\,\mathrm{Hz}$ and $f_2 = 11.8\,\mathrm{Hz}$. The first mode is translational in the direction parallel to the wooden beams, while the second is orthogonal to them.

Dynamic shaking table tests were performed considering three different natural ground motion events recorded during the Central Italy seismic sequence in 2016.
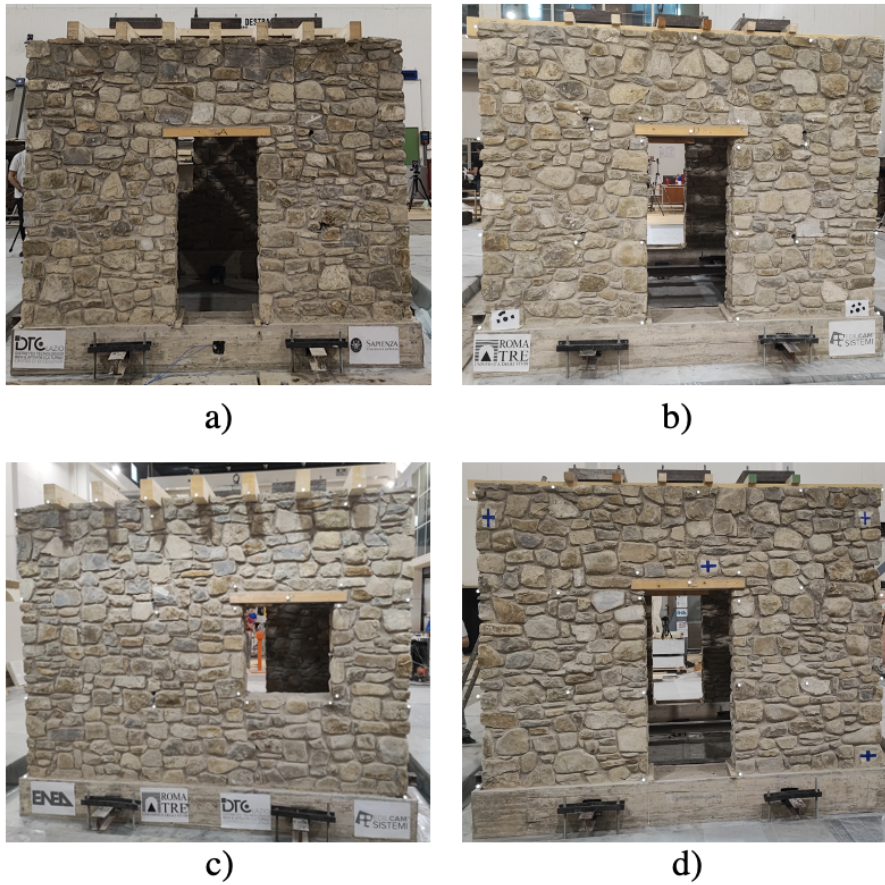
Figure 6.12: Unreinforced masonry prototype: front wall (a); right wall (b); rear wall (c); left wall (d)

In particular, the events recorded on the 24/08/2016, 26/10/2016 and 30/10/2016 at the stations of Norcia (NRC), Amatrice (AMT) e di Castelsantangelo sul Nera (CNE), respectively, are considered. The three components of each record are assigned simultaneously to the shaking table. The $N-S$ component is assigned in the Y direction (parallel to right and left walls), the $E-W$ component, which experienced the higher acceleration value, is assigned in the X direction (parallel to front and rear walls), while, of course, the vertical component is assigned to the Z direction. Each record is normalized with respect to the peak value of the strongest component, and then scaled considering increasing scale factors equal to $0.05 - 0.1 - 0.15 - 0.2 - 0.25 - 0.3 - 0.35 - 0.4 - 0.45 - 0.5\,\mathrm{g}$. As an example, the Amatrice ground motion record scaled at a maximum peak value

equal to 0.15 g is given in Fig. 6.13. The purpose is to test the prototype by subjecting it to incremental damage until reaching a condition close to collapse, in order to evaluate the maximum acceleration it can withstand. In each run, corresponding to a single peak acceleration value, the three accelerograms are assigned in the order AMT - CNE - NRC. A white noise is assigned between one scale factor value and the following with the purpose of identifying the natural frequencies of the specimen during the tests. Moreover, during the tests, short pauses between the single event were made, during which it was possible to inspect the experienced damage and crack patterns along the walls.
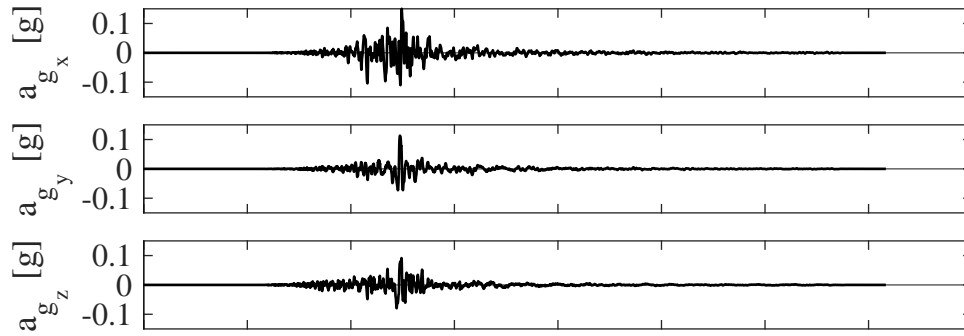
Figure 6.13: Amatrice ground motion record (AMT 26/10/2016) in directions X, Y and Z, respectively

Optic-fiber control markers are used for monitoring the dynamic response in terms of displacements.

First cracking was experienced during the 0.2 g run. After the 0.25 g run, cracks width started to increase, passing in some cases through the thickness of the wall. The crack patterns evolved then until the last run, showing the estabilishment of shear damage in the piers of the front, left and right walls, together with out-of-plane flexural mechanisms experienced by all the spandrels. The front wall piers also experienced minor sliding mechanisms at the base. Some of the stones of the external masonry leaf of the right wall were also expelled, in correspondence of the flexural damage of the spandrel. On the contrary, the rear wall experienced very limited damage to the piers, while slight cracks were localised at the ends of the spandrel, highlighting the out-of-plane flexural mechanism. Moreover, the

onset of an expulsion mechanisms relative to the corner between the front and the left walls can be distinguished. Fig. 6.14 shows the state of the prototype at the end of the 0.5 g run, where all the described mechanisms can be distinguished.

a)   b)

c)   d)
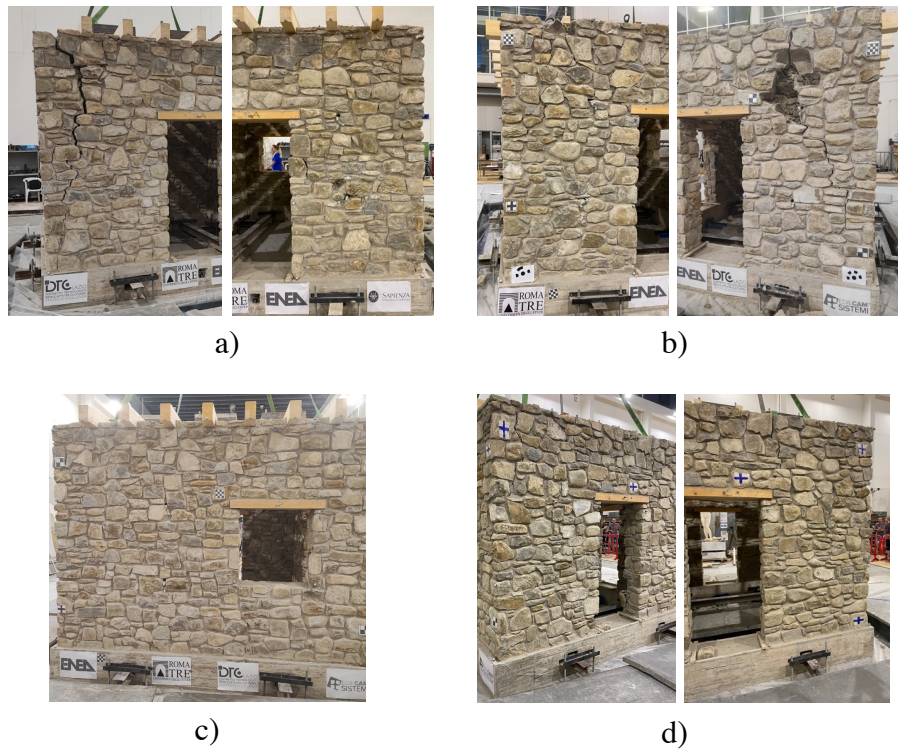
Figure 6.14: Unreinforced masonry prototype damage patterns after the 0.5 g run: front wall (a); right wall (b); rear wall (c); left wall (d)

6.2.2   Numerical results

The outcomes of the shaking table tests performed on the prototype presented in Section 6.2.1 are reproduced through a numerical model in which the structure is schematized adopting the macroelement model described in Section 5. The equivalent frame approach is adopted to model each wall of the prototype, adopting one macroelement for each pier or spandrel, and rigid offsets in correspondence of the panel zones. Fig. 6.15 shows how the two different typologies of walls are reduced to equivalent frames, in particular in Fig. 6.15 (a) the model and dimensions of the front, right and left walls are given, while in Fig. 6.15 (b) the

schematization of the rear wall is represented. The formulation proposed in Dolce (1991) is adopted to evaluate the length of the rigid offsets. The presence of the architraves is neglected.
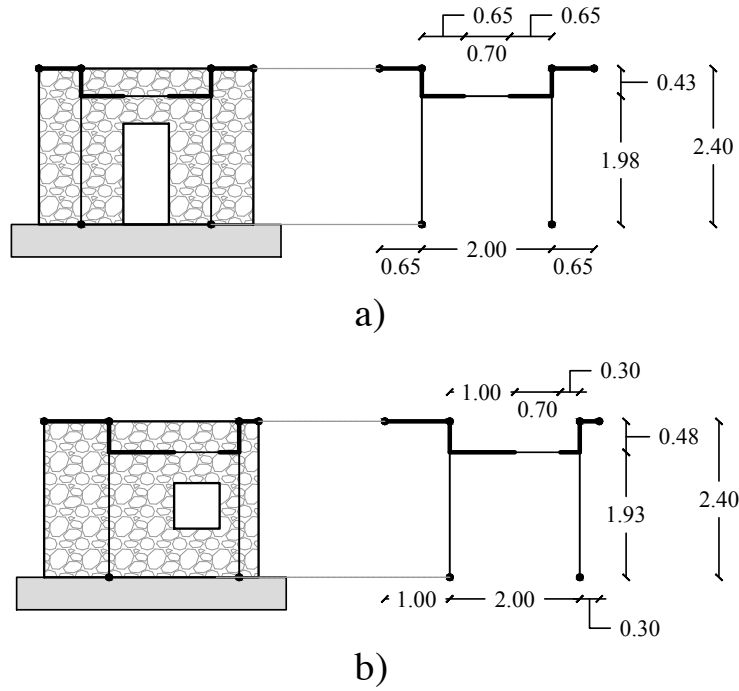
Figure 6.15: Equivalent frame schematization of the prototype: front, right and left wall (a); rear wall (b)

The mechanical parameters adopted for the homogeneized masonry material of the prototype differ from those of the wall tested through the Sheppard test. The two specimen were, in fact, built at different intervals, resulting in different periods of curing and hardening of the mortar and thus, settling of the masonry composite material. The Young's modulus E is identified by adopting an inverse process, being the first two modal frequencies of the prototype known, while the shear modulus G is calculated by considering a Poisson ratio equal to 0.2. The values of compressive f_c and shear f_v strengths are taken from the Italian Standard Code (NTC, 2018), as well as the value adopted for masonry mass density. All the material parameters are listed in Tab. 6.3. The parameters of the modified Bouc-Wen hysteretic model are listed in Tab. 6.4. The damage parameters, namely

δ_D and δ_K, are the same adopted in Section 6.1.2 for the numerical model of the Sheppard test specimen. They are also adopted for the flexural hinges in the out-of-plane direction. The hardening parameters are re-calibrated to allow the plastic behavior not only in the shear hinges, but also for the flexural hinges.

A damping coefficient equal to 5% is assumed, which allows to evaluate the coefficients adopted for the Rayleigh damping of the system, that is $a_0 = 3.29\,\mathrm{s}^{-1}$ and $a_1 = 0.0007\,\mathrm{s}$.

Table 6.3: Masonry mechanical parameters of the prototype

E	ν	G	ρ	f_c	f_{v0}
kN/m^2	–	kN/m^2	t/m^3	kN/m^2	kN/m^2
$530\,10^3$	0.2	$230\,10^3$	1.94	1000	78

Table 6.4: Modifed Bouc-Wen hysteresis parameters for the prototype

Flexural hinges			Shear hinges			OOP Flexural hinges		
a	δ_D	δ_K	a	δ_D	δ_K	a	δ_D	δ_K
–	kJ^{-1}	kJ^{-1}	–	kJ^{-1}	kJ^{-1}	–	kJ^{-1}	kJ^{-1}
0.02	0.8	10.0	0.05	0.8	10.0	0.02	0.8	10.0

According to the equivalent frame approach, the nodes of each macorelement are located exclusively at the intersections between the elements. It is not possible, therefore, to model the presence of concentrated loads positioned along the axis of the structural element, when they are not in correspondance of nodes. To overcome this issue and properly model the presence of the wooden beams that support additional masses, equivalent concentrated loads are evaluated by dividing the overall area of the floor into influence areas. These are then assigned only to the load bearing walls, which are the front and the rear walls.

The numerical results are presented only for some of the seismic events tested. In particular, the Amatrice (AMT) seismic event has been chosen, and the peak

intensities equal to 0.15 g, 0.25 g and 0.50 g are selected. The 0.15 g case is selected due to the absence of cracks or damage detected, with the aim of reproducing the initial elastic behavior, thus constituting a reference for the following intensities. The investigation of slight ongoing damage is the reason why the intensity equal to 0.25 g has been selected, while the 0.50 g intensity has been chosen to study the capability of the model to reproduce the final damage patterns and the activation of possible mechanisms. It is noteworthy that each record is assigned to the structure starting from an undamaged condition. This is an accurate assumption in the case of 0.15 g and 0.25 g, for both of which the initial condition is almost elastic, but is less accurate in the case of 0.50 g, as the prototype has already experienced major damage after the 0.45 g run. To this end, for this latter case the initial elastic and strength parameters are reduced to simulate the presence of initial damage, in particular those related to the shear behavior, i.e. the modulus G and the shear strength f_v, and the hysteretic parameters are diminished as well to simulate the reduced dissipative capacity of the system, due to pre-experienced damage. Moreover, to guarantee a good match between the numerical and the experimental outcomes, the acceleration recorded at the base of the prototype in the three directions is assigned as acceleration input in the numerical model. The theoretical and the measured values of the acceleration are compared in Fig. 6.16, showing the difference in some of the peak values, especially in Y direction, as well as the overall intensity values in the Z direction.

In the following, the results are shown in terms of relative displacement with respect to time.

Four representative markers are chosen for the displacement numerical - experimental comparison, positioned at the tops of one pier for each wall, in order to have control points nearby the nodes of the macroelement.

Figs. 6.17, 6.18, 6.19 and 6.20 show the results relative to the acceleration intensity equal to 0.15 g, of the front, right, left and rear wall, respectively. The numerical outcomes, represented in solid red line, show a good agreement with the experimental monitored displacements, represented in solid black line, in the X and Y directions. The response remains substantially elastic for the entire prototype. The Z component, on the contrary, show visibly different results. Wide oscillations are captured by the monitoring system, that are not reproduced
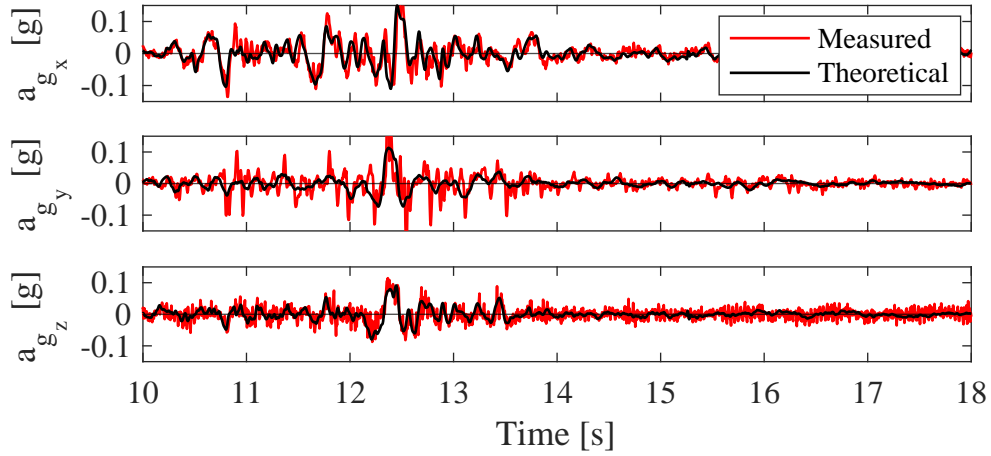
Figure 6.16: Amatrice ground motion record (AMT 26/10/2016) compared to the acceleration measured in directions X, Y and Z, respectively

by the numerical model. This is probably caused by the limited deformability capacity of the model in the vertical direction, which corresponds to the axial directions of the piers. The model remains in fact elastic in the axial direction and completely decoupled from the flexural behavior.

Figure 6.17: Experimental (black) vs. numerical (red) comparison for the directions X, Y, and Z respectively for the front wall, for the 0.15 g intensity record
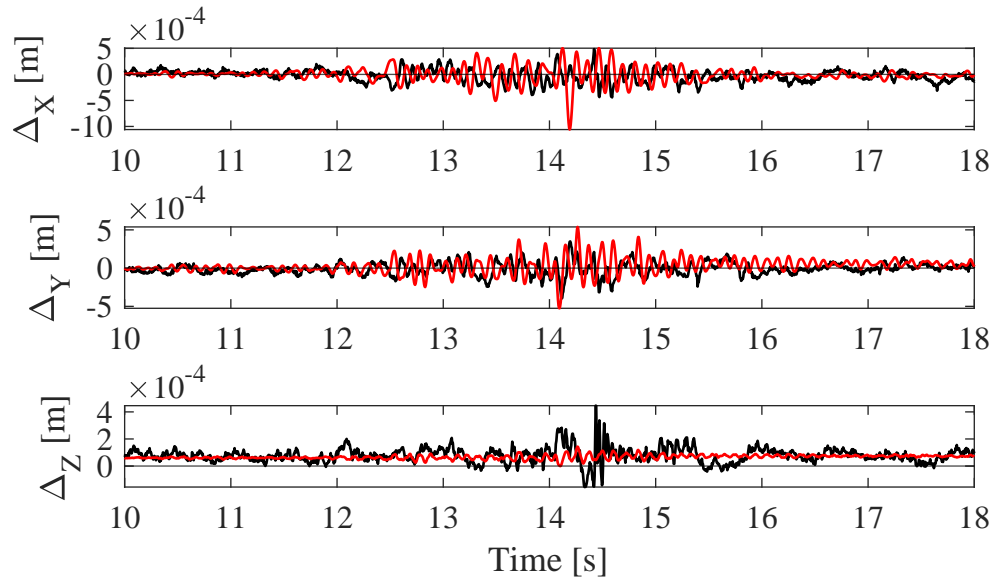
Figure 6.18: Experimental (black) vs. numerical (red) comparison for the directions X, Y, and Z respectively for the right wall, for the $0.15\,\mathrm{g}$ intensity record
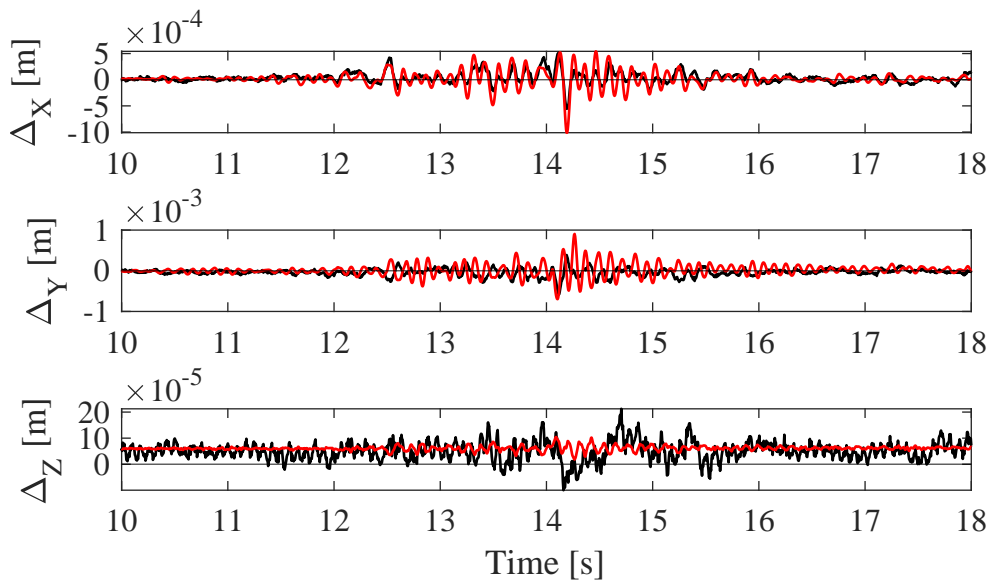
Figure 6.19: Experimental (black) vs. numerical (red) comparison for the directions X, Y, and Z respectively for the left wall, for the $0.15\,\mathrm{g}$ intensity record

On the overall, a good agreement in the X and Y directions of the time history results can be seen also in the case of the $0.25\,\mathrm{g}$ intensity, which are shown in Figs.
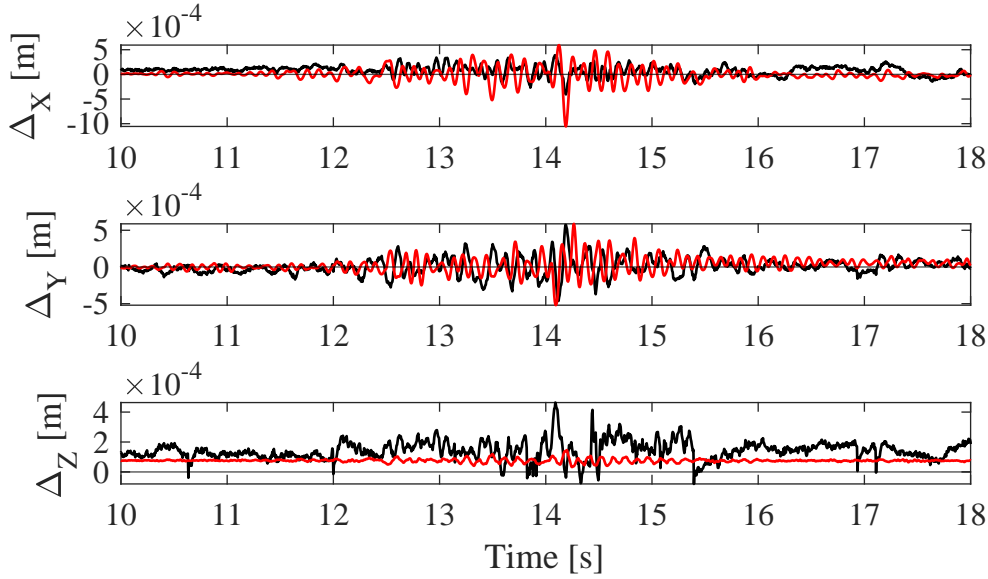
Figure 6.20: Experimental (black) vs. numerical (red) comparison for the directions X, Y, and Z respectively for the rear wall, for the $0.15\,\mathrm{g}$ intensity record

6.21, 6.22, 6.23 and 6.24. The displacement peaks are captured quite accurately especially in the X directions, together with the oscillation period. In the Y direction the numerical results of the front wall show residual displacements much higher than the experimental results. This is probably caused by the onset and evolution of damage, which may have caused residual displacement and deformation at the hinge level. Regarding the Z direction, the same issues highlighted for the $0.15\,\mathrm{g}$ intensity case are detected. Regarding damage evolution, most of the hinges show limited damage, especially in the spandrels, while few piers experienced higher damage, until reaching values of the damage variable equal to $D = 0.25$.

Regarding the case of the $0.50\,\mathrm{g}$ intensity, shown in Figs. 6.25, 6.26, 6.27 and 6.28, marked differences can be observed between experimental and numerical data, highlighting substantial displacement variations. In particular, the experimental outcomes show significantly higher displacements, especially in the Y direction. This phenomenon can be attributed to the possible detachment of the block on which the marker is placed, an aspect that the numerical model is unable to capture, since the use of an homogeneized medium does not allow to

Figure 6.21: Experimental (black) vs. numerical (red) comparison for the directions X, Y, and Z respectively for the front wall, for the 0.25 g intensity record

Figure 6.22: Experimental (black) vs. numerical (red) comparison for the directions X, Y, and Z respectively for the right wall, for the 0.25 g intensity record

describe such local failures. Moreover, the wide oscillation period is not reproduced, as the numerical results show lower period. It is noteworthy that during

Figure 6.23: Experimental (black) vs. numerical (red) comparison for the directions X, Y, and Z respectively for the left wall, for the $0.25\,\mathrm{g}$ intensity record
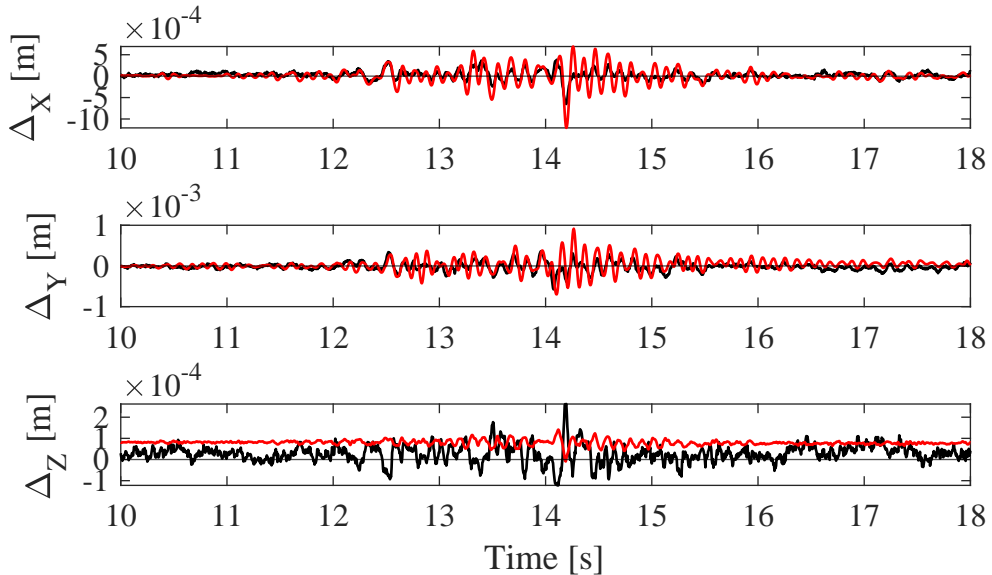

Figure 6.24: Experimental (black) vs. numerical (red) comparison for the directions X, Y, and Z respectively for the rear wall, for the $0.25\,\mathrm{g}$ intensity record

the experimental campaign, the $0.50\,\mathrm{g}$ intensity ground motion has been given as last input, after the entire sequence. This means that the prototype is already

in a damaged configuration. To reproduce the presence of pre-existing damage, the shear modulus G equal to a half with respect to the inital modulus is taken ($G = 115000 \, \text{kN/m}^2$), the shear strength is reduced by 10%. The parameters of the hinges are also modified, to consider the reduced dissipative capacity of the hysteretic model, which starts from a damaged condition. In particular, the value of the flexibility increase parameter is reduced to $\delta_K = 2 \, \text{kJ}^{-1}$. Some of the peaks are captured, such as the case of the front and left wall in the X direction (Figs. 6.25 and 6.27 respectively) or the Y direction of the rear wall (Fig. 6.28).

Moreover, the shear hinges of all the piers are activated, with values of the damage variable ranging between $D = 0.013$ and $D = 0.016$ for the piers of the rear wall, which in fact resulted slightly damaged from the experimental test, to values about equal to $D = 0.55$ or $D = 0.57$ for the piers of the left and right walls.

Figure 6.25: Experimental (black) vs. numerical (red) comparison for the directions X, Y, and Z respectively for the front wall, for the 0.50 g intensity record

To study the effect of damage cumulation, a ground motion sequence is also studied. The two seismic events already tested, with intensities equal to 0.25 g and 0.50 g, are considered with 10 s of white noise in between, to allow the dissipation of free oscillations. Figs. 6.29, 6.30, 6.31 and 6.32 show the results obtained in

Figure 6.26: Experimental (black) vs. numerical (red) comparison for the directions X, Y, and Z respectively for the right wall, for the $0.50\,\mathrm{g}$ intensity record
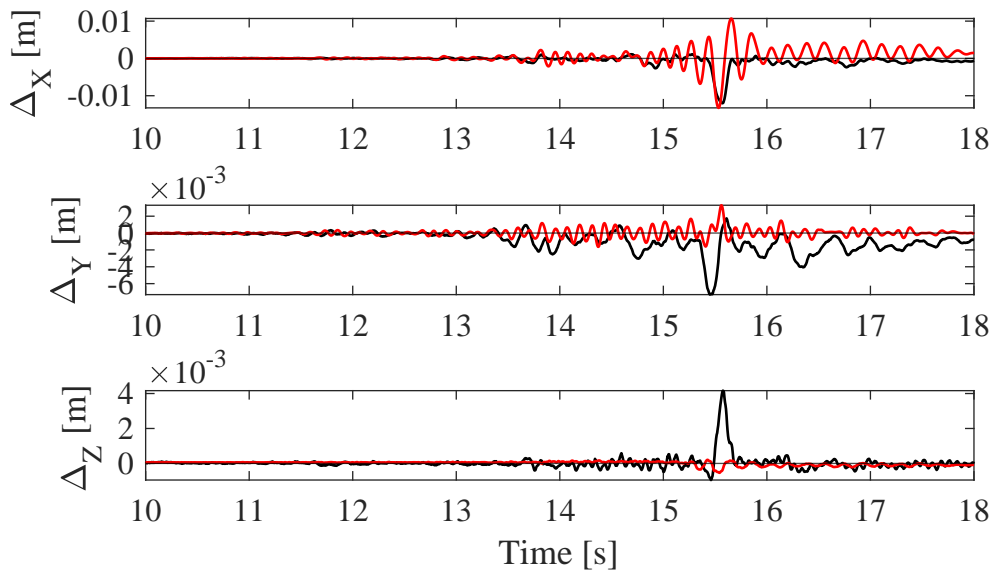
Figure 6.27: Experimental (black) vs. numerical (red) comparison for the directions X, Y, and Z respectively for the left wall, for the $0.50\,\mathrm{g}$ intensity record

terms of displacements.

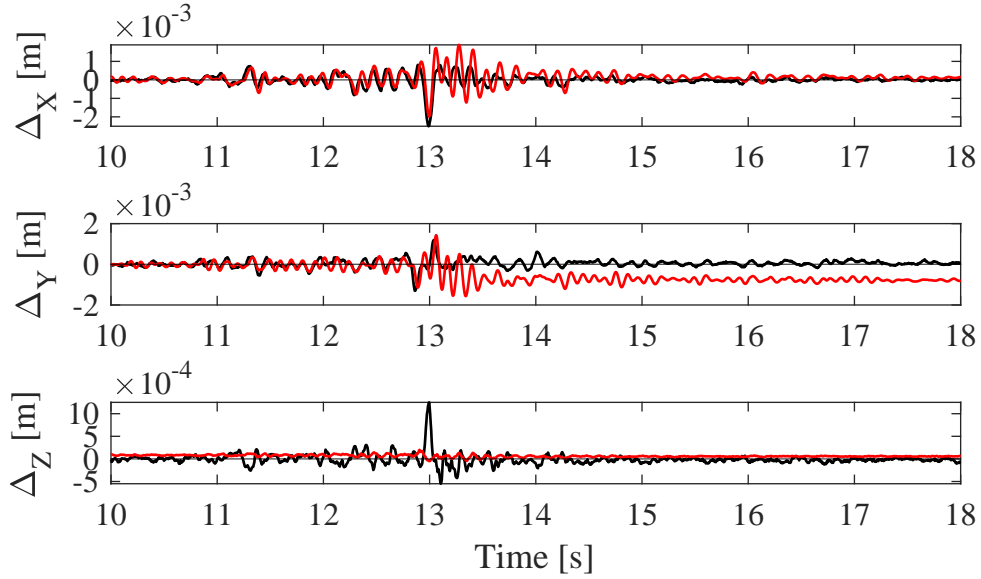Both the front and the right walls showed high discrepancies between the
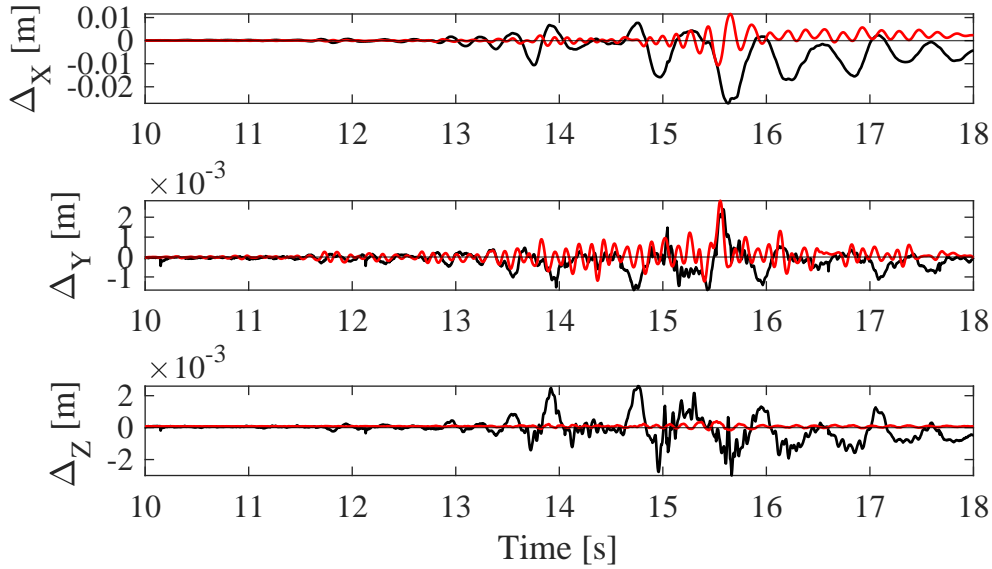
Figure 6.28: Experimental (black) vs. numerical (red) comparison for the directions X, Y, and Z respectively for the rear wall, for the 0.50 g intensity record

numerical and the experimental results. In particular, the front wall in the Y direction (Fig. 6.29) experienced positive residual displacements in the experimental test, but negative displacements are obtained by the numerical model. The right wall instead (Fig. 6.30), even if the sign of the residual dispalcement is consistent between the numerical and the experimental results, shows values which are significantly lower for the numerical case, and similarly for the rear wall (Fig. 6.32). Good accuracy of the results is obtained for the left wall (Fig. 6.31).

Almost all cases, however, underestimate the maximum and the residual displacements obtained during the tests. This is probably caused by the high oscillation that the prototype experienced due to the opening and reclosure of major cracks during the tests, which cannot be reproduced by the numerical model except in a qualitative manner. However, the shear hinges of the front, left and right walls were activated, experiencing medium to high values of damage, going from 0.2 to 0.8 at the end of the analysis. The out-of-plane flexural hinges of the spandrels experienced low damage, as well as those of the piers.
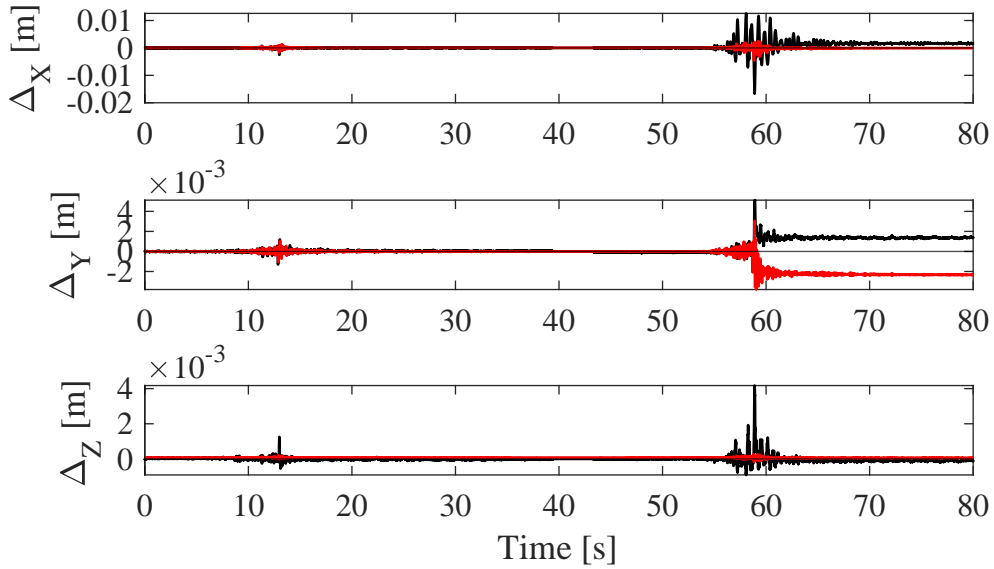
Figure 6.29: Experimental (black) vs. numerical (red) comparison for the directions X, Y, and Z respectively for the front wall, for the $0.25 - 0.50\,\mathrm{g}$ record sequance
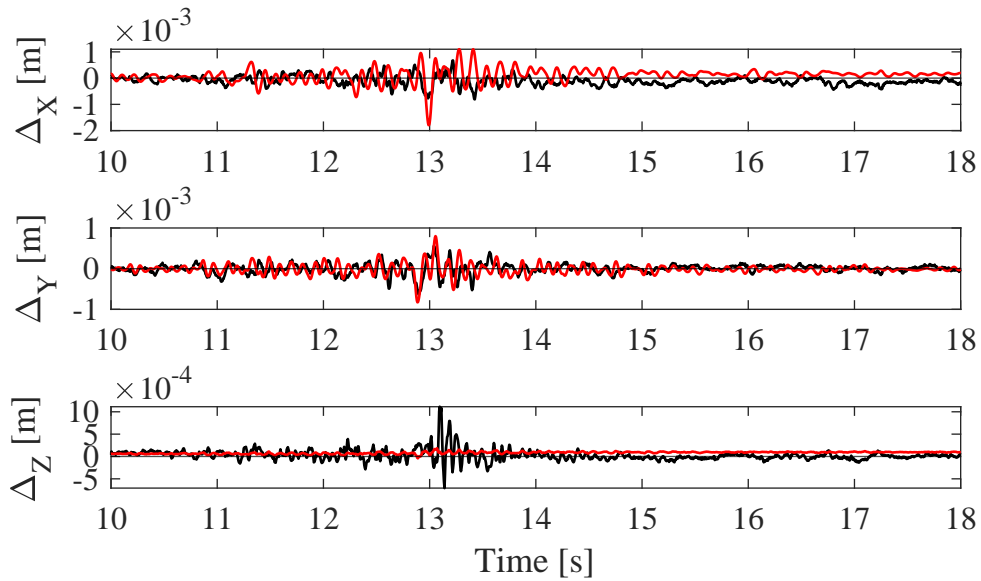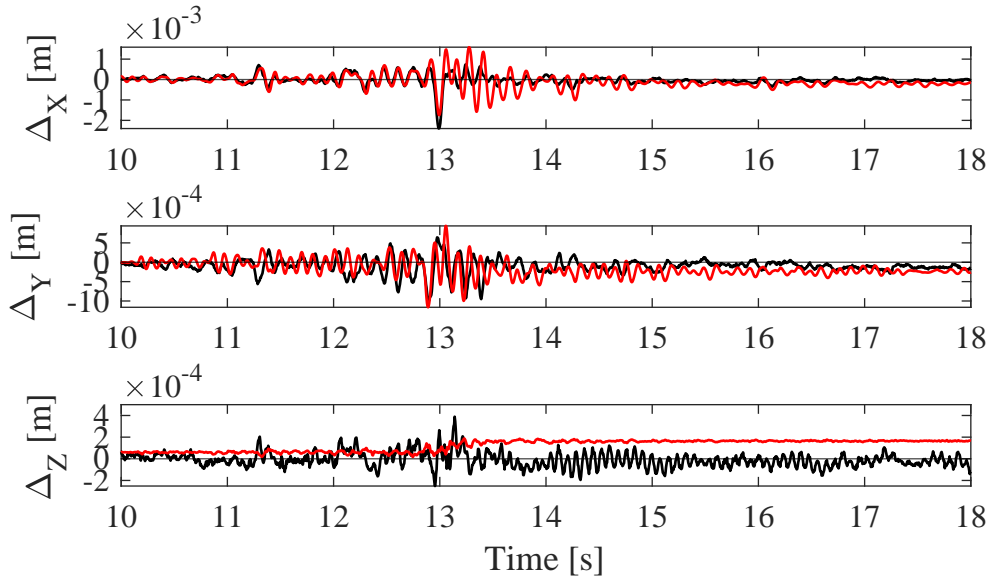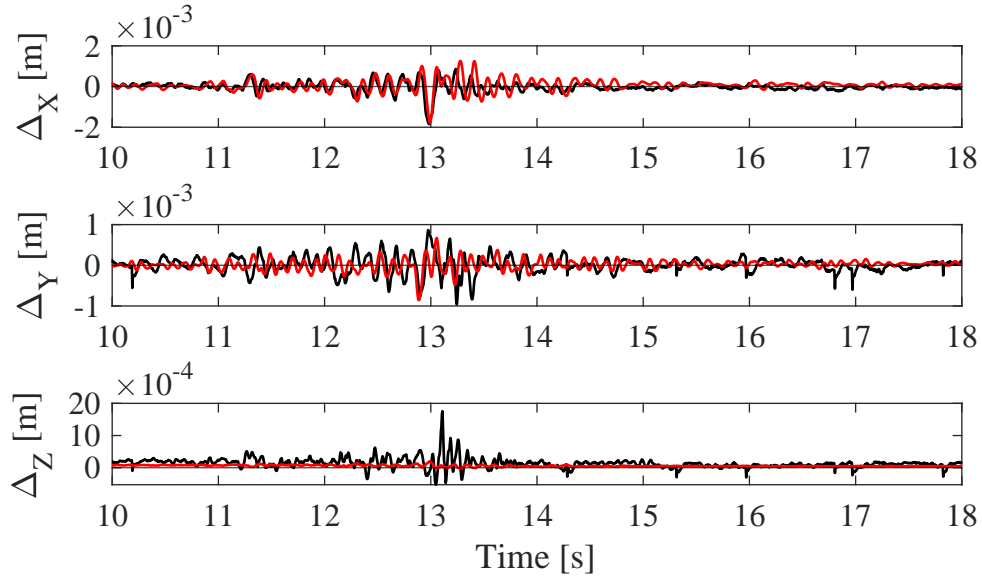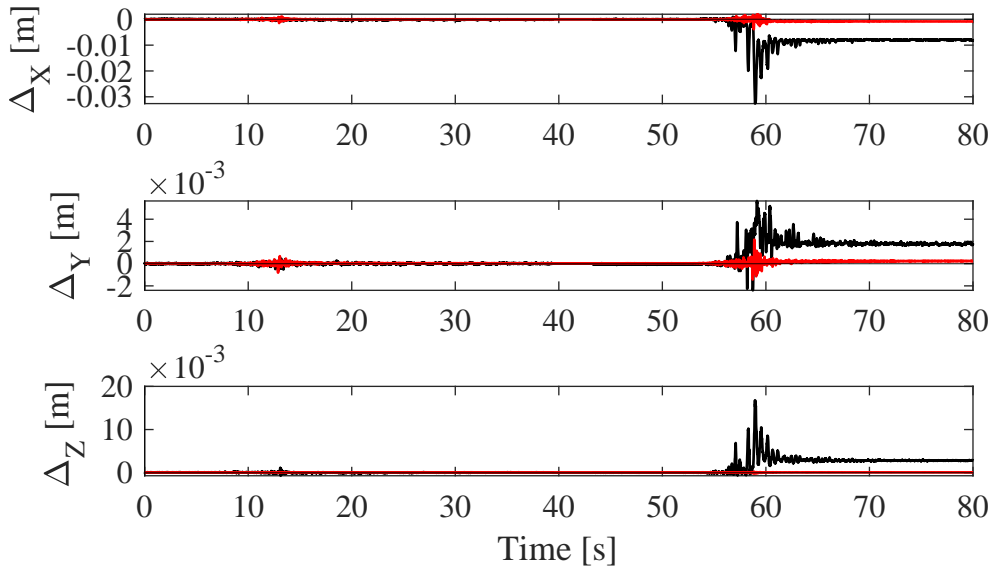

Figure 6.30: Experimental (black) vs. numerical (red) comparison for the directions X, Y, and Z respectively for the right wall, for the $0.25 - 0.50\,\mathrm{g}$ record sequance
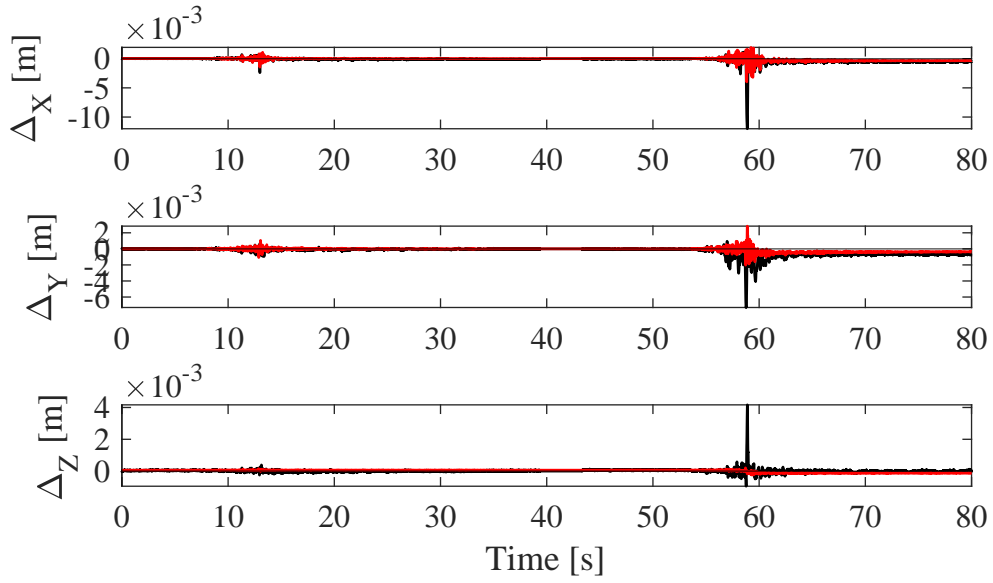
Figure 6.31: Experimental (black) vs. numerical (red) comparison for the directions X, Y, and Z respectively for the left wall, for the $0.25 - 0.50\,\mathrm{g}$ record sequance
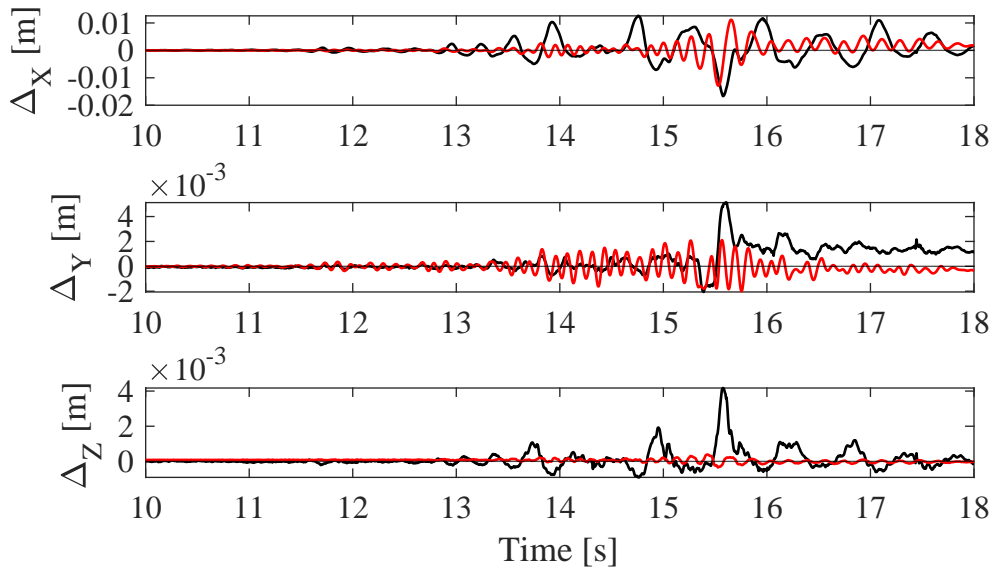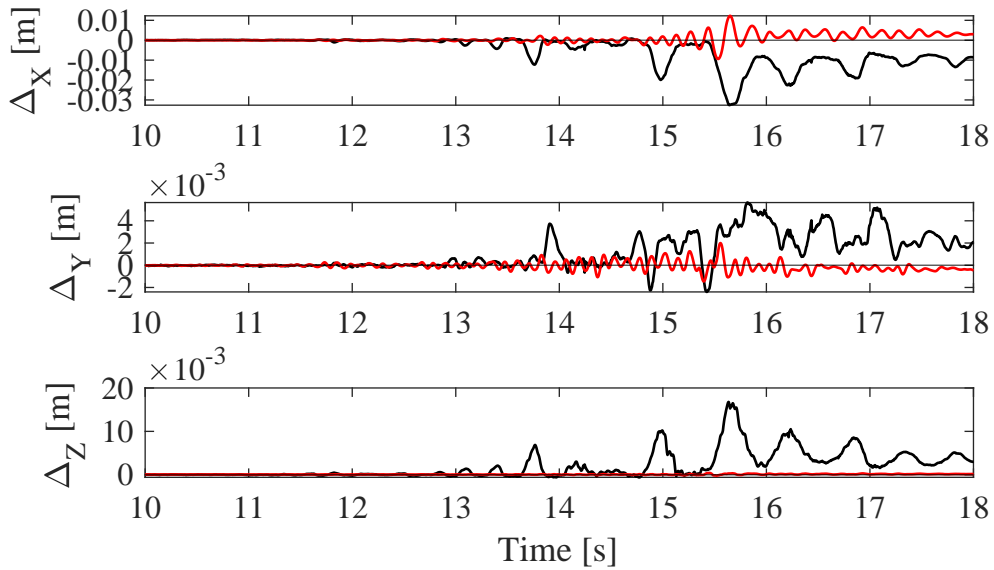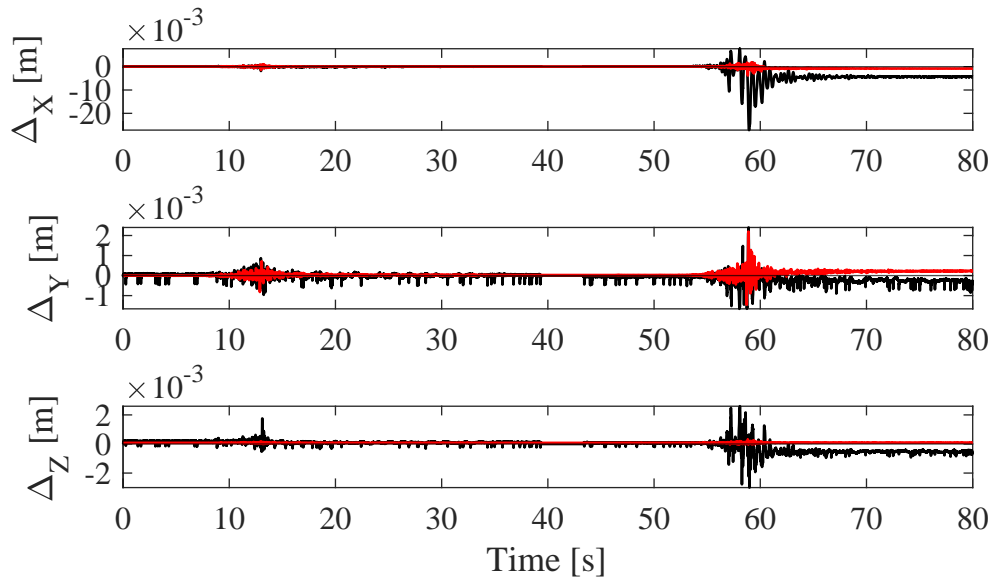

Figure 6.32: Experimental (black) vs. numerical (red) comparison for the directions X, Y, and Z respectively for the rear wall, for the $0.25 - 0.50\,\mathrm{g}$ record sequance

Chapter 7

Conclusions

The main purpose of this work was to propose and validate a refined macroelement model, in the framework of the equivalent frame approach, for the analysis of the response of historical masonry structures, investigating the in-plane and out-of-plane degrading behavior of structural elements without overlooking at a reduced computational burden. The formulation of an advanced constitutive law, obtained by enhancing an existing formulation available in the literature, capable of describing with good efficiency the strength and stiffness degradation of the masonry material, was the initial step. A proper description of the complex and highly nonlinear masonry behavior was, in fact, the main focus of the thesis, being fundamental to rely on a refined constitutive law when simplified approaches, such as the macroelement one, are considered.

An additional degradation, named flexibility increase, was added to a modified Bouc-Wen hysteretic model proposed in Liberatore et al. (2019), which already included damage as a scalar variable affecting the hysteretic force evaluation. The differential equation governing the basic hysteretic model, formulated in terms of non-dimensional quantities, was not modified by the introduction of damage and flexibility increase, which instead modified the scale factors which transform the non-dimensional quantities into force and displacement. Damage has then been defined as a *reduction* of the hysteretic force, resulting in both stiffness and strength degradation, while flexibility increase as an *expansion* of the elastic displacement, resulting in stiffness degradation. The expression of the dissipated

energy as the difference between total and elastic energy, which in turn depend on dissipated energy, leads to a differential equation, whose solution was derived. Moreover, the fundamental properties of dissipated energy were investigated. The basic hysteretic model and the model with flexibility increase showed to have no upper bound on dissipated energy, while this latter arises when damage is present. Considerations about the thermodynamic admissibility were then carried on. The required non-decreasing trend of the dissipated energy resulted in a constraint on the model parameters, satisfied in most practical cases, while additional constraints were obtained from the transformations from non-dimensional to dimensional quantities. The total set of constraints lead to trace an admissible domain for model parameters. Drucker's postulate was investigated, showing that the hysteretic model with flexibility increase is work hardening according to Drucker if the basic hysteretic model is, while the model with damage, in general, is not work hardening. Basic parametric analyses were conducted to study the separate influence of damage and flexibility increase, and comparisons highlighting the accuracy of the enhanced model with respect to the previous are made by reproducing the results of well-known experimental tests available in the literature. In particular, the good accuracy in the reproduction of both the energy dissipated during the cyclic analysis and the stiffness degradation was emphasized, being both fundamental characteristics of the nonlinear masonry degrading behavior.

The modified Bouc-Wen hysteresis was introduced in the framework of a 2D force-based beam macroelement, where it was adopted to model lumped flexural and shear plastic hinges. The proposed macroelement has the aim of modeling structural elements, namely piers and spandrels, being also corredated with rigid offsets to reproduce the high stiffness tyipical of panel zones. An iterative procedure to enforce equilibrium conditions between the elastic beam element, the flexural and shear hinges was also developed. The macroelement model has proved to accurately capture the response of well-known experimental tests, by reproducing the behavior of a squat and a slender panel, highlighting the main characteristics of their response. The activation of the flexural hinges in the slender panel and shear hinge in the squat panel, while the contributions of the remaining hinges were negligible, allowed to capture the degrading mechanisms experienced during the tests.

The model was thereafter enriched with a dynamic formulation. The possibility to model dynamic excitations represents a fundamental aspect for an adequate study of the response of historical masonry structures and for their preservation. Seismic excitations, in fact, are a common and relevant excitation that cannot be neglected for an adequate assessment procedure. First, the behavior of the modified Bouc-Wen hysteretic model in the dynamic field was investigated adopting a lumped mass formulation, being this latter the most common approach for mass description in equivalent frame models. A slender and a squat panel, both restrained only at the base, were analyzed. Sweeps with constant, increasing and decreasing ratios between the frequency of the excitation and that of the panel were considered. The modified Bouc-Wen hysteresis, which considers strength and stiffness degradation and plasticity, was compared with the behavior of a classical Bouc-Wen hysteretic model, characterized exclusively by plasticity. The results of the squat panel showed that, as expected, the presence of flexibility increase allowed the system to reach higher shear strain values with respect to the classical Bouc-Wen models, also driving the cycles to be thinner and have a lower equivalent stiffness during the progression of the cycles. Comparing this latter case with a model with damage only, higher values of the damage variable D regarding the case with damage only, with respect to the case with flexibility increase, were detected, due to the lower dissipated energy reached during the analysis caused by the increase of the elastic displacement and the thinner cycles experienced. Regarding the slender panel, similar considerations hold. Moreover, damage resulted to cause an increase of the period, while the flexibility increase caused a thinning of the cycles experienced during the analysis. The variation of the amplitude of the acceleration history showed that the greater the amplitude of the excitation, the more rapid the degradation, and the higher the period. On the opposite, the smaller the amplitude, the softer the degradation, and the smaller the period, which were more spread over time.

The numerical results of a very slender wall were considered as a benchmark to validate the accuracy of the macroelement model against a finite element macromechanical model. Comparison of modal frequencies lead to considerations regarding the accuracy of the use of a lumped mass matrix approach to analyze the response of individual panels, being too different given the same stiff-

ness results. This allowed the model to be further refined with the introduction of a mass matrix formulation consistent with the force-based macroelement formulation, through the Unit Load method, obtaining more satisfactory accordance between the frequencies of the two numerical models. Time-history analyses were therefore carried out, to study the evolution of damage with the increase of the ground motion intensity. Similar results were obtained in terms of displacements between the two models, although with different oscillation trends, due to the different evolution of damage. In particular, in the proposed model, when maximum damage was explicated, a residual elastic response appeared to take over, resulting in extremely large oscillations in terms of both period and amplitude.

The out-of-plane response was subsequently investigated. The study of out-of-plane collapse mechanisms typical of historic masonry buildings is an issue often neglected when the main hypoteses valid for classical equivalent frame models are followed. Local mechanisms, such as out-of-plane mechanicsms, in fact, are typically assumed to be avoided in favor of in-plane mechanisms. Indeed, neglecting them can lead to severe overestimation of structural capacity, compromising an adequate performance description and verification. In particular, the force-based formulation has been extended with the description of the three-dimensional response of the beam element, with the addition of lumped plastic flexural hinges in the out-of-plane direction suitable for the reproduction of one-way bending behavior typical of slender panels, being located in correspondence of the end nodes. A validation was proposed by analyzing a wall subjected to a two-way bending mechanism, using two macroelements to model the panel. A good accuracy in the response reproduction was obtained. Subsequently, to be consistent with the force-based approach and with the purpose of using a single macroelement for the description of each structural element, the formulation was further expanded. An additional degree of freedom for the description of a rotation located at the center of the element in the out-of-plane direction was introduced, to which corresponds the introduction of a lumped flexural hinge with the purpose of being able to capture, through the application of distributed loads, the out-of-plane deformations caused by two-way bending mechanisms.

The results of an experimental test performed at the ENEA Research Center in Casaccia, as part of the RIPARA Project, were considered for the conclusive

validation of the model. In particular, the experimental results of a quasi-static cyclic Sheppard test were reproduced through the in-plane static macroelement. The numerical results showed a good agreement with the experimental outcomes. A qualitative description of the damage experienced by the wall was obtained, especially at the end of the analysis, when the damage pattern observed during the experiment was compared to the numerical results. In addition, the activation of the shear hinge, with negligible contribution of the flexural hinges, showed the capability of the model of appropriately capturing the mechanisms actually experienced. A single-storey prototype building, whose mechanical properties aimed at reproducing common features of typical Central Italy masonry buildings, was subsequently analyzed through shaking table tests. A seismic sequence of accelerograms with increasing intensity was considered. Three of the intensities tested in the laboratory were selected and reproduced through the numerical model, also comparing the results obtained by testing individual accelerograms or a sequence, to study the damage trend. The presence of pre-existing damage was accounted in two different manners, namely by reducing the initial elastic parameters and the damage parameters when considering the single event, and by performing a sequence of multiple events. Overall, the results were satisfactory and the model showed to be adequately accurate in describing the structural response. Most of the residual displacements were captured, and some of the most damaged walls of the prototype were also detected by the numerical model.

On the overall, the macroelement model showed to reproduce in a quite accurate way the static and dynamic behavior of the masonry structures analyzed.

However, additional tests can be done on different types of buildings in order to further evaluate the performance of the model in more complex contexts. For instance, being a simplified model, it would be possible to analyze the structural response of historical buildings or aggregates by maintaining the advantage of a low computational burden also in large-scale analyses. Nonetheless, it is necessary to recall some of the basic assumptions on which the equivalent frame model is based, and that since it is intended to be a suitable tool for the study and preservation of existing buildings, it is the responsibility of the designer to assess the applicability of the model to each specific case. As an example, cases in which crumbling of masonry is expected cannot be well reproduced by this kind of model,

as well as cases with irregular geometries that cannot be reduced through simple element schematization.

In general, improvements are still required, especially for a better representation of the out-of-plane response, and the applicability of the model as a prediction tool can be tested. To this end, the following future developments are proposed:

- Implementation and verification of the enhanced formulation with three flexural hinges in the out-of-plane direction is required. Comparisons regarding the accuracy of this refined model with the one which employs two flexural hinges but a higher number of macroelements to model the two-way bending mechanism can be made;

- The model could also be refined in order to consider other important phenomena that usually affect structural behavior of masonry walls, such as the introduction of P-Δ effects especially for out-of-plane loaded walls without restraints on top;

- The adoption of a phenomenological constitutive law enables the study of the homogenized response of a complex material such as masonry. In this regard, since the parameters adopted for stiffness and strength degradation depend on the particular typology of masonry adopted, an interesting development may be to determine the different sets of parameters best suitable for describing the degradation of different types of masonry, through extensive comparison analyses with experimental results;

- The accuracy of the model can be additionally tested by reproducing the behavior of different types of buildings, in order to study its performance in capturing more complex responses, as well as in investigating their degrading behavior;

- The possibility to reproduce the effects of the presence of structural reinforcements can be studied. The most common practice for equivalent frame models in which reinforcing techniques are applied, is usually to modify the initial strength and stiffness paramenters of the macroelement, which is still

applicable in the presented approach. However, considering the lumped approach adopted for the description of nonlinearity, the influence of reinforcements could also be accounted by modifying "ad hoc" the constitutive law implemented in the nonlinear hinges. The effect of the reinforcements could thus be described through the use of specific constitutive laws for a more accurate representation of their contribution to the structural response.

Appendix A

Numerical solution for the Bouc-Wen model with damage and flexibility increase

Chapter 3 presented a Bouc-Wen model modified with the introduction of an additional term, called flexibility increase, in the evaluation of the elastic displacement. This affects the loading and unloading stiffness of the cyclic behavior by giving degradation. In the following, the numerical procedure that allows to derive the response of the system in terms of dissipated energy, hysteretic force and non-dimensional dispalcement is presented.

The response of the system can be calculated numerically assuming that the quantities governing the response are known at time step i and shall be calculated at time step $i + 1$. The quantities at time step i are denoted by $\bullet_i$ and those at time step $i + 1$ by $\bullet_{i+1}$.

Assuming initially that u_{i+1} is known, z_{i+1} can be calculated according to the forward Euler method:

$$z_{i+1} = z_i + \kappa_i(u_{i+1} - u_i) \tag{A.1}$$

where κ_i is the derivative of z with respect to u at step i, which is function of z_i

and $\text{sign}(\dot{v}_i)$. The latter can be replaced by $\text{sign}(v_{i+1} - v_i)$:

$$\kappa_i = \frac{dz}{du}\bigg|_{u=u_i} = f[z_i, \text{sign}(v_{i+1} - v_i)] \tag{A.2}$$

The dissipated energy U^h_{i+1} can be calculated by enforcing the energy balance stated by Eq. 3.29 at time steps i and $i+1$, i.e.:

$$U_i = U^e_i + U^h_i \tag{A.3}$$

$$U_{i+1} = U^e_{i+1} + U^h_{i+1} \tag{A.4}$$

The increment of the dissipated energy is:

$$U^h_{i+1} - U^h_i = U^e_i + U_{i+1} - U_i - U^e_{i+1} \tag{A.5}$$

The physical meaning of Eq. A.5 is shown graphically in Fig. A.1. The increment of the total energy can be expressed through the trapezoidal rule:

$$\begin{aligned}
U_{i+1} - U_i &= \frac{1}{2}(F^h_i + F^h_{i+1})(v_{i+1} - v_i) \\
&= \frac{1}{2}\, k\, v_y^2\, (1-a)[(1 - \delta_D U^h_i)z_i + (1 - \delta_D U^h_{i+1})z_{i+1}] \cdot \\
&\quad \cdot [(1 + \delta_K U^h_{i+1})z_{i+1} + u^p_{i+1} - (1 + \delta_K U^h_i)z_i - u^p_i]
\end{aligned} \tag{A.6}$$

The elastic energy at time step i results as:

$$U^e_i = \frac{1}{2}F^h_i v_y(1 + \delta_K U^h_i)z_i = \frac{1}{2}\, k\, v_y^2\, (1-a)(1 - \delta_D U^h_i)(1 + \delta_K U^h_i)z_i^2 \tag{A.7}$$

and at time step $i+1$:

$$\begin{aligned}
U^e_{i+1} &= \frac{1}{2}F^h_{i+1} v_y(1 + \delta_K U^h_{i+1})z_{i+1} \\
&= \frac{1}{2}kv_y^2(1-a)(1 - \delta_D U^h_{i+1})(1 + \delta_K U^h_{i+1})z_{i+1}^2
\end{aligned} \tag{A.8}$$

The increment of the dissipated energy can be obtained by substituting Eqs.
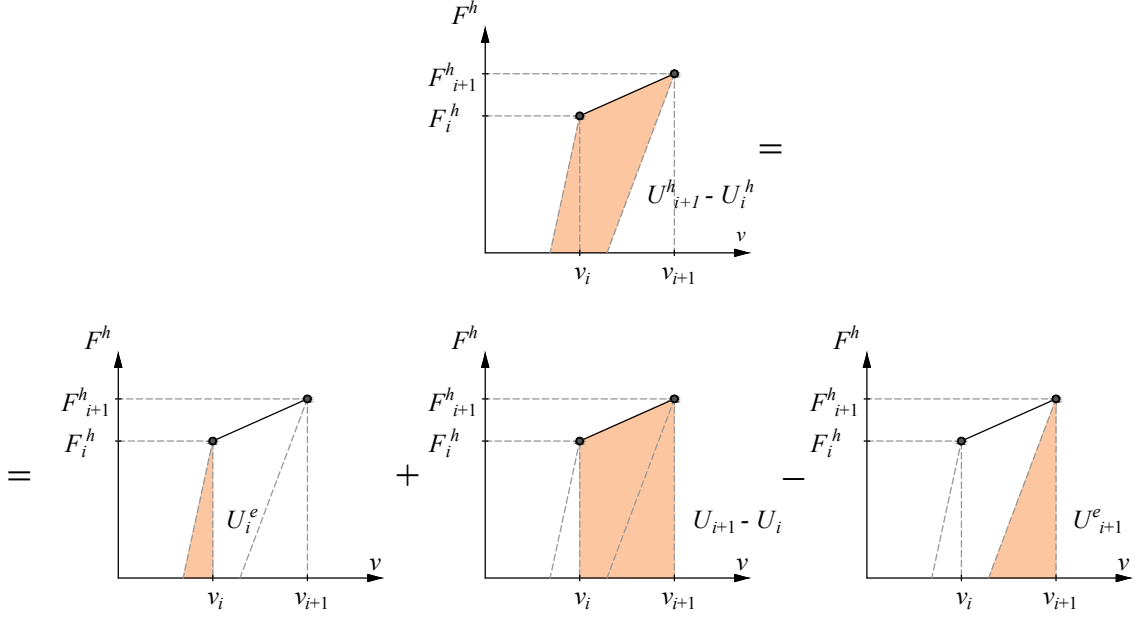
Figure A.1: Dissipated energy increment

A.6, A.7 and A.8 into Eq. A.5. After some manipulations, it follows:

$$
\begin{aligned}
U_{i+1}^h - U_i^h = &\frac{1}{2}kv_y^2(1-a) \cdot [(\delta_D + \delta_K)(U_{i+1}^h - U_i^h)z_i z_{i+1} + \\
&+ (z_i + z_{i+1} - \delta_D U_i^h z_i - \delta_D U_{i+1}^h z_{i+1})(u_{i+1}^p - u_i^p)]
\end{aligned}
\tag{A.9}
$$

and solving with respect to U_{i+1}^h:

$$
\begin{aligned}
U_{i+1}^h = &\frac{U_i^h + \frac{1}{2} k v_y^2 (1-a)\{[-(\delta_D + \delta_K)z_{i+1} - \delta_D(u_{i+1}^p - u_i^p)]z_i U_i^h}{1 + \frac{1}{2} k v_y^2 (1-a)[-(\delta_D + \delta_K)z_i + \delta_D(u_{i+1}^p - u_i^p)]z_{i+1}} + \\
&+ \frac{(z_i + z_{i+1})(u_{i+1}^p - u_i^p)\}}{1 + \frac{1}{2} k v_y^2 (1-a)[-(\delta_D + \delta_K)z_i + \delta_D(u_{i+1}^p - u_i^p)]z_{i+1}}
\end{aligned}
\tag{A.10}
$$

It can be observed that the dissipated energy at time step $i + 1$ can be alternatively obtained by means of numerical calculation of the integral on the RHS of Eq. 3.43. However, using Eq. A.10 is preferable as this preserves the energy balance expressed by Eqs. A.3, A.4, from which it is derived, whereas the numerical evaluation of Eq. 3.43 in general does not. Finally, the hysteretic force at time

171

step $i + 1$ is calculated as:

$$F_{i+1}^h = (1 - \delta_D U_{i+1}^h)(1 - a)\, k_i\, v_y\, z_{i+1} \tag{A.11}$$

The previous equations apply when the non-dimensional total displacement u_{i+1} is known. However, in practical numerical analysis, the dimensional total displacement v_{i+1} is known, and u_{i+1} shall be calculated starting from v_{i+1}.

In case of pure damage ($\delta_D > 0, \delta_K = 0$), the calculation of u_{i+1} is straightforward, recalling Eq. 3.5:

$$u_{i+1} = \frac{v_{i+1}}{v_y} \tag{A.12}$$

Instead, in the general case of damage and flexibility increase ($\delta_D > 0, \delta_K \neq 0$), the relationship between u_{i+1} and v_{i+1} involves U_{i+1}^h, which is unknown. This problem can be overcome by writing v_{i+1} according to Eq. 3.28 as:

$$v_{i+1} = v_y[(1 + \delta_K U_{i+1}^h)z_{i+1} + u_{i+1}^p] \tag{A.13}$$

and expressing the quantities on the RHS as functions of u_{i+1}. After some manipulations, this results in an algebraic equation of third-degree in u_{i+1}:

$$a_0 u_{i+1}^3 + a_1 u_{i+1}^2 + a_2 u_{i+1} + a_3 = 0 \tag{A.14}$$

The derivation of Eq. A.14, along with the coefficients a_0, a_1, a_2, a_3, is reported in Section A.2. After dividing by a_0, Eq. A.14 becomes:

$$u_{i+1}^3 + b_1 u_{i+1}^2 + b_2 u_{i+1} + b_3 = 0 \tag{A.15}$$

where $b_1 = a_1/a_0; b_2 = a_2/a_0; b_3 = a_3/a_0$.

Setting:

$$u_{i+1} = \zeta - \frac{b_1}{3} \tag{A.16}$$

Eq. A.15 can be rewritten as:

$$\zeta^3 + \left(b_2 - \frac{b_1^2}{3}\right)\zeta + 2\left(\frac{b_1}{3}\right)^3 - \frac{b_1 b_2}{3} + b_3 = 0 \tag{A.17}$$

By defining:

$$r = b_2 - \frac{b_1^2}{3}; \quad s = 2\left(\frac{b_1}{3}\right)^3 - \frac{b_1 b_2}{3} + b_3 \tag{A.18}$$

Eq. A.17 can be rewritten as:

$$\zeta^3 + r\zeta + s = 0 \tag{A.19}$$

Three different cases may occur, depending on the sign of the discriminant:

$$\Delta = \left(\frac{s}{2}\right)^2 + \left(\frac{r}{3}\right)^3 \tag{A.20}$$

a) $\Delta > 0$

The equation has one real root and two complex conjugate roots. The real root is:

$$\zeta = \sqrt[3]{-\frac{s}{2} + \sqrt{\left(\frac{s}{2}\right)^2 + \left(\frac{r}{3}\right)^3}} + \sqrt[3]{-\frac{s}{2} - \sqrt{\left(\frac{s}{2}\right)^2 + \left(\frac{r}{3}\right)^3}} \tag{A.21}$$

giving:

$$u_{i+1} = \sqrt[3]{-\frac{s}{2} + \sqrt{\left(\frac{s}{2}\right)^2 + \left(\frac{r}{3}\right)^3}} + \sqrt[3]{-\frac{s}{2} - \sqrt{\left(\frac{s}{2}\right)^2 + \left(\frac{r}{3}\right)^3}} - \frac{b_1}{3} \tag{A.22}$$

b) $\Delta = 0$

The equation has a single real root:

$$u_{i+1,1} = -2\sqrt[3]{\frac{s}{2}} - \frac{b_1}{3} \tag{A.23}$$

and a double real root:

$$u_{i+1,2} = u_{i+1,3} = \sqrt[3]{\frac{s}{2}} - \frac{b_1}{3} \tag{A.24}$$

c) $\Delta < 0$

The equation has three distinct real roots. After transforming the complex number $(-s/2, \sqrt{-\Delta})$ into its trigonometric form $(\rho \cos \theta, \rho \sin \theta)$, where $\rho \cos \theta = -s/2$, $\rho \sin \theta = \sqrt{-\Delta}$, the roots are given by:

$$u_{i+1,1} = 2\sqrt{-\frac{r}{3}} \cos \frac{\theta}{3} - \frac{b_1}{3} \tag{A.25}$$

$$u_{i+1,2} = 2\sqrt{-\frac{r}{3}} \cos \frac{\theta + 2\pi}{3} - \frac{b_1}{3} \tag{A.26}$$

$$u_{i+1,3} = 2\sqrt{-\frac{r}{3}} \cos \frac{\theta + 4\pi}{3} - \frac{b_1}{3} \tag{A.27}$$

The cases b) and c) only occur for $\delta_D > 0$. In these cases, having more than one real solution, only one satisfies the bounds on U_h and z:

$$0 \le U_{i+1}^h < \frac{1}{\delta_D}; \quad |z_{i+1}| \le 1 \tag{A.28}$$

A.1 Special cases

a) $a_0 = 0, a_1 \ne 0$

The third-degree equation degenerates into a second-degree equation, which has the root:

$$u_{i+1} = \frac{-\frac{a_2}{2} - \sqrt{(\frac{a_2}{2})^2 - a_1 a_3}}{a_3} \tag{A.29}$$

whereas the root:

$$u_{i+1} = \frac{-\frac{a_2}{2} + \sqrt{(\frac{a_2}{2})^2 - a_1 a_3}}{a_3} \tag{A.30}$$

has no physical meaning, as this gives an indeterminate value of the dissipated energy $U_{i+1}^h = 0/0$. The case $a_0 = 0, a_1 \ne 0$ occurs when $\delta_K > -\delta_D$ in elastic unloading branches, where $\kappa_i = 1$. In this case, as an alternative to the solution of the second-degree equation, it can be noticed that the

dissipated energy and the plastic displacement are constant, resulting as:

$$U_{i+1}^h = U_i^h; \quad u_{i+1}^p = u_i^p \tag{A.31}$$

It follows:

$$v_{i+1} = v_y[(1 + \delta_K U_i^h)z_{i+1} + u_i^p] \tag{A.32}$$

Solving with respect to z_{i+1}:

$$z_{i+1} = \frac{\frac{v_{i+1}}{v_y} - u_i^p}{1 + \delta_K U_i^h} \tag{A.33}$$

provides:

$$u_{i+1} = z_{i+1} + u_i^p = \frac{\frac{v_{i+1}}{v_y} + \delta_K U_i^h u_i^p}{1 + \delta_K U_i^h} \tag{A.34}$$

which can be shown to be equivalent to Eq. *A.29*.

b) $a_0 = 0, a_1 = 0$

The solution is straightforward and it results:

$$u_{i+1} = -\frac{a_3}{a_2} \tag{A.35}$$

This case corresponds to $\delta_K = -\delta_D$ (strength decay) in elastic unloading branches. As an alternative to Eq. *A.35*, Eqs. *A.33*, *A.34* can be used.

This case also occurs at the first step of the analysis $i+1 = 1$, where $U_1^h = 0$. The following equations hold:

$$u_0 = u_0^p = z_0 = 0 \tag{A.36}$$

$$\kappa_0 = 1 \tag{A.37}$$

$$z_1 = \kappa_0 u_1 = u_1 \tag{A.38}$$

$$u_1^p = u_1 - z_1 = 0 \tag{A.39}$$

$$U_1^h = 0 \tag{A.40}$$

$$u_1 = \frac{v_1}{v_y} \tag{A.41}$$

which can be shown to be equivalent to Eq. $A.35$ at step $i + 1 = 1$.

A.2 Derivation of the non-dimensional displacement solution

The derivation of the third-degree algebraic equation in Eq. A.14 which arrives from Eq. A.13 is given here.

The increment of non-dimensional plastic displacement from step i to step $i+1$ is:

$$u_{i+1}^p - u_i^p = u_{i+1} - z_{i+1} - u_i + z_i = (1 - \kappa_i)(u_{i+1} - u_i) \tag{A.42}$$

The displacement at step $i + 1$ can be written, according to Eq. 3.28:

$$
\begin{aligned}
v_{i+1} &= v_y[(1 + \delta_K U_{i+1}^h)z_{i+1} + u_{i+1}^p] \\
&= v_y(u_{i+1} + \delta_K U_{i+1}^h z_{i+1})
\end{aligned} \tag{A.43}
$$

Recalling Eq. $A.10$, and setting:

$$
\begin{aligned}
B =&U_i^h + \frac{1}{2}\,k\,v_y^2(1 - a)\{[-(\delta_D + \delta_K)z_{i+1} - \delta_D(u_{i+1}^p - u_i^p)]z_i U_i^h + \\
&+ (z_i + z_{i+1})(u_{i+1}^p - u_i^p)\}
\end{aligned} \tag{A.44}
$$

$$C = 1 + \frac{1}{2}\,k\,v_y^2(1 - a)[-(\delta_D + \delta_K)z_i + \delta_D(u_{i+1}^p - u_i^p)]z_{i+1} \tag{A.45}$$

the displacement at step $i + 1$ can be written as:

$$v_{i+1} = v_y\left(u_{i+1} + \delta_K z_{i+1}\frac{B}{C}\right) \tag{A.46}$$

or:

$$v_{i+1}C = v_y(u_{i+1}C + \delta_K z_{i+1}B) \tag{A.47}$$

After some manipulations, the term B can be written as:

$$B = G\,u_{i+1}^2 + H\,u_{i+1} + I \tag{A.48}$$

where:

$$G = \frac{1}{2}\,k\,v_y^2(1-a)\kappa_i(1-\kappa_i) \tag{A.49}$$

$$H = \frac{1}{2}\,k\,v_y^2(1-a)[-(\delta_D + \kappa_i\delta_K)z_iU_i^h + 2(1-\kappa_i)(z_i - \kappa_iu_i)] \tag{A.50}$$

$$I = U_i^h + \frac{1}{2}\,k\,v_y^2(1-a)\{[-(\delta_D + \delta_K)(z_i - \kappa_iu_i) + \delta_D(1-\kappa_i)u_i]z_iU_i^h - \\ - (1-\kappa_i)(2z_i - \kappa_iu_i)u_i\} \tag{A.51}$$

and the term C:

$$C = L\,u_{i+1}^2 + M\,u_{i+1} + N \tag{A.52}$$

where:

$$L = \frac{1}{2}\,k\,v_y^2(1-a)\delta_D\kappa_i(1-\kappa_i) = \delta_D G \tag{A.53}$$

$$M = \frac{1}{2}\,k\,v_y^2(1-a)[\delta_D(1-\kappa_i)(z_i - 2\kappa_iu_i) - (\delta_D + \delta_K)\kappa_iz_i] \tag{A.54}$$

$$N = 1 - \frac{1}{2}\,k\,v_y^2(1-a)[\delta_D(1-\kappa_i)u_i + (\delta_D + \delta_K)z_i](z_i - \kappa_iu_i) \tag{A.55}$$

Eq. $A.47$ becomes:

$$\begin{aligned} v_{i+1}C &= v_y\{L\,u_{i+1}^3 + M\,u_{i+1}^2 + N\,u_{i+1} + \delta_K[z_i + \kappa_i(u_{i+1} - u_i)]\cdot \\ &\quad \cdot (G\,u_{i+1}^2 + H\,u_{i+1} + I)\} = \\ &= v_y\{(L + \delta_K G\,\kappa_i)u_{i+1}^3 + [M + \delta_K G(z_i - \kappa_iu_i) + \delta_K H\,\kappa_i]u_{i+1}^2 + \\ &\quad + [N + \delta_K H\,(z_i - \kappa_iu_i) + \delta_K I\,\kappa_i]u_{i+1} + \delta_K I\,(z_i - \kappa_iu_i)\} \end{aligned} \tag{A.56}$$

which is a third-degree algebraic equation in the unknown u_{i+1}:

$$a_0u_{i+1}^3 + a_1u_{i+1}^2 + a_2u_{i+1} + a_3 = 0 \tag{A.57}$$

with:

$$a_0 = -v_y(L + \delta_K G\,\kappa_i) \tag{A.58}$$

$$a_1 = L\,v_{i+1} - v_y\{M + \delta_K[G\,(z_i - \kappa_i u_i) + H\,\kappa_i]\} \tag{A.59}$$

$$a_2 = M\,v_{i+1} - v_y\{N + \delta_K[H\,(z_i - \kappa_i u_i) + I\,\kappa_i]\} \tag{A.60}$$

$$a_3 = N\,v_{i+1} - v_y\delta_K I\,(z_i - \kappa_i u_i) \tag{A.61}$$

Appendix B

Elastic-plastic model with flexibility increase

The relation between the total non-dimensional displacement u and the elastic non-dimensional displacement z, expressed in its general form in Eq. 3.8 through the derivative of z with respect to u, depends on the particular hysteresis considered, as stated in Chapter 3. This means that the Bouc-Wen model is not the only which the flexibility increase formulation can be applied to.

In the following, the modification to the elastic displacement defined in the flexibility increase procedure is applied to an elastic-plastic case with hardening, considering the following equation describing the costitutive law:

$$\frac{\mathrm{d}z}{\mathrm{d}u} = 1 - [1 + \text{sign}(|z| - 1)]\langle\text{sign}(z\dot{v})\rangle \tag{B.1}$$

with $|z| \leq 1$, and where the Macaulay's brackets $\langle\bullet\rangle$ evaluate the positive part of the argument.

This model with hardening is usually employed to describe the behavior of metals characterized by a sharp transition from elastic to plastic state, due to the sliding of dislocations in crystal lattice, or the contact with friction between two bodies, with yielding shear force depending on normal force. Decay of friction could occur because of the abrasion of contact surfaces.

Following Eq. B.1, the elastic-perfectly plastic model can be obtained by

setting $a = 0$ in Eqs. 3.2, 3.3. The plastic state occurs when:

$$|z| = 1; \quad z\dot{v} > 0 \qquad \text{(B.2)}$$

resulting in $\mathrm{d}z/\mathrm{d}u = 0$, indicating that no increment of elastic displacement and force occurs. All the other conditions, namely:

$$|z| < 1 \qquad \text{(B.3)}$$

or:

$$|z| = 1; \quad z\dot{v} < 0 \qquad \text{(B.4)}$$

result in $\mathrm{d}z/\mathrm{d}u = 1$, indicating that the system is elastic. The derivative $\mathrm{d}z/\mathrm{d}u$ could assume either the values 0 or 1, when the state is plastic or elastic, respectively. In both cases, according to Eqs. *A.49, A.53, A.58*, $G = 0$, $L = 0$, $a_0 = 0$, as shown in Section A.2, respectively, and Eq. *A.14* reduces to a second-degree equation, as in Section A.1. At the transition from elastic to plastic state, the forward Euler formula generally provides $|z_{i+1}| > 1$. This problem can be overcome by modifying Eq. 3.47 at the transition, as follows:

$$z_{i+1} = \mathrm{sign}\{z_i + f[z_i, \mathrm{sign}(v_{i+1} - v_i)](u_{i+1} - u_i)\} \qquad \text{(B.5)}$$

The elastic-plastic model with hardening satisfies both thermodynamic admissibility and Drucker's postulate. When introducing damage and flexibility increase, the general results of Sections 3.3.2 and 3.3.4 apply. In particular, thermodynamic admissibility is expressed by Eq. 3.51, or equivalently by Eq. 3.52, and the additional constraints on the parameters by Eqs. 3.58, 3.60. Since the elastic-plastic model with hardening satisfies Drucker's postulate, the model with flexibility increase does as well, whereas the model with damage in general does not.

A parametric analysis is performed in order to explore the performance of the damage and flexibility increase parameters. The hysteretic response of the system, whose mechanical parameters are listed in Tab. B.1, is evaluated considering an applied quasi-static cyclic forcing action made of three cycles of increasing ampli-

Table B.1: Mechanical parameters for the elastic-plastic cases

a	k	v_y
$-$	kN/m	m
0.1	20000	0.01

(a)

(b)

(c)

(d)
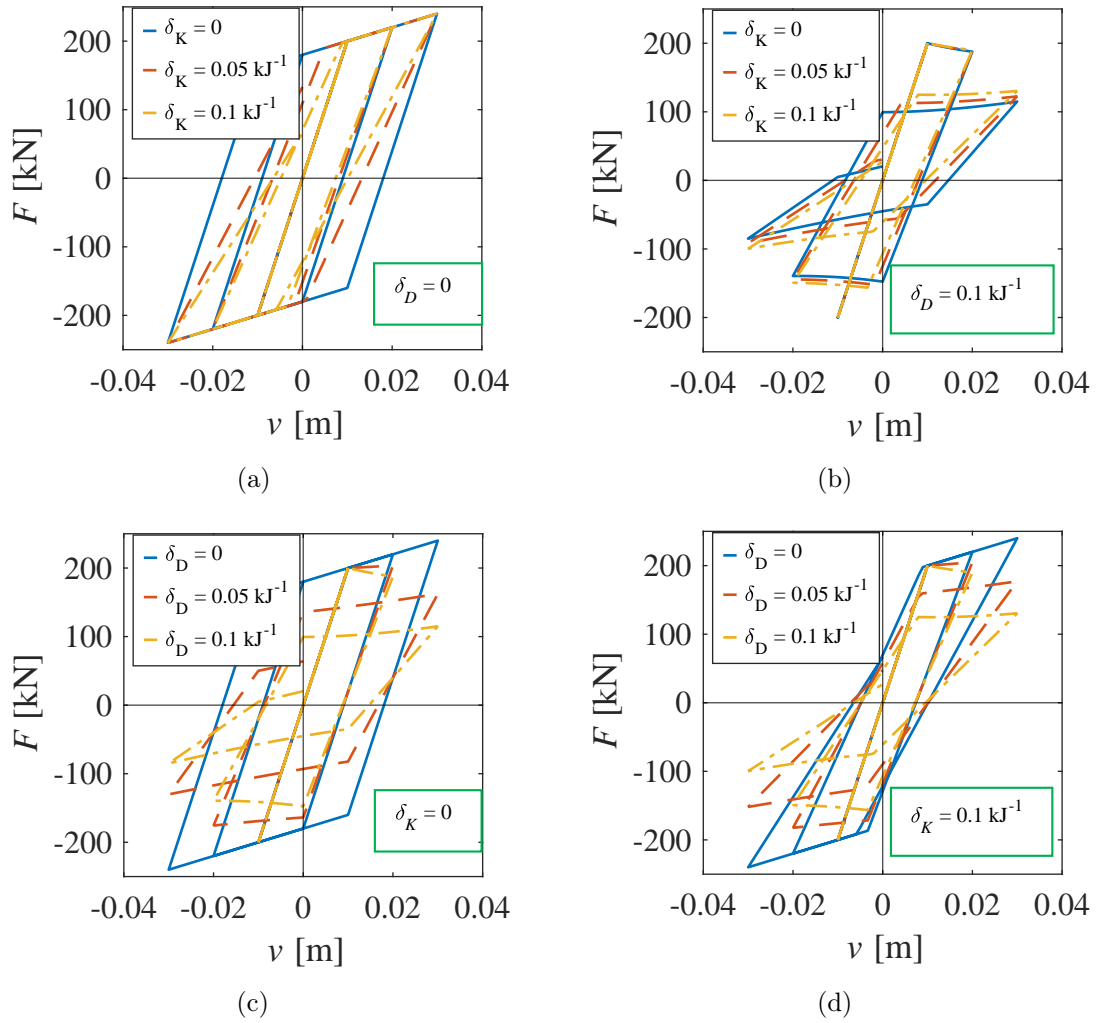
Figure B.1: Elastic-plastic responses varying δ_D and δ_K

tude, in order to highlight the progression of damage and flexibility increase with

181

the increase of the number of cycles, and the displacement history experienced by the system. In each analysis, one of the two scalar parameters, δ_K and δ_D, varies, while the other is kept constant, with the aim of separately evaluating their effect. The cyclic response in terms of displacement and restoring force is reported in Fig. B.1. When the parameter δ_D is kept constant and equal to 0, while δ_K varies (Fig. B.1 (a)), the restoring force peaks at the assigned displacement are constant. The higher the parameter δ_K, the lower the area of the displacement – force cycles, and consequently the dissipated energy, when the number of the experienced cycles increases. When δ_D is equal to $0.1\,\text{kJ}^{-1}$ (Fig. B.1 (b)), the combined effect of damage and flexibility increase can be perceived, influencing both the strength and stiffness degradation. When the flexibility increase parameter is kept constant and set equal to 0 (Fig. B.1 (c)), the effect of damage can be analyzed and a strong influence on the post-yielding stiffness can be detected when δ_D is incremented, which reaches a negative slope. Finally, when δ_K is equal to $0.1\,\text{kJ}^{-1}$ (Fig. B.1 (d)), thinner cycles can be seen compared to case (c) and the post-yielding stiffness reaches a negative slope when δ_D is incremented.

Bibliography

Abrams, D.P., AlShawa, O., Lourenço, P.B., Sorrentino, L., 2017. Out-of-plane seismic response of unreinforced masonry walls: conceptual discussion, research needs, and modeling issues. International Journal of Architectural Heritage 11, 22–30.

Addessi, D., Ciampi, V., 2006. A regularized force-based beam element with a damage–plastic section constitutive law. International Journal for Numerical Methods in Engineering 70, 610–629.

Addessi, D., Gatta, C., Nocera, M., Liberatore, D., 2021. Nonlinear dynamic analysis of a masonry arch bridge accounting for damage evolution. Geosciences 11, 343.

Addessi, D., Liberatore, D., Masiani, R., 2015. Force-based beam finite element (fe) for the pushover analysis of masonry buildings. International Journal of Architectural Heritage 9, 231–243.

Addessi, D., Liberatore, D., Nocera, M., 2022. Damaging behavior of masonry arch bridges: Analysis of 'ponte delle torri'in spoleto, italy. Journal of Earthquake Engineering 26, 449–474.

Addessi, D., Marfia, S., Sacco, E., 2002. A plastic nonlocal damage model. Computer methods in applied mechanics and engineering 191, 1291–1310.

Addessi, D., Mastrandrea, A., Sacco, E., 2014. An equilibrated macro-element for nonlinear analysis of masonry structures. Engineering Structures 70, 82–93.

183

Addessi, D., Sacco, E., 2012. A multi-scale enriched model for the analysis of masonry panels. International Journal of Solids and Structures 49, 865–880.

Addessi, D., Sacco, E., 2016. Nonlinear analysis of masonry panels using a kinematic enriched plane state formulation. International Journal of Solids and Structures 90, 194–214.

Addessi, D., Sacco, E., Paolone, A., 2010. Cosserat model for periodic masonry deduced by nonlinear homogenization. European Journal of Mechanics-A/Solids 29, 724–737.

Alexandris, A., Protopapa, E., Psycharis, I., 2004. Collapse mechanisms of masonry buildings derived by the distinct element method, in: Proceedings of the 13th world conference on earthquake engineering, p. 60.

Alfano, G., Rosati, L., Valoroso, N., 2000. A numerical strategy for finite element analysis of no-tension materials. International journal for numerical methods in engineering 48, 317–350.

Angelillo, M., 1994. A finite element approach to the study of no-tension structures. Finite elements in analysis and design 17, 57–73.

Anthoine, A., 1995. Derivation of the in-plane elastic characteristics of masonry through homogenization theory. International journal of solids and structures 32, 137–163.

Anthoine, A., Magonette, G., Magenes, G., 1995. Shear-compression testing and analysis of brick masonry walls. Proceedings of the 10th European conference on earthquake engineering, Balkema, Rotterdam (The Netherlands) , 1657–1662.

Archer, J.S., 1965. Consistent matrix formulations for structural analysis using finite-element techniques. AIAA journal 3, 1910–1918.

Atkinson, R., Noland, J., 1983. A proposed failure theory for brick masonry in compression, in: Proc., 3rd Canadian Masonry Symp, pp. 5–1.

Baber, T.T., Noori, M.N., 1985. Random vibration of degrading, pinching systems. Journal of Engineering Mechanics 111, 1010–1026.

Baber, T.T., Wen, Y.K., 1981. Random vibration of hysteretic degrading systems. Journal of the Engineering Mechanics Division 107, 1069–1087.

Bacigalupo, A., Gambarotta, L., 2012. Computational two-scale homogenization of periodic masonry: characteristic lengths and dispersive waves. Computer Methods in Applied Mechanics and Engineering 213, 16–28.

Backes, H., 1985. On the behavior of masonry under tension in the direction of the bed joints. Aachen University of Technology .

Baggio, C., Trovalusci, P., et al., 2000. Collapse behaviour of three-dimensional brick-block systems using non-linear programming. Structural Engineering and Mechanics 10, 181.

Belmouden, Y., Lestuzzi, P., 2009. An equivalent frame model for seismic analysis of masonry and reinforced concrete buildings. Construction and building materials 23, 40–53.

Berti, M., Salvatori, L., Orlando, M., Spinelli, P., 2017. Unreinforced masonry walls with irregular opening layouts: reliability of equivalent-frame modelling for seismic vulnerability assessment. Bulletin of earthquake engineering 15, 1213–1239.

Berto, L., Saetta, A., Scotta, R., Vitaliani, R., 2002. An orthotropic damage model for masonry structures. International Journal for Numerical Methods in Engineering 55, 127–157.

Betti, M., Vignoli, A., 2011. Numerical assessment of the static and seismic behaviour of the basilica of santa maria all'impruneta (italy). Construction and Building Materials 25, 4308–4324.

Bouc, R., 1971. A mathematical model for hysteresis. Acta Acustica united with Acustica 24, 16–25.

Bracchi, S., Galasco, A., Penna, A., 2021. A novel macroelement model for the nonlinear analysis of masonry buildings. part 1: axial and flexural behavior. Earthquake Engineering & Structural Dynamics 50, 2233–2252.

Bracchi, S., Penna, A., 2021. A novel macroelement model for the nonlinear analysis of masonry buildings. part 2: shear behavior. Earthquake Engineering & Structural Dynamics 50, 2212–2232.

Braga, F., Liberatore, D., et al., 1990. A finite element for the analysis of the response of masonry buildings under seismic actions, in: Proc. of the 5th North American Masonry Conference, The Masonry Society. pp. 201–212.

Brencich, A., Lagomarsino, S., 1998. A macroelement dynamic model for masonry shear walls. Computer methods in structural masonry 4, 67–75.

Bruggi, M., Taliercio, A., 2015. Analysis of no-tension structures under monotonic loading through an energy-based method. Computers & Structures 159, 14–25.

Bruggi, M., Taliercio, A., et al., 2018. Analysis of 3d no-tension masonry-like walls, in: European Mechanics Society ESMC 2018 Bologna-Book of Abstracts.

Calderini, C., Cattari, S., Lagomarsino, S., 2009. In-plane strength of unreinforced masonry piers. Earthquake engineering & structural dynamics 38, 243–267.

Caliò, I., Marletta, M., Pantò, B., 2012. A new discrete element model for the evaluation of the seismic behaviour of unreinforced masonry buildings. Engineering Structures 40, 327–338.

Camata, G., Marano, C., Sepe, V., Spacone, E., Siano, R., Petracca, M., Roca, P., Pelà, L., 2022. Validation of non-linear equivalent-frame models for irregular masonry walls. Engineering Structures 253, 113755.

Camilletti, D., Cattari, S., Lagomarsino, S., 2018. In plane seismic response of irregular urm walls through equivalent frame and finite element models, in: Proceedings of the 16th European conference on earthquake engineering. Thessaloniki, Greece, pp. 1–12.

Carocci, C.F., 2002. Guidelines for the safety and preservation of historical centres in seismic areas, in: Actas del 6° Coloquio Internacional de las Ciudades del Patrimonio Mundial, pp. p–80.

Casciati, F., 1989. Stochastic dynamics of hysteretic media. Structural safety 6, 259–269.

Casolo, S., 2006. Macroscopic modelling of structured materials: relationship between orthotropic cosserat continuum and rigid elements. International Journal of Solids and Structures 43, 475–496.

Cattari, S., Camilletti, D., D'Altri, A.M., Lagomarsino, S., 2021. On the use of continuum finite element and equivalent frame models for the seismic assessment of masonry walls. Journal of Building Engineering 43, 102519.

Cattari, S., Camilletti, D., Lagomarsino, S., Bracchi, S., Rota, M., Penna, A., 2018. Masonry italian code-conforming buildings. part 2: nonlinear modelling and time-history analysis. Journal of Earthquake Engineering 22, 2010–2040.

Cavalagli, N., Cluni, F., Gusella, V., 2011. Strength domain of non-periodic masonry by homogenization in generalized plane state. European Journal of Mechanics-A/Solids 30, 113–126.

Chácara, C., Cannizzaro, F., Pantò, B., Caliò, I., Lourenço, P.B., 2018. Assessment of the dynamic response of unreinforced masonry structures using a macroelement modeling approach. Earthquake Engineering & Structural Dynamics 47, 2426–2446.

Charalampakis, A.E., Koumousis, V.K., 2008a. Identification of Bouc-Wen hysteretic systems by a hybrid evolutionary algorithm. Journal of Sound and Vibration 314, 571–585.

Charalampakis, A.E., Koumousis, V.K., 2008b. On the response and dissipated energy of Bouc-Wen hysteretic model. Journal of Sound and Vibration 309, 887–895.

Charalampakis, A.E., Koumousis, V.K., 2009. A Bouc-Wen model compatible with plasticity postulates. Journal of Sound and Vibration 322, 954–968.

Chen, S.Y., Moon, F., Yi, T., 2008. A macroelement for the nonlinear analysis of in-plane unreinforced masonry piers. Engineering Structures 30, 2242–2252.

Cheng, J., Shing, P.B., 2022. A beam-column element for modeling nonlinear flexural and shear behaviors of reinforced masonry walls. Earthquake Engineering & Structural Dynamics 51, 1918–1942.

Constantinou, M.C., Adnane, M., 1987. Dynamics of Soil-base-isolated-structure Systems: Evaluation of two models for yielding systems. Drexel University.

Cundall, P.A., 1971. A computer model for simulating progressive, large-scale movement in blocky rock system, in: Proceedings of the international symposium on rock mechanics, pp. 129–136.

D'Altri, A.M., Messali, F., Rots, J., Castellazzi, G., de Miranda, S., 2019. A damaging block-based model for the analysis of the cyclic behaviour of full-scale masonry structures. Engineering Fracture Mechanics 209, 423–448.

Damiola, M., Esposito, R., Messali, F., Rots, J.G., 2018. Quasi-static cyclic two-way out-of-plane bending tests and analytical models comparison for urm walls, in: 10th international masonry conference (IMC). Milan, Italy.

De Bellis, M.L., Addessi, D., 2011. A cosserat based multi-scale model for masonry structures. International Journal for Multiscale Computational Engineering 9.

Degli Abbati, S., D'Altri, A.M., Ottonelli, D., Castellazzi, G., Cattari, S., de Miranda, S., Lagomarsino, S., 2019. Seismic assessment of interacting structural units in complex historic masonry constructions by nonlinear static analyses. Computers & Structures 213, 51–71.

Dhanasekar, M., Page, A., Kleeman, P., 1985. The failure of brick masonry under biaxial stresses. Proceedings of the Institution of Civil Engineers 79, 295–313.

Di Re, P., Addessi, D., Paolone, A., 2019. Mixed beam formulation with cross-section warping for dynamic analysis of thin-walled structures. Thin-Walled Structures 141, 554–575.

Doherty, K., Griffith, M.C., Lam, N., Wilson, J., 2002. Displacement-based seismic analysis for out-of-plane bending of unreinforced masonry walls. Earthquake engineering & structural dynamics 31, 833–850.

Dolce, M., 1991. Schematizzazione e modellazione degli edifici in muratura soggetti ad azioni sismiche. Industria delle costruzioni 25, 44–57.

Drucker, D.C., 1950. Some implications of work hardening and ideal plasticity. Quarterly of Applied Mathematics 7, 411–418.

Drysdale, R., Vanderkeyl, R., Hamid, A., 1982. Shear strength of brick masonry joints, in: Proc. 5 th Int. Brick Masonry Conf.(VIBMaC) held in Washington, DC, 5-10 Oct., 1979. Edited by J. A. Wintz and A. H. Yorkdale. McLean, Virginia, p. 106.

Dvorak, G.J., 1992. Transformation field analysis of inelastic composite materials. Proceedings of the Royal Society of London. Series A: Mathematical and Physical Sciences 437, 311–327.

D'Altri, A.M., Sarhosis, V., Milani, G., Rots, J., Cattari, S., Lagomarsino, S., Sacco, E., Tralli, A., Castellazzi, G., de Miranda, S., 2020. Modeling strategies for the computational analysis of unreinforced masonry structures: review and classification. Archives of computational methods in engineering 27, 1153–1185.

Elyamani, A., Roca, P., Caselles, O., Clapes, J., 2017. Seismic safety assessment of historical structures using updated numerical models: The case of mallorca cathedral in spain. Engineering Failure Analysis 74, 54–79.

Erlicher, S., Bursi, O.S., 2008. Bouc-Wen-type models with stiffness degradation: thermodynamic analysis and applications. Journal of engineering mechanics 134, 843–855.

Erlicher, S., Point, N., 2004. Thermodynamic admissibility of Bouc-Wen type hysteresis models. Comptes rendus mecanique 332, 51–57.

Gambarotta, L., Lagomarsino, S., 1996. On dynamic response of masonry panels, in: Proceedings of National Conference on Masonry Mechanics between Theory and Practice, Messina, Italy.

Gambarotta, L., Lagomarsino, S., 1997. Damage models for the seismic response of brick masonry shear walls. part i: the mortar joint model and its applications. Earthquake engineering & structural dynamics 26, 423–439.

Ganz, H., Thürlimann, B., 1982. Tests on the biaxial strength of masonry. Rep. No. 7502 3.

Gatta, C., Addessi, D., Vestroni, F., 2018. Static and dynamic nonlinear response of masonry walls. International Journal of Solids and Structures 155, 291–303.

Gatta, C., et al., 2019. Masonry nonlinear response: modeling and analysis of the effects of damaging mechanisms .

Gattulli, V., Antonacci, E., Vestroni, F., 2013. Field observations and failure analysis of the basilica s. maria di collemaggio after the 2009 l'aquila earthquake. Engineering failure analysis 34, 715–734.

Giuffrè, A., 1991. Letture sulla meccanica delle murature storiche. .

Giuffrè, A., 1994. Seismic safety and strengthening of historical buildings and urban fabrics, in: Proceedings of the 10th World Conference on Earthquake Engineering, pp. 6583–6596.

Griffith, M.C., Lam, N.T., Wilson, J.L., Doherty, K., 2004. Experimental investigation of unreinforced brick masonry walls in flexure. Journal of Structural Engineering 130, 423–432.

Griffith, M.C., Vaculik, J., Lam, N., Wilson, J., Lumantarna, E., 2007. Cyclic testing of unreinforced masonry walls in two-way bending. Earthquake Engineering & Structural Dynamics 36, 801–821.

Heyman, J., 1966. The stone skeleton. International Journal of solids and structures 2, 249–279.

Hilsdorf, H.K., 1969. Investigation into the failure mechanism of brick masonry loaded in axial compression. Designing engineering and constructing with masonry products , 34–41.

Ismail, M., Ikhouane, F., Rodellar, J., 2009. The hysteresis Bouc-Wen model, a survey. Archives of computational methods in engineering 16, 161–188.

Jirásek, M., 2011. Damage and smeared crack models, in: Numerical modeling of concrete cracking. Springer, pp. 1–49.

Kachanov, L., 1958. Rupture time under creep conditions. Izv. Akad. Nauk SSSR 8, 26–31.

Kaushik, H.B., Rai, D.C., Jain, S.K., 2007. Stress-strain characteristics of clay brick masonry under uniaxial compression. Journal of materials in Civil Engineering 19, 728–739.

Kottari, A.K., Charalampakis, A.E., Koumousis, V.K., 2014. A consistent degrading Bouc-Wen model. Engineering Structures 60, 235–240.

Lagomarsino, S., Cattari, S., Angiolilli, M., Bracchi, S., Rota, M., Penna, A., 2023. Modelling and seismic response analysis of existing urm structures. part 2: Archetypes of italian historical buildings. Journal of Earthquake Engineering 27, 1849–1874.

Lagomarsino, S., Penna, A., Galasco, A., Cattari, S., 2013. Tremuri program: an equivalent frame model for the nonlinear seismic analysis of masonry buildings. Engineering structures 56, 1787–1799.

Lee, J., Fenves, G.L., 1998. Plastic-damage model for cyclic loading of concrete structures. Journal of engineering mechanics 124, 892–900.

Leissa, A., Zhang, Z.d., 1983. On the three-dimensional vibrations of the cantilevered rectangular parallelepiped. The Journal of the Acoustical Society of America 73, 2013–2021.

Lemaitre, J., Chaboche, J.L., 1994. Mechanics of solid materials. Cambridge university press.

Lemos, J.V., 2007. Discrete element modeling of masonry structures. International Journal of Architectural Heritage 1, 190–213.

Leonetti, L., Greco, F., Trovalusci, P., Luciano, R., Masiani, R., 2018. A multiscale damage analysis of periodic composites using a couple-stress/cauchy multido-

main model: Application to masonry structures. Composites Part B: Engineering 141, 50–59.

Liberatore, D., Addessi, D., 2015. Strength domains and return algorithm for the lumped plasticity equivalent frame model of masonry structures. Engineering Structures 91, 167–181.

Liberatore, D., Addessi, D., Sangirardi, M., 2019. An enriched Bouc-Wen model with damage. European Journal of Mechanics-A/Solids 77, 103771.

Lloberas-Valls, O., Rixen, D.J., Simone, A., Sluys, L., 2012. Multiscale domain decomposition analysis of quasi-brittle heterogeneous materials. International Journal for Numerical Methods in Engineering 89, 1337–1366.

Løland, K., 1980. Continuous damage model for load-response estimation of concrete. Cement and Concrete research 10, 395–402.

Lourenço, P.B., 1998. Experimental and numerical issues in the modelling of the mechanical behaviour of masonry .

Lourénço, P.B., De Borst, R., Rots, J.G., 1997. A plane stress softening plasticity model for orthotropic materials. International Journal for Numerical Methods in Engineering 40, 4033–4057.

Lourenço, P.B., Rots, J.G., 1997. Multisurface interface model for analysis of masonry structures. Journal of engineering mechanics 123, 660–668.

Lubliner, J., 2008. Plasticity theory. Courier Corporation.

Lubliner, J., Oliver, J., Oller, S., Onate, E., 1989. A plastic-damage model for concrete. International Journal of solids and structures 25, 299–326.

Luciano, R., Sacco, E., 1997. Homogenization technique and damage model for old masonry material. International Journal of Solids and Structures 34, 3191–3208.

Ma, F., Zhang, H., Bockstedte, A., Foliente, G.C., Paevere, P.J., 2004. Parameter analysis of the differential model of hysteresis. J. Appl. Mech. 71, 342–349.

Magenes, G., 2006. Masonry building design in seismic areas: recent experiences and prospects from a european standpoint, in: 1st European conference on earthquake engineering and seismology, pp. 1–22.

Magenes, G., Calvi, G., Kingsley, G., et al., 1995. Seismic testing of a full-scale, two-story masonry building: test procedure and measured experimental response, in: Experimental and Numerical Investigation on a brick Masonry Building Prototype-Numerical Prediction of the Experiment, Report 3.0. Roma.

Magenes, G., Calvi, G.M., 1997. In-plane seismic response of brick masonry walls. Earthquake engineering & structural dynamics 26, 1091–1112.

Maier, G., Nappi, A., 1990. A theory of no-tension discretized structural systems. Engineering structures 12, 227–234.

Malomo, D., DeJong, M., 2021. A macro-distinct element model (m-dem) for out-of-plane analysis of unreinforced masonry structures. Engineering Structures 244, 112754.

Malomo, D., DeJong, M.J., 2022. A macro-distinct element model (m-dem) for simulating in-plane/out-of-plane interaction and combined failure mechanisms of unreinforced masonry structures. Earthquake Engineering & Structural Dynamics 51, 793–811.

Malomo, D., Pinho, R., Penna, A., 2018. Using the applied element method for modelling calcium silicate brick masonry subjected to in-plane cyclic loading. Earthquake Engineering & Structural Dynamics 47, 1610–1630.

Marfia, S., 2007. Modellazione del calcestruzzo fibrorinforzato .

Massart, T., Peerlings, R., Geers, M., 2007. An enhanced multi-scale approach for masonry wall computations with localization of damage. International journal for numerical methods in engineering 69, 1022–1059.

McNary, W.S., Abrams, D.P., 1985. Mechanics of masonry in compression. Journal of Structural Engineering 111, 857–870.

Messali, F., Ravenshorst, G., Esposito, R., Rots, J., 2017. Large-scale testing program for the seismic characterization of dutch masonry walls, in: Proceedings of 16th world conference on earthquake (WCEE), Santiago, Chile.

Milani, G., 2011. Simple lower bound limit analysis homogenization model for in-and out-of-plane loaded masonry walls. Construction and Building Materials 25, 4426–4443.

Milani, G., Valente, M., 2015. Failure analysis of seven masonry churches severely damaged during the 2012 emilia-romagna (italy) earthquake: Non-linear dynamic analyses vs conventional static approaches. Engineering Failure Analysis 54, 13–56.

Minga, E., Macorini, L., Izzuddin, B., Calio, I., 2020. 3d macroelement approach for nonlinear fe analysis of urm components subjected to in-plane and out-of-plane cyclic loading. Engineering Structures 220, 110951.

Molins, C., Roca, P., Barbat, A., 1998. Flexibility-based linear dynamic analysis of complex structures with curved-3d members. Earthquake engineering & structural dynamics 27, 731–747.

Naraine, K., Sinha, S., 1991. Cyclic behavior of brick masonry under biaxial compression. Journal of Structural Engineering 117, 1336–1355.

Naraine, K., Sinha, S., 1992. Stress-strain curves for brick masonry in biaxial compression. Journal of Structural Engineering 118, 1451–1461.

NTC, 2018. DMIT. Decreto del Ministro delle Infrastrutture e dei Trasporti, 17 gennaio 2018. Aggiornamento delle "Norme tecniche per le costruzioni". Gazzetta Ufficiale della Repubblica Italiana n. 42 del 20 febbraio 2018 .

Oliveira, D.V., Lourenço, P.B., 2004. Implementation and validation of a constitutive model for the cyclic behaviour of interface elements. Computers & structures 82, 1451–1461.

Orduña, A., Lourenço, P.B., 2005. Three-dimensional limit analysis of rigid blocks assemblages. part i: Torsion failure on frictional interfaces and limit analysis formulation. International Journal of Solids and Structures 42, 5140–5160.

Page, A., 1981. The biaxial compressive strength of brick masonry. Proceedings of the Institution of Civil Engineers 71, 893–906.

Page, A., 1983. The strength of brick masonry under biaxial tension-compression. International journal of masonry construction 3, 26–31.

Page, A.W., 1978. Finite element model for masonry. Journal of the Structural Division 104, 1267–1285.

Pantò, B., Cannizzaro, F., Caliò, I., Lourenço, P.B., 2017. Numerical and experimental validation of a 3d macro-model for the in-plane and out-of-plane behavior of unreinforced masonry walls. International Journal of Architectural Heritage 11, 946–964.

Parisi, F., Augenti, N., 2013. Seismic capacity of irregular unreinforced masonry walls with openings. Earthquake Engineering & Structural Dynamics 42, 101–121.

Pavanetto, M., Sbrogiò, L., Salvalaggio, M., Valluzzi, M.R., 2020. Equivalent frame modelling of an unreinforced masonry building in finite element environment, in: Proceedings of XXIV AIMETA Conference 2019 24, Springer. pp. 2006–2021.

Pelà, L., Aprile, A., Benedetti, A., 2009. Seismic assessment of masonry arch bridges. Engineering Structures 31, 1777–1788.

Pelà, L., Cervera, M., Roca, P., 2013. An orthotropic damage model for the analysis of masonry structures. Construction and Building Materials 41, 957–967.

Penna, A., Lagomarsino, S., Galasco, A., 2014. A nonlinear macroelement model for the seismic analysis of masonry buildings. Earthquake Engineering & Structural Dynamics 43, 159–179.

Peruch, M., Spacone, E., Camata, G., 2019. Nonlinear analysis of masonry structures using fiber-section line elements. Earthquake Engineering & Structural Dynamics 48, 1345–1364.

Van der Pluijm, R., 1993. Shear behaviour of bed joints .

van der Pluijm, R., 1997. Non-linear behaviour of masonry under tension. Heron 42, 25–54.

Van der Pluijm, R., Rutten, H., Ceelen, M., 2000. Shear behaviour of bed joints 12th international brick, in: Block Masonry Conference.

Quagliarini, E., Maracchini, G., Clementi, F., 2017. Uses and limits of the equivalent frame model on existing unreinforced masonry buildings for assessing their seismic risk: A review. Journal of Building Engineering 10, 166–182.

Raka, E., Spacone, E., Sepe, V., Camata, G., 2015. Advanced frame element for seismic analysis of masonry structures: model formulation and validation. Earthquake Engineering & Structural Dynamics 44, 2489–2506.

Rashid, Y.R., 1968. Ultimate strength analysis of prestressed concrete pressure vessels. Nuclear engineering and design 7, 334–344.

Ravenshorst, G., Messali, F., 2016. Out-of-plane tests on replicated masonry walls. Delft University of Technology. Final report 29.

Rinaldin, G., Amadio, C., Macorini, L., 2016. A macro-model with nonlinear springs for seismic analysis of urm buildings. Earthquake Engineering & Structural Dynamics 45, 2261–2281.

Roca, P., Cervera, M., Gariup, G., Pela', L., 2010. Structural analysis of masonry historical constructions. classical and advanced approaches. Archives of computational methods in engineering 17, 299–325.

Roca, P., Molins, C., Marí, A.R., 2005. Strength capacity of masonry wall structures by the equivalent frame method. Journal of structural engineering 131, 1601–1610.

Rots, J.G., De Borst, R., 1987. Analysis of mixed-mode fracture in concrete. Journal of engineering mechanics 113, 1739–1758.

Sacco, E., 2009. A nonlinear homogenization procedure for periodic masonry. European Journal of Mechanics-A/Solids 28, 209–222.

Sacco, E., Toti, J., 2010. Interface elements for the analysis of masonry structures. International Journal for Computational Methods in Engineering Science and Mechanics 11, 354–373.

Sangirardi, M., Liberatore, D., Addessi, D., 2019. Equivalent frame modelling of masonry walls based on plasticity and damage. International Journal of Architectural Heritage 13, 1098–1109.

Shen, Y., Chen, X., Jiang, W., Luo, X., 2014. Spatial force-based non-prismatic beam element for static and dynamic analyses of circular flexure hinges in compliant mechanisms. Precision Engineering 38, 311–320.

Shuang, L., Lili, X., Yuequan, B., 2009. Analysis of beam with variable cross-section by using direct element-based equilibrium framework. Chinese Journal of computational mechanics .

Sivaselvan, M.V., Reinhorn, A.M., 2000. Hysteretic models for deteriorating inelastic structures. Journal of engineering mechanics 126, 633–640.

Sorrentino, L., D'Ayala, D., de Felice, G., Griffith, M.C., Lagomarsino, S., Magenes, G., 2017. Review of out-of-plane seismic assessment techniques applied to existing masonry buildings. International Journal of Architectural Heritage 11, 2–21.

de Souza, R.M., Filippou, F.C., Pereira, A.M.B., Aranha Jr, G.Y., 2003. Force formulation of a non-prismatic timoshenko beam finite element for dynamic analysis of frames, in: XXIV Iberian Latin-American Congress in Computational Methods in Engineering, Ouro Preto, Brazil. pp. 789–813.

Soydas, O., Saritas, A., 2017. Free vibration characteristics of a 3d mixed formulation beam element with force-based consistent mass matrix. Journal of Vibration and Control 23, 2635–2655.

Spacone, E., Filippou, F.C., Taucer, F.F., 1996. Fibre beam–column model for non-linear analysis of r/c frames: Part i. formulation. Earthquake Engineering & Structural Dynamics 25, 711–725.

Stefanou, I., Sab, K., Heck, J.V., 2015. Three dimensional homogenization of masonry structures with building blocks of finite strength: A closed form strength domain. International Journal of Solids and Structures 54, 258–270.

Taliercio, A., 2014. Closed-form expressions for the macroscopic in-plane elastic and creep coefficients of brick masonry. International Journal of Solids and Structures 51, 2949–2963.

Taylor, R.L., 2017. FEAP - A finite element analysis program, version 8.5 .

Tomaževič, M., 1978. The computer program por. Report ZRMK 846.

Valanis, K.C., 1976. Thermodynamics of internal variables in the presence of internal forces. Journal of Applied Physics 47, 4765–4767.

Valente, M., Milani, G., 2016. Non-linear dynamic and static analyses on eight historical masonry towers in the north-east of italy. Engineering Structures 114, 241–270.

Vanin, F., Penna, A., Beyer, K., 2020a. Equivalent-frame modeling of two shaking table tests of masonry buildings accounting for their out-of-plane response. Frontiers in Built Environment 6, 42.

Vanin, F., Penna, A., Beyer, K., 2020b. A three-dimensional macroelement for modelling the in-plane and out-of-plane response of masonry walls. Earthquake Engineering & Structural Dynamics 49, 1365–1387.

Wen, Y.K., 1976. Method for random vibration of hysteretic systems. Journal of the engineering mechanics division 102, 249–263.

Zucchini, A., Lourenço, P.B., 2009. A micro-mechanical homogenisation model for masonry: Application to shear walls. International Journal of Solids and Structures 46, 871–886.